

University of Denver

Digital Commons @ DU

Electronic Theses and Dissertations

Graduate Studies

2020

Instrument and Application Development in Saturation Recovery and Rapid Scan Electron Paramagnetic Resonance

Joseph E. McPeak
University of Denver

Follow this and additional works at: <https://digitalcommons.du.edu/etd>



Part of the [Electrical and Computer Engineering Commons](#), [Other Chemistry Commons](#), and the [Physical Chemistry Commons](#)

Recommended Citation

McPeak, Joseph E., "Instrument and Application Development in Saturation Recovery and Rapid Scan Electron Paramagnetic Resonance" (2020). *Electronic Theses and Dissertations*. 1808.
<https://digitalcommons.du.edu/etd/1808>

This Dissertation is brought to you for free and open access by the Graduate Studies at Digital Commons @ DU. It has been accepted for inclusion in Electronic Theses and Dissertations by an authorized administrator of Digital Commons @ DU. For more information, please contact jennifer.cox@du.edu, dig-commons@du.edu.

Instrument and Application Development in Saturation Recovery and Rapid Scan

Electron Paramagnetic Resonance

A Dissertation

Presented to

the Faculty of the College of Natural Sciences and Mathematics

University of Denver

In Partial Fulfillment

of the Requirements for the Degree

Doctor of Philosophy

by

Joseph E. McPeak

August 2020

Advisors: Gareth R. Eaton and Sandra S. Eaton

©Copyright by Joseph E. McPeak 2020

All Rights Reserved

Author: Joseph E. McPeak

Title: Instrument and Application Development in Saturation Recovery and Rapid Scan Electron Paramagnetic Resonance

Advisors: Gareth R. Eaton and Sandra S. Eaton

Degree Date: August 2020

Abstract

Enhanced signal sensitivity by the use of Rapid Scan (RS) electron paramagnetic resonance (EPR), a technique that allows for much faster magnetic field scans than traditional field-swept techniques, has facilitated improved data acquisition for many types of samples. For example, irradiated fingernails for radiation dosimetry have been studied using RS-EPR, which resulted in substantial decreases in detection limits. Samarium-mediated reduction mechanisms in organic synthesis have been investigated by RS-EPR providing evidence for a radical intermediate. Spectra of organic radicals exhibiting both narrow lines and closely spaced hyperfine interactions have been recorded via RS-EPR. Well-resolved spectra can be recorded at a rate of 40 spectra/minute to gain insight into molecular changes on this timescale. RS-EPR performed at low temperatures using a closed cycle helium system and a cryostat containing a region with low electrical conductivity provides very wide (>9000 G) spectra free of passage effects near 5 K, expanding the capabilities of RS-EPR.

Recent developments in arbitrary wave form generators (AWGs) provide digital waveform synthesis at high enough frequencies to be used in EPR experiments at ca. 9 GHz (X-band). A new saturation recovery (SR) EPR spectrometer has been constructed with an AWG as the microwave source. Circuit design focuses on implementation of an X-band crossed-loop resonator with a reduced quality factor (Q) to minimize dead time due to resonator ring down processes. Increased accuracy of the AWG instrument relative

to conventional sources has made nitroxide spin-lattice relaxation time measurements possible via SR-EPR with S/N high enough to permit separation of electron and nuclear spin-lattice relaxation contributions. These results enabled more accurate estimation of the saturation factor in dynamic nuclear polarization (DNP) experiments.

Acknowledgements

The work detailed in this dissertation would not have been possible without the love and support from my wonderful and amazing fiancée Kathryn. I am forever grateful for her perseverance throughout the entirety of this process. I am also thankful for the love and support I have received from our parents during my studies in hopes that their investments would one day pay dividends.

The electrical engineering concepts outlined during the designing, building, and testing of the digital saturation recovery spectrometer were only possible with the expertise of Richard W. Quine. His lessons have been an inspiration in my current studies, and I will retain an unending gratitude for his advice. I continue to appreciate the guidance of Dr. Joshua Biller with whom I hope to continue collaborating with in the future. I am thankful for the instruction of Dr. Hanan Elajaili, requiring unending patience to overcome my stubbornness. Dr. Bryan Cowen and his then student, Dr. Chris Aretz, deserve significant appreciation for allowing me to explore organic chemistry concepts in their lab. My colleagues, Dr. Laura Buchanan, Lukas Woodcock, and Whylder Moore deserve special recognition both for their contributions to my projects and their contribution to the retaining of my sanity.

The lessons learned while working under Drs. Gareth and Sandra Eaton will not soon be forgotten. Relentless in their mentoring and spectacular in their ability to tackle all problems I encountered (and caused), I have nothing but the most gratitude. Together, they taught me to never give up, even when faced with the most formidable of reviewers. I am thankful to have been allowed to work under funding opportunities, NIH NCI AIP grant CA177744 and NSF grant CHE-1117992 awarded to Drs. Gareth and Sandra Eaton.

Table of Contents

Chapter One: An introduction to EPR Techniques.....	1
1.1 A brief introduction to the EPR experiment.....	3
1.2 EPR techniques and required instrumentation.....	8
1.2.1 Continuous wave.....	12
1.2.2 Rapid scan.....	15
1.2.3 Saturation recovery.....	21
1.3 Focus and scope of this dissertation.....	25
Chapter Two: Applications of RS-EPR for chemical investigations.....	27
2.1 Irradiated fingernails and implications for dosimetry analysis.....	29
2.1.1 S/N comparisons between CW and RS-EPR.....	30
2.2 Spin-trapping samarium mediated reductions.....	37
2.2.1 Reductive cyclization of 5-bromo-6-oxo-6-phenylhexyl methanesulfonate.....	39
2.2.2 Hyperfine analysis and mechanistic insight.....	49
2.3 High resolution RS-EPR.....	52
2.3.1 Bandwidth considerations.....	53
2.3.2 High resolution spectra.....	56
2.4 Fast acquisition RS-EPR.....	68
2.4.1 Data throughput and digitizer considerations.....	69
2.4.2 Tempol reduction via RS-EPR – How fast can we go?.....	71
2.4.3 Decay of common spin traps via bromine oxidation.....	75
Chapter Three: Development of a digital SR-EPR instrument.....	80
3.1 Instrument design and performance.....	82
3.1.1 Use of arbitrary waveform generators.....	83
3.1.2 Component layout and overview.....	86
3.1.3 Power delivery and tuning.....	88
3.1.4 The detection system.....	93
3.1.5 Testing system performance.....	97
3.2 Comparisons with a conventional SR spectrometer.....	110
3.3 Resonators.....	113
3.3.1 An X-band crossed-loop resonator.....	115
3.4 Nitroxides relevant to dynamic nuclear polarization.....	120
3.4.1 Carboxylproxyl and tempol measurements.....	125
Chapter Four: Adapting rapid scan EPR to low temperatures.....	130
4.1 Temperature dependence of relaxation.....	132
4.1.1 Passage effects.....	133
4.2 Instrument considerations.....	135
4.2.1 A metal-free, closed-loop cryogen EPR system.....	137
4.2.2 The RS scanning and detection systems.....	140
4.2.3 Resonator background at low temperatures.....	143

4.3 Low temperature spectroscopy.....	146
4.3.1 Slowly relaxing metal centers.....	147
4.3.2 Lanthanide aquo-ions.....	152
Chapter Five: Conclusions and comments on future work.....	158
5.1 Proposed improvements to the saturation recovery spectrometer	159
5.2 Expanded use of the X-band crossed-loop resonator.....	161
5.3 The next challenge in low temperature rapid scan.....	164
5.4 The greatest barriers to rapid scan kinetics experiments	166
Bibliography	169
Appendices:	
A.1 Matlab programs for generating waveforms for Digital SR	185
A.2 List of equations by section	189
A.3 List of abbreviations and common names.....	192
A.4 Publications and presentations	194

List of Figures

1.1 Resonance condition for a spin $\frac{1}{2}$ unpaired electron	5
1.2 Simple EPR spectrometer block diagram	9
1.3 Effects of modulation on the EPR absorption signal	14
1.4 Differences in modulation between CW and RS	16
1.5 Block diagram of an RS spectrometer	17
1.6 Total resistance vs. scan frequency in solid wire and Litz wire coils.....	18
1.7 Effects of increasing scan rate on the observed RS signal.....	20
1.8 Overview of the experiment.....	22
1.9 Comparison between SR and other methods to measure T_1	23
2.1 Comparison of RS in irradiated fingernails	31
2.2 Comparison of the RS and CW power saturation behavior in irradiated fingernails	32
2.3 Comparison of RS and CW in irradiated fingernails	33
2.4 S/N vs. the square root of microwave power in RS of irradiated fingernails	34
2.5 Power saturation behavior for irradiated fingernails via RS at 35 kHz	36
2.6 Possible reaction schemes for the samarium mediated reduction of 5-bromo-6-oxo-6-phenylhexyl methanesulfonate	40
2.7 RS spectra of the reaction of SmI_2 and substrates in the presence of PBN	44
2.8 RS spectra of the reaction of SmI_2 and substrates in the presence of MNP	45
2.9 RS spectra of the reaction of SmI_2 and substrates in the presence of MNP after an aqueous workup and evacuation of O_2	47
2.10 RS spectra of DTBN for comparison with the reaction of MNP and SmI_2	48
2.11 Measurements of stability in spin-trapped adducts comparing S/N between CW and RS	50
2.12 Summary of the supported mechanism for the Sm mediated reduction of 5-bromo-6-oxo-6-phenylhexyl methanesulfonate	52
2.13 Radicals investigated in the demonstration of high-resolution RS spectra	57
2.14 RS spectra of CTPO.....	60
2.15 RS and CW spectra of CTPO.....	62
2.16 RS and CW spectra of DPNO.....	64
2.17 RS and CW spectra of galvinoxyl.....	66
2.18 CW and RS experiments with tempol and ascorbic acid.....	72
2.19 Kinetics of the reaction between tempol and ascorbic acid recorded via CW and RS	73
2.20 Signal intensity vs. time for varying ascorbic acid concentrations when reacting with tempol	74
2.21 Proposed reaction of commonly used spin-traps in the presence of Br_2	76
2.22 RS spectrum and reaction kinetics of the oxidation of DMPO.....	77
2.23 RS spectra and reaction kinetics of the oxidation of PBN.....	78
3.1 Differences in analog and digitally synthesized waveforms.....	85

3.2	Block diagram of the digital SR spectrometer microwave bridge	87
3.3	Block diagram of the excitation pathways within the DSR bridge.....	90
3.4	Block diagram of the tuning paths within the DSR bridge.....	92
3.5	Block diagram of the detection system within the DSR bridge.....	94
3.6	Block diagram of the video amplifier within the DSR bridge	96
3.7	Errors associated with the output of a fundamental oscillator.....	98
3.8	Comparison of source noise in a Bruker Gunn diode, a Tektronix AWG and the same AWG with a Wenzel external clock source	100
3.9	Increases in noise with incongruent repetition of waveform synthesis	101
3.10	Relationship between gain and noise figure of an ideal amplifier.....	104
3.11	SR data collected with the DSR with residual analyses	107
3.12	SR data of irradiated quartz at different field positions	108
3.13	Stability of the DSR when performing SR measurements.....	110
3.14	Tuning adjustment diagram in the excitation resonator of the X-band CLR.....	116
3.15	Pictures and diagrams of the X-band CLR	116
3.16	SR measurements of coal and DICPO using the X-band CLR.....	118
3.17	S/N observed when using the X-band CLR with waveguide connections	119
3.18	Molecular structures of tempol and carboxyproxyl	124
3.19	Relaxation times obtained using the DSR for tempol and carboxyproxyl with varying concentrations	126
3.20	Residual analysis of biexponential and single exponential fits of tempol and carboxyproxyl SR relaxation data	127
4.1	Examples of passage effects observed by CW	135
4.2	Pictures of the RS spectrometer with both the metal-free cryostat and Stinger system in operation	138
4.3	Stability of the low temperature system over a period of a few weeks	140
4.4	Investigations of eddy currents present in the metal-free cryostat using trityl-CD ₃ and Cu(dtc) ₂	142
4.5	Block diagram and recorded attenuation of the high pass filters employed in low temperature FSDD measurements	143
4.6	Spectra of the ER4118X-MD-5 resonator background at low temperatures	145
4.7	Spectra of slowly relaxing metal centers at low temperatures.....	150
4.8	Spectra of rapidly relaxing lanthanide ions in frozen solution	156
5.1	Proposed modifications to the DSR bridge to expand pulse capabilities	160
5.2	Frequency-stepped SR measurements of coal using a frequency difference of 62 MHz.....	164

List of Tables

1.1 Collected references to further explain the topics of EPR	3
2.1 Differences in trapping mechanisms in aminoxyl, nitron, and nitroso spin traps	37
2.2 Molecular structures of several spin traps used in the investigation of Sm mediated reductions	42
2.3 Hyperfine coupling observed in the spin-trapped adducts of the reaction of SmI ₂ and 5-bromo-6-oxo-6-phenylhexyl methanesulfonate.....	49
2.4 S/N observed in CW and RS when investigating the stability of the observed spin-trapped adducts	51
2.5 S/N observed in CW and RS when collecting high-resolution RS spectra.....	67
2.6 Molecular structures of several spin traps used in the investigation of oxidation kinetics via RS	69
2.7 Comparison of data throughput when performing kinetics experiments with CW and RS	70
3.1 Summary of components present in the DSR bridge.....	88
3.2 Molecular structures of the samples used to evaluate the capabilities of the DSR.....	106
3.3 Comparison of the overall gain and noise figure of the DSR and a conventional SR spectrometer	111
3.4 Comparison of the S/N in experiments using the DSR and a conventional SR spectrometer	112
3.5 Efficiencies, loaded Q, and instrumental dead time of several resonators when performing SR experiments with the DSR.....	114
3.6 Properties of the orthogonal resonators within the X-band CLR	117
3.7 S/N observed when using the CLR vs. a conventional TE ₁₀₂ cavity resonator for SR measurements	120
4.1 Relaxation times in slowly relaxing metal centers at temperatures between 4-10 K	149
4.2 Electronic configurations of the trivalent lanthanide ions	154
4.3 Relaxation times in rapidly relaxing lanthanide ions at temperatures between 4-10 K	155

Chapter One: An Introduction to EPR Techniques

“Your task is to know everything we knew yesterday, today.”

- Dr. Gareth Eaton

The abridged selection of introductory topics included in this chapter serves as a survey of concepts explored and experiments performed in pursuit of the doctoral degree under the direction of Drs. Gareth and Sandra Eaton. Along with many other talented and dedicated professors and engineers, Drs. Eaton have authored a multitude of manuscripts ranging from introductory topics to rigorous experimental endeavors and original findings in the field of EPR spectroscopy. Under their guidance, the concepts of continuous wave, saturation recovery, rapid scan, and various pulse EPR techniques were explored to provide a breadth of application and instrument development. The overarching focus of this dissertation is the development and application of EPR methods; however, the greatest lesson to be learned from Drs. Gareth and Sandra Eaton pertains to the methods of exploration.

The motivation for this dissertation stems from *EPR at Work* edited by Dr. James S. Hyde, Gareth R. Eaton, and Sandra S. Eaton and *Electron Spin Resonance* by Dr. Charles P. Poole Jr., as well as the copious publications by Richard W. Quine, as these collections have provided considerable framework for the research performed in the pursuit of my doctoral degree.^{1,2,11,12,3-10} The examples collected in *EPR at Work* provide

a conceptual framework of the multitude of applications to be studied using EPR and serve as a statement of purpose when studying new methodology.¹⁻⁴ To apply new methodology, new developments in instrumentation are often necessary and as such the teachings of Dr. Charles P. Poole Jr. are an excellent reference, providing detailed explanations of the inner workings of the spectrometer.⁵ These explanations formed a basis such that the advanced component and instrument designs of Richard W. Quine may be accessible to the chemist lacking formal engineering training, of which there have been many.⁶⁻¹² These collected works have influenced the structure and goals of the doctoral research described herein.

The introductory topics described in the beginning sections are not the focus of this dissertation; and, will only serve as a primer such that the chapters to follow may be somewhat digested without the need of a thorough understanding of the techniques employed. Because the focus of this dissertation is development, the sections explicitly describing an experimental technique will primarily be explained in the context of the EPR spectrometer hardware and capabilities rather than a detailed account of the physics of the spin system to be investigated. A table of reference volumes that have proven useful to me in the understanding of EPR is provided (Table 1.1).

Table 1.1: Collected references that have been paramount to understanding the complexities of the EPR experiment and spectrometer.

Title	Authors/Edited by	Reference
Electron Spin Resonance, 2 nd ed.	Charles P. Poole Jr.	5
Quantitative EPR	Gareth R. Eaton, Sandra S. Eaton, David P. Barr, Ralph T. Weber	13
Electron Paramagnetic Resonance of Transition Ions	A. Abragam and B. Bleaney	14
Electron Paramagnetic Resonance, 2 nd ed.	John A. Weil and James R. Bolton	15
Principles of Pulse Electron Paramagnetic Resonance	Arthur Schweiger and Gunnar Jeschke	16
Multifrequency Electron Paramagnetic Resonance	Sushil K. Misra	17

1.1 A brief introduction to the EPR experiment

The first electron paramagnetic resonance experiment was performed by E. K. Zavoisky in January of 1944, giving birth to what is now a large community of physicists, chemists, biologists, and practitioners of medicine.¹⁸ Zavoisky's early experiments investigated the magnetic properties of manganese and copper using frequencies and magnetic field strengths that may be considered low in the context of the modern spectrometer.^{15,18,19} The development of the EPR spectrometer was largely facilitated by the efforts to improve RADAR technologies during World War II, expanding both the capabilities and, more importantly, the availabilities of critical microwave components such as microwave generating klystrons and sensitive crystal detectors.²⁰ These developments did not result in widespread usage of EPR; and, through 1974 it was a good year if Varian sold more than 50-60 spectrometers.²⁰ The modern CW spectrometer marketed by Bruker Biospin features a high quality resonator and a Gunn diode source, two key components that greatly improved the EPR spectrometer

functionality. Additional improvements were made by the incorporation of a reference arm, high-isolation circulators, and magnetic field modulation in CW experiments. These spectrometers are now found in many academic and commercial labs throughout the world. Spectrometer development includes step-functions, making large strides only when considerable hardware improvements are implemented. RS and low noise, programmable microwave sources will likely provide the next steps in increased potential for experimentation.

Concerning the EPR experiment, an understanding of the underlying physics is necessary. The magnetic moment of the electron is a fundamental quantum mechanical property and is directly related to its spin and orbital momentum.⁵ The intrinsic properties of the electron may be visualized as analogous to a spinning top, revolving around a central nucleus.²¹ The EPR experiment aims to study paramagnetic electron spin systems. Paramagnetism is a classification given to systems that exhibit a magnetic moment in the presence of a magnetic field and do not in the absence of a magnetic field.¹⁴ This phenomenon in the context of spectroscopy is referred to as the Zeeman effect; and, when studying electrons via EPR, gives rise to the observed spectrum.^{13,21} In this way, EPR seeks to characterize the input of energy into the spin system for the observation of interactions of the spin system with the external world. In the magnetic field, the magnetic moment may be aligned with or against the magnetic field, giving rise to two quantized energy levels separated by the energy supplied to fulfill the resonance condition (Fig 1.1).^{13,21} The separation in energy between the two levels, assuming a spin $\frac{1}{2}$ system, is described by the following equation,

$$\Delta E = h\nu = g\mu_B B_0 \quad \text{Eq. 1.1}$$

where B_0 is the magnetic field, ν the microwave frequency, g is the Lande g factor, μ_B is the Bohr magneton.¹³ The Bohr magneton is defined as follows,

$$\mu_B = \frac{|e|\hbar}{2m_e} = 9.27400949(80) \times 10^{-24} \text{ JT}^{-1} \quad \text{Eq. 1.2}$$

where e is the charge of the electron, \hbar is Planck's constant in angular units, and m_e is the mass of the electron.¹⁵ The free electron g factor, g_e , is unitless and equal to 2.002319304617(15).¹⁵ The g factor of the observed paramagnetic species in the EPR experiment gives a unique identifier that is independent of microwave frequency and magnetic field, allowing for the comparison and characterization of paramagnetic species similar to the chemical shift in nuclear magnetic resonance.¹³ Ligands and adjacent atoms, as well as electron delocalization and spin-orbit coupling, cause deviation of the observed g factor from the free electron g factor, g_e , and give some clues as to the electronic environment of the paramagnetic center under investigation.¹³

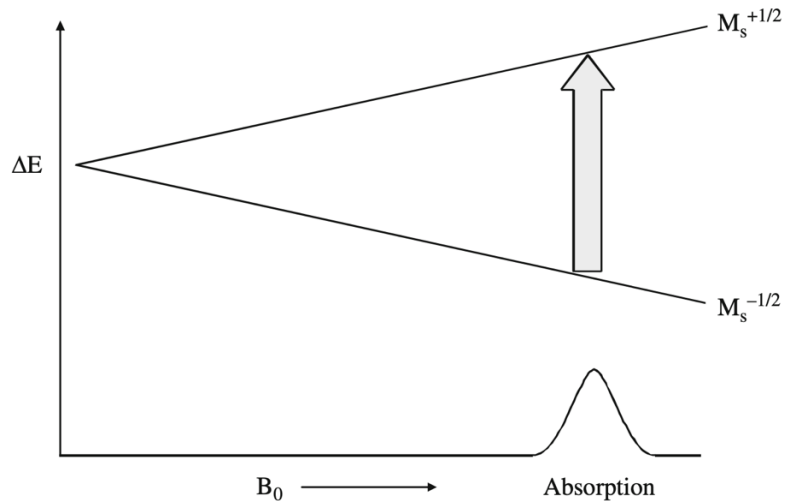


Fig 1.1: Resonance condition for a spin $\frac{1}{2}$ unpaired electron. The absorption of energy occurs at the g position that is satisfied by the magnetic field and microwave frequency of the EPR spectrometer. Adapted from Eaton et al.¹³

The EPR experiment currently is not sensitive enough to detect a single unpaired electron; and, the observed EPR signal is the sum of all magnetic moments present in the resonator.^{13,21} Therefore, the signal is proportional to the difference in populations between those spins in the low energy state aligned in the direction of the magnetic field or the high energy state aligned in the opposite direction of the magnetic field.¹³ The population difference is governed by the Maxwell-Boltzmann distribution described as follows,

$$\frac{n_{\text{antiparallel}}}{n_{\text{parallel}}} = e^{-\frac{\Delta E}{kT}} \quad \text{Eq. 1.3}$$

where k is the Boltzmann constant and T is the temperature of the experiment.^{13,21} The differences in the number of spins aligned parallel to the main magnetic field and those aligned antiparallel is quite small, only 0.08% at X-band (ca. 9 GHz) and room temperature.¹³ Application of a microwave excitation field perpendicular to the main magnetic field disturbs the thermal equilibrium of these populations, and gives rise to the EPR absorption signal, which is the net effect of absorption and emission of energy.^{13,18}

A single unpaired electron in an isolated environment, hypothetically, would yield an EPR spectrum consisting of a single absorption line that is very sharp and narrow. Not only is this case impossible to obtain, it is unsuitable for the characterization of a magnetic environment that is interesting to the investigator. In practice, deviations from the hypothetical free electron spectrum may give a wealth of information about the electronic environment, such as interactions with neighboring magnetic moment containing particles like nuclei or other electron spins, especially when considering the ensemble average typically observed.¹³ It is possible to observe phenomena unrelated to

the spin system by manipulation, or more likely poor optimization, of the selected spectrometer operating parameters and these will be discussed in detail when relevant.

The most commonly observed interactions are those with nearby nuclei containing magnetic moments, defined as hyperfine interactions.^{5,13-15} The nuclear spins contribute to the net magnetic field at the unpaired electron. In small organic molecules, these are typically nearby neighbors of an isolated radical. In large, metal-ligand centers, hyperfine interactions may arise from both the nuclear spin of the metal center and from organic ligands. The interaction with a nearby nuclear spin splits the EPR absorption signal into multiple lines, with different energy for each transition.^{5,15} Because nuclear spin energy levels in the presence of a magnetic field are quantized as electron spin energy levels are, the hyperfine splitting observed is discrete; and, the number of spectral lines may be calculated based on the following equation,

$$N_{HFS} = \prod_i (2n_i I_i + 1) \quad \text{Eq. 1.4}$$

which combines the contributions from all nuclear spin interactions.⁵ Here, the number of hyperfine components in the EPR spectrum results from both the number of equivalent nuclei, n_i , and the spin associated with each nucleus, I_i .⁵ When multiple nuclei are interacting with the spin system under investigation, additional information concerning the energy levels present may be gained by comparing the intensity of the absorption lines with respect to hyperfine interactions.^{5,15} The degeneracy present arising from the interaction with nearby nuclei results in the ratio of intensities of the EPR signals coupled by hyperfine interactions.^{5,15}

Spectra resulting from more complex spin systems ($S > 1/2$, such as Fe(II) or Cr(III)) further complicates spectral assignment, as do the presence of multiple homo and heteronuclei and intrinsic nuclear spin in metal paramagnetic centers. In some paramagnetic systems differing isotopes may have distinguishable nuclear spins and can have transitions that are not located at the same magnetic field positions; and, in these cases anisotropy may also be observed in both g and hyperfine coupling.^{14,15} Much like in the interaction with nuclear spins, additional spectral information is present when nearby unpaired electrons interact with one another.^{14,15} These interactions may arise from several scenarios such as magnetically concentrated $S = 1/2$ samples, multiple spin centers tethered by an organic linker, or metal centers that contain multiple unpaired electrons.^{14,15} Extraordinary efforts have produced simulation packages that allow calculation of these interactions by least-squares analysis of a recorded EPR spectrum and are often employed in the investigation of newly discovered paramagnetic centers.^{17,22,23}

1.2 EPR techniques and required instrumentation

Various instrument applications of EPR have been designed to encompass a variety of frequencies and fields of observation and a wealth of effort has been dedicated to improving experimental aspects of the spectrometer with each iteration. The modern EPR spectroscopist now has access to a multitude of techniques and methods that may be tailored readily to the desired information concerning the spin system of study. Though techniques, methods, and therefore instrumentation now take many forms, the overall technical basis has changed very little from the introductory efforts of the field. The

primary basis of any EPR spectrometer in the simplest construction consists of four core systems; the microwave source, the resonator, the main field magnet, and the signal recorder (Fig 1.2).⁵ Each of these components is adapted and developed to the task at hand in purpose-built spectrometers; and, many multi-use components exist allowing for versatile instrumentation to be developed.^{5,6,8,9}

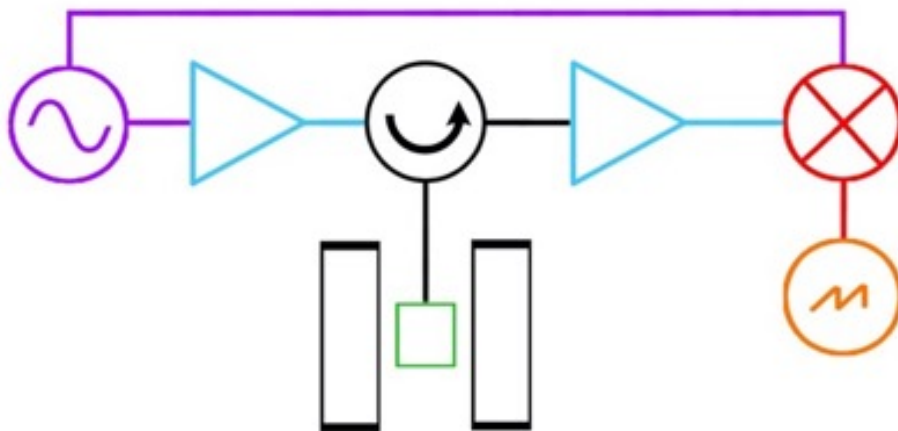


Fig 1.2: Simple EPR spectrometer consisting of a microwave source (*purple*), power and signal amplifiers (*blue*), the main magnet (*black*), the resonator (*green*), a detector (*red*), and a signal recorder or digitizer (*orange*), connected in series for signal excitation and observation. A circulator directs the microwave signal from the source, to the resonator, and to the detector.

The microwave source forms the basis of the experiment and supplies a frequency for the resonance condition, defined by the resonator and sample of interest.⁵ The most often used frequency is ca. 9 GHz due to the increased availability of microwave sources operating at this frequency, specifically klystrons, resulting from RADAR development during WWII.^{13,15,19} In the modern common spectrometer, the klystron has often been replaced by a Gunn diode; and in some cases, an arbitrary waveform generator is employed to increase experimental flexibility.^{13,24} Currently, the Gunn diode is the standard microwave source in EPR spectrometers due to the prevalence of diodes with low source noise, sometimes called phase noise.¹⁵ For very specific applications, voltage-

controlled oscillators chained by multipliers have been employed as the microwave source, mostly in EPR on a chip configurations and other applications where low cost is a priority.²⁵ Additionally, multiple microwave sources may be employed to modulate the result obtained with a single source or to excite multiple spin centers of differing resonances.²⁶

The resonator houses the spin system to be studied and is purposefully chosen such that when power is supplied at a specific frequency an excitation field (B_1) is created.^{5,13,27} The resulting microwave field, properly concentrated at the sample of interest, will excite the magnetic dipoles of the sample for observation.^{13,27} In most cases, the observable signal is very small relative to the input power and the instrument must be designed with this consideration. Resonator qualities vary widely based on the required application and will be discussed in context with the respective experiment descriptions to follow. All resonators; however, will dissipate some input energy as heat due to having a finite Q value and this may be detrimental to the EPR experiment.

In most commercial and homebuilt spectrometers, amplifiers are placed before and/or after the resonator; each with a separate purpose.^{5-8,28} When using digital microwave sources, an amplifier placed after the microwave source but before the resonator is often required due to insufficient power output from the microwave source to adequately excite the spin system.^{28,29} The EPR experiment typically requires a large range of adjustable power to the resonator to study differing spin systems.²⁹ Because of this, even when output power from the microwave source is sufficient for some experiments, both an amplifier and attenuator will follow the microwave source to increase the range of power incident on the resonator such that vastly different spin

systems may be studied.^{5,13,29} An amplifier placed after the resonator and before the detector is necessary for techniques that require low incident power on the spin system during observation of the signal, or in pulse systems when there is no power to the sample during observation of the echo.^{29,30} These techniques are designed to minimize perturbation of the spin environment and the resulting signal must be amplified to reach a great enough intensity to be measurable by the detector.^{29,30}

At lower frequencies (ca. 1 GHz or less) where the signal may be adequately detected and recorded at baseband, the detector and signal recorder may immediately record the amplified signal coming from the resonator. A crystal detector is often used in modern spectrometers and is followed by a computer-controlled analog-to-digital (A/D) converter or digitizer.^{5,13,15} However, when operating at higher frequencies (>1 GHz) it is advantageous to utilize a double-balanced mixer as a phase sensitive detector.³¹ When supplied with a reference signal, the detected signal is near DC levels and may be digitized by A/D converters with much lower sampling rates than would be needed for digitization at the resonant frequency.^{29,31}

The EPR spectrometer is designed with a single goal in mind, to measure the response of an excited spin system. The observable voltage change in the resonator differs widely by experiment. The subsequent sections will describe the EPR methods employed within this dissertation, outlining instrumental considerations as they relate to the expected observable voltage and the information to be gained about the spin system from this observation. All experiments detailed herein were performed at ca. 9 GHz (X-band).

1.2.1 Continuous wave

In a CW experiment, the microwave frequency is held constant and at low power while the magnetic field is swept at a rate that is slow relative to relaxation.^{13,21} The resulting resonance is recorded on a magnetic field axis such that lineshape, linewidth, hyperfine coupling, saturation behavior, and molecular tumbling rate may be examined.^{13,21} CW is by far the most widely used EPR technique and is often considered the most accessible due to less expensive equipment, low operating power, and friendliness to the end-user for commercial applications. In most cases, a klystron or Gunn diode is used as the microwave source and the source power is sufficient that a power amplifier is not required before the resonator.⁵ The microwave excitation is performed at low power to disturb the spin system very little and careful attention must be paid to the saturating conditions of the sample.¹³

When performing the CW experiment, the voltage of the observed signal may be expressed according to the equation,

$$V_s = \chi'' \eta Q \sqrt{P_A Z_0} \quad \text{Eq. 1.5}$$

where V_s is the resultant signal voltage, χ'' is the magnetic susceptibility of the sample, η is the filling factor of the sample in the resonator, Q describes the quality factor of the resonator, P_A is the power incident on the resonator, and Z_0 describes the transmission line impedance connecting the resonator.³¹ The incident power on the resonator depends greatly on the microwave source and the quality of the transmission lines. The typical CW microwave source has a maximum power output of 200 mW and is often attenuated to avoid saturating conditions.¹³ Because of the microwave loss in commonly used SMA cables at frequencies above a few GHz, waveguide is often the preferred transmission

line at X-band and higher frequencies. The typically employed transmission line impedance is 50 ohms.¹³ When properly performed, the observed signal voltage is proportional to the magnetic susceptibility, representative of the number of unpaired spins in the sample.¹⁴

The resonator filling factor and quality factor are inherent to the design of the resonator employed for the CW experiment.¹³ It is imperative to maximize the resultant signal voltage, which requires maximizing the resonator quality factor with the sample inside the resonator. A commonly used expression of resonator quality factor is as follows,

$$Q = \frac{\nu}{\Delta\nu} \quad \text{Eq. 1.6}$$

where ν is the resonant frequency and $\Delta\nu$ is the bandwidth of the resonator when critically coupled.¹³ Maximizing Q requires minimizing the bandwidth of the resonator, which has limitations dependent on resonator construction. The filling factor may be described as the ratio of sample to non-sample volume within the microwave excitation field.¹³ Early CW resonators primarily consisted of metal cavities and suffered from low filling factors; however, modern CW resonators may have smaller dimensions and may use dielectric materials such that much greater filling factors are achieved while maintaining high quality factors. Both resonator Q and filling factor increase signal voltage in a linear fashion, resulting in larger S/N for high resonator Q and filling factor relative to measurements made where these quantities are low.

Despite these advances, the resultant signal voltage is still very small relative to detectable noise levels of the instrument. Because of this, additional modulation and lock-in detection are used to modulate the signal for phase-sensitive detection.^{5,13} This is

accomplished by supplying a rapidly modulating magnetic field that is superimposed on the discretely stepped main field.^{5,13} The modulation field is typically much smaller than the total field sweep and results in the lock-in detection of the first derivative signal of the EPR absorption line shape (Fig 1.3).⁵ This modulated signal is broadened if the amplitude is too large and care must be taken to minimize the modulation field relative to the expected signal width such that broadening is not observed.¹³

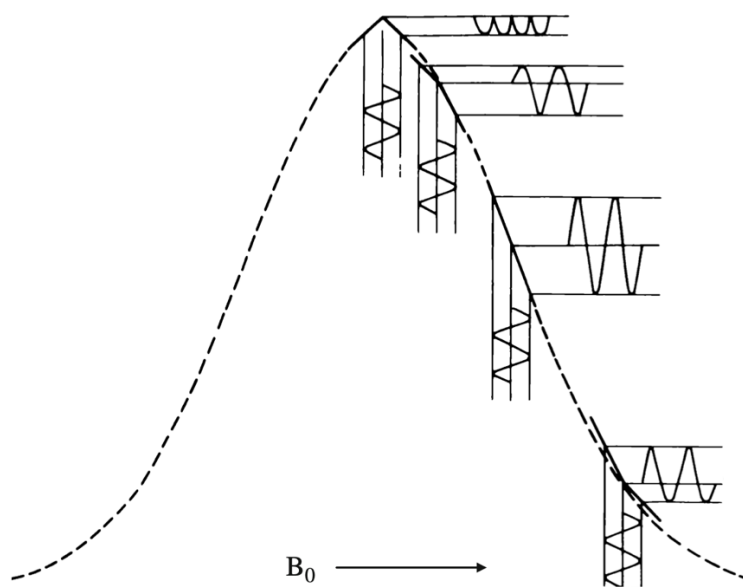


Fig 1.3: Effects of magnetic field modulation on the EPR absorption signal. The recorded derivative signal is a measure of the rate of change, in voltage, of the EPR absorption signal between the extremes of modulation. Adapted from Poole.⁵

In some cases, even with modulation and lock-in detection, the signal voltage is still rather small relative to noise. Signal averaging is employed in these cases and results in an increase in accumulated voltage relative to the accumulated noise in the spectrum by co-adding several spectra sequentially.¹³ When signal voltage is properly maximized, the modern CW spectrometer becomes a versatile tool for measuring the electron resonance environment. CW is by far the most used technique due to the affordability of

commercial CW spectrometers compared to more advanced pulse and transient spectrometers.

1.2.2 Rapid scan

Rapid scan EPR is a field-swept EPR technique where the magnetic field is swept rapidly relative to the relaxation rate of the spin system under investigation; which, has traditionally been a problem for CW.^{17,32} In a typical CW experiment, the main magnetic field is slowly incremented accompanied by field modulation that does not encompass the complete EPR linewidth. Small modulation coils are placed near the sample, often inside the resonator housing, creating a modulating scan field across the sample. In contrast to this, in RS the main magnetic field is held constant and large field modulation is employed, with field sweeps that often encompass the entire linewidth of the EPR spectrum in a single modulation cycle (Fig 1.4).³² This is accomplished by placing large scan coils external to the resonator housing for a large, uniform scan field that is homogeneous over the entirety of the resonator B_1 field.³²⁻³⁴ The lock-in amplification and phase-sensitive detection employed in CW is not used in RS, and instead, a transient digitizer is used to record the EPR signal in quadrature.^{17,32,34} Signal acquired during multiple cycles of the continuously oscillating magnetic field may be combined to increase the number of spectral averages in addition to signal averaging in the digitizer; and, both real and imaginary signal may be combined to further increase the intensity of the detected signal (Fig 1.4).^{17,32,35,36}

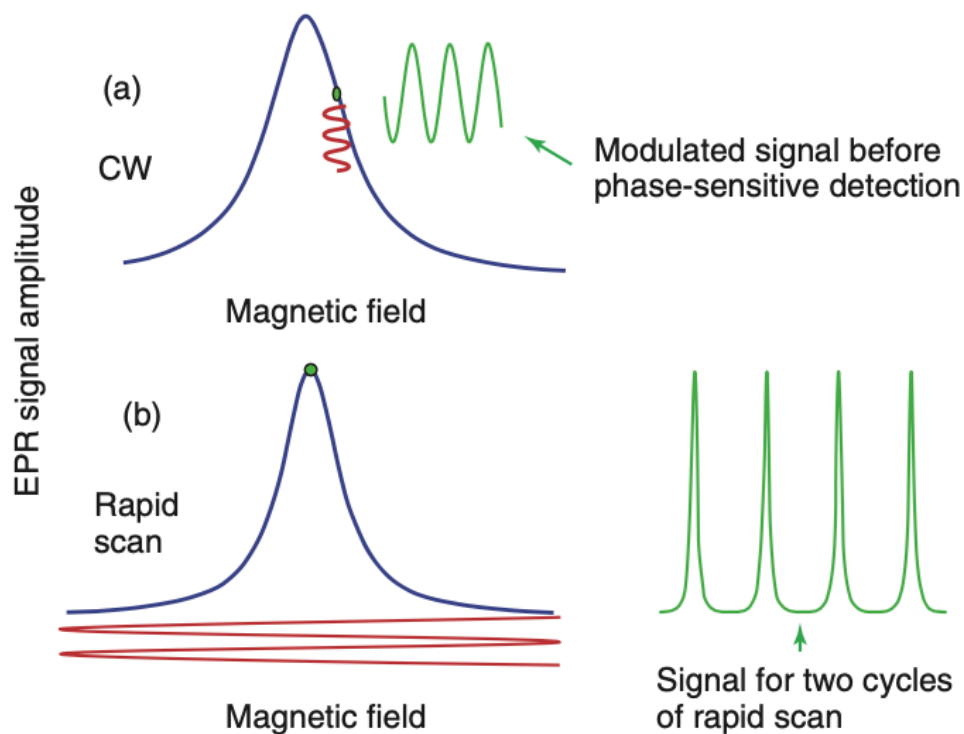


Fig 1.4: Differences in modulation present in CW (a) and RS (b). Multiple cycles of modulation are shown in both cases; however, only in RS does each modulation cycle produce an entire field-swept spectrum. Reproduced with permission from Eaton et al.³⁵

Significant modifications to the traditional CW spectrometer are required to perform RS experiments with high fidelity over large sample spaces. A simplified diagram of an RS spectrometer is given in Fig 1.5.³² The primary differences consist of replacing the typically employed lock-in detection with quadrature detection and a transient digitizer.^{32,34} The RS detection system also requires greater bandwidth than in typical CW bridges. It is possible to perform RS measurements using existing CW modulation coils within typical CW resonators; however, these coils are typically very small and restrict sample size greatly when considering homogeneous scan fields are required.^{37,38} Instead, it is preferable to use external scan coils, mounted on the outside of the resonator, and a dedicated coil driver that is properly adjusted to the performance of

the scan coils.^{10,12} Because a large and rapidly-varying magnetic field is imposed on the resonator, it is imperative that the resonator be constructed primarily from non-conducting components such that eddy currents induced in the resonator are minimized.³² The resonator employed in all RS experiments described herein was a Bruker ER4118X-MD-5 dielectric resonator composed of sapphire. Signals obtained with this resonator display minimal broadening attributed to eddy currents.³³

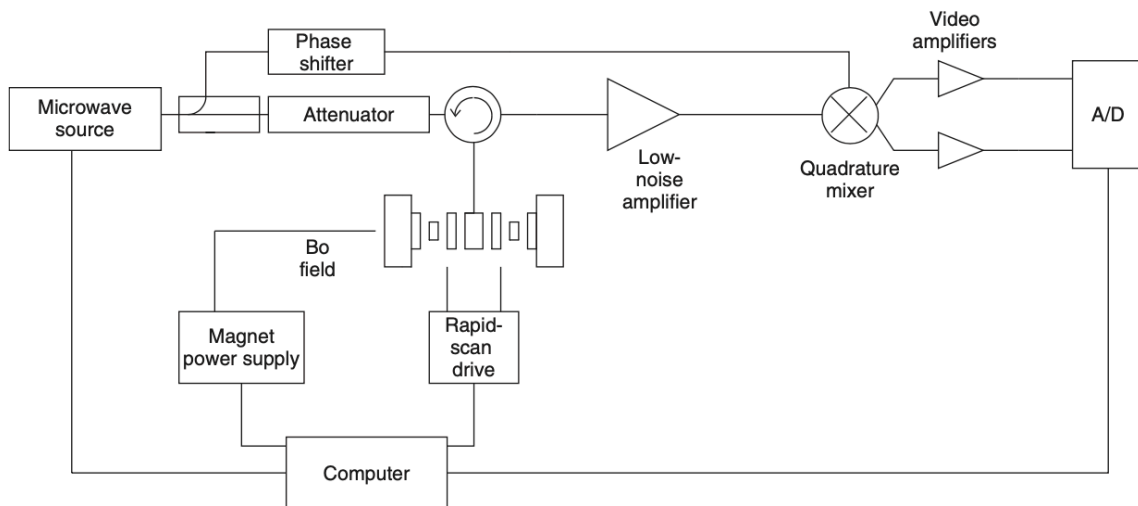


Fig 1.5: Block diagram of an RS spectrometer with RS coil driver, quadrature detector, and two channel transient digitizer shown. The coil driver may be controlled by software in the computer or manually. A low voltage signal is sent from the coil driver to the digitizer to trigger data collection, not shown. Reproduced with permission from Eaton et al.³²

For quantitative measurements, careful attention must be paid to the scan coil and coil driver construction and operation. The current implementations of RS coil drivers consists of both linearly driven and resonated circuit scan drivers, each with a specific application in the RS experiment.^{10,12} Because the voltage required to produce an arbitrary current in the scan coils is much greater than that of a sinusoidal current produced from a resonated circuit, the scan driver requirements are much less strenuous when considering RS experiments using resonated, sinusoidal scanning waveforms.

Additionally, coil design plays a significant role in driver requirements. Small, Litz wire scan coils are preferred due the smaller increase in resistance of the coils with increasing scan frequency (Fig 1.6).^{39,40} Lowering the resistance of the scan coils ensures the driver can provide a constant, low error, scanning waveform with proper voltage output.³⁹ A high-gain compensation network is necessary when performing RS experiments with arbitrary scanning waveforms. Compensation is not required when using resonated circuits, and hence sinusoidal waveforms.³⁹ It is therefore advantageous to employ a resonated sinusoidal scanning waveform when large magnetic field sweep widths are desired. The continuously variable scan rate in a sinusoidal scan can lead to variations across the spectrum, broadening the spectrum due to bandwidth limitations and signal saturation.

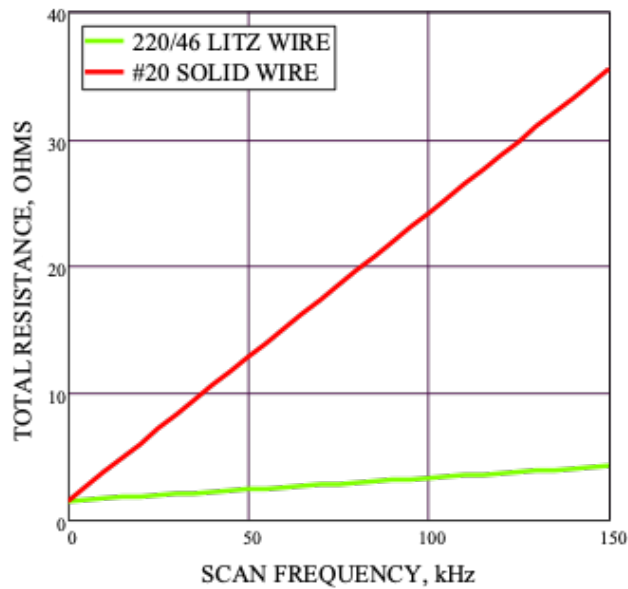


Fig 1.6: Total resistance, in Ohms, observed for two 60 turn, 76 mm diameter coils made of either solid wire (*red*) or 220/46 Litz wire (*green*) as a function of scan frequency. Lower resistance decreases scan driver hardware requirements considerably. From Quine et al, *unpublished*.³⁹

Unlike CW data, RS data are not presented as a derivative spectrum and instead the absorption and dispersion signals may be recorded via quadrature detection and later combined into a final spectrum.^{32,36} The absorption spectrum is directly detected; and, therefore any transient effects resulting from fast scan rates are observed in the EPR spectrum.³² At very fast scan rates relative to the relaxation of the irradiated signal, an FID-like oscillation is detected resulting from magnetization in the x-y plane imposed by the rapid field scan (Fig 1.7, *left*).³² The detected EPR signal in RS experiments is described as the convolution of a driving function with the “slow-scan” oscillation-free EPR spectrum. The signal may be deconvolved in the Fourier domain to recover the oscillation-free EPR spectrum.³² The recovered slow-scan spectrum compares well with spectra recorded by CW methods. In the absence of oscillations due to scan rate, the deconvolution process does not change the shape of the observed spectrum (Fig 1.7, *right*). Beyond oscillations, both a sinusoidally varying background signal and a slowly varying polynomial background signal are typically present in the deconvolved, slow-scan spectrum. Both may be fit and removed via post-processing, using either open source or locally written programs.

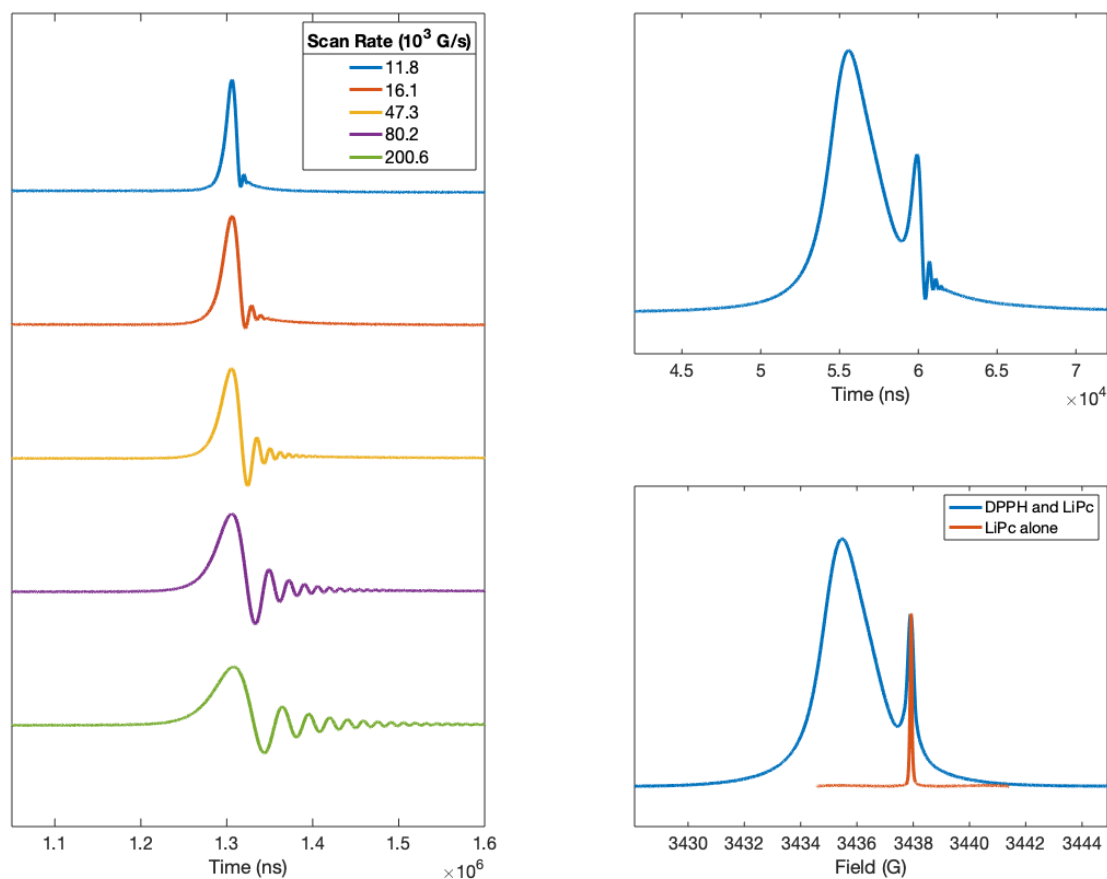


Fig 1.7: Effects of increasing scan rate (in Gauss per second, G/s) on the observed RS spectrum of LiPc before deconvolution (*left*). The observed RS spectrum of overlapping signals from LiPc with oscillations and DPPH that does not exhibit oscillations, recorded at a scan rate of 5.84×10^5 G/s (*top, right*). After deconvolution of rapid passage effects, the “slow scan” spectrum is recovered free of artifacts in both DPPH and LiPc (*bottom, right*). The rate was much faster when recording DPPH and LiPc together, broadening the LiPc linewidth.

In the current generation of RS spectrometers in the Eaton lab, a limit in scan driver capabilities restricts the width of the magnetic field scan to less than 155 G sweep width.⁴¹ However, it has been demonstrated that large field sweeps are possible by combining several RS spectra of smaller width, obtained in sequence by incrementing the main magnet field in discrete steps.^{40,42} This method enables wide field scans via RS spectroscopy while preserving the deconvolution processes and S/N advantages afforded by RS.

1.2.3 Saturation recovery

Saturation recovery EPR is a technique that may be performed by either pulse or CW methods to measure spin lattice relaxation time T_1 .^{16,30} As it relates to this dissertation, saturation recovery is performed by CW methods without field modulation. Under CW excitation conditions, the resulting CW signal increases linearly with increasing incident power at small B_1 .¹³ When saturated at higher B_1 , the signal deviates from linear dependence and eventually decreases and is accompanied by signal broadening.⁷ Because saturation recovery in this context is a CW technique, the prior discussion of signal voltage directly applies to the saturation recovery experiment.^{13,31} The saturation factor, s , is the saturation of the resonance of the electron spin,

$$s = \frac{\gamma_e^2 B_1^2 T_{1e} T_{2e}}{1 + \gamma_e^2 B_1^2 T_{1e} T_{2e}} \quad \text{Eq. 1.7}$$

where T_{1e} and T_{2e} are the electron spin-lattice and spin-spin relaxation times, respectively and B_1 is the microwave excitation field.^{30,43,44} As shown in the equation, at high B_1 the signal intensity is reduced relative to that at low B_1 . It is generally assumed that the spin-spin relaxation time is much faster than the spin-lattice relaxation time.

Practically, the CW saturation recovery experiment is performed by applying a long, low power pulse to saturate the spin system at a constant magnetic field and microwave frequency.^{7,30} Once saturated, the microwave power is switched from saturating power levels to non-saturating power levels.^{7,30} The switching of power levels is performed quickly relative to the relaxation time of the spin system.⁷ The observed EPR intensity after removing the saturating conditions is an exponentially increasing voltage with a time constant directly related to the spin-lattice relaxation time (Fig 1.8).⁷

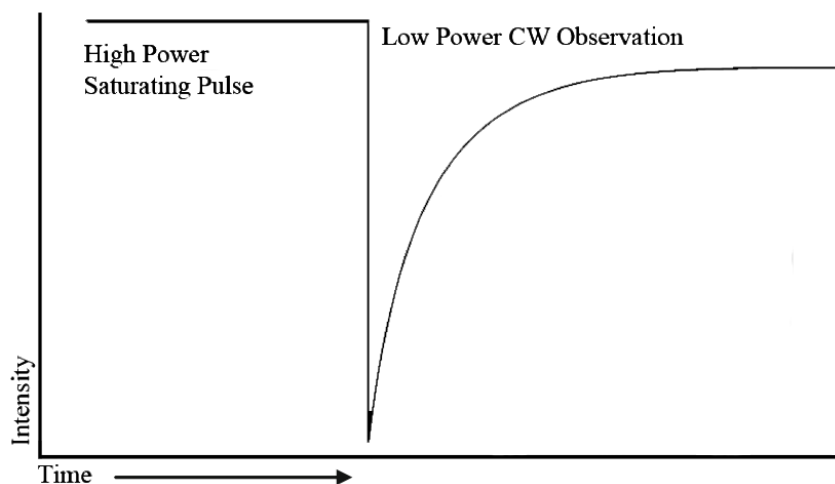
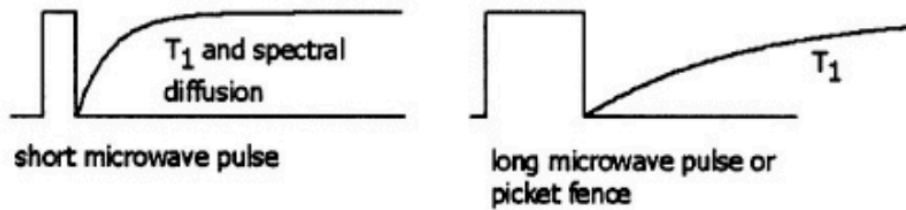


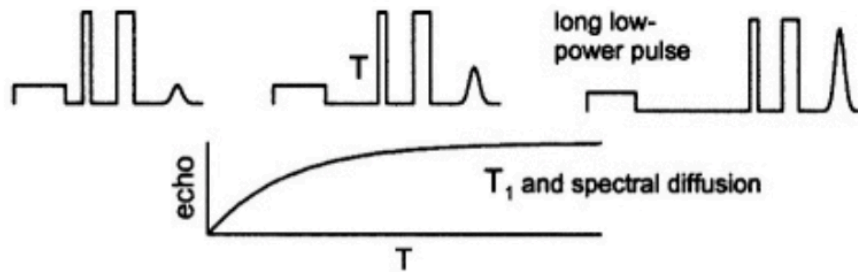
Fig 1.8: Overview of the CW saturation recovery experiment. The recovery of the signal intensity after switching to non-saturating conditions is fit with an exponential model.

CW saturation recovery is the primary method of performing spin-lattice relaxation measurements for samples where T_2 is too short to perform spin-echo experiments.³⁰ Additionally, because the saturating pulse in saturation recovery experiments allows for an establishment of equilibrium over a larger spectral width, artifacts from spectral diffusion are minimized in the resulting recovery curve.³⁰ Spectral diffusion may occur any time the bandwidth of the saturating pulse is insufficient to excite all of the spins present in the observed lineshape such that the unexcited spins may affect the longitudinal relaxation of the excited spins.¹⁶ It is therefore necessary, for complete characterization of the longitudinal or spin-lattice relaxation behavior of a specific spin system to employ a combination of inversion recovery, saturation recovery, and in some instances electron-electron double resonance techniques to elucidate the spectral diffusion behavior (Fig 1.9).^{16,30,45}

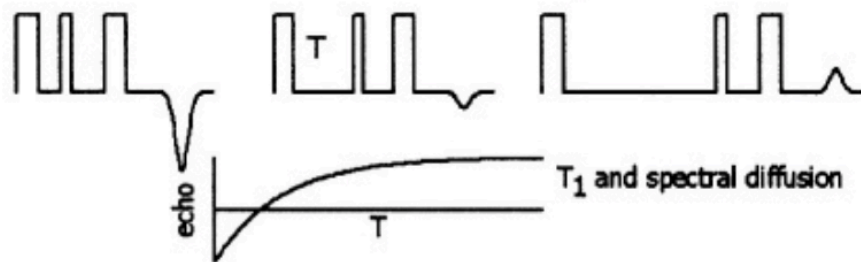
Continuous Wave Saturation Recovery



Two-Pulse Echo-detected Saturation Recovery



Three-Pulse Inversion Recovery



T = Interpulse spacings, T_1 = spin-lattice relaxation time

Fig 1.9: Comparison of CW saturation recovery using long low power pulses with other techniques used to measure spin-lattice relaxation processes. Spectral diffusion is assumed to have reached an equilibrium in long pulse saturation recovery experiments. Adapted from Eaton et al.³⁰

Relative to the standard CW spectrometer, the saturation recovery spectrometer requires fast switching hardware to facilitate rapid attenuation of the microwave power.⁷ The observed signal voltage is very low relative to other experiments and much attention must be paid to the amplification systems that follow the resonator.²⁹ Additionally, a critically coupled resonator with high quality factor experiences long resonator ring-down, which is the process by which the resonator dissipates excess energy other than interacting with the spin system.¹³ This energy dissipation is also an exponential decay

and often greatly overpowers the signal of interest.^{11,29} Subtraction of a spectrum collected off resonance, with the magnetic field set to a value that does not satisfy the resonance condition can remove resonator ring-down effects from the spectrum.²⁹ The digitizer must be of adequate dynamic range to fully digitize the ring-down signal, which is much larger than the EPR signal and degrades the resultant S/N of the EPR signal. Rapid repetition of the experiment for significant signal averaging is required for adequate S/N when using the saturation recovery experiment.

When properly calibrated, the saturation recovery experiment may give a wealth of information pertaining to the spin system and is not limited to spin-lattice relaxation measurements alone. When combined with other pulse measurements, the total contributions to the effective relaxation rate observed may be elucidated and differentiated with respect to molecular tumbling, nuclear relaxation, and in some instances cross relaxation.^{30,45} In the context of nitroxide radicals, much work has been done to explore the overall contributions to spin-lattice relaxation and a wealth of effort has been put forth towards modeling independent contributions.⁴⁵⁻⁴⁷ This has translated to investigations into the dynamics of spin labels, resulting in the adaptation of the saturation recovery technique to many protein structure and dynamics problems.⁴⁸ Developments in saturation recovery methods have allowed for measurements of secondary structure, solvent accessibility, interspin distances, and conformational exchange in protein systems and will likely continue to be a necessary method in the EPR toolkit.⁴⁸

1.3 Focus and scope of this dissertation

The overwhelming focus of this dissertation is the development of the instrumentation and methods for observing the EPR phenomenon and the subsequent practical information gained from its application. It is impractical to consider all of the theoretical considerations of the EPR experiment at the beginning of this dissertation given that not all of the rules and considerations approached are intuitive prior to experimentation. Because of this, various segments of theoretical considerations and descriptions are inserted where appropriate for consideration in experimental context.

Chapter 2 describes the applications of RS using the X-band instrument constructed at the University of Denver. The concepts of bandwidth and spectral filtering as they relate to the RS experiment are considered in chapter 2 because bandwidth calculations and the employment of mathematical filters are invoked in the explanations of linewidth resolution and S/N increases observed in RS relative to CW. Spectral simulation is described when first utilized during the elucidation of reaction intermediates in samarium-mediated reduction chemistry, also in chapter 2. The application of RS to fast, full-spectrum data acquisition for the investigation of radical kinetics is also included in chapter 2. A description of the digitizers used and their advantages and disadvantages gives some idea of the limits of RS in its current state.

Chapter 3 describes the development and use of an AWG-based saturation recovery spectrometer. An in-depth discussion on the inner workings of the EPR spectrometer is given in chapter 3 with a wealth of supplementary information regarding figures of merit of the spectrometer and their investigation during the design and implementation of the AWG-based instrument. Also present in the digital saturation

recovery bridge description is a thorough consideration of resonator performance and overall characteristics relative to the task at hand. It is most relevant when describing the development and characterization of a crossed-loop resonator and its use at X-band. Following the validation of the SR instrument, fast-relaxing nitroxide radicals were explored using the digital SR instrument. Matlab scripts to synthesize waveforms similar to those used during the experiments described in chapter 3 are given in the appendix.

Lastly, the development of RS instrumentation and application for use at cryogenic temperatures is the focus of chapter 4. Some discussion of motivation regarding passage effects with respect to relaxation rate are given; and, support for these descriptions is present in the concluding section of the chapter with examples of both slowly relaxing and rapidly relaxing spin systems investigated below 10 K. Hardware adaptations such as a metal-free cryostat, a closed-loop helium system, larger scan coils, and high-pass filters are all described in chapter 4, as is bench-testing and stability tests of the low temperature system in operation. Conclusions and comments on future work are given in chapter 5 summarizing the work of the three preceding chapters before giving a brief outlook on future research.

Chapter Two: Applications of RS-EPR for chemical investigations

“Why don’t you just explore a little?”

- Dr. Sandra Eaton

Enhanced signal-to-noise (S/N) has been demonstrated with RS for many types of radicals.^{32,49,50} Signal enhancements have been demonstrated for narrow-line spectra of α,γ -bisdiphenylene- β -phenylallyl (BDPA), lithium phthalocyanine (LiPc), a nitrogen defect in diamond, N@C60, and semiquinone in RS experiments.^{38,51,52} The hyperfine couplings have been resolved in spectra of BMPO-OOH spin trapped radicals and other nitroxide radicals.^{53,54} A major focus in spectra of prior studies was the enhanced S/N for RS relative to CW, specifically in radicals with long relaxation times.⁵¹ Increased S/N in RS experiments has been exploited to improve image quality in EPR imaging experiments by improving the S/N of the gradient-collected spectra and in shorter times than CW imaging experiments.³⁵

The investigations in this chapter were pursued both to highlight the improved S/N obtained via RS experiments for a range of experiments *and* to expand the capabilities of the technique. The kinetics experiments demonstrate new opportunities for the EPR spectroscopist. Though not described in the chronological order in which they were pursued, the studies detailed in this chapter provided me with a fundamental understanding of both the EPR spectrometer and the RS technique and were necessary for

the development of a digital EPR spectrometer (Ch. 3) and the adaptation of RS to low temperatures (Ch. 4) that were pursued either after or in tandem with the experiments described in this chapter.

Of the four investigations detailed within this chapter, each sought to highlight or expand a different advantage of RS exploited for chemical investigations. Because the resonance condition is satisfied for a very short time in RS, more microwave power may be used without signal saturation.³² This concept was explored in irradiated fingernail samples to increase S/N and improve the correlation coefficient of the dose-response curve, a topic of interest for many labs.⁵⁵⁻⁵⁷ Similarly, in RS, the magnetic field is scanned at rates on the order of kHz to tens of kHz, or once per millisecond at the slowest, and does not require stepping of the slow, main magnetic field like in CW measurements.³² This allows signal averaging to be performed very quickly such that species in a reaction mixture may be observed, which has been applied to spin-trapped species in samarium mediated reductions.⁵⁸ The limits of resolution in multiline spectra via RS were explored in radical species exhibiting both narrow and closely spaced hyperfine splittings. A detailed description of bandwidth as it relates to RS is given in the context of these samples. Lastly, the data-throughput of the RS spectrometer is examined in the context of chemical reductions. Spectra were collected sequentially and rapidly with respect to time to assemble reaction progress curves in model systems where signal decays with reaction progress. Each example detailed is an expansion on the capabilities of the RS technique.

2.1 Irradiated fingernails and implications for dosimetry analysis

The concept of measuring radiation damage in a living being is of considerable interest given the history of relevant radiation releasing natural disasters, such as Fukushima and Chernobyl. A quantitative measurement of radiation has been sought after for some time; however, such a measurement by current methods is considerably invasive. Given the implied morbidity in extreme cases; post-mortem analysis may be feasible and sufficient in many unfortunate cases. It has been shown that both bone and keratin are capable of providing some insight into the radiation damage to an individual.^{57,59} While one of these is considerably less invasive the accurate prediction of implied health risks is a topic under heavy debate. Radiation induced radicals present a novel application of EPR and may allow for quick and convenient assessment of radiation exposure and presumed future health concerns in living beings and have been the subject of investigation of many concerned with the subject.^{55-57,60,61} Although some radiation dosimetry has been developed based on teeth and tooth enamel, it is highly desirable to develop an accurate dose-response model based upon the radiation exposure to external keratin in living beings, and more specifically, fingernail clippings.^{57,59,61,62}

An adult human fingernail grows at a rate of ~2 mm per month, such that in the event of a large exposure to detrimental radiation it is expected that fingernails will be both present and preserved up to a maximum dose of ~20 Gy when the fingernails may dislodge from healthy tissue.^{63,64} Because of this, fingernails are an attractive target for estimating the total exposed radiation dose and thereby assessing any future adverse long-term health effects of said radiation exposure. Fingernail collection is non-invasive which

is desirable during triage. EPR signals in fingernails have been shown to report accurately on radiation exposure when collected as long as two months after exposure.⁵⁶

There are two varieties of EPR signals in irradiated fingernails: mechanically induced signals (MIS) and radiation induced signals (RIS) with RIS being the signals of interest for dosimetry.⁵⁷ The MIS, largely introduced from the shearing required when collecting fingernail samples, may be adequately reduced or even eliminated by collecting samples while performing an aqueous rinse.⁵⁷ The MIS decay much faster than RIS.⁵⁷ It may then be assumed that after some delay, the major signal present is due to irradiation and this signal is dose-dependent.⁵⁷ The sample was chosen to highlight the benefits of RS vs. CW in radiation dosimetry in fingernails and results of this study are reported in Ref.⁶² In this collaborative project my role was to support Dr. Hanan Elajaili in optimizing RS experiments and filtering parameters. I also performed S/N calculations on the recorded RS and CW spectra. CW experiments were performed by Dr. Hanan Elajili. Relaxation measurements were performed by Dr. Priyanka Aggarwaal.

2.1.1 S/N comparisons between CW and RS-EPR

Previous work from the Eaton lab had demonstrated RS as the preferred method when investigating dosimetry response in tooth enamel.⁵⁹ In the study reported here we applied RS to measure the radiation induced signal in irradiated fingernails. A comparison of CW and RS was undertaken on irradiated fingernail samples, collected using sharp scissors from a healthy male volunteer that had been soaked in distilled water before being irradiated.⁶² Samples irradiated to 0 Gy (control), 5 Gy, and 10 Gy were graciously provided by Dr. Romanyukha to test the ability of RS to resolve dose-

dependent differences and to evaluate any potential improvements in the dose-response curve. An example of the signal investigated is in the right panel of Fig 2.1.^{59,62}

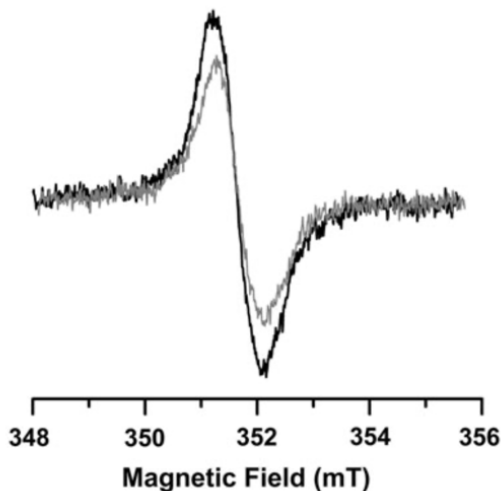


Figure 2.1: Comparison of a 0 Gy (*grey*) control vs. a 10 Gy (*black*) irradiated fingernail sample collected from a healthy male volunteer and recorded via CW. Reproduced with permission from Elajaili et al.⁶²

As described previously, a major benefit of RS relative to CW is the increased S/N, largely from the increased microwave power that can be used without saturating the spin system. The use of higher B_1 was advantageous in the measurements of irradiated tooth enamel and was anticipated to be the case when investigating irradiated fingernails via RS. Power saturation curves for CW and RS for irradiated fingernails are shown in Fig 2.2. The B_1 at which spectra were recorded was selected as the value at which saturation broadens the EPR linewidth by approximately 2-5%.^{59,62}

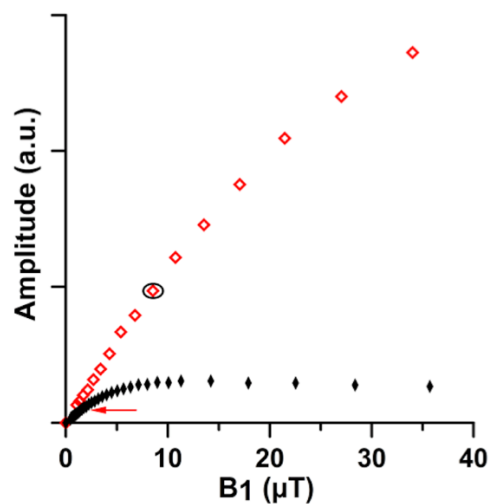


Figure 2.2: Comparison of the power saturation behavior of the RIS, 10 Gy, observed when performing RS (*red*) vs. CW (*black*) of irradiated fingernails. The circle and arrow mark the B_1 at which the RS and CW data were acquired, respectively. Reproduced with permission from Elajaili et al.⁶²

The S/N of a RS spectrum of irradiated fingernails was greater than 2000, which is too large to measure accurately, after 30 seconds of data collection using a microwave power of 0.5 mW ($B_1 = 8.5 \mu\text{T}$). For comparable acquisition times, a CW spectrum of the same sample using a microwave power of 0.13 mW ($B_1 = 2.3 \mu\text{T}$) and modulation amplitude of 0.2 mT gave an S/N of approximately 30. The derivative of the collected RS spectra was compared to the CW, and S/N of the RS derivative spectra was greater than 1200 and still considered too large for accurate calculation. To more accurately compare RS and CW S/N, additional CW experiments were performed using a microwave B_1 of $3.2 \mu\text{T}$ and a larger modulation amplitude (0.4 mT). These parameters increased S/N to 90 but resulted in a linewidth that was broadened by 7%. Under conditions that do not cause linewidth broadening in CW experiments, good agreement was found between RS and CW linewidths as shown in Fig 2.3, below.⁶²

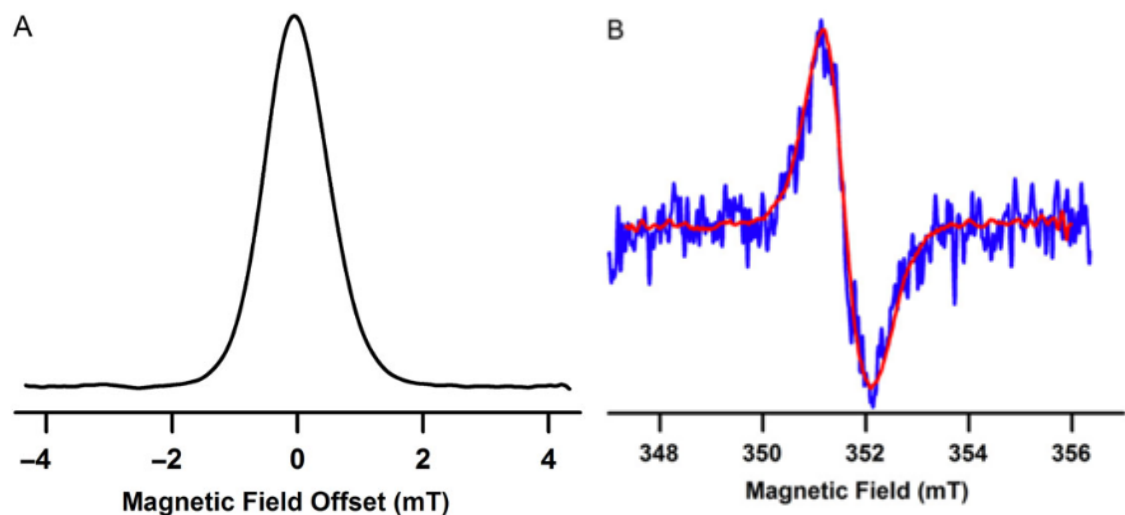


Figure 2.3: Comparison of RS and CW in irradiated fingernails. RS absorption spectrum (*left*) has $S/N > 2000$, which is considered too high to calculate accurately. RS derivative (*right, red*) and CW spectrum (*right, blue*) are overlaid to demonstrate lineshape agreement. Reproduced with permission from Elajaili et al.⁶²

Motivated by the significant increase in S/N obtained by RS relative to CW, we sought to determine the limits of S/N increase via RS. An investigation into the S/N observed when increasing scan frequency, and thereby increasing the scan rate was performed on an irradiated fingernail sample (10 Gy) and the results are shown in Fig 2.4. It was found that S/N increased with increasing scan frequency up to about 50-60 kHz, where S/N then began to decrease drastically. The increase in S/N with increasing scan rate is expected given that faster rates allow for more microwave power to be utilized, resulting in larger signal intensities for a given acquisition time. Additionally, the increased scan frequency allows for significantly increased signal-averaging per unit time, greatly increasing the signal intensity. The linewidth of this signal is large so the bandwidth is low and resonator Q did not impose bandwidth constraints (*see* Section 2.3.1). The observed limit of increasing S/N relative to scan rate demonstrates a hardware limitation. Rapidly changing magnetic fields induce mechanical vibrations and eddy

currents in conducting materials that offset the magnetic field and contribute to field inhomogeneities that distort the spectrum.³³ These eddy currents and mechanical vibrations in the resonator assembly contribute to increases in the rapid-scan background, which is an often-distorted scanning wave that is present in the recorded spectrum. Increasing scan rate greatly increases the magnitude of this background, which can overwhelm the intensity of the signal of interest. High dynamic range of the digitizer is required to obtain adequate definition of the EPR signal in the presence of large background signals. If the background signal includes higher harmonics of the scan frequency, correction of the background is difficult.^{65,66} Large background signals typically are accompanied by decreases in the S/N of the reconstructed RS spectrum. Utilization of non-conducting or vibration dampening materials decreases the magnitude of eddy currents when performing RS experiments; however, this is not always possible for critical components and to some extent eddy currents cannot be avoided.^{33,59}

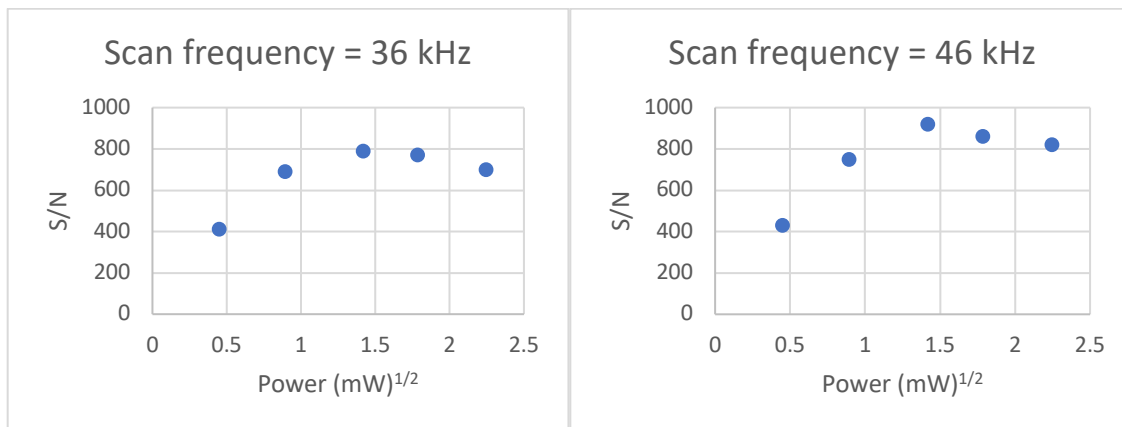


Figure 2.4: S/N vs. the square root of power for selected scan frequencies, 36 kHz (*left*) and 46 kHz (*right*), when keeping scan current and acquisition time constant. The maximum S/N at 61 kHz scan frequency was ~ 250 and is not included in this comparison because of large signal distortions and RS background.

While the current state of the art is still a work in progress, the goal of the field is to thoroughly characterize the dependence of the EPR signal on radiation exposure. We

constructed a dose-response curve similar to those previously published including an analysis of the dependence of the power saturation behavior on irradiation dose.^{56,57} The dose-response curve is non-linear, with lower slope at higher doses, which makes the accuracy of dose-assessment less reliable at high doses than at lower doses.^{56,57} Above doses of 40 Gy, signal intensity rapidly decreases, demonstrating saturation behavior and may be indicative of the maximum absorbable radiation dose in keratin materials. Beyond 30 Gy exposure, it is likely that other radiation-induced symptoms will become apparent, such that keratin-based triage is no longer necessary.⁶⁴

Power saturation behavior was investigated for the three irradiated fingernail samples (0 Gy, 5 Gy, and 10 Gy) and compared to determine the linearity of the dose response at different microwave power levels (Fig 2.5). Differences in power saturation behavior may arise from different contributions to the signal intensity due to differences in relaxation times of overlapping signals. The fingernail samples exposed to the highest dose of radiation investigated, 10 Gy, gave much larger signal intensities at higher microwave powers relative to the lower 5 Gy dose and negative control. Additionally, the 10 Gy sample appeared to saturate at higher microwave power levels relative to the lower 5 Gy dose and negative control. At low power, minimal differences are observed between the 5 Gy sample and the negative control, indicating that lower dose samples may be a challenge during triage. The high S/N observed in these samples by RS indicates that the ability to distinguish between 0 and 5 Gy samples may be dependent on sample preparation. An increase in linearity of dose response is likely to be observed at higher microwave power due to differences in saturating behavior previously reported in

different signals present in the EPR spectra of irradiated fingernails; however, this cannot be determined in the present study due to only two radiation doses studied.⁵⁷

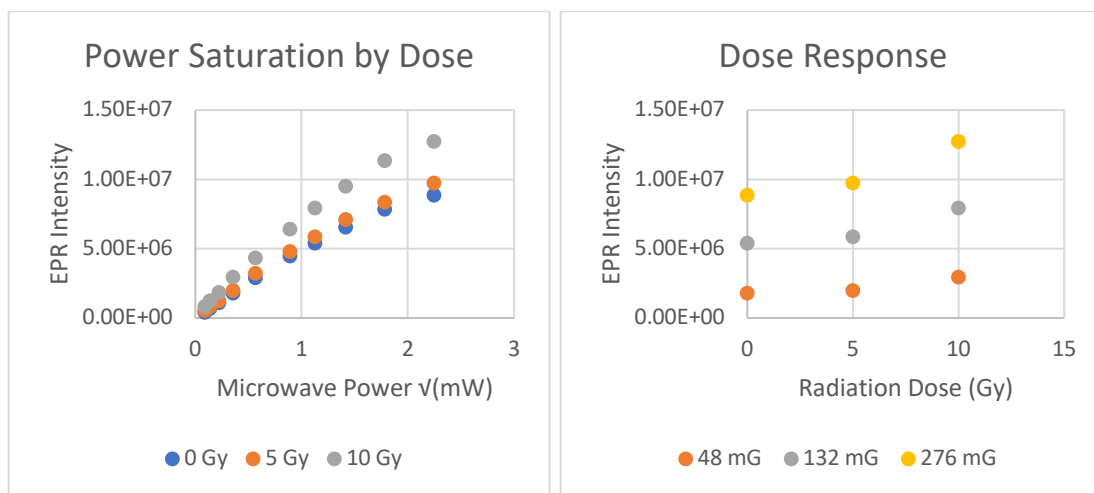


Figure 2.5: Power saturation data for 0, 5, and 10 Gy irradiated fingernails (*left*) and dose-response curve (*right*) generated from differing microwave B_1 recorded via RS at 35 kHz.

Irradiated fingernails may be a viable alternative in radiation dosimetry to tooth enamel. RS demonstrates clear advantages vs. CW for estimation of radiation dose from the observed signal intensity evidenced by the drastic increases in S/N. Linearity of the dose response curve may be improved by repetitive measurements; and, alternatives to fingernails are being explored that may be better EPR reporters. In one study, it was observed that unexposed keratin materials, such as toenails shielded by closed shoes, may yield a linear dose-response curve over much greater dose variation.⁵⁶ It has also been considered that possessions an individual has on their person, such as the glass present in a cell phone, may be a welcomed alternative to the sampling of human tissue for estimates of radiation exposure by EPR methods.⁶⁷ Regardless of the sample matrix chosen, it is likely that RS will give increased S/N per unit time vs. CW which will be valuable to improve EPR dosimetry.

2.2 Spin-trapping samarium-mediated reductions

Single-electron transfer (SET) presents a considerable challenge given the often-transient nature of the reaction intermediates or transition states necessary for electron transfer reactions. Studies of the mechanism of these reactions have been performed with a variety of spin-probe molecules with varying degrees of success.^{68–70} Three types of nitroxide-containing spin-probes have been used to investigate the mechanism of organic reactions.^{69,71–74} The three classes of probes (nitroxide or aminoxyl, nitrone, or nitroso) each interact with a single electron differently (Table 2.1).⁶⁹

Table 2.1: Aminoxyl, nitrone, and nitroso spin traps commonly used in mechanistic investigations. Adapted from Perkins.⁶⁹

Probe type	Structure and resulting reaction
Aminoxyl	$ \begin{array}{c} \text{Bu}^t \\ \diagdown \\ \text{N}-\text{O}\cdot \\ \diagup \\ \text{Bu}^t\text{O} \end{array} \begin{array}{l} \longrightarrow \\ \longrightarrow \\ \longrightarrow \end{array} \begin{array}{l} \text{Bu}^t\text{N}=\text{O} + \text{Bu}^t\text{O}\cdot \\ \text{Bu}^t\text{ONO} + \text{Bu}^t\cdot \\ \text{Bu}^t\text{NO}_2 + \text{Bu}^t\cdot \end{array} $
Nitron	$ \begin{array}{c} \text{Ph} \\ \diagdown \\ \text{C}=\text{N}^+\text{O}^- \\ \diagup \\ \text{H} \end{array} \begin{array}{l} \\ \\ \\ \end{array} \begin{array}{c} \text{O}^- \\ \diagdown \\ \text{N} \\ \diagup \\ \text{Bu}^t \end{array} \longrightarrow \begin{array}{c} \text{Ph} \\ \diagdown \\ \text{H}-\text{C}-\text{N} \\ \diagup \\ \text{OH} \end{array} \begin{array}{l} \text{O}\cdot \\ \diagdown \\ \text{N} \\ \diagup \\ \text{Bu}^t \end{array} $
Nitroso	$ \text{Bu}^t\text{N}=\text{O} \longrightarrow \begin{array}{c} \text{CH}_3 \\ \diagdown \\ \text{N}-\text{O}\cdot \\ \diagup \\ \text{Bu}^t \end{array} $

Aminoxyl radicals are particularly useful in the affirmation of single-electron processes. The EPR signal decays over time as the aminoxyl group participates in single-electron reductions, quenching the already present radical on the nitroxide group; however, in most instances no new bonds are formed outside of proton exchanges and little information is derived concerning the source of the electron without careful control of the reactants.^{69,75,76} Nitrones capture a transient, single electron containing molecule at the unsaturated carbon adjacent to the nitrone and a new, often more stable molecule is

formed.^{69,77} This class of spin traps has been well established in the literature and many examples exist for the specific targeting of certain radical species, such as superoxide or sulfur containing radicals.⁷⁷⁻⁸⁰ These spin-traps, along with the nitroxide molecules have been tailored to a wealth of environments, both aqueous and non-aqueous, and have been utilized in many *in vitro* and *in vivo* applications.^{77,81-84} The third class of spin trap molecules, the nitroso compounds, react with transient single electron containing species directly on the nitrogen.^{69,77,85} These molecules, while significantly more difficult to adapt to an aqueous environment, report the most information in relation to the newly formed species and were found to be particularly useful in the identification of the intermediates in samarium mediated reductions.^{58,77,85} An extremely detailed tabulation of observed hyperfine for different types of trapped radicals may be found in the works of GR Buettner.⁷⁷

The spin trapping experiments described in this section were performed in collaboration with Dr. Bryan Cowen and his student, now Dr. Chris Aretz. Synthesis of all substrates that were not purchased commercially was performed by Dr. Aretz. Spin-trapping experiments and aqueous separations were performed by both Dr. Aretz and myself. I evacuated and removed O₂ from EPR samples before Dr. Gareth Eaton flame sealed them, when reported as such. Dr. Aretz and I worked together on experimental design and data interpretation. NMR experiments were performed by Dr. Aretz. I performed data analyses and simulation of EPR spectra. High resolution mass spectrometry was performed by Central Analytical Laboratory, University of Colorado Boulder. This work was published in the Journal of Organic Chemistry and is the first

publication to feature only RS data.⁵⁸ No CW comparisons were included in the published manuscript.⁵⁸

2.2.1 Reductive cyclization of 5-bromo-6-oxo-6-phenylhexyl methanesulfonate

We investigated the reductive cyclization of 5-bromo-6-oxo-6-phenylhexyl methanesulfonate **1**, an α -bromoketone (Fig 2.6) using spin trapping methods to determine the reactive intermediate formed during two consecutive single-electron reductions evidenced by a prior optimization of the reaction with a 2:1 ratio of samarium to reactant.^{86,87} Aretz and coworkers have previously demonstrated samarium mediated intramolecular cyclization to form cyclopentane products via the Reformatsky aldol cyclization.^{88,89} It was hypothesized that the most efficient route to product formation may be either through a carbon-centered radical generated at the carbonyl group (*Pathway A*, Fig 2.6) or a carbon-centered radical formed by the reductive elimination of bromine (*Pathway B*, Fig 2.6).⁸⁷ It has been shown previously that samarium chelates with both oxygen and the halogen in reagents containing a halogen adjacent to a ketone and this was the basis for the proposed synthetic routes to product.⁹⁰ It must then be considered that the terminal leaving group in 5-bromo-6-oxo-6-phenylhexyl methanesulfonate **1** and in those previously considered by Aretz and coworkers could be involved in the chelation with samarium and may contribute to the yields observed.^{88,90}

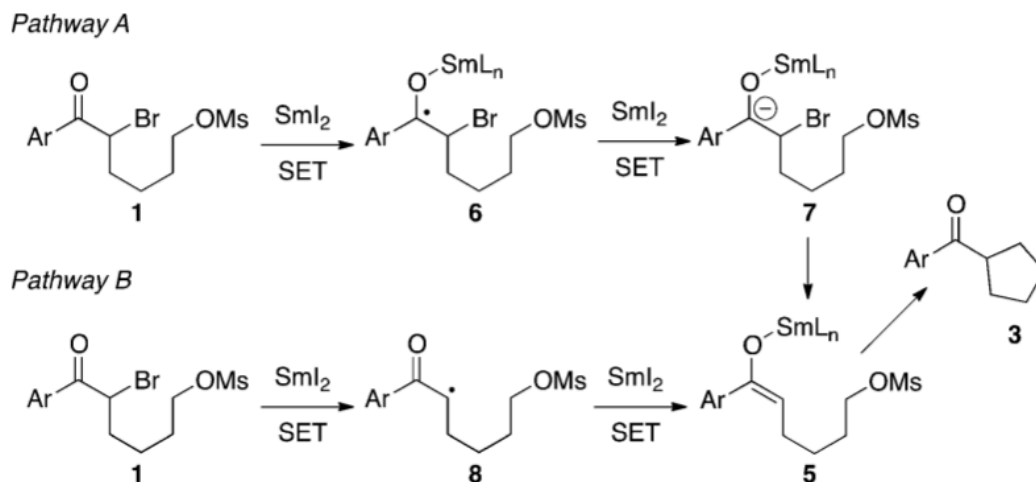
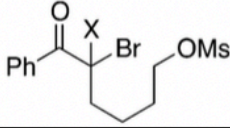
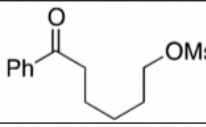
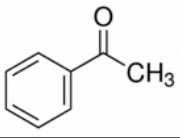
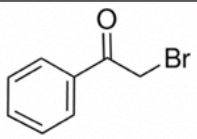
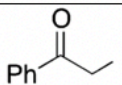
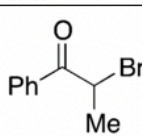
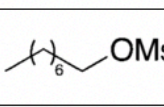
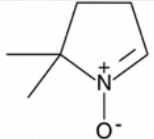
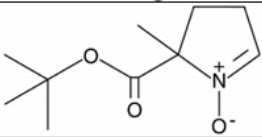
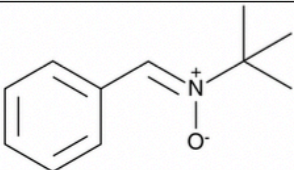
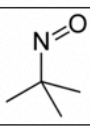
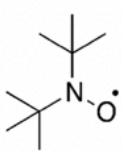


Figure 2.6: Hypothesized reactive intermediates in route to the product of the samarium-mediated reductive cyclization of 5-bromo-6-oxo-6-phenylhexyl methanesulfonate. Pathway A proceeds through a ketyl radical intermediate and Pathway B proceeds through a carbon-centered radical where the single electron is localized adjacent to the ketone. Reproduced with permission from Aretz et al.⁵⁸

Both the reaction conditions and prior evidence supported the presence of a single electron containing reactive intermediate.^{86,87,89,90} The aminoxyl spin-probes were not considered for this investigation as it is unlikely that mechanistic insight would be gained from a radical quenching reaction. One possible product of reactions involving a nitron is the reduced spin trap. It was predicted that the trapping of aryl carbon-centered radical **6** would result in smaller nitrogen hyperfine coupling than the reduced trap alone due to the increased delocalization of the single electron into the orbitals of the aryl carbon-oxygen bonds, as evidenced in prior studies.^{77,91,92} Alternatively, the trapping of species **8** would produce a radical with nitrogen hyperfine similar to that of the reduced trap. Observation of additional hyperfine splitting due to a neighboring proton or resolved bromine hyperfine could provide information about the trapped radical.^{77,93} Only in rare instances has coupling to bromine been observed, and in these cases the hyperfine coupling is very large with respect to typical nitrogen hyperfine couplings.⁹³⁻⁹⁵

To determine the mechanism of the samarium-mediated reduction, several nitrones and one nitroso probe were utilized. EPR spectra of spin-trapped adducts for reactions of **1** and for several related substrates were studied. Selective deuteration of **1**, at the position adjacent to the aryl carbon was used to probe the hyperfine observed in the nitron-trapped adduct EPR spectrum. A summary of the substrates and spin traps investigated is given in Table 2.2.

Table 2.2: Substrates and spin traps investigated in this section.

Name	Structure
5-bromo-6-oxo-6-phenylhexyl methanesulfonate 1 (X = H or D)	
(desbromo)-6-oxo-6-phenylhexyl methanesulfonate	
Acetophenone	
2-bromo-acetophenone	
Propiophenone	
2-bromo-propiophenone	
Mesylate-protected n-octanol	
DMPO	
BMPO	
PBN	
MNP	
DTBN	

In reactions with **1** cyclic nitron spin traps DMPO, BMPO, and deuterated DMPO were investigated. DMPO was purchased from Sigma and used as received. BMPO was graciously provided by Dr. Gerald Rosen, University of Maryland. Deuteration of DMPO was performed by nonspecific hydrogen deuterium exchange in NaOD/D₂O via slow evaporation to reduce the number of hyperfine interactions in the spin-trapped adduct EPR spectrum.⁹⁶ In all cases control experiments were performed by reacting the spin trap with the samarium reagent, SmI₂. The cyclic nitrones produced EPR active species when reacted with SmI₂ alone, but no EPR active species was observed with when reacting **1** with SmI₂. It is likely that samarium preferentially reduces **1** in mixtures containing the spin traps and that the steric bulk of the cyclic spin traps prevents reaction of the single electron-containing-intermediate with the nitron. Cyclic spin traps were not considered after initial experiments due to lack of reaction with the substrate of interest.

The linear spin trap, PBN, in the presence of SmI₂ and **1** resulted in a species with modest increases in the nitrogen and proton hyperfine relative to when reacting with SmI₂ alone; however, no additional hyperfine was observed. Because of the ambiguity of the results obtained with PBN and **1**, spin trapping experiments were performed on closely-related reactants acetophenone and 2-bromo-acetophenone. Similar increases in nitrogen and proton hyperfine were observed for the species produced by reaction of acetophenone with SmI₂ in the presence of PBN. A larger increase in proton hyperfine was observed for the radical trapped by PBN in reactions of 2-bromo-acetophenone with SmI₂ but no pronounced effect on the nitrogen hyperfine coupling was observed. A summary of the results obtained with the linear nitron spin trap, PBN, are shown in Fig 2.7.

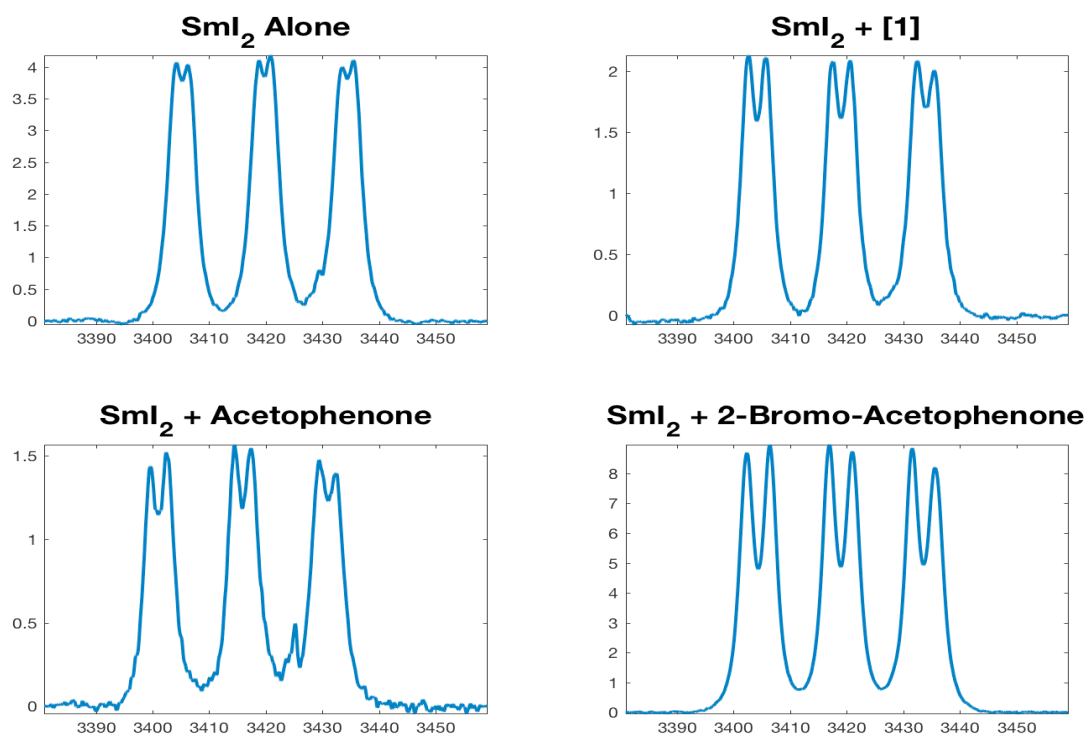


Figure 2.7: RS spectra of the reactions of SmI_2 and various substrates in the presence of PBN. Top left, a negative control reaction of SmI_2 and PBN alone. Top right, 5-bromo-6-oxo-6-phenylhexyl methanesulfonate **1**. Bottom left, acetophenone. Bottom right, 2-bromo-acetophenone. The 3-line hyperfine splitting of ~ 14 G is due to the nitroxyl nitrogen and the smaller doublet splitting is due to the proton on the alpha-carbon of the spin trap.

The small nitroso spin trap MNP was used because it does not have a proton on the alpha-carbon and therefore spectra of adducts of MNP do not have the proton hyperfine splitting that complicates spectra of PBN adducts. Reactions of **1**, acetophenone, and 2-bromo-acetophenone with SmI_2 were performed in the presence of MNP and the hyperfine observed for the resulting radical was compared to the hyperfine observed when reacting MNP with SmI_2 alone. Slight increases in the nitrogen hyperfine were observed when acetophenone and 2-bromo-acetophenone were reacted with SmI_2 in the presence of MNP. In contrast, the nitrogen hyperfine was significantly smaller for the adduct obtained by reacting **1** with SmI_2 in the presence of MNP and an additional proton

hyperfine splitting was observed. A summary of the results obtained with MNP are shown in Fig 2.8 and a summary of the hyperfine coupling constants is given in Table 2.3.

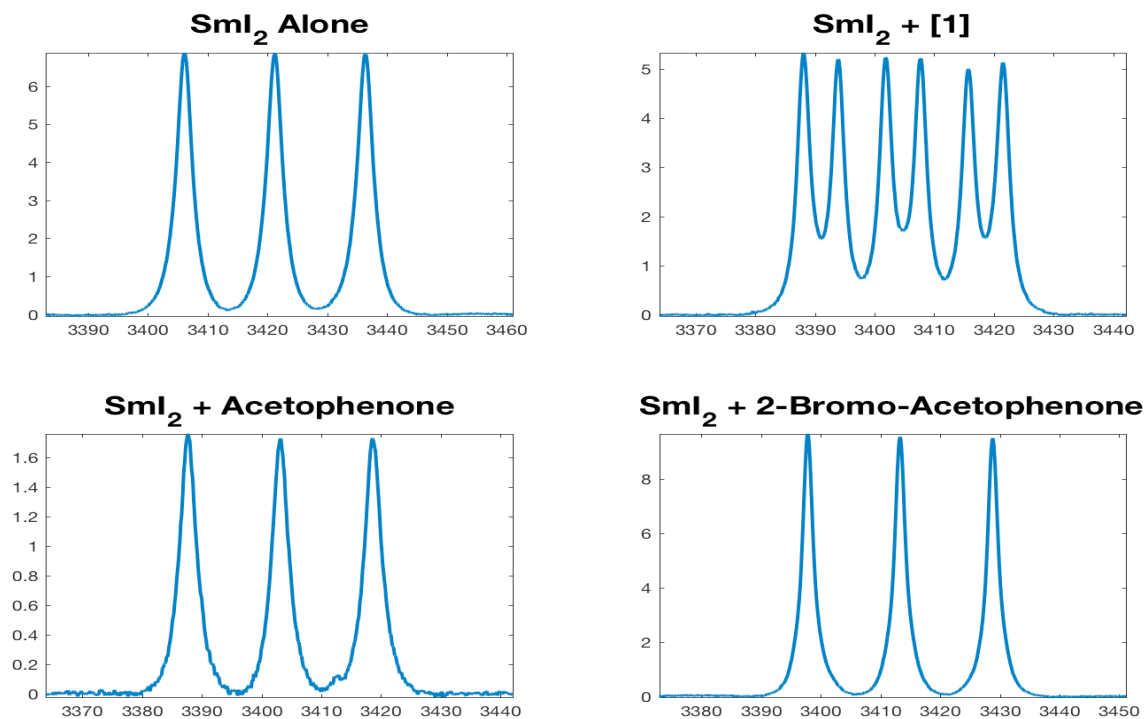


Figure 2.8: RS spectra of the reactions of SmI_2 and various substrates in the presence of MNP. Top left, a negative control reaction of SmI_2 and MNP alone. Top right, 5-bromo-6-oxo-6-phenylhexyl methanesulfonate. Bottom left, acetophenone. Bottom right, 2-bromo-acetophenone.

To more accurately measure the differences in hyperfine splitting in the radicals formed by the reaction of **1** with SmI_2 in the presence of MNP, reaction mixtures were washed with an aqueous sodium bicarbonate followed by an aqueous sodium chloride solution. Aqueous solutions were extracted with acetonitrile, evaporated to dryness under vacuum, and redissolved in THF. Analogous reactions were performed using propiophenone, 2-bromopropiophenone, and mesyl-protected n-octanol. Radicals produced in the reaction of propiophenone and the mesyl-protected n-octanol with SmI_2 in the presence of MNP were similar to those from the reaction of MNP and SmI_2 and to

what was observed with acetophenone and bromoacetophenone. However, 2-bromopropiophenone when reacted with SmI_2 in the presence of MNP produced an adduct with additional proton hyperfine splitting similar to what was observed with **1** (Fig 2.9). Having observed additional hyperfine splitting in spectra of adducts formed from reactions with both **1** and 2-bromopropiophenone, it became necessary to investigate the source of the additional hyperfine observed. A synthesis of 5(D)-5-bromo-6-oxo-6-phenylhexyl methanesulfonate was performed by Dr. Chris Aretz and the selectively deuterated substrate was reacted with SmI_2 in the presence of MNP. The nitrogen hyperfine was in good agreement with that for the product obtained for the reaction of **1** with SmI_2 in the presence of MNP; however, the additional hyperfine observed in both 5-bromo-6-oxo-6-phenylhexyl methanesulfonate and 2-bromopropiophenone was considerably decreased in 5(D)-5-bromo-6-oxo-6-phenylhexyl methanesulfonate (Fig 2.9, left). Reaction mixtures in THF were degassed by performing several freeze-pump-thaw cycles and RS spectra were recorded. Removing O_2 from the solutions greatly decreased EPR linewidths and increased resolution of both nitrogen and proton/deuterium coupling in the EPR spectra permitting quantification of the difference in hyperfine coupling (Fig 2.9, right). The hyperfine coupling decreased by approximately a factor of 6.5 when the substrate was selectively deuterated (Table 2.3).

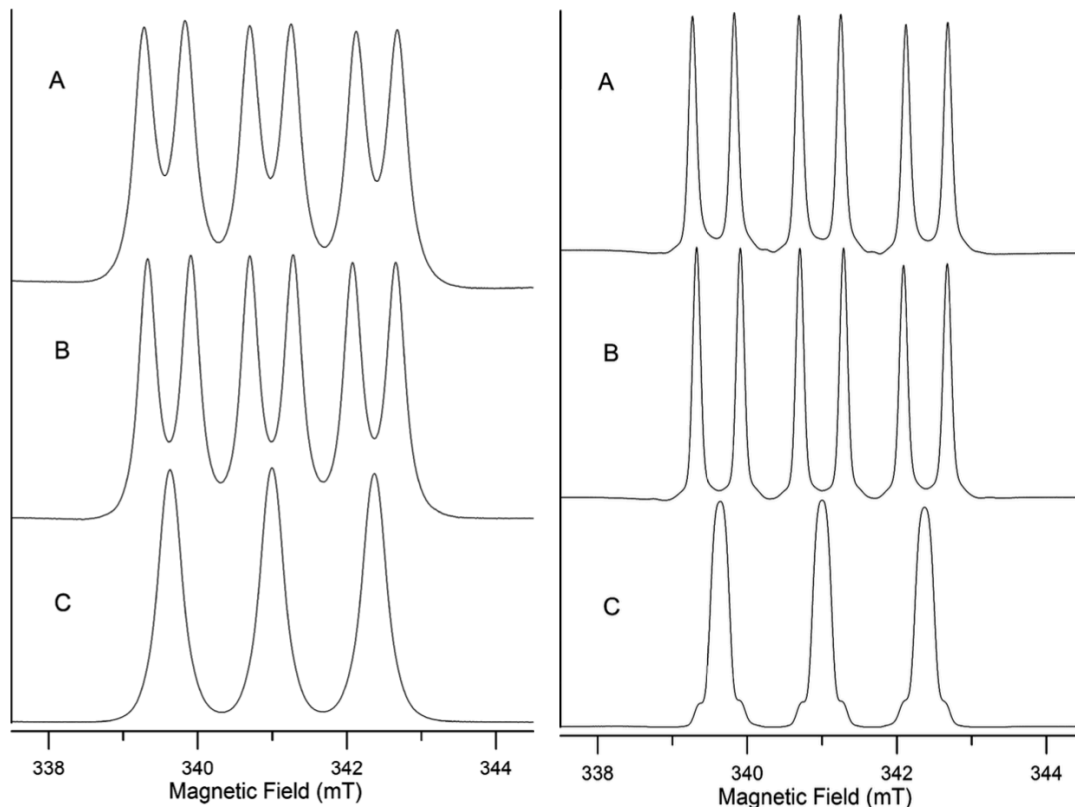


Figure 2.9: RS spectra recorded after reaction of 2-bromopropiophenone (*top*), **1** (*middle*), and 5(D)-5-bromo-6-oxo-6-phenylhexyl methanesulfonate (*bottom*) with SmI_2 in the presence of MNP. Spectra recorded in air (*left*) and after removal of O_2 (*right*) are shown. For comparison, 1 mT = 10 G. Reproduced with permission from Aretz et al.⁵⁸

A synthesis of (desbromo)-6-oxo-6-phenylhexyl methanesulfonate, as well as 5,5-(D)-(desbromo)-6-oxo-6-phenylhexyl methanesulfonate was performed by Dr. Chris Aretz and the substrates were reacted with SmI_2 in the presence of MNP. The recorded EPR spectra, much like those of acetophenone, 2-bromoacetophenone, propiophenone, and mesyl-protected n-octanol, did not significantly differ from the spectrum recorded when reacting MNP and SmI_2 alone. It has been demonstrated previously that under UV irradiation, MNP may fragment to form NO and tert-butyl radicals which may then be trapped by other MNP molecules forming di-tert-butyl-nitron (DTBN).^{97,98} Commercially available DTBN was dissolved in THF and subjected to freeze-pump-thaw

methods analogous to those employed during spin-trapping experiments with MNP. The EPR spectrum of the resulting adducts was recorded via RS. The nitrogen hyperfine values in the EPR spectra of the DTBN samples were in good agreement with values observed for samples obtained by the reaction of MNP and SmI_2 . In all cases reported where nitrogen hyperfine values did not significantly differ from this control experiment, the EPR active species is likely DTBN (Fig 2.10).

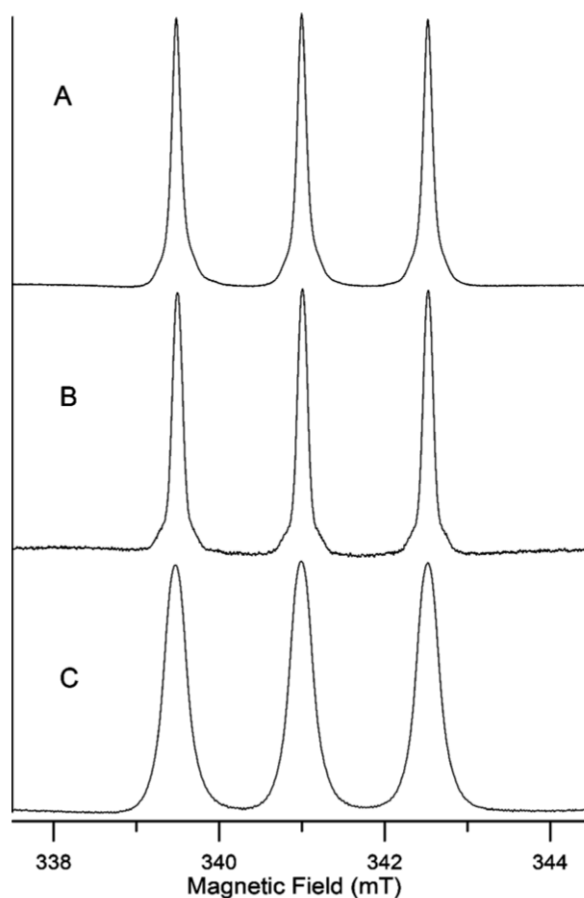


Figure 2.10: RS spectra obtained from DTBN in THF (*top, A*) and from the reaction of MNP and SmI_2 , before degassing (*bottom, C*) and after degassing (*middle, B*). For comparison, 1 mT = 10 G. Reproduced with permission from Aretz et al.⁵⁸

2.2.2 Hyperfine analysis and mechanistic insight

A summary of the hyperfine coupling constants found via spectral simulation using EasySpin for spin trapping experiments using MNP are listed in Table 2.3.^{58,99} Only the most informative experiments are reported. Cyclic nitron experiments were not included due to their lack of trapping ability when investigating the reaction of **1** and SmI₂. The reactions performed with PBN were also relatively uninformative in identifying the trapped species because of the small changes in hyperfine interactions and likely would have been more useful if samples had been subjected to aqueous workup and degassing similar to the MNP experiments. Likewise, control experiments that did not significantly differ from the collected spectra of either DTBN or the reaction of SmI₂ and MNP alone were not reported. The ratio of proton coupling to deuterium coupling was found to be approximately a factor of 6.5 and is consistent with prior reports.¹⁰⁰ Additional experiments were performed to determine if any contributions from bromine radicals were present in spin-trapping reactions and it was found that participation from bromine is unlikely.

Table 2.3: Summary of the hyperfine couplings for trapped radicals observed during the reactions of substrates with SmI₂ in the presence of MNP.

Substrate/Reactant	A _N (mT)	A _H (mT)	A _D (mT)
2-bromopropiophenone	1.43	0.56	
5-bromo-6-oxo-6-phenylhexyl methanesulfonate	1.39	0.59	
5(D)-5-bromo-6-oxo-6-phenylhexyl methanesulfonate	1.39		0.093
DTBN	1.52		
SmI ₂ + MNP	1.52		

Values were obtained via simulation using EasySpin from spectra recorded of degassed solutions. For comparison, 1 mT = 10 G. Reproduced with permission from Aretz et al.⁵⁸

While the comparison of hyperfine couplings was not as informative as we had hoped, measurements as a function of time provided evidence that the reaction of **1** with

SmI₂ in the presence of PBN generated a spin-trapped adduct that is significantly different than what was formed in reactions of PBN and SmI₂ alone. RS and CW spectra collected for both reactions are shown in Fig 2.11 for several times after initiation of the reaction.

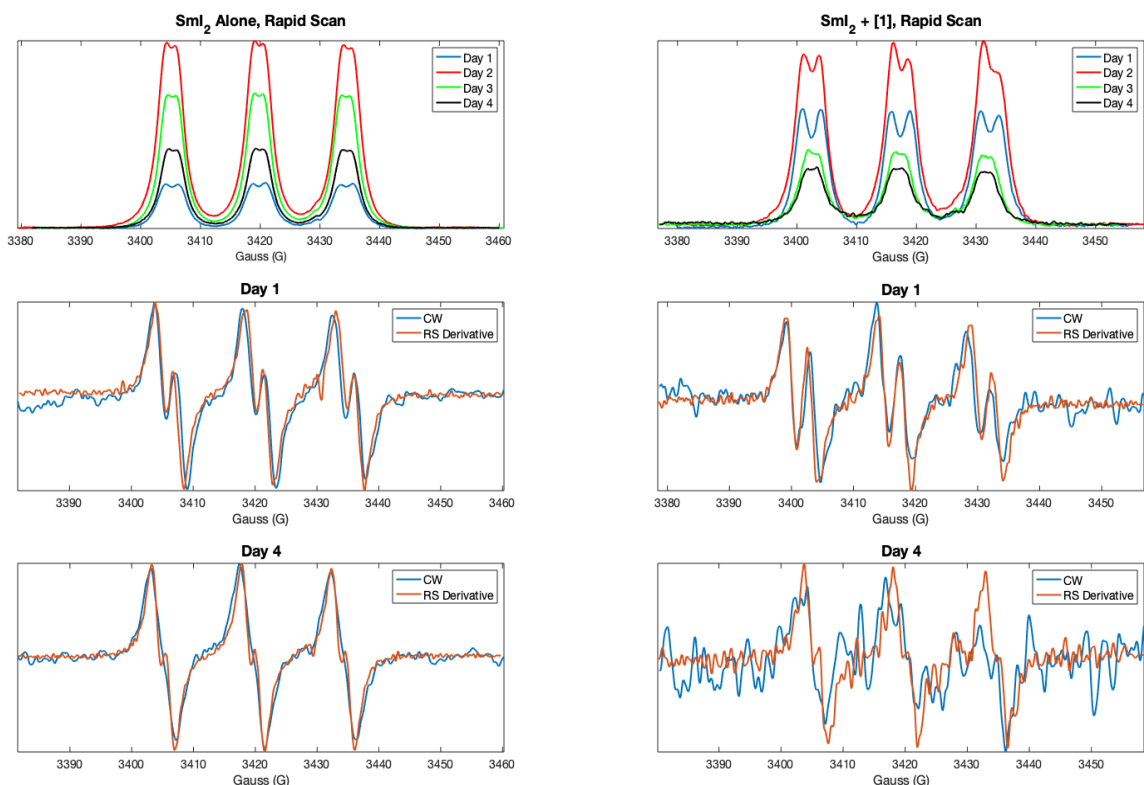


Figure 2.11: Time dependence of the signal for the spin-trapped adducts from the reaction of SmI₂ alone (*left*) and SmI₂ and **1** (*right*) in the presence of PBN. The upper panel shows the RS absorption spectra on 4 successive days (Day 1, *blue*, Day 2, *red*, Day 3, *green*, Day 4, *black*). The CW (*blue*) and first derivatives of the RS (*orange*) signals are compared for day 1 and day 4 in the middle and lower panels.

For both reactions the signal is more intense on days 2 than on day 1, which may be due to oxidation of the hydroxylamine back to free nitroxide.^{76,101} The increase between day 1 and 2 is larger in the absence of **1** than in its presence. The radical formed in the presence of **1** decays more rapidly than what is formed in its absence. Additionally, chelation of excess samarium(III) by **1** may impact differences in stability that were

observed in experiments where excess samarium(III) was not removed by the aqueous workup.¹⁰² These spectra also demonstrate improved S/N for the RS signals at each time point for both reactions (Table 2.4). At the earliest time points used in the comparisons, S/N in RS experiments relative to CW experiments was increased up to 13 fold (Table 2.4), which highlights the advantages of RS relative to CW for spin-trapping investigations and is consistent with prior studies.⁵³

Table 2.4: S/N obtained from the RS and CW spectra recorded after reactions of 5-bromo-6-oxo-6-phenylhexyl methanesulfonate with SmI₂ in the presence of PBN and of PBN and SmI₂ alone.

Reaction progress	SmI ₂ + PBN alone	1 + SmI ₂ + PBN
Day 1	S/N	S/N
RS Absorption	800	900
RS Derivative	200	300
CW	60	50
Day 4		
RS Absorption	900	200
RS Derivative	300	70
CW	60	10

In reference to the proposed pathways to product shown in Fig 2.6, the proton hyperfine splitting in the spectra of the spin trapped adducts are in support of pathway B. The comparison of hyperfine coupling constants in the spectra obtained when natural abundance and selectively deuterated **1** are reduced by SmI₂ in the presence of MNP provide support for the overall spin-trapped adduct reaction scheme in Fig 2.12, where X is the site of selective deuteration. Though there is evidence of ketyl radical formation in the literature, only in rare instances is spin trapping possible.^{103,104} Because of this and a lack of quantification of the trapped radical adducts, pathway A cannot be ruled out as a rational path to product; however, the experiments performed support pathway B. This mechanism is supported by results for other substrates showing that the chemistry

reported requires bromine on the carbon adjacent to the ketone, further supporting pathway B and the scheme reported in Fig 2.12.

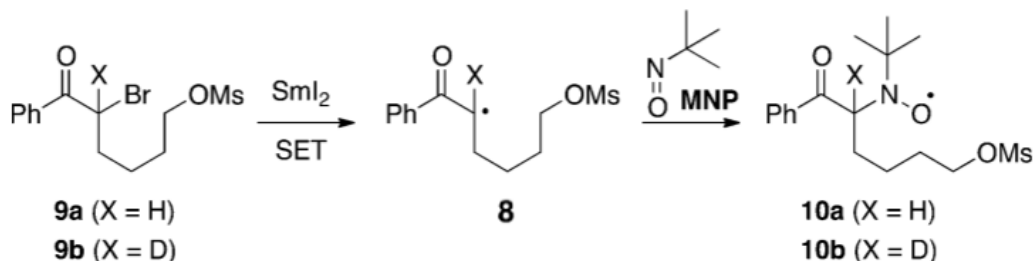


Figure 2.12: Summary of spin trapping experiments for the samarium-mediated reduction of **1** in the presence of MNP. The results shown support the presence of intermediate **8** in pathway B (Fig 2.6). Reproduced with permission from Aretz et al.⁵⁸

Spin trapping has and will continue to be useful in probing reactions with radical intermediates. For this reason, the RS experiment has been utilized to highlight improvements over CW. Increased S/N and faster scan rates seen in RS relative to CW improve the possibility that spin-trapped species are recorded with sufficient fidelity to permit spectral simulation of hyperfine coupling constants.

2.3 High resolution RS-EPR

Enhanced S/N has been obtained using RS for many types of radicals, especially those with long relaxation times.^{52,54,105} Here, we report investigations of the hyperfine resolution that can be obtained with the current generation of RS hardware under development at the University of Denver. As in CW, proper selection of acquisition parameters, such as scan rate relative to signal and resonator bandwidths, is needed to optimize resolution of closely spaced narrow EPR lines. Demonstrations of the impact of parameters of the RS experiment on spectral resolution are presented. Highly resolved spectra of 3-carbamoyl-2,2,5,5-tetramethyl-3-pyrroline-1-yloxy (CTPO), diphenyl

nitroxide (DPNO), and a galvinoxyl radical demonstrate the capabilities of the RS technique to resolve very-small, well-resolved hyperfine couplings. Parallel studies are underway at Bruker Biospin to observe narrow lines in the spectrum of the perylene radical by RS. Narrow and closely spaced hyperfine splittings on the order of tens to hundreds of milligauss are well defined in the spectra shown.

The observed spectra in both RS and CW experiments may be greatly impacted by the selection of acquisition parameters. The effect of CW modulation amplitude and frequency, incident microwave power, non-linearity of these across the dimensions of the sample, and time constant are described in detail in *Quantitative EPR*.¹³ Analogously, in RS the spectrum bandwidth, resonator bandwidth, incident microwave power, eddy currents in the resonator, and nonlinearity of scan rate across the sample influence the resultant spectrum and may give rise to artifacts or unwanted lineshape broadening.³² For either CW or RS, each of these parameters is selected in accordance with the desired optimization for a particular sample. For example, higher modulation amplitude and incident power may broaden a line, but also result in higher S/N in CW spectra. In RS, scan rates that are faster than optimum for the spectral and resonator bandwidths may improve S/N but broaden the spectrum as discussed in the following paragraphs. Faster scan rates permit use of higher microwave power while still avoiding power saturation, which also improves S/N in RS relative to CW.⁵⁴

2.3.1 Bandwidth considerations

The scan rate in a sinusoidal scan varies continuously across the spectrum. The maximum rate at the center of the scan, a_s , is given by

$$a_s = \pi f_s B_m \text{ G s}^{-1} \quad \text{Eq. 2.1}$$

where a_s is the sinusoidal scan rate, f_s is the scan frequency, and B_m is the scan width in gauss.³² In triangular scans the scan rate a_t is independent of position in the scan.

$$a_t = 2 f_s B_m \text{ G s}^{-1} \quad \text{Eq. 2.2}$$

A resonator acts as a filter for the RS signal. The deconvolution process restores the unbroadened linewidth only if the signal bandwidth is less than the effective resonator bandwidth. Resonator Q can be expressed in many ways, but one that is convenient for discussion of RS is in terms of the frequency bandwidth of the resonator, $\Delta\nu$, which is defined as BW_{res} to distinguish from other bandwidths mentioned in this dissertation.³²

$$Q = \frac{\nu}{\Delta\nu} = \frac{\nu}{BW_{\text{res}}} \quad \text{Eq. 2.3}$$

Since each half cycle of a rapid-scan experiment is recorded with either increasing or decreasing field/frequency, the relevant bandwidth that is available for a rapid-scan signal (BW_{RS}) is only half of the resonator bandwidth.

$$BW_{\text{RS}} = \frac{\nu}{2Q} \quad \text{Eq. 2.4}$$

For an X-band resonator with $\nu = 9.3 \times 10^9$ Hz and $Q = 300$, $\Delta\nu = BW_{\text{res}} = 31$ MHz, and the resonator bandwidth that is relevant for selecting rapid-scan parameters (BW_{RS}) is lower by a factor of 2 which is 15.5 MHz. To take advantage of this bandwidth, the spectrometer detection and amplification bandwidths should be at least 15.5 MHz, preferably greater. For a sample with narrow lines the experiment requires either lowering Q to increase resonator bandwidth and/or decreasing the scan rate to lower the signal bandwidth. Microwave loss is introduced in the resonator by adding water or other lossy solvents to the sample tube in either sealed capillaries or thin Teflon tubing to lower

Q and obtain appropriate bandwidth. The practical limit to lowering Q is the ability to tune and operate the automated frequency control of the spectrometer which may be greatly diminished at low Q values. However, lowering resonator Q decreases S/N in the recorded spectrum so it is preferable to operate at the highest resonator Q that is consistent with the required signal bandwidth.¹⁰⁶

The bandwidth of a rapid-scan signal is linewidth-determined and is given by the following equation,

$$BW_{sig} = \frac{N\gamma}{2\pi} \alpha T_2^* \quad \text{Eq. 2.5}$$

where the value of N depends on the acceptable extent of line broadening and α is either a_s or a_t .³² T_2^* is the time constant for decay of the oscillations on the trailing edge of the signal and is also the decay time constant that would be observed for a free induction decay (FID).³² T_2^* is equal to the relaxation time T_2 if there is no unresolved hyperfine splitting. Although the definition of the rapid-scan regime is that the magnetic field scans through the signal in a time that is less than T_2 , the frequency bandwidth of the spectrum depends on T_2^* .³² The larger the value of N , the less the signal is broadened. To obtain the most accurate lineshapes, conservative values of N (typically 5 to 10) are used for the calculation of BW_{sig} . If the goals are, for example, increasing S/N, precision of spin counting, or acquiring transient signals as quickly as possible greater signal broadening may be acceptable.

For a Lorentzian lineshape T_2^* is given by the following,

$$T_2^* = T_2 = \frac{2}{\sqrt{3}\gamma\Delta B_{pp}} \quad \text{Eq. 2.6}$$

where ΔB_{pp} is the peak-to-peak first derivative linewidth.³² The bandwidth for the rapid-scan signal from a Lorentzian line is then

$$BW_{sig} = \frac{Na}{\sqrt{3}\pi\Delta B_{pp}} \quad \text{Eq. 2.7}$$

which may be determined empirically by decreasing scan rate until no further changes in linewidth are observed, similar to decreasing modulation amplitude to find determine linewidths in CW experiments.³² The relationship between T_2^* and ΔB_{pp} depends on the lineshape. Unresolved hyperfine results in EPR line broadening that is approximately Gaussian and decreases the signal bandwidth, which therefore permits use of faster scan rates without spectral broadening. The assumption of a Lorentzian lineshape is a useful starting point for estimating signal bandwidth, which is required to select a scan rate that is consistent with a particular resonator Q .

2.3.2 High resolution spectra

CTPO and galvinoxyl were purchased from Sigma and used as received. DPNO was synthesized by the oxidation of the secondary amine via oxone and tetra-n-butylammonium hydrogen sulfate as reported by Brik.¹⁰⁷ A red oil was obtained at room temperature by low pressure evaporation and was found to decompose quickly in solution. For increased shelf life, DPNO was stored by co-crystallization with benzophenone via slow evaporation of an ethanol or hexane solution.^{108,109} Solutions of CTPO (0.2 mM) and DPNO (~ 0.1 mM) were prepared in ethanol and drawn into ~3 mm OD quartz EPR tubes with a sample height of 3-5 mm and sample volume of approximately 10-15 μL . Solutions were purged of O_2 by repeated cycles of freezing and

evacuating the sample before flame sealing. The 0.1 mM toluene solution of galvinoxyl was prepared in a ~4 mm OD quartz EPR tube with equivalent sample height and similarly purged of O₂ by repeated cycles of freezing and evacuating before flame sealing. To lower the resonator Q to perform experiments with galvinoxyl, a sealed quartz tube of water was added to the EPR tube, submerged in the sample solution. The molecular structures of the radicals investigated are shown in Fig 2.13.

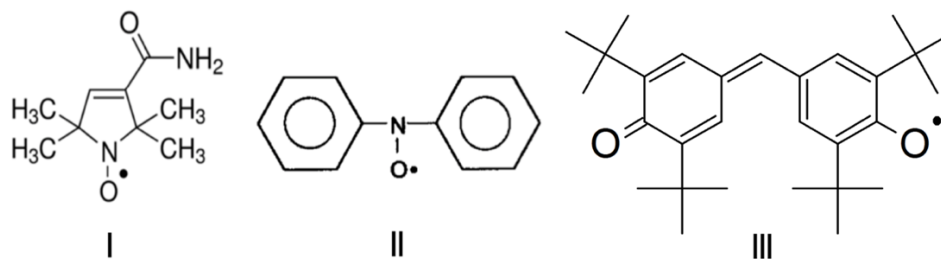


Figure 2.13: 3-carbamoyl-2,2,5,5-tetramethyl-3-pyrroline-1-yloxy (CTPO, I), diphenyl nitroxide (DNPO, II), and the galvinoxyl radical (III).

RS spectra were obtained on a Bruker E500T X-band E500T transient CW spectrometer that was modified by adding magnetic field scan coils mounted on the outside of a Bruker FlexLine ER4118-X-MD5 dielectric resonator. The scan coils are driven by a RS driver that was designed for a minimum scan rate of 200 Hz. Lower frequencies may be driven using external frequency and waveform input.¹² Low frequency RS measurements are complicated by mechanical resonances and baseline drifts typically preventing operation below about 500 Hz. The scan coils used are approximately 7.6 cm in diameter, composed of 200 turns of 175/46 Litz wire. The RS signal is detected with a microwave quadrature mixer, amplified in the Bruker E500T bridge, and digitized in a Bruker SpecJet II. The detection system has a selectable 20 or 200 MHz bandwidth and adjustable gain (0-66 dB). The dielectric resonator was selected to minimize eddy currents induced by the rapidly changing magnetic fields. The first

derivative of the RS absorption spectrum was calculated and a Gaussian filter applied, which gives S/N similar to what has been obtained previously with pseudomodulation.¹¹⁰ The spectrometer employed for RS measurements also has the capability to perform traditional CW measurements. Unless otherwise noted, the same spectrometer and resonator were used in the comparisons shown. Microwave power was chosen to be within the linear response region of the spin system with respect to microwave B_1 and was determined independently for CW and RS experiments.

In a sinusoidal scan if the rate in the center of the spectrum is too fast, the resolution of hyperfine may be better in the extremes of the spectrum where the scan rate is slower. While sinusoidal RS is advantageous in terms of hardware requirements, triangular scans are preferred when the signal bandwidth is large because of the uniform scan rate across the spectrum.¹¹¹ The extensive proton hyperfine splitting in spectra for well deoxygenated samples of rapidly tumbling CTPO provides a test of spectrometer performance and of both the type of scan and scan rate selection. Resolution of proton hyperfine is similar for the low-field and center-field lines of the spectrum of CTPO obtained by CW with low modulation amplitude (Fig 2.14, *blue*) and in triangular scans obtained with sufficiently slow scan rate (Fig 2.14, *orange*). Resolution is lower for the high-field lines because of incomplete motional averaging of g and A anisotropy. Spectra obtained with varying sinusoidal scan rates demonstrate the changes in hyperfine resolution in the low-field line relative to the center-field line (Fig 2.14, *yellow, purple, and green*). The maximum scan rate for a sinusoidal scan is in the center which is therefore the region of the scan with the largest BW_{sig} and poorest hyperfine resolution (Fig 2.14, *green*). The slower rates for the extremes of the scan yield better resolution.

However, a slower rate may contribute to power saturation of the signal relative to the faster rates, distorting the signal.¹¹¹ To avoid saturation, power should be selected based on the saturation observed at the extremes of the spectrum. Independent of the shape of the scan, faster scan rates increase broadening and filter narrow linewidths when BW_{sig} is larger than the BW_{res} . In the CTPO experiments presented in Fig 2.14, the CTPO narrow hyperfine linewidths were broadened by 30 mG at a rate of 6.8×10^4 G/s, 50 mG at a rate of 2.5×10^5 G/s, 70 mG at a rate of 4.3×10^5 G/s, and 180 mG at a rate of 7.4×10^5 G/s in addition to the observed inconsistencies attributed to sinusoidal scanning. These values are a first approximation using an isotropically tumbling model and a least squares analysis in EasySpin.⁹⁹ The BW_{sig} is less than BW_{res} in all but the fastest scan rate.

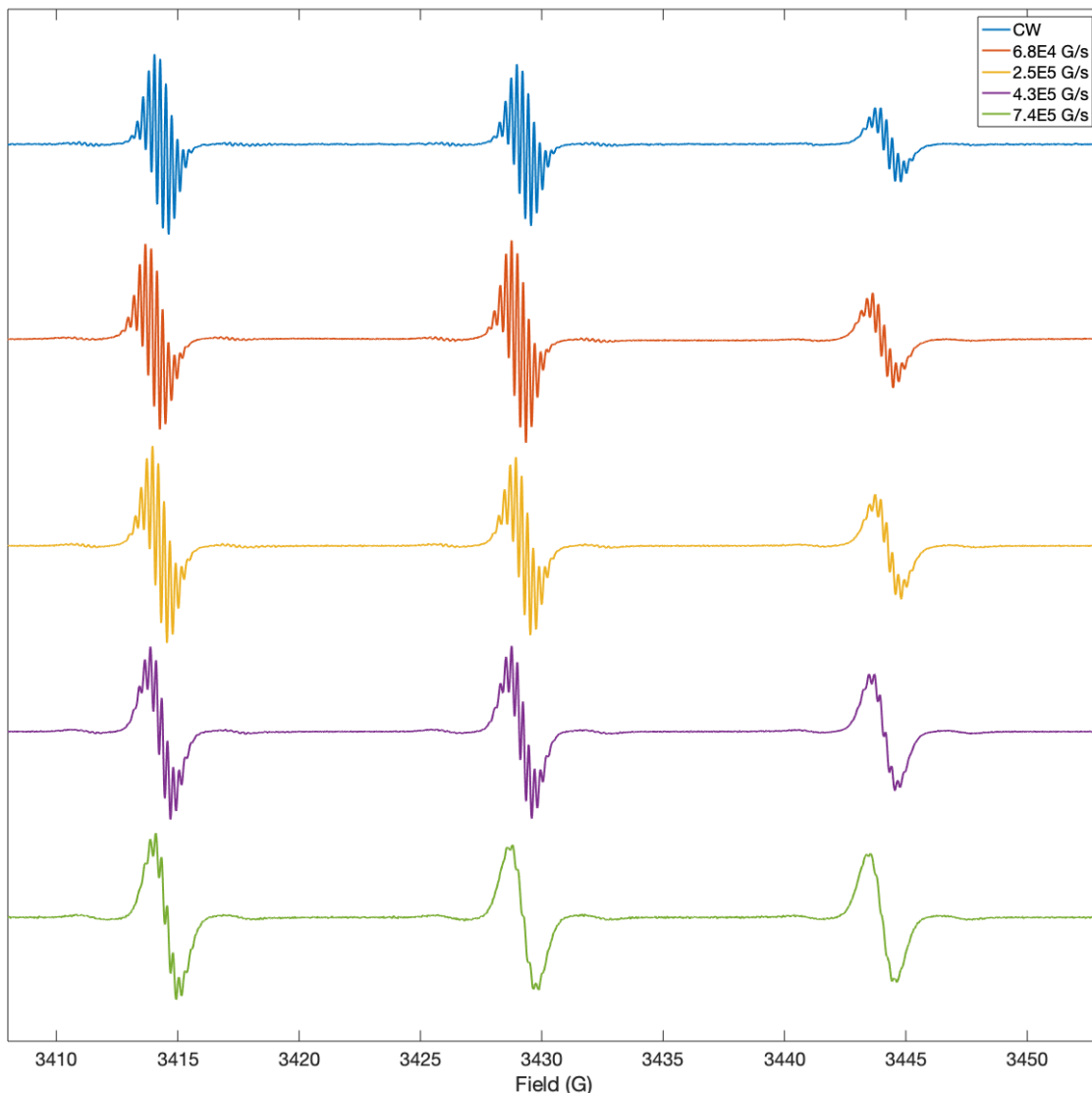


Figure 2.14: Effects of increasing scan rate on the resolution of the RS spectrum of 0.2 mM CTPO in deoxygenated ethanol with a sample height of ~ 10 mm after deconvolution and calculation of the first derivative. A 50 mG Gaussian filter was applied to all spectra. Spectra are scaled to be similar amplitude. The CW spectrum was recorded using 50 mG modulation amplitude and 20 kHz modulation frequency. RS spectra were recorded using the modulation rates reported in the figure legend.

Spectra in Fig 2.14 were obtained with a sample height of ~ 10 mm. Broadening of the signals with increasing scan rate was greater than predicted based only on resonator bandwidth constraints. Additional broadening of the EPR linewidth may result from eddy currents occurring in metallic components generated from a the rapidly oscillating RS

scan field.^{33,34,112} These eddy currents have been shown to broaden the linewidth of both LiPc and trityl-CD₃ by as much as 23 mG at very fast modulation rates.³³ When using the Bruker FlexLine ER4118-X-MD5 dielectric resonator it was previously reported that 7-10 mG broadening may occur depending on the observed resonator Q but that this broadening may be minimized if the sample is placed slightly below the center, maximizing the distance from the inductive coupling antenna.³³ This presents a particular constraint when using fluid solution samples because the EPR tube outer diameter must be smaller than the resonator diameter (~5 mm) and the sample height must be far from the coupling antenna at the top of the resonator and still within the active space of the resonator (~10 mm total height). In RS experiments with CTPO using slow, linear scans, as much as 30 mG broadening was observed when using a sample height of 10 mm when compared to a slow CW scan with a sample height of 3 mm, placed slightly below the center of the resonator. When performing RS experiments on the 3 mm sample height CTPO sample placed slightly below the center of the resonator, the observed broadening was reduced to 10 mG relative to the 10 mm sample. The optimized RS spectrum of CTPO is shown in Fig 2.15. The improved resolution of the spectrum obtained for the 3 mm sample with 2.4×10^5 G/s scan rate in Fig 2.15 than for the same scan rate with the 10 mm sample in Fig 2.14 shows the impact of decreasing the influence of eddy currents in the coupling antenna. The *S/N* of the CW spectrum obtained in the same data acquisition time (Fig. 2.15, *yellow*) is much lower than for the rapid scan spectrum. Since the eddy current effects that required the shorter sample for the RS experiments do not impact the CW spectra a longer sample could have been used to improve the *S/N* for

the CW spectrum by about a factor of 3, but the S/N would still be substantially less for the CW spectrum than for the RS experiment.

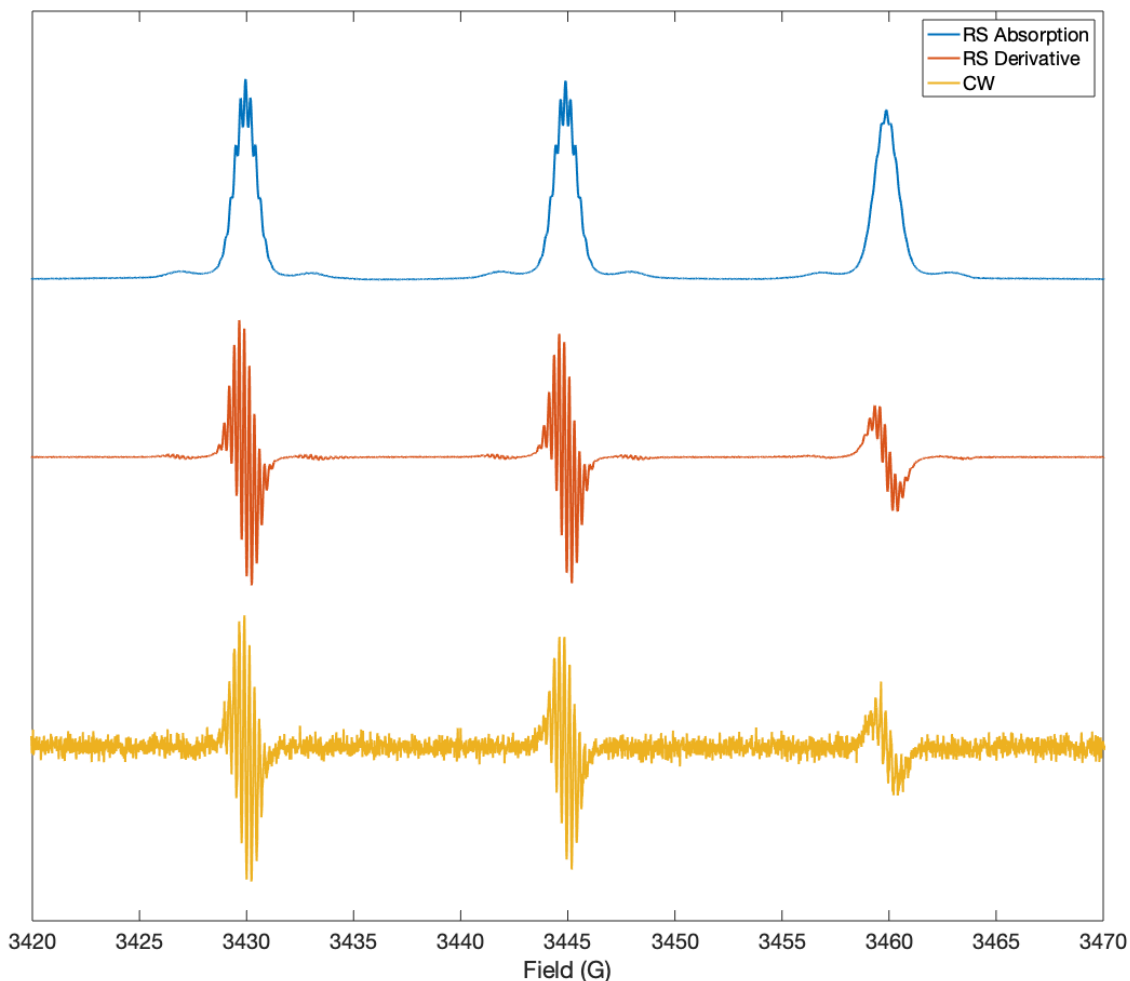


Figure 2.15: RS spectra of CTPO, 0.2 mM, in ethanol with a sample height of 3 mm after deconvolution compared with CW spectra obtained with 15 mG modulation amplitude at 20 kHz. RS spectrum was acquired using triangular scans at a rate of 2.4×10^5 G/s. A 30 mG Gaussian filter was applied to the RS derivative and CW spectra. The absorption spectrum (*blue*), and the mathematical derivative of the absorption spectrum (*red*) compare well with the CW spectrum (*yellow*). Spectra are scaled to constant y-axis amplitude.

Triangular RS and CW spectra of DPNO are shown in Fig 2.16. More than 60 lines can be resolved in these spectra. The CW spectrum of DPNO was obtained with 15 mG, 20 kHz modulation which causes slight broadening of the spectrum. RS spectra reported in previous papers from the Eaton lab were usually obtained with scan rates of

many kHz.^{38,51-54} However, to have sufficient resonator bandwidth to resolve the hyperfine in O₂-free dilute solutions of DPNO, and to encompass the entire spectrum, a 60 G scan was performed with 1.76 kHz scan frequency, which gives $a_t = 2.2 \times 10^5$ G/s. The resonator Q was 1500 with the sample present giving a resonator bandwidth for RS of 3.2 MHz. The BW_{sig} calculated based on the smallest ΔB_{pp} of 130 mG with a 2.2×10^5 G/s scan rate and $N = 5$ was 1.8 MHz. This BW_{sig} is approximately a factor of two times lower than the BW_{res} which is a conservative selection. Note that even with these “slow” rapid scans, more than 3500 full field-swept spectra may be co-added every second using both the increasing field and decreasing field components of the triangular scans. The post-acquisition analysis also uses both the real and imaginary outputs of the quadrature detector, yielding improved S/N over CW spectra.³⁶ With these data acquisition parameters, the first derivative of the RS absorption spectrum exhibits hyperfine resolution that is similar to the CW spectrum. Use of faster scans or higher Q would decrease the resolution of the RS spectrum. The S/N for the RS spectrum in Fig. 2.16 is much higher than for the CW spectrum shown in Fig. 4C. Analogous to the results for CTPO, a longer sample could have been used for the CW spectrum than for the RS experiment, but the S/N would still be much lower for CW than for RS.

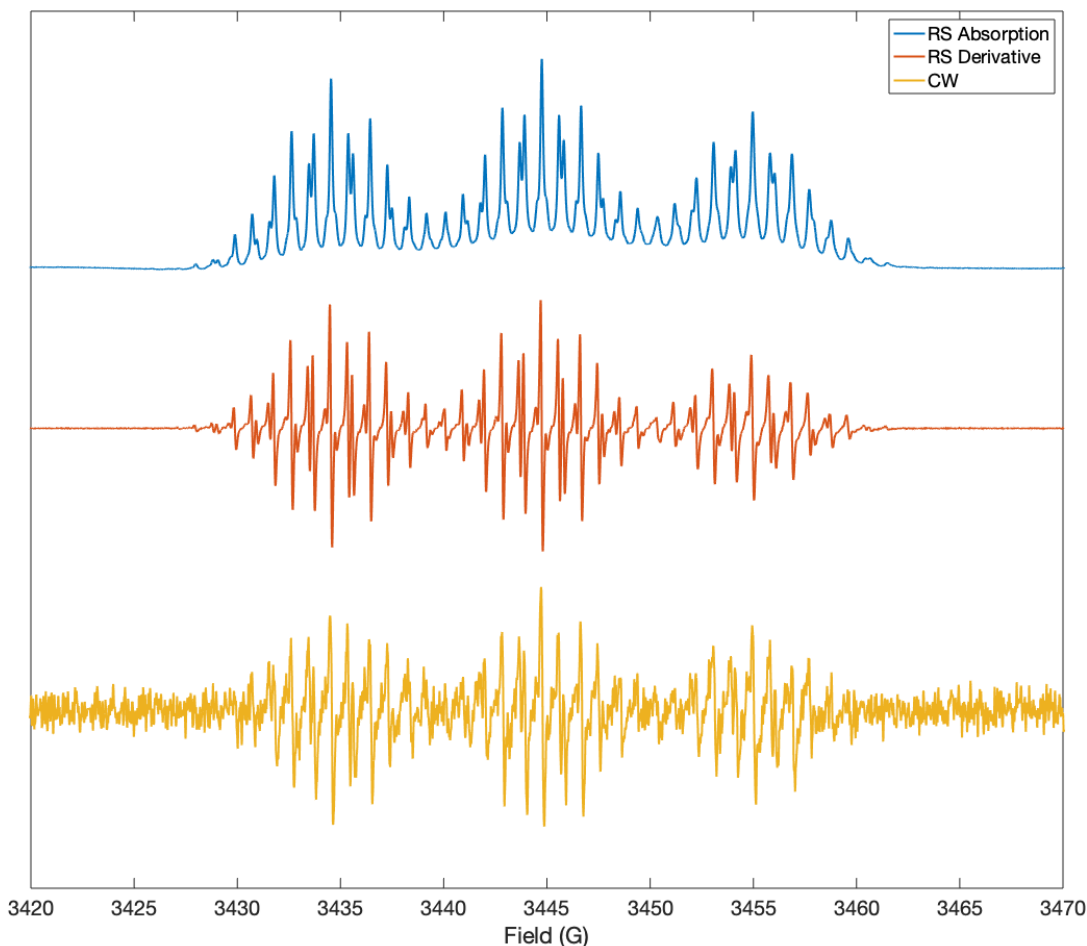


Figure 2.16: RS spectra of DPNO, ~ 0.1 mM, in ethanol after deconvolution compared with CW spectra obtained with 15 mG modulation amplitude at 20 kHz. RS spectrum was acquired using triangular scans at a rate of 2.2×10^5 G/s. A 30 mG Gaussian filter was applied to the RS derivative and CW spectra. The absorption spectrum (*blue*), and the mathematical derivative of the absorption spectrum (*red*) compare well with the CW spectrum (*yellow*). Spectra are scaled to be similar amplitude.

Triangular RS and CW spectra of galvinoxyl are shown in Fig. 2.17. The CW spectrum of galvinoxyl was obtained with a modulation amplitude of 30 mG at 20 kHz modulation which causes slight broadening of the spectrum. The ΔB_{pp} is about 50 mG. This spectrum is a challenge for CW spectroscopy because even slight drift in magnetic field or frequency can cause line broadening when spectra are signal averaged. To record CW spectra with the narrowest lines, a single scan was collected with very high conversion time, 163.84 ms, for a total data acquisition time of 2700 s. RS spectra were

collected using 27 G scan and 1.7 kHz scan frequency, which gives $a_t = 9.2 \times 10^4$ G/s. The resonator Q was 900 with the sample present giving a BW_{RS} of 5.4 MHz. The BW_{sig} was calculated based on the smallest ΔB_{pp} of 50 mG and $N = 5$ to give 1.7 MHz, which is conservative relative to BW_{RS} . The rapid scans permitted use of substantially higher B_1 (16 mG) than could be used for CW (1 mG). The S/N for the RS signals in Fig. 5 is much higher than for the CW obtained in the same data acquisition time. For this sample in low-loss toluene a larger sample volume could have been used for the CW spectroscopy than for rapid scan. The eddy currents in the particular resonator used for these experiments limit operation to small volumes and is not a general limitation for rapid scan. To achieve the large bandwidth required for rapid scans on these narrow lines the resonator Q was lowered substantially, which decreases S/N . This is a fundamental requirement for resolution of narrow lines in RS spectra. For the toluene sample a higher Q could have been used for the CW experiments which would have improved the S/N .

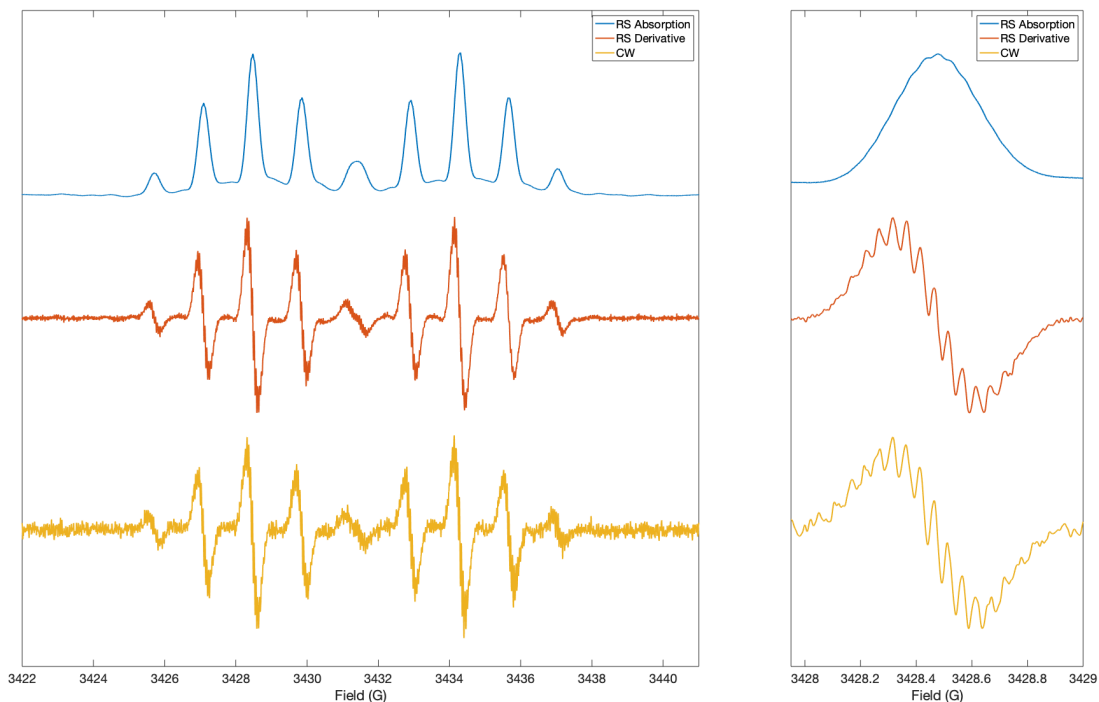


Figure 2.17: RS spectra of galvinoxyl, 0.1 mM, in toluene after deconvolution compared with CW spectra obtained with 30 mG modulation amplitude at 20 kHz. RS spectrum was acquired using triangular scans at a rate of 9.2×10^4 G/s. A 10 mG Gaussian filter was applied to the RS derivative and CW spectra. The absorption spectrum (*blue*), and the mathematical derivative of the absorption spectrum (*red*) compare well with the CW spectrum (*yellow*). Spectra are scaled to be similar amplitude.

A summary of the parameters of the experiments performed and resulting S/N of the data presented is given in Table 2.5. The spectra of these three radicals demonstrate that in both CW and in RS the fine details of the spectra obtained depend on careful selection of acquisition parameters. For example, 30 mG wide lines would be obscured by using 0.1 G, 100 kHz magnetic field modulation and/or partially saturating incident microwave power. Likewise, in RS experiments, hyperfine lines of similar width (~ 30 mG) will be greatly obscured when using 50 G magnetic field sweeps at 30 kHz if the resonator bandwidth is 5 MHz from a Q of 1000. In addition to spectral and instrumental parameters, very small hyperfine lines may also be broadened by very small field drifts when using long signal averaging times that often are employed to better define low

intensity peaks in the spectrum. Specifically, in the case of the galvinoxyl radical, it was found that a single, slow CW scan provided better resolution than performing extensive signal averaging due to source frequency drifts.¹¹³ RS has the advantage that complete spectra are collected very quickly, reducing additional loss of resolution from instrumental instabilities.

Table 2.5: Overview of CW and RS parameters selected and the resulting S/N comparison between CW and RS.

	Exp.	Min. obs. linewidth* (mG)	B ₁ (mG)	Q	BW** (RS/Signal)	Acq. time (s)	S/N
CTPO	RS Abs	120	29	1500	1.8	1100	>1000
	RS Deriv		29			1100	>1000
	RS Abs		29			200	920
	RS Deriv		29			200	410
	CW		20			1100	40
DPNO	RS Abs	130	41	1500	2.1	1100	770
	RS Deriv					1100	630
	RS Abs					200	370
	RS Deriv					200	250
	CW					1100	30
Galvinoxyl	RS Abs	50	16	900	1.3	2600	430
	RS Deriv		16			2600	160
	RS Abs		16			700	380
	RS Deriv		16			700	80
	CW		0.9			2700	50

*Linewidths found by spectral simulation in EasySpin.⁹⁹

**Bandwidth is given as a ratio of the bandwidth available for the RS experiment divided by the required signal bandwidth calculated based on the minimum expected linewidth and scan rate. A value of $N=5$ was used in all bandwidth calculations.

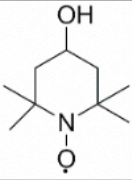
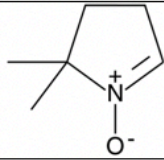
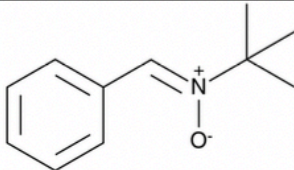
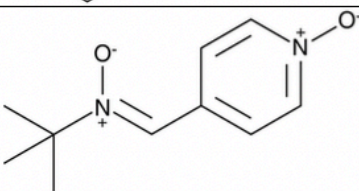
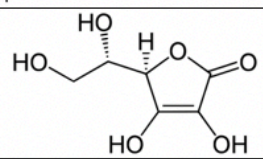
Spectra for these samples demonstrate that hyperfine structure of organic radicals with narrow, and closely spaced, EPR lines can be obtained with good fidelity by RS. As in CW, proper selection of acquisition parameters is needed to optimize the spectral features of interest. The bandwidth of the RS spectrometer must be set to record the highest frequency component of the narrowest lines present in the spectrum when

accurate lineshape and high spectral resolution are desired. As in CW, S/N can be improved at the cost of broadening the spectrum by increasing scan rate beyond the resonator bandwidth-limited rate in RS experiments. This application of RS to organic radicals that exhibit highly resolved hyperfine coupling demonstrates that even in this very demanding realm of EPR, RS can replace CW.

2.4 Fast acquisition RS-EPR

This study extends RS to full spectra as a function of time with an acquisition timescale that is faster than conventional CW to improve detection of dynamic processes that occur on the spectral acquisition timescale. Data are shown for the reduction of tempol by ascorbic acid and the decay of commonly used spin traps via bromine-mediated reductions. The molecular structures of the nitroxides and spin traps studied is given in Table 2.6.

Table 2.6: The reagents employed in the investigation of RS kinetics experiments.

Reagent	Molecular structure
Tempol	
DMPO	
PBN	
POBN	
Ascorbic acid	

2.4.1 Data throughput and digitizer considerations

Experiments were performed on a Bruker E500T X-band spectrometer equipped with a SpecJet II digitizer for transient data collection and a Bruker SPU for CW data collection. A previously described, locally-built RS coil driver provided a sinusoidal scanning waveform to Litz wire coils operated at 20 kHz.¹² For 100 G sinusoidal sweeps at 20 kHz, the maximum rate at the center of the scan is 6.3 MG/s. The time required for one half-cycle scan, or one full EPR field-swept spectrum, was 2.5×10^{-5} seconds. Typical times required to collect a full field-swept EPR spectrum in RS and CW experiments is given in Table 2.7. The primary difference in the time for the experiments

is the slow field sweep time for CW experiments. Fast digitizers improve the rate of RS data collection, which may ultimately be limited by the RS rate and the digitizer overhead.

Table 2.7: A comparison between spectral acquisition times observed when performing both CW and RS on a Bruker E500T.

Experiment	Sweep Time (s)	Acquisition Time (s)	Averages
CW	3.93	8.37	1
RS	2.5×10^{-5}	1.50	9216

Acquisition time includes the sweep time for all accumulated averages, digitizer rearm time, and the time required to record data on the spectrometer PC. Data were collected using Bruker Xepr and the included Python API.

To limit the time between the beginning of the reaction and initial spectral observation, reactions were performed on the benchtop adjacent to the magnet and solutions were injected into a Bruker ER4118X-MD5 FlexLine dielectric resonator via hand-driven syringes and either Teflon (~0.9 mm ID) or Tygon (~1.6 mm ID) flexible tubing. To limit dead time during faster reactions, a plastic junction was used as a mixing cell and the reaction proceeded as the sample volume was injected into the resonator. In slower spin-trap experiments, reagents were mixed on the benchtop and pulled through tubing that extended through the resonator using a hand driven syringe. In all experiments, the spectrometer was tuned with a representative sample in the tubing through the resonator to provide a stable, similar environment for the duration of the experiment. To decrease instrumental dead time, repetitive experiments were performed using locally written scripts in Python and Bruker Xepr software and were programmed to begin data collection before injection. This allowed for a true dead-time free experimental design when not confounded by changing signal intensities due to slight fluctuations in sample volume during injection.

2.4.2 Tempol reductions via RS-EPR – How fast can we go?

The reaction of tempol and ascorbic acid is well known and was employed to test the advantages of RS when recording successive spectra quickly.⁷⁵ Tempol is reduced by one equivalent of ascorbic acid to form the hydroxylamine and an ascorbate radical.⁷⁵ Two equivalents of ascorbate radical may then disproportionate to form dehydroascorbic acid and an ascorbate dianion.⁷⁵ The availability of reagents, relative simplicity of the reaction, ability to view the reaction progress by EPR, and excellent water solubility of both reactants contributed to the selection of this reaction for comparison between CW and RS methods to monitor reaction kinetics. Traditional CW methods rely on sweeping the main field magnet which is a large and slowly responding coil system. If too fast a sweep is attempted, the actual field lags behind the input current and the signal appears at an incorrectly labeled field (Fig 2.18, *left*). Small auxiliary coils that offset the main field are used in RS, allowing the main field to be held constant and field scans to be performed much faster (Fig 2.18, *right*). Most standard and commercially available CW spectrometers are not able to continuously sweep the main field back and forth and instead require significant time between sweeps (~1-5 s) before the field is stable again to collect the next field sweep. In sinusoidal RS experiments, the scan coils are resonated and a full field sweep is performed twice for every period of the sinusoidal scan. At a scan rate of 6.3 MG/s, a 100 G sweep occurs approximately every 25 μ s (Table 2.8) and is free of the field inaccuracies observed in rapid CW experiments.

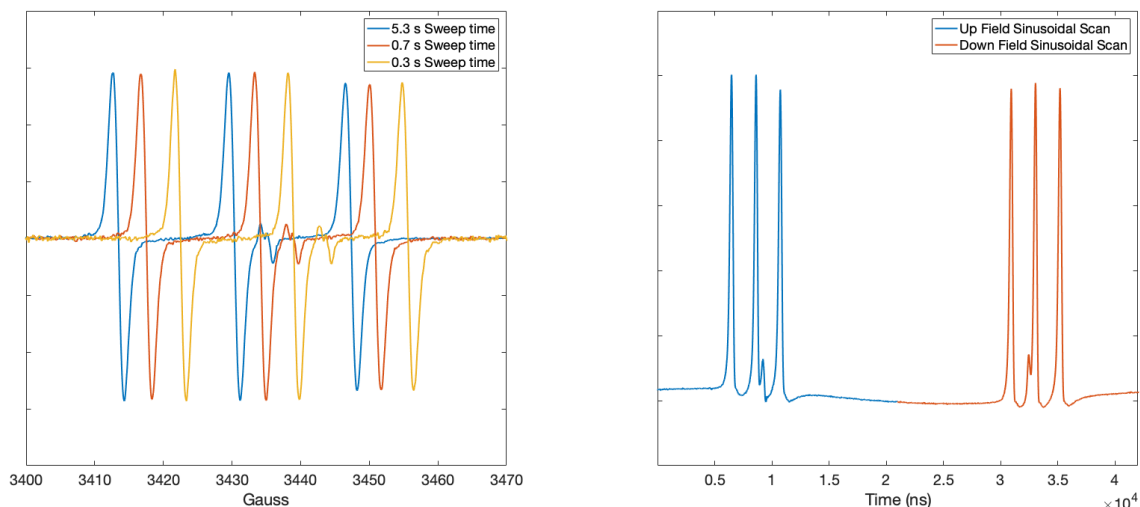


Fig 2.18: Spectra of tempol plus ascorbate radical mixture recorded via CW (*left*) and RS (*right*). The 3-line signal is from tempol and the sharper, single line is from the ascorbyl radical. The apparent change in field position of the spectrum in CW experiments results from a lag between the field set by the controller and the actual field at the sample. Because RS experiments are recorded with more agile scan coils, the magnetic field at the sample is better defined.

For the same concentrations of reagents (1 mM tempol, 10 mM ascorbic acid) in deionized water, the S/N observed in each field-swept EPR spectrum is higher (factor of ~ 1.7) in RS experiments than for CW (Fig 2.19, *left, inset*). This leads to less uncertainty in the measurements of signal intensity with respect to time, and the resulting decay curves generated from RS intensities have significantly lower standard deviation than CW experiments (Fig 2.19, *left*). Spectra can be acquired much more rapidly in RS giving about an order of magnitude increase in the number of acquired spectra per unit time (Fig 2.19, *right*). The reaction of tempol (10 mM) and excess ascorbic acid was repeated 5 times and data co-added to decrease error. RS spectra were collected in a single half-cycle and were used without deconvolution (Fig 2.19, *right, inset*). The decay curve, generated from the observed intensity of the RS field-swept spectra, was fit with a biexponential decay model.

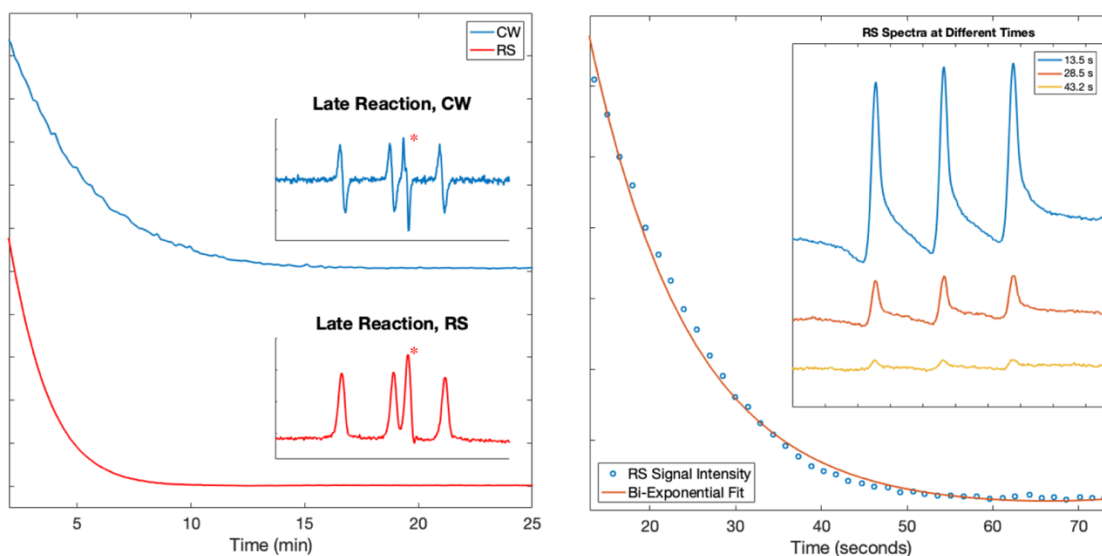


Fig 2.19: Tempol reduction by ascorbic acid recorded at similar concentrations (1 mM tempol, 10 mM ascorbate) by CW and RS (*left*) and with saturating concentrations (10 mM tempol, excess ascorbate) via RS only (*right*). Each data point represents a full field-swept spectrum, shown in the inset to each decay curve. The 3-line signal is from tempol and the sharper, single line is from the ascorbyl radical, marked with a red asterisk (*left*).

To characterize the reaction rate the concentration of ascorbic acid was varied and RS measurements performed (Fig 2.20). The reaction was performed by mixing 5 mL of 1 mM tempol and between 0.2-1 mL of 10 mM ascorbic acid in a small beaker before pulling the reaction mixture into the resonator via a negative pressure syringe driven Teflon transfer line that is approximately 0.9 mm ID. Because of this, concentration of tempol varied slightly depending on the final volume of the reaction mixture after addition of a variable volume of 10 mM ascorbic acid. At the beginning of the EPR experiment, the instrument is tuned using 1.0 mM tempol in the transfer line. In each measurement, 300 independent field-swept RS spectra were recorded over a period of approximately 48 minutes. Each spectrum consisted of 30,720 spectral averages, each with seven field-swept spectra in the time domain (3.5 sinusoidal scan cycles) for a total number of 215,040 spectral averages per spectrum. The experiment was performed such

that data collection begins during the reaction and before injection into the resonator. For this reason, the first few spectra recorded are not of the reaction but instead of the standard tempol solution already present in the resonator. Approximately 60 spectra were used in the calculation of the data presented in Fig 2.20, beginning at 100 seconds following initial recording and approximately 40-60 seconds following injection. The results support that, when properly controlled for starting concentration, RS gives improved resolution of spectral changes that occur on the EPR timescale.

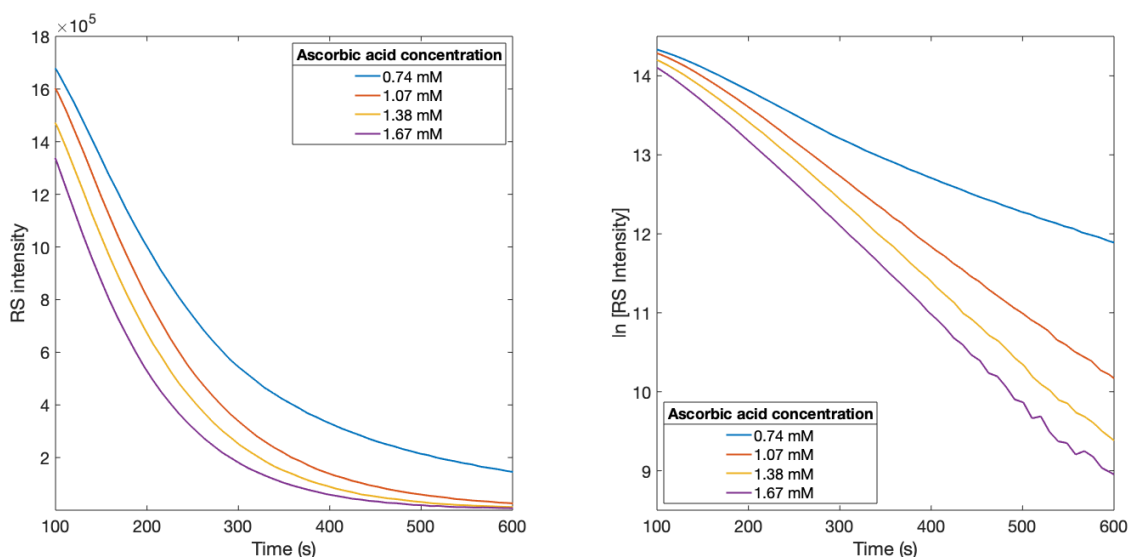


Fig 2.20: Reaction of approximately 0.8-0.9 mM tempol with varying concentrations of ascorbic acid. Maximum EPR intensity at the start of the reaction was assumed to be the starting concentration of tempol which varied slightly between experiments.

The use of RS allows molecular dynamics to be monitored on a timescale of seconds which is significantly shorter than the CW timescale of tens of seconds when using commercially available digitizers and realistic spectral acquisition parameters. In the pursuit of faster data acquisition, it is possible in a CW experiment to forego the field-swept spectrum and only record intensity as a function of time at a single field position. Monitoring a single field position greatly enhances data collection rate; however, spectral

averaging is limited and any change in spectral features is lost. In the pursuit of both fast data acquisition and full field-swept spectra, faster RS data acquisition will be possible as digitizers are improved and spectrometer overhead is decreased.

2.4.3 Decay of common spin traps via bromine oxidation

Many commonly used spin traps contain an unsaturated carbon adjacent to a nitrogen-oxygen bond. This carbon is vulnerable to oxidation and subsequent carbonyl formation in the presence of some oxidizing agents.^{114,115} In the experiments with Dr. Chris Aretz pertaining to samarium mediated reductions, described in section 2.2 and in Ref⁵⁸, it was observed that an unexpected product was formed when a solution of DMPO was mixed with Br₂ and exposed to white light. The product exhibited nitrogen hyperfine coupling that was smaller than expected for oxidized DMPO (*~16 G expected, ~7 G observed*).^{77,116,117} The unexpected signal was first recorded during the control experiments to determine if the bromine atom in 5-bromo-6-oxo-6-phenylhexyl methanesulfonate was reacting with the spin trap. Similar spectra have been reported in the literature, and attributed to the formation of an acyl-nitroxide, DMPOX.¹¹⁴ The proposed acyl-nitroxide is unstable for linear spin traps, such as PBN and POBN, and rapidly fragments, in the presence of a proton source, to an EPR-silent aldehyde and a nitroxide radical according to the scheme in Fig 2.21.

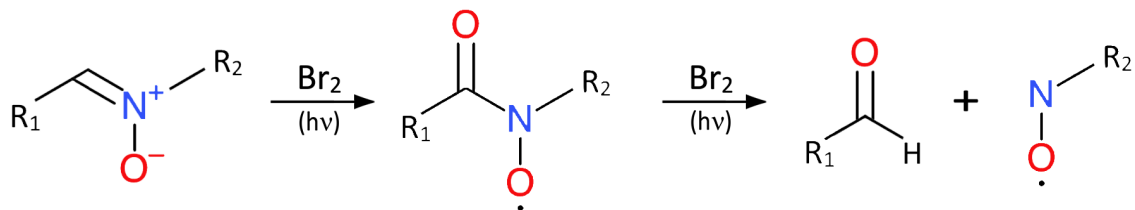


Fig 2.21: Proposed reaction scheme of common spin trapping molecules in the presence of bromine and light.

The acyl-nitroxide formed from the cyclic pyrrolidine spin trap, DMPO, and the product, DMPOX, is more stable than for linear traps. DMPOX has a distinctive nitrogen hyperfine splitting (~ 7 G) and forms over the course of an hour with excess Br₂ (Fig 2.22).^{114,117} RS experiments were performed similar to those for tempol plus ascorbate. DMPO (40 mM) was exposed to ambient light in the presence of excess bromine before being drawn into the negative pressure syringe driven Teflon tubing and into the EPR resonator. Two full sinusoidal cycles and 204,800 spectral averages were collected for each RS spectrum (Fig 2.22, *left*) for a total of 819,200 averaged full field-swept spectra. Approximately 300 RS spectra were collected sequentially over a period of 110 minutes. The growth curve was constructed from the signal amplitude of the RS spectra with respect to time. The reaction proceeded over the course of 60 minutes and no changes in spectra were observed after formation of DMPOX.

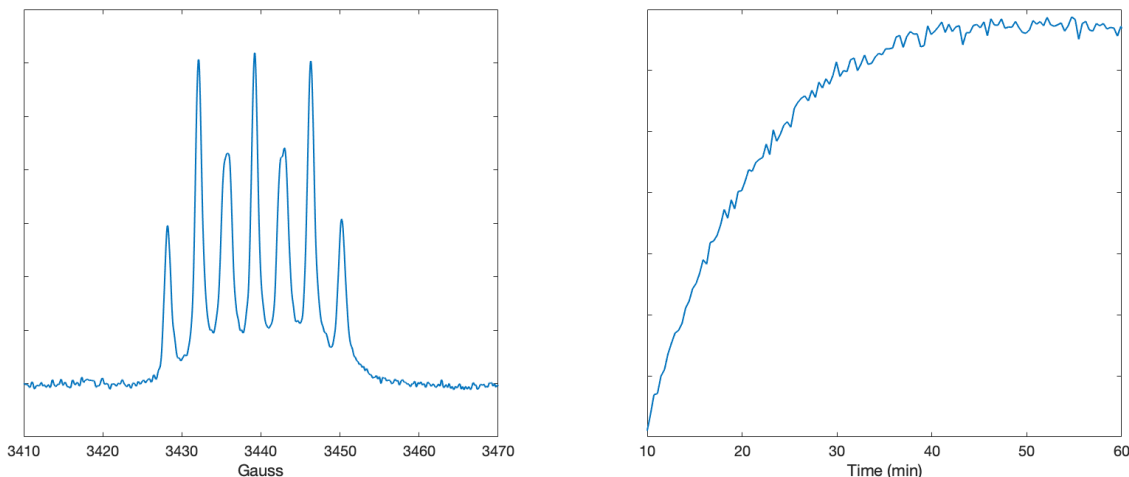


Fig 2.22: RS spectrum and the kinetics of formation of DMPOX from DMPO in aqueous Br_2 . The reaction was monitored by observation of the maximum EPR intensity present throughout the spectrum.

Similar RS experiments were performed for linear spin traps PBN and POBN similar to those above. PBN (40 mM) was exposed to ambient light in the presence of excess bromine before being drawn into the negative pressure syringe driven Teflon tubing and into the EPR resonator. Two full sinusoidal cycles and 204,800 spectral averages were collected for each RS spectrum (Fig 2.23, *left*) for a total of 819,200 averaged full field-swept spectra. Approximately 300 RS spectra were collected sequentially over a period of 110 minutes. A lag phase was observed before the reaction mixture became spectroscopically active. The growth curve was constructed from the signal amplitude of the RS spectra with respect to time (Fig 2.23, *right*). The reaction proceeded over the course of 120 minutes. There appears to be several nitroxide products within the late reaction RS spectra, and it is only in the early RS spectra that a PBNOX-like nitroxide may be present alone (Fig 2.23, *left*). In the case of PBN, benzaldehyde and a tert-butyl nitroxide fragment are the likely products with evidence of a benzaldehyde initially suspected from the odor of late reaction mixtures. In both PBN and POBN,

proton splitting indicative of an aldehyde was observed by NMR following a benzene extraction of the reaction mixture. Further experiments are necessary to support the identity of all products observed.

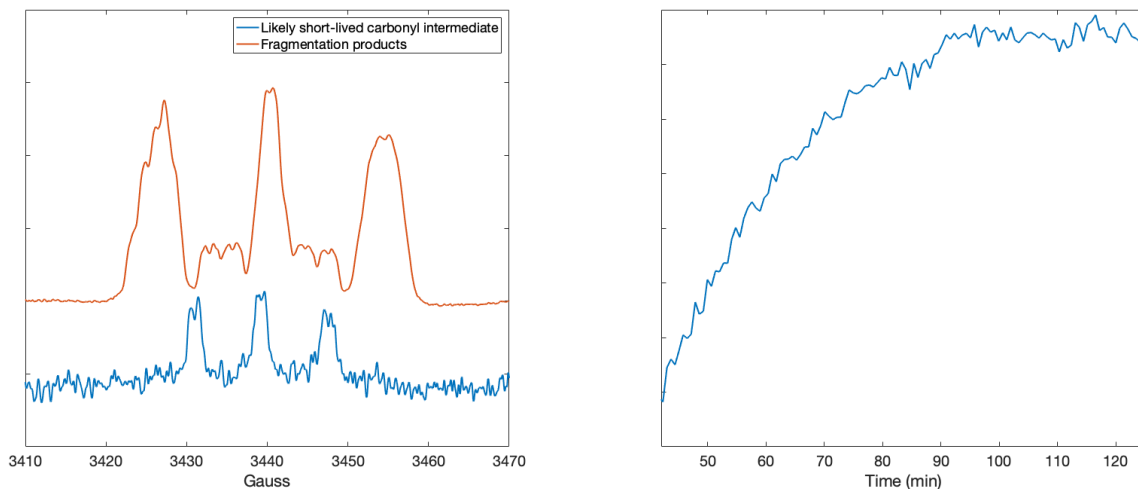


Fig 2.23: RS spectra of the formation of PBNOX and other fragmentation products from PBN in aqueous Br_2 . The reaction was monitored by observation of the maximum EPR intensity present throughout the spectrum.

Though the reaction times investigated with regards to spin trap decay are quite long in comparison to the faster examples for tempol and ascorbate, the S/N and data acquisition speed required to observe the acyl-nitroxide spectrum when performing experiments with linear spin traps was only made possible by RS. Because nitroxides and spin traps are commonly used to probe varying redox environments, it is necessary to characterize both the formulation and decay products of spin-trapped adducts. Of particular importance is bromine, which has recently been found to contribute to collagen formation, and is redox active in systems that are already complicated in the number of differing redox species present.¹¹⁸ Of particular interest in these environments is the approach of fingerprinting, using several different spin traps in a single system to

elucidate trends.⁸⁴ RS will be paramount in these investigations from both an S/N perspective and a data collection perspective.

Chapter Three: Development of a digital Saturation Recovery instrument

“When chasing gremlins, they often get much worse before getting better.”

- Richard Quine

Dedicated saturation recovery (SR) EPR spectrometers have been previously reported at frequencies of 250 MHz, 1 GHz and 9 GHz.^{7,8,119–122} Due to the advent of arbitrary waveform generators (AWGs), it is possible to reconsider the complicated construction of standalone saturation recovery spectrometers and, in particular, the switching processes necessary to perform the saturation recovery experiment. AWGs have formed the basis of several EPR spectrometers documented in the literature demonstrating the effectiveness of replacing traditional microwave sources with new, wideband AWGs that may be operated with very precise timing control.^{24,123–125} Our goal was the construction of an A WG-based digital microwave bridge for performing saturation recovery experiments similar to prior homebuilt systems at X-band.^{7,119–121} AWGs available at X-band suffer from considerably high phase noise relative to traditional microwave sources.^{24,29} With the guidance and direction of Richard Quine, the overall design of the spectrometer was conceived to satisfy three figures of merit, listed below with decreasing priority.

Flexibility: It was decided early in the design of the digital saturation recovery bridge that the most important benefits of the digital spectrometer would be the expanded

flexibilities offered by the AWG, including microwave generation, timing, and pulse shaping. Timing events may be controlled by several event markers with high accuracy, eliminating traditional hardware switching and increasing both the resolution with which switching events may occur and the number of unique switching events. This design would effectively decrease the spectrometer footprint while expanding the repertoire of EPR experiments that may be performed in a single instrument. AWGs are wideband and able to synthesize any frequency below the hardware-limited maximum sampling rate. For EPR spectrometers, the bandwidth limiting component is usually the resonator due to critical coupling requirements. The digital saturation recovery bridge was designed to accommodate many different resonators, further increasing flexibility of the instrument.

Accuracy: Digital waveform synthesis allows for increased reproducibility while preserving variability in microwave frequency relative to solid state sources. Because the waveform begins as a mathematical function, variability is only introduced by error associated with the fundamental oscillator and subsequent multipliers within the AWG. When adequately controlling variations in the operating environment of the spectrometer that can impact the resonator frequency, such as ambient temperature and humidity, there is no need to adjust the source frequency during experiments. Prior SR instruments required an automated frequency control circuit that was set to monitor an external resonator to adjust for drifts in both source and resonator frequency; however, both the AFC circuitry and external cavity are no longer necessary in the digital SR spectrometer. In most cases, the error associated with frequency synthesis in AWG-based experiments is decreased relative to adjustable analog microwave sources, leading to more precise relaxation measurements and greater reproducibility in the S/N of the resultant recovery

curve. It was thereby anticipated that the AWG-based SR spectrometer would improve the overall reproducibility of the experiments performed relative to prior spectrometers.

Noise Suppression: SR is widely considered a “low S/N” technique because of the small signal detected. Current specifications for source noise for an AWG are poorer than the Gunn diode sources used in modern SR systems. This raises a concern that use of an AWG would increase noise in the detected signal if not controlled appropriately. There are inherent flaws when synthesizing microwaves from a discretely defined digital waveform, such as increased jitter if waveforms are not designed to loop appropriately or when the fundamental oscillator within the AWG demonstrates particularly high source noise relative to other microwave sources. It was necessary to develop a microwave bridge design that suppressed resultant noise relative to the signal of interest. Careful attention was given to component specification and placement within the microwave bridge to minimize noise while maximizing the voltage of the acquired signal. Overall gain and noise figures were recorded at many iterative stages of instrument design, dictating necessary revisions that would ultimately yield an instrument capable of further decreasing the limit of detection to lower spin concentrations relative to prior SR spectrometers.

3.1 Instrument design and performance

The fundamental measurement by the EPR spectrometer is of voltage.³¹ The recorded EPR signal, in voltage, must be properly isolated from all other voltage sources within the instrument for accurate signal detection. Artifact signals from non-EPR sources often contribute to the detected voltage, typically having distinct frequencies or

spectral patterns that aid in identification and isolation relative to the signal of interest. The detected voltage in an SR experiment is the same as in CW experiments (*Eq. 1.5*); however, because the signal is detected directly without magnetic field modulation and at low power, the signal voltage is lower and more difficult to distinguish from random noise than what is typically seen in a CW experiment.

The primary functions leading to increased signal voltage within the SR spectrometer are microwave excitation power, resonator quality factor, and detection system gain.¹³ Source noise, poor resonator coupling, and the associated noise figure of the detection system all increase the “noise floor” of the EPR signal measurement.^{31,126,127} Additionally, microwave loss is considerably larger at X-band than at lower frequencies and every component prior to the detector that requires independent microwave connectors and cabling decreases the signal.^{31,126} All of these factors were considered in the design of the digital SR instrument.

3.1.1 Use of arbitrary waveform generators

When replacing an analog microwave source with one performing digital waveform synthesis, considerations of synthetic error are necessary. Decades of development surrounding the klystron and Gunn Diode microwave sources specifically for the EPR spectrometer have resulted in low noise, stable frequency output over a variety of power levels. However, with these microwave sources it is difficult to rapidly change the frequency or amplitude of the output to perform SR experiments or generate shaped pulses. The AWG is a relatively new feat of engineering, allowing the

experimentalist to generate many frequencies while simultaneously manipulating the shape, duration, and excitation profile of the resultant waveform.^{24,123–125}

Analog microwave sources produce an operating frequency that is a continuous output that does not vary with time; however, these sources suffer from large susceptibilities to the environment when attempting to output stable frequency while maintaining some adjustability.¹²⁸ Digital waveform synthesis, such as in an arbitrary waveform generator, has a defined resolution, specified in sample rate, shown in Fig 3.1.^{128,129} Each sample is an individual, discretely defined point in the resulting waveform.¹²⁸ This discretization results in greatly increased frequency stability due to the ability to mathematically describe the requested waveform. Both analog and digital frequency synthesis suffer from “jitter”, a term typically used to describe the error associated with time-domain signal synthesis.^{130–132} Jitter within the microwave source generates a very small bandwidth of frequencies centered around the requested frequency and results from fluctuations in analog sources.^{130–132} In digital synthesis, the resulting jitter may be estimated from the length of adjacent, individual discretized values when hardware jitter is not considered. The maximum discretization induced jitter is then the sum of all jitter over the difference in time of the beginning of one discretized step to the end of the next step and defines the maximum variance within the synthesized waveform.¹³²

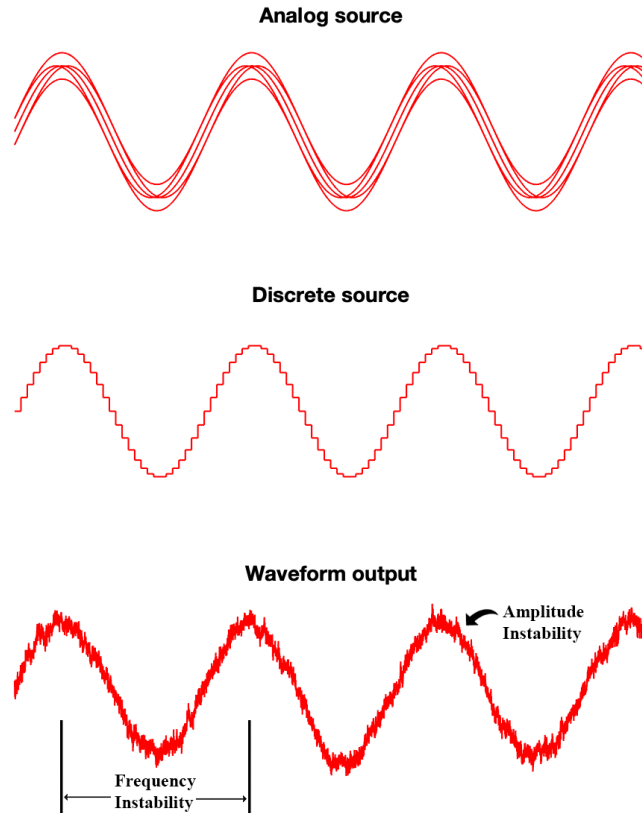


Fig 3.1: Analog-generated and discretely generated sinusoidal waveforms. Jitter from analog frequency generation results in a small band of frequencies due to inconsistent oscillator stability (*top*). Jitter from digital sources results from error associated with frequency synthesis in discrete steps (*middle*). A representation of the oscillator output and associated errors is presented (*bottom*). Digitization steps are typically smoothed by the impedance of the system. Adapted from IEEE Standard definitions.¹²⁹

Defining a sinusoidal oscillator digitally requires sufficient sampling of the desired frequency and is described by the Nyquist-Shannon sampling rate theorem,¹³³

“If a function $f(x)$ contains no frequencies higher than W cps [cycles per second], it is completely determined by giving its ordinates at a series of points spaced $1/2W$ seconds apart.” By this reasoning, a 10 GHz waveform may be generated from an AWG sampling at a rate of 20 gigasamples per second (GSa/s). Typically, the impedance of the system results in a rounded off sinusoidal waveform when using a fundamental oscillator of only two points per cycle. In practice as it relates to the EPR experiment, using so few

points in the mathematically described waveform results in increases in noise generated by the microwave source. This noise, often referred to as source noise or phase noise, is much greater for AWGs than for analog sources and is a significant problem at X-band frequencies.^{130,131} Because the microwave frequency is required for both excitation and detection in SR experiments, this noise may be present in the final EPR spectrum and should be minimized as much as possible. It is possible to utilize a fundamental oscillator as the reference clock input to the AWG rather than using the internal oscillator, giving the opportunity to preserve the capability of waveform synthesis while taking advantage of low noise oscillators. With proper selection, a reference clock may greatly decrease source noise in waveform synthesis. The digital SR system is reported in Ref.²⁹ Richard Quine provided invaluable advice on the design and testing of the instrument. The video amplifiers and transistor-transistor logic (TTL) circuit were designed and built by Richard Quine. Early designs of the instrument are detailed in the dissertation of Dr. Zhelin Yu in Ref.¹³⁴

3.1.2 Component layout and overview

The digital SR instrument was designed to utilize an AWG as the microwave source, the control system for fast switching of the microwave power, and for triggering of the digitizer. The SR system described in this chapter is an accessory to a Bruker E500T instrument, such that only the main field magnet and digitizer from the Bruker system are used. This approach was chosen to employ Bruker Xepr software for field control and data collection. In addition to two Bruker resonators, an ER4118X-MS-5 and an ER4118X-MD-5, several additional resonators aided in the characterization of figures

of merit and overall instrument performance. The system was designed to accommodate both reflection and crossed-loop resonators. A schematic of the instrument is in Fig 3.2, followed by a list of components used in Table 3.1.

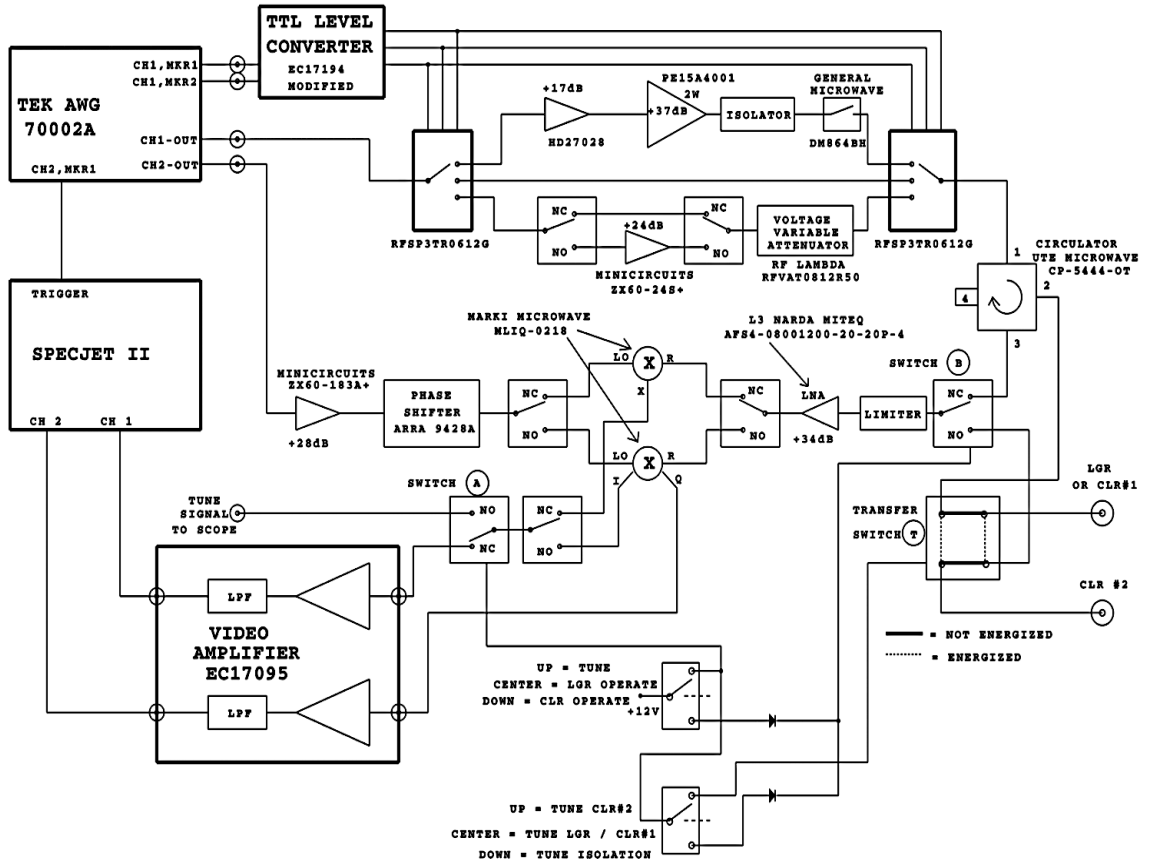


Fig 3.2: Block diagram of the instrument. Reproduced with permission from McPeak et al.²⁹

Table 3.1: Overview of the components used within the AWG-SR bridge. Reproduced with permission from McPeak et al.²⁹

Component	Manufacturer (Part Number)	Gain/loss (db)	Noise figure (db)	Bandwidth (GHz)	Max input (dBm)	Output power* (dBm)
Preamplifier	HD Communications (HD27028)	17	1.9	7-14	5	13
2-W amplifier	Pasternack (PE15A4001)	35	6	6-12	17	33
RF amplifier	Mini-Circuits (ZX60-24+)	24	6.5	5-20	20	18
Detection LNA	L3 Narda Miteq (AFS4-08001200-20-20P-4)	34	1.3**	8-12		23
LO amplifier	Mini-Circuits (ZX60-183A+)	28	5	6-18	20	18
Quadrature mixer	Marki Microwave (MLIQ-0218L)	5***		2-18	11-18	
Low-loss mixer	Marki Microwave (MM1-0626S)	1.5** *		6-24	17-23	
Voltage controlled attenuator	RF-Lambda (RFVAT0812R50)	1.2		8-12	30	
Phase shifter	ARRA (9828A)	0.75		0-18		
Circulator	UTE Microwave (CP-5444-OT)	0.8		7-11		
Limiter	Aertech (A9L111B)	0.6				

*At 1 dB compression point.

**The effective noise figure is increased to 4.3 dB by the 3 dB loss of the switches, cabling, and limiter on its input when using about 1 ft of cable to connect to a resonator.

***When the double balanced mixer is used as a phase sensitive detector, the estimated loss is about 1.5 dB.³¹ When the quadrature mixer is used as a phase sensitive detector, the estimated loss is about 5 dB.

3.1.3 Power delivery and tuning

The microwave source is comprised of a Tektronix 70002A AWG and a Wenzel Associates 500-29237 rev. C low noise clock source. The Wenzel source produces a

constant 12.5 GHz frequency that then serves as the input to the AWG. A final multiplier within the Tektronix AWG generates the fundamental sampling rate of 25 GSa/s. There are two independent microwave outputs, each with a nominal 330 μ W, as well as one additional dependent microwave output per channel for a total of four microwave outputs. The dependent microwave outputs produce the equivalent output of their respective channel, phase rotated by 90°. Two independent microwave outputs form the excitation frequency and a reference waveform to supply local oscillator input for the mixer in the bridge. In cases where the fundamental and reference waveforms may be the same frequency, one independent microwave output and one dependent, equivalent output may be used; however, it is convenient for resonator matching to use independent microwave outputs.

Each independent microwave output is associated with four event markers for a total of eight event markers. The event markers produce 1.4 V in the high state; however, switching components in the bridge require 5 V. A transistor-transistor logic gate within the bridge increases the marker voltage from 1.4 V to 5 V and creates 3 logical outputs from two inputs, further increasing the total event marker outputs available for various component triggering. Switching from high, saturating power to low, attenuated power in a time that is short relative to the SR experiment is performed in this manner, controlled by three TTL logical outputs. An additional event marker direct from the AWG triggers either the SpecJet II digitizer or a LeCroy WaveRunner oscilloscope.

The SR experiment requires a period of continuous saturating power followed immediately by a very low, continuous, excitation power. To perform these tasks, three microwave excitation pathways exist within the bridge, each with differing power

amplification abilities. The path used for saturating the spin system contains a 17 dB gain amplifier followed by a 2-Watt power amplifier resulting in 800 mW available at the resonator input for adequate saturation of the spin system. The low power excitation pathway contains a 24 dB gain amplifier for observing the recovery of the spin system from saturation. These microwave paths are shown in Fig 3.3, taken from the larger figure presented earlier. The change in power, from saturating to low observation levels, must be fast relative to the recovery of the spin system from saturation. This is accomplished by the two 3-position microwave switches at the beginning and end of the excitation path diagram (Fig 3.3). These switches are controlled via the AWG event markers and the TTL circuit as they require 5 V for switching. Due to the large power levels present from the saturation path, an additional isolator and switch are required to prevent leakage to other, low power observation paths. The switch is controlled by the same event marker as the microwave path selection switches and serves to further isolate the high-power amplifier path when using lower power paths.

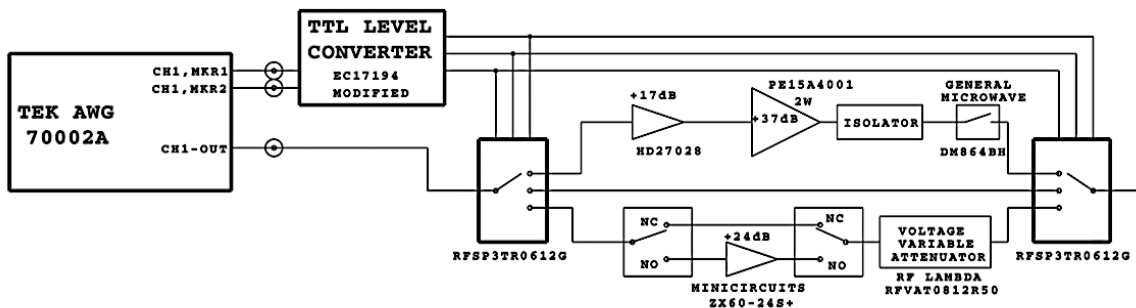


Fig 3.3: Microwave excitation pathways for saturating and observing the recovery of the spin system. The microwave switches can switch between microwave paths in approximately 50 ns. Adapted from McPeak et al.²⁹

The observation path contains additional switches, controlled from the bridge front panel, to bypass the 24 dB amplifier present in this path. A voltage-controlled attenuator, also controlled from the bridge front panel, allows for both attenuation of the

amplified signal and attenuation of the microwave output of the AWG when bypassing the amplifier. This creates a wide array of available observation power levels from a few nanowatts to a maximum of ~ 7 mW of available power at the input to the resonator when connected by 12" of coaxial cabling. A third, straight-through path is available for diagnostics and troubleshooting of instrument performance and is easily accessible from a removable top panel.

Because the microwave power is present during observation, the resonator must be critically coupled to minimize reflected power and prevent saturation of the detection system. Resonator matching, or tuning, is performed by synthesizing a frequency chirp and a reference waveform in the AWG such that the Fourier transform of the reflected waveform may be observed on a lower performance oscilloscope (< 500 MHz bandwidth, typically). The frequency chirp is often of wider bandwidth than the resonator to adequately perform the Fourier transform free of baseline drift. The reference waveform, typically a constant frequency set at the lowest frequency present in the chirp waveform, provides the local oscillator input to a double balanced mixer. The resulting signal after mixing, now a frequency chirp from near DC to ca. < 500 MHz during routine operation, may be viewed on a low frequency oscilloscope rather than observing the resonator absorption profile near the carrier frequency of ca. 9 GHz. To view frequencies that are significantly higher than the bandwidth of the video amplifier (< 5 MHz) by Fourier transform, a switch on the instrument front panel bypasses the video amplifier.

The tuning circuitry (Fig 3.4) allows observation of the reflection profile of two independent resonators and the resulting isolation between them, measured in dB and was designed to incorporate a crossed-loop resonator (CLR). A circulator directs microwaves

to a transfer switch, which then directs microwaves to either resonator. The reflected waveform is directed by the circulator to the detection system. When energized, the same transfer switch directs excitation microwaves to one resonator, while directing the resultant EPR signal in the orthogonal resonator to the detection system. A final microwave switch controls the input to the detection system and selects for either the reflected microwaves from a single resonator via the circulator or the transmitted microwaves through a transmission resonator or CLR.

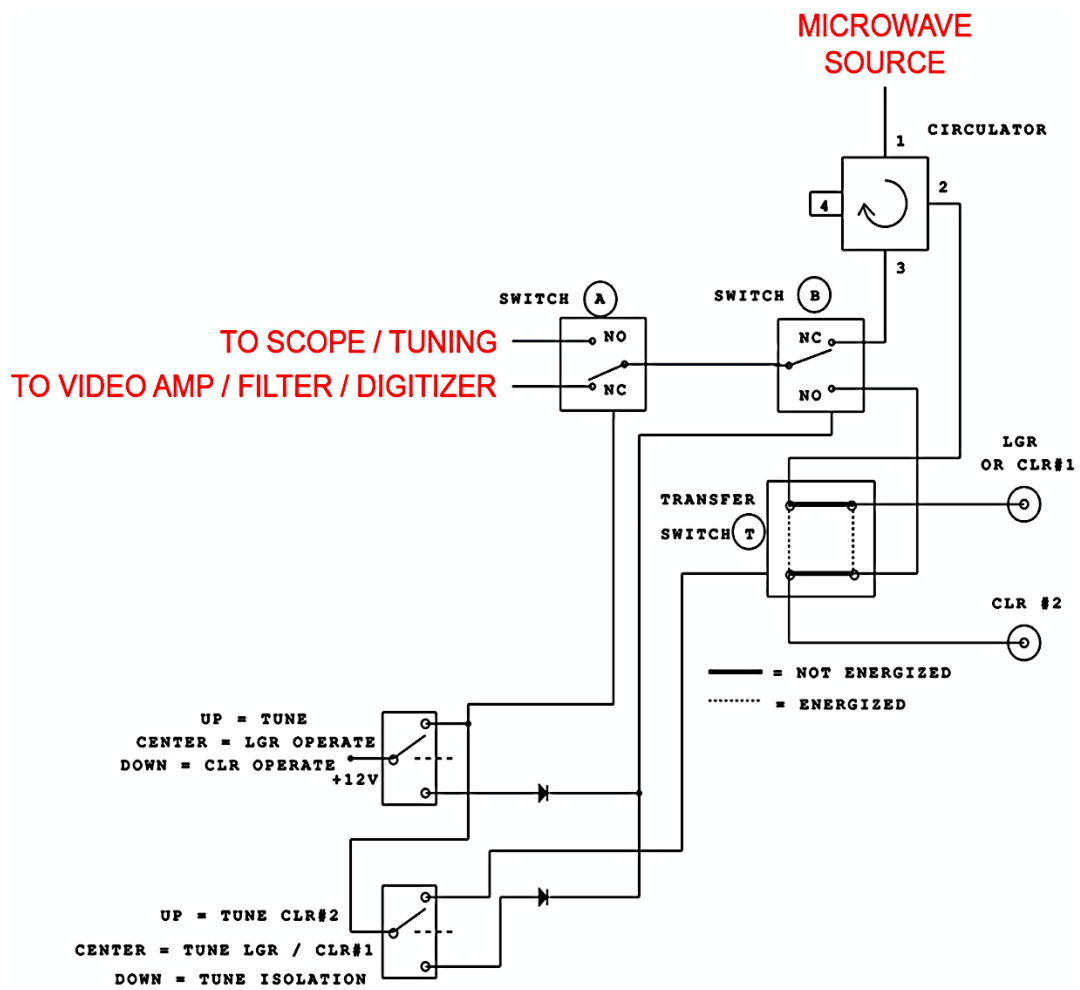


Fig 3.4: An abridged diagram of the circuitry necessary for tuning either a reflection resonator (LGR or CLR #1 *only*), a transmission resonator (CLR #1 to CLR #2), or a crossed-loop resonator (CLR #1 to CLR #2, *with isolation adjustment*). Reproduced with permission from Rinard et al.¹³⁵

The system was designed to accommodate either reflection or transmission resonators with the specific purpose of developing a crossed-loop resonator for use at X-band. In a crossed-loop resonator, two orthogonal resonators surround a single sample space. If properly oriented with respect to one another, the isolation between resonators may be as high as ~33 dB in the resonator designed and built at DU and is measurable using the selection switches on the front panel and a standard oscilloscope. Though complicated in circuitry, tuning path selection is minimized to only two switches on the front panel. One switch selects for “tune” mode or “operate” mode and controls both microwave switches, labeled A and B in Fig 3.4, which bypasses the video amplifier for tuning. A second switch selects for operation of the transfer switch and directs microwaves to either of two resonators while also selecting detector input. Isolation between two resonators of a crossed-loop resonator is adjusted by monitoring signal transmission magnitude (in dB) on an oscilloscope.

3.1.4 The detection system

The detection system (Fig 3.5) consists of a 34 dB low noise microwave amplifier, either a double balanced or quadrature mixer and a video amplifier designed and built by Richard Quine (Fig 3.6) that is based on a similar, previous design.^{7,31} A limiter is placed on the input to the microwave amplifier to protect the system from reflected power that may be present if the resonator is not well tuned. The mixer is selectable from the front panel. The video amplifier contains two identical channels. Each channel contains selectable 4-pole Butterworth filters (10 kHz, 100 kHz, 2 MHz) for controlling bandwidth and variable gain settings (34, 40, 46, 54 dB) to adequately

increase the signal voltage to an appropriate level for input to the digitizer (Fig 3.6). The digitizer in the system is a Bruker SpecJet II; however, after mixing to near DC levels any digitizer with appropriate speed and resolution may be used.

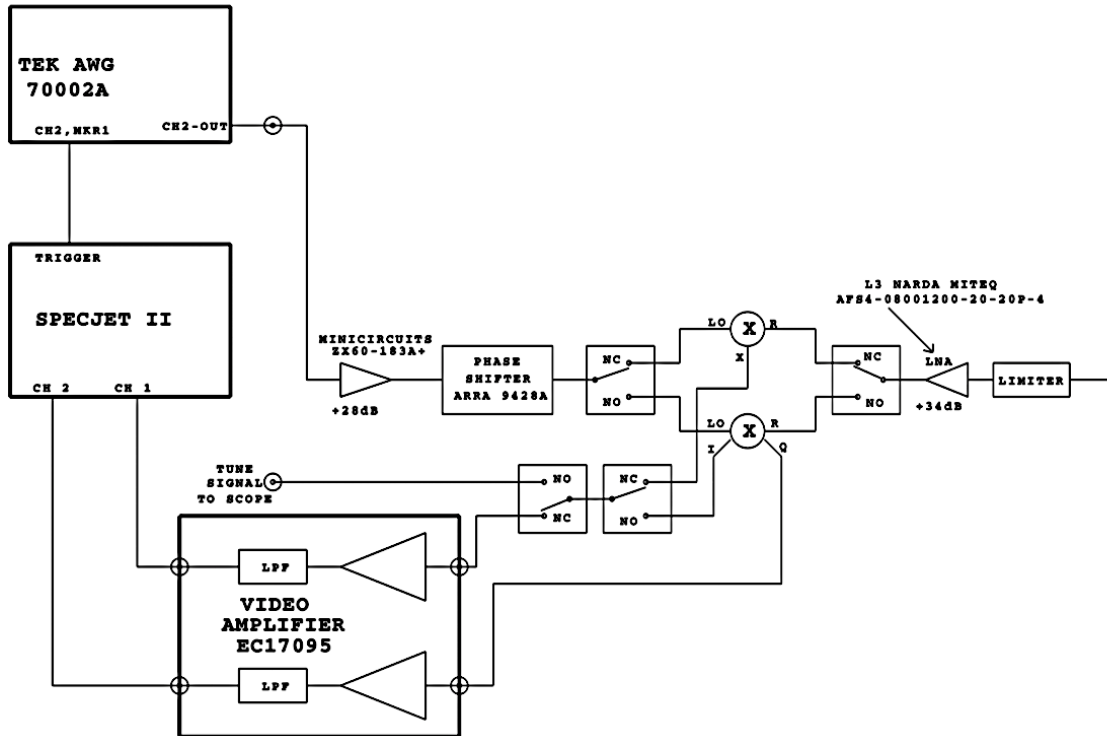
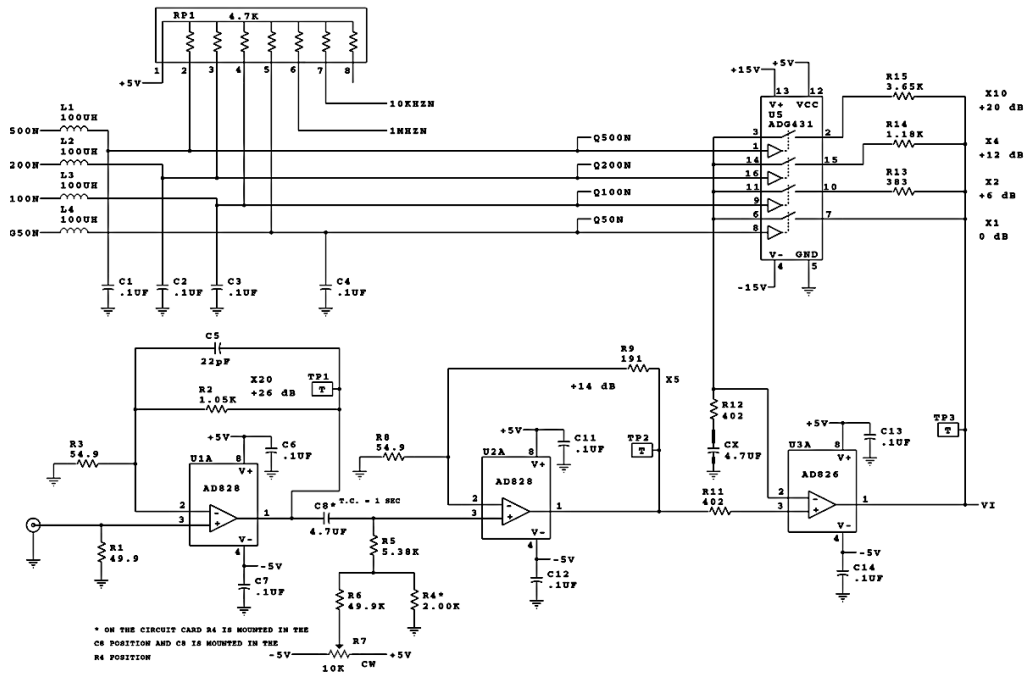


Fig 3.5: An overview of the detection system in the digital SR bridge. Adapted from McPeak et al.²⁹

Both the quadrature mixer and the double balanced mixer were used as phase sensitive detectors.³¹ In this application, a reference waveform establishes the bandwidth of the mixer allowing only the microwave frequency of interest to be transmitted, greatly rejecting noise.³¹ The reference waveform is synthesized by the AWG. A 28 dB microwave amplifier provides appropriate power to either mixer. A phase shifter is placed after the amplifier both to match the phase of the microwave signal input to the mixer and to account for mismatches in path length between the microwave excitation path and the local oscillator path. To prevent saturation of the video amplifier due to the

high gain of the microwave amplifier, the voltage of the reference waveform is set to zero during the saturating period and for a very brief period following saturation. The double balanced mixer requires both a reference waveform and sufficient power from the reference to adequately detect a signal. Without either of these inputs, the mixer acts as a blanking switch and prevents excess power from saturating the video amplifier. This control by the reference waveform is often referred to as detector blanking and the timing is managed by the output of the AWG. An event marker output of the AWG is used to trigger the SpecJet II digitizer.

Gain



4-Pole Butterworth Low Pass Filter

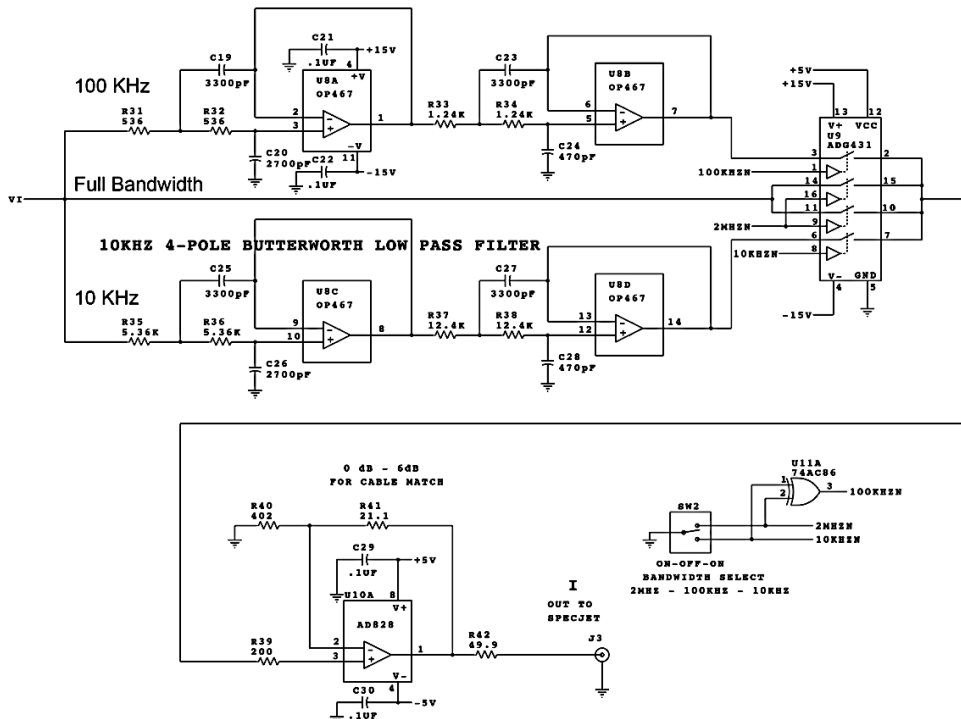


Fig 3.6: An overview of both the gain circuit (*top*) and filter circuit (*bottom*) of the video amplifier. Only one channel is shown; however, the bridge contains two identical channels within the video amplifier. Both gain and filter settings are selectable from the front panel of the SR bridge. Reproduced with permission from McPeak et al.²⁹

3.1.5 Testing system performance

An ideal oscillator produces a sinusoid at a single frequency that may be defined by an infinitely narrow peak in the Fourier domain.¹²⁸ No oscillator is ideal and in many cases the oscillator has significant uncertainty, leading to many frequencies present in Fourier domain.¹²⁹ Source noise, or phase noise, is the deviation of the output of a microwave source from a single sinusoid and is defined by the amplitudes of the frequencies present near the targeted frequency in the Fourier domain, referred to as sidebands.¹³² Integration of the amplitudes of the frequencies in the sidebands from the target frequency, or carrier, to a specified bandwidth enables the comparison of different microwave sources.^{132,136} This measurement is reported in units of decibels (dB) below the carrier and is a measure of the intensity of the integrated sideband amplitudes relative to the carrier amplitude in the Fourier domain.¹³² Sideband frequencies arise from inconsistencies in the fundamental oscillator in the time domain and increase with increasing uncertainty in the oscillator (Fig 3.7).¹²⁹ These inconsistencies can be defined by the variance in the zero-crossing point in the time domain oscillation.¹²⁹⁻¹³² Previously described by Shannon and coworkers, a microwave frequency of 10 GHz (near X-band) requires an oscillator operating at a minimum of 20 GSa/s.¹³³ The AWG employed in the digital SR spectrometer has a maximum sampling rate of 25 GSa/s and may define a 10 GHz oscillation at a rate of 2.5 samples per cycle. Phase noise decreases with increasing samples per cycle due to fewer inconsistencies present in the zero-point crossing of the time domain signal.¹²⁹

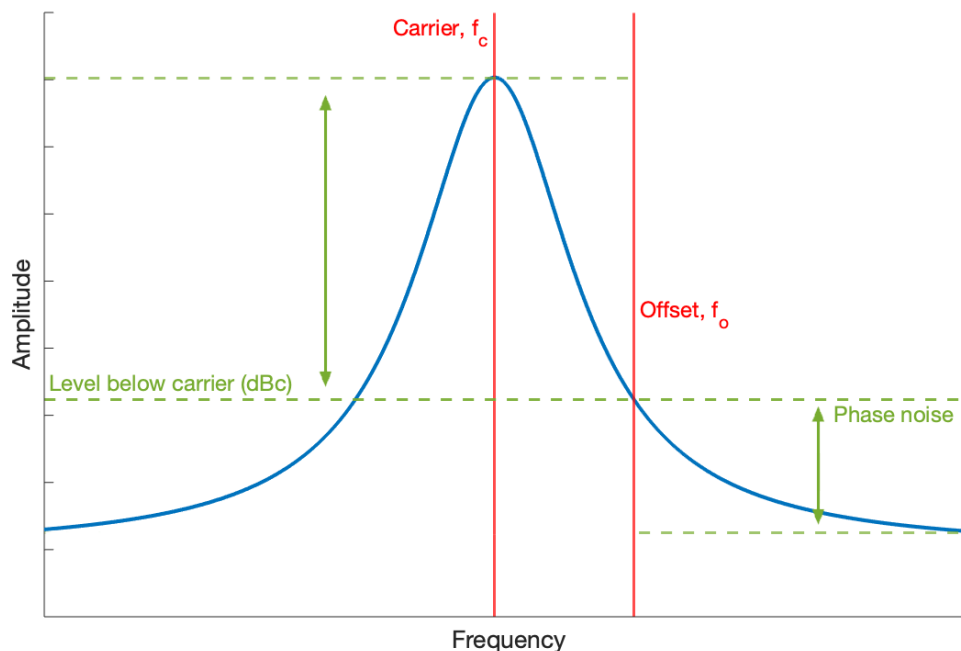


Fig 3.7: Errors in the time domain signal of the fundamental oscillator yield significant increases in sideband noise that can be seen in a Fourier transform of the oscillating signal. It is common to only report a single sideband noise specification. Adapted from *Electronics Notes*.¹³⁷

Because phase noise contributes to noise in the detected SR signal, it was important to compare the phase noise when operating with the AWG to that of a standard EPR spectrometer microwave source. Additionally, the phase noise of the AWG was measured when using a Wenzel Associates Golden frequency source as a fundamental oscillator for the AWG. The internal AWG oscillator, the AWG with Wenzel source, and a Gunn diode microwave source from a Bruker Elexys E500T commercial spectrometer were compared. The phase noise typical of commercial EPR spectrometers is about -140 dBc at a 100 kHz offset, which is the typical modulation frequency used in CW spectrometers. The phase noise of the internal oscillator of the Tektronix AWG is about -100 dBc at 100 kHz and this is decreased to -136 dBc at 100 kHz offset when using the Wenzel source with the AWG.

To quantify the effects of source noise on the SR experiment, the noise present in the reflected signal as a function of increasing power was recorded using each of the three sources listed above (Fig 3.8). The standard deviation of the time domain signal was calculated in Matlab (MathWorks). For this comparison, a Bruker ER4118X-MD-5 resonator with sufficiently high Q was used. A constant X-band frequency was generated (~ 330 uW) from each of the three sources and used as the input to the digital SR bridge. The resultant noise was recorded as the microwave power was varied within the limits of the voltage-controlled attenuator. The phase noise was integrated over a bandwidth of 2 MHz which is the full bandwidth of the video amplifier and is limited by the operational amplifiers. A video gain of 54 dB was used.

The standard deviation of the noise was independent of incident power up to about 1 microwatt for all three microwave sources, which is attributed to other noise sources in the instrument. Power on the order of microwatts to ten microwatts is routinely used during SR experiments. At these power levels, standard deviation of the noise present is significantly less in all three microwave sources than at higher powers. At relatively high observe powers for the SR experiment (~ 1 mW), the standard deviation of the noise when using the AWG internal clock is about a factor of 10 greater than for the Bruker Gunn diode. Addition of the Wenzel clock decreases the standard deviation of the noise by a factor of six when compared to the AWG internal clock. The Wenzel external clock source reduces noise at higher powers when using the AWG as a microwave source and in practice the Wenzel clock was always used when performing measurements with the digital SR spectrometer.

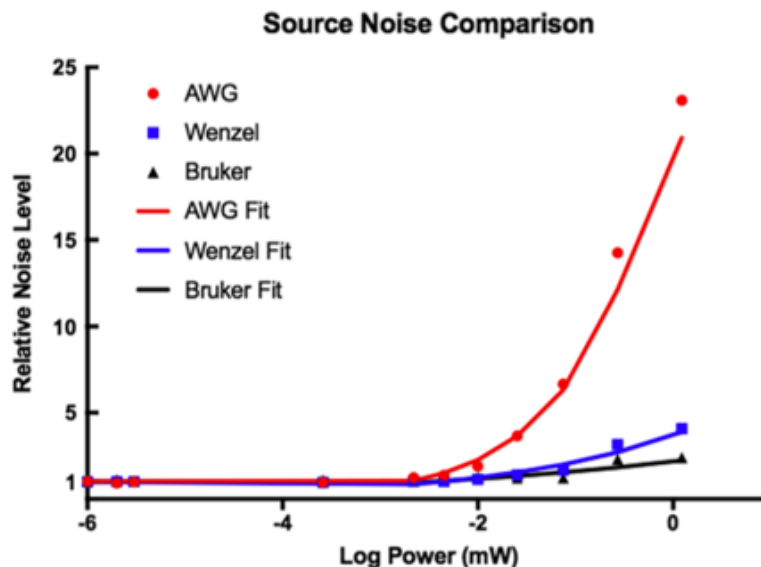


Fig 3.8: The noise in the detected signal, integrated over a bandwidth of 2 MHz, when using either a Bruker Gunn diode, the AWG internal clock, and the Wenzel clock input to the AWG. The increase in noise above the threshold value at low power is assigned to source noise. Reproduced with permission from McPeak et al.²⁹

To perform experiments at ca. 9 GHz, the AWG must synthesize waveforms using slightly more than 2.5 average samples per cycle given the maximum sampling rate of 25 GSa/s. This may be accomplished in a number of ways. Early in the instrument design and before incorporating the Wenzel external clock, waveforms were synthesized with a constant 2.5 samples per cycle and the AWG sampling rate was decreased to match the output frequency to the absorption frequency of the resonator.¹³⁴ This method has the advantage of permitting rapid calculation of the waveform to compensate for resonator heating or changes in the external environment of the spectrometer. However, it was observed that the ending of the first waveform in the observation window did not match the beginning of the preceding waveform, creating an imperfect transition when performing experiments where waveforms are repeated for continuous microwave output. This imperfection in the waveform increases source noise (Fig 3.9) due to the coherent

jitter associated with an error occurring at a specific, lower frequency of the fundamental oscillator.¹³⁸

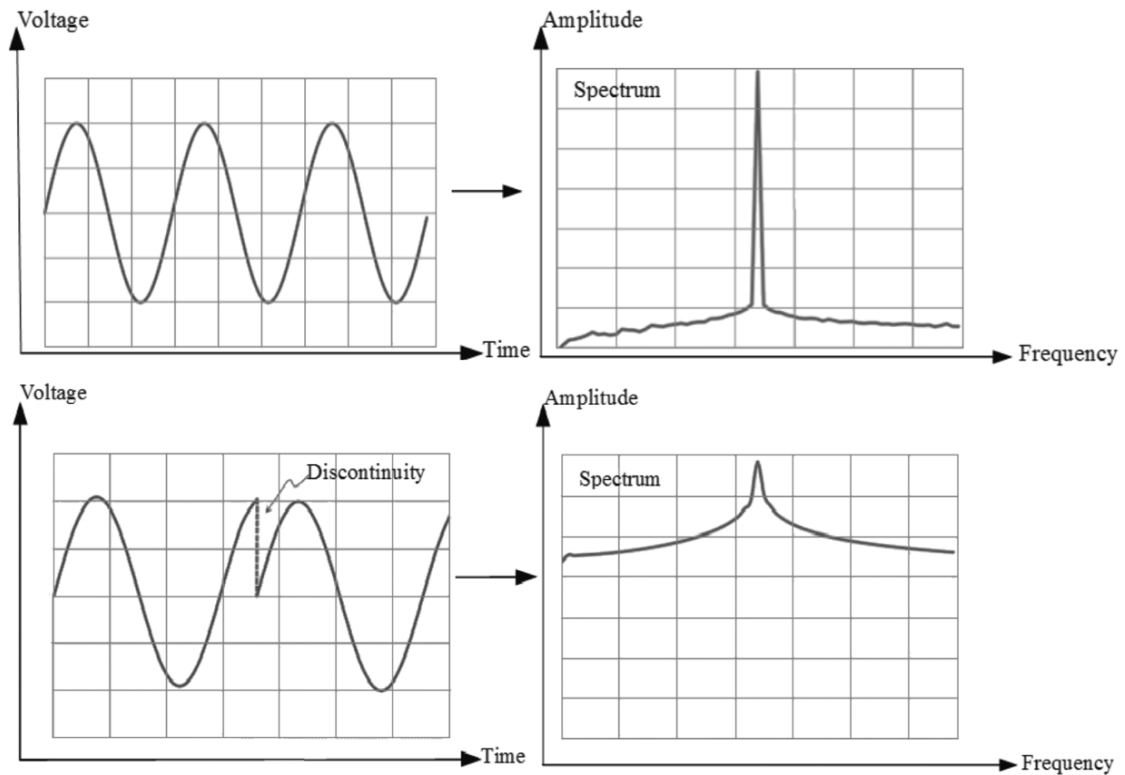


Fig 3.9: The increase in noise when synthesizing the microwave signal from a non-continuous, looping waveform is observed as a broadening of the peak width in a Fourier transformation. Adapted from Göğüş et al.¹³⁸

To minimize this error, waveforms were synthesized with a varying number of points per cycle and a constant sampling rate. Instead of varying the clock rate of the AWG and defining the number of points per cycle, the output frequency and the sample rate are explicitly defined while allowing the number of points per cycle to vary. The appropriate number of full cycles is calculated to be the greatest common divisor of both the sample rate and the required carrier frequency (ca. 9 GHz), resulting in synthesized waveforms that vary in length but are continuous when looped.¹³⁹ This is considerably less flexible in terms of experimental design. However, the reduction in source noise

observed when looping transitions are smooth greatly improves spectrometer performance. Source noise was reduced by as much as 6 dB at 700 MHz when using the “greatest common divisor” method of waveform generation relative to the source noise observed when varying the clock rate to reach the desired frequency.²⁸

The absolute gain and noise figure of the detection system were modeled. The gain may be approximated based on the total gain present in the system minus the microwave losses. The total noise figure can be modeled by the following equation for high gain networks,

$$F_{1,2...n} = F_1 + \frac{(F_2 - 1)}{G_1} + \frac{(F_3 - 1)}{G_1 G_2} + \dots + \frac{(F_n - 1)}{G_1 G_2 \dots G_{n-1}} \quad \text{Eq. 3.1}$$

where F is the noise figure and G is the gain of the amplifiers in the order of signal amplification, in series.⁵ The two amplifiers in the detection system of the digital SR spectrometer are (1) a 34 dB, L3 Narda Miteq AFS4-08001200- 20-20P-4 with a 1.3 dB noise figure and (2) a video amplifier built by Richard Quine with selectable gain (34, 40, 46, 54 dB) and a noise figure of 28 dB. The first stage was chosen to be particularly high gain and low noise figure to minimize the effects of the video amplifier due to its high noise figure. In addition to component selection, the total microwave losses must be considered, which are significant at X-band (ca. 9 GHz). In the path of lowest microwave loss within the detection system, a total of 3 dB microwave loss was measured before the input to the first detection amplifier, increasing the noise figure of the first stage from 1.3 dB to 4.3 dB in the above calculation.

The end-to-end gains and noise figures in the digital SR spectrometer were measured using a wideband calibrated noise source and a Lecroy Waverunner

oscilloscope. Because the gain is constant for the system and should be independent of incident power, a linear relationship is expected between the power input and output with a scaling factor that is the gain of the amplifier (Fig 3.10).¹⁴⁰ The noise figure is calculated based on the relationship between the amplifier performance and the performance of an ideal amplifier (Fig 3.10).¹⁴⁰ A calculation of overall gain and noise figure may be made from two relatively simple measurements, $P_{out,hot}$ and $P_{out,cold}$, where each refers to the recorded output of an amplifier or series of amplifiers in the presence or absence of a calibrated reference. In the calculations, a calibrated noise source (28 dB at ca. 9 GHz) was used. It is necessary for the calculation of $P_{in,cold}$ and $P_{in,hot}$ to know the expected thermal noise of the system and the additional noise provided by the calibrated source. The expected thermal noise is given by,

$$P_{in,cold} = -174 + (10 * \log(Bandwidth)) \quad \text{Eq. 3.2}$$

where -174 is the input noise of a hypothetical noise-free amplifier operating over a 1 Hz bandwidth, in decibels per milliwatt (dBm).¹⁴¹ $P_{in,hot}$ is calculated by summing $P_{in,cold}$ and the noise introduced by the calibrated noise source. $P_{out,cold}$ and $P_{out,hot}$ may then be measured, and the resultant overall gain calculated based on the following equation.

$$Gain = \frac{\Delta P_{out}}{\Delta P_{in}} \quad \text{Eq. 3.3}$$

With the gain measured, a calculation of noise figure based on the behavior of an ideal amplifier is performed by comparing the expected output relative to the measured output, as follows;

$$P_{in} + Gain = Expected P_{out} \quad \text{Eq. 3.4}$$

$$Measured P_{out} - Expected P_{out} = Noise Figure (NF) \quad \text{Eq. 3.5}$$

where all measurements are made with the calibrated noise source active. The calculations of gain and noise figure may be performed for a single component or for a series of components, as has been performed in the digital SR bridge.

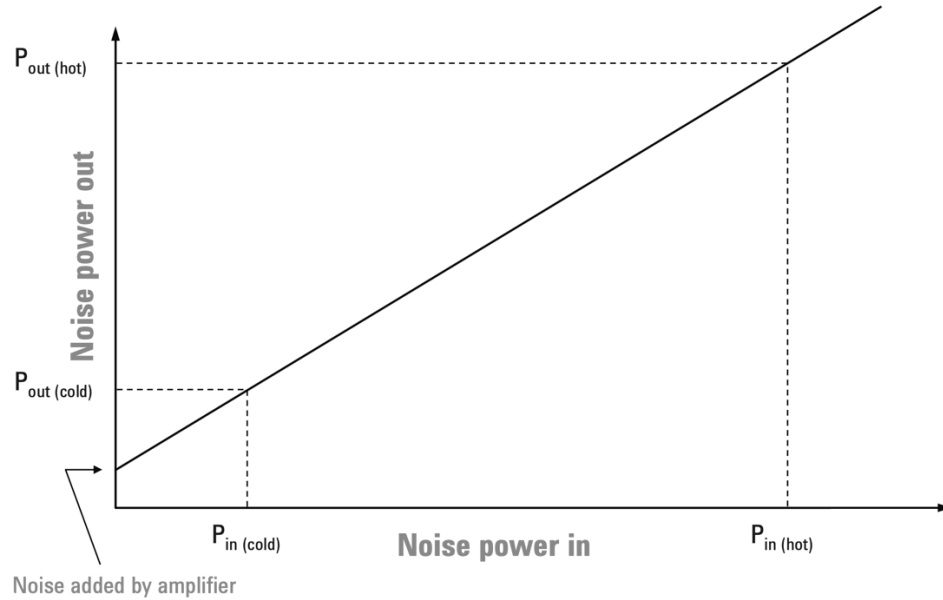


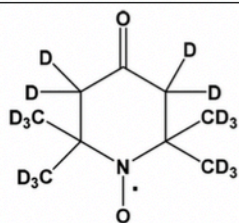
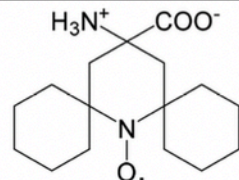
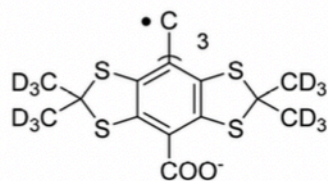
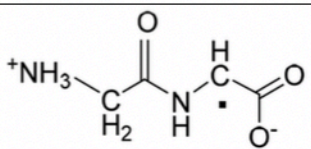
Fig 3.10: An illustration of the relationship of gain and noise figure relative to an ideal amplifier, allowing for measurement of both. In this example, “cold” and “hot” refer to presence or absence of a calibrated reference input. Adapted from Keysight *PNA-X Series Application Notes*.¹⁴⁰

To measure the overall gain and noise figure of the detection system on the digital SR spectrometer, the calibrated noise source was placed on port 2 (CLR #2). This port is used with a CLR or transmission resonator. Reflection resonators are used in port 1 (LGR or CLR #1). The associated noise figure is significantly increased when using a reflection resonator due to additional microwave loss in this path. The overall gain and noise figure associated with the CLR #2 detection path were found to be 84 dB and 7 dB, respectively, when using the maximum available video gain, 54 dB (Table 3.3).

Several standard samples were investigated during testing and optimization of the instrument, with relaxation times ranging from 500 ns to 200 μ s and numbers of spins

from 10^{15} to 10^{17} . Samples included fluid solutions, single crystals, crushed solids, and powders. All samples were placed in approximately 4 mm OD quartz EPR tubes. The samples of 0.4 mM PDT in heavy mineral oil, trityl-CD₃, and the amino acid nitroxide crushed solid sample, DICPO in PVA/Borate glass, were all degassed to remove oxygen by freeze-pump-thaw methods and flame sealed. Trityl-CD₃ was placed in 0.9 mm OD Teflon tubing supported in the EPR tube. Coal and irradiated glycylglycine were powder samples. For the longest relaxation times observed, a 24.4 Mrad rod of fused quartz was used. Relaxation measurements were validated by comparison with prior reports in the literature or with pulse and conventional SR-EPR measurements performed specifically for comparison.¹⁴²⁻¹⁴⁵ A summary of the standard samples investigated is in Table 3.2.

Table 3.2: Samples used during optimization of the digital SR instrument. Reproduced with permission from McPeak et al.²⁹

Sample	Radical	Number of spins in the active volume of the resonator	T ₁ measured with new spectrometer (μs)	T ₁ previously reported or measured for comparison (μs)
0.4 mM PDT in heavy mineral oil		3×10^{16}	0.54 ± 0.01	0.49 ± 0.01
Amino acid DICPO in PVA/borate glass		8×10^{17}	11.0 ± 0.2	10.9 ± 0.8
0.4 mM Trityl-CD ₃		1×10^{15}	16.0 ± 0.3	17 ± 1
Coal		2×10^{16}	26.2 ± 0.2	26.5 ± 1.5
Irradiated glycylglycine		1×10^{17}	58.1 ± 0.5	53
Irradiated fused quartz		2×10^{16}	182 ± 4	180

Data were collected with a microwave B₁ that ranged from 3.2 to 150 mG, where longer values of T₁ necessitated the use of lower B₁. Spectra collected for standard samples are shown in Fig 3.11. SR curves of coal, glycylglycine, trityl-CD₃ and PDT were fit with an exponential model and both the residual analysis and an off-resonance collected data set are shown. Data were collected using a 2 MHz detection bandwidth and either a Bruker ER4118-MS5 or a 5-loop-4-gap resonator. A variable delay was added to

prevent saturation of the digitizer ranging from 0.8 to 8 μs . Total data acquisition time was under 15 seconds in all cases. The CW spectra of each sample is also shown as an inset to each recovery curve presented in Fig 3.11.

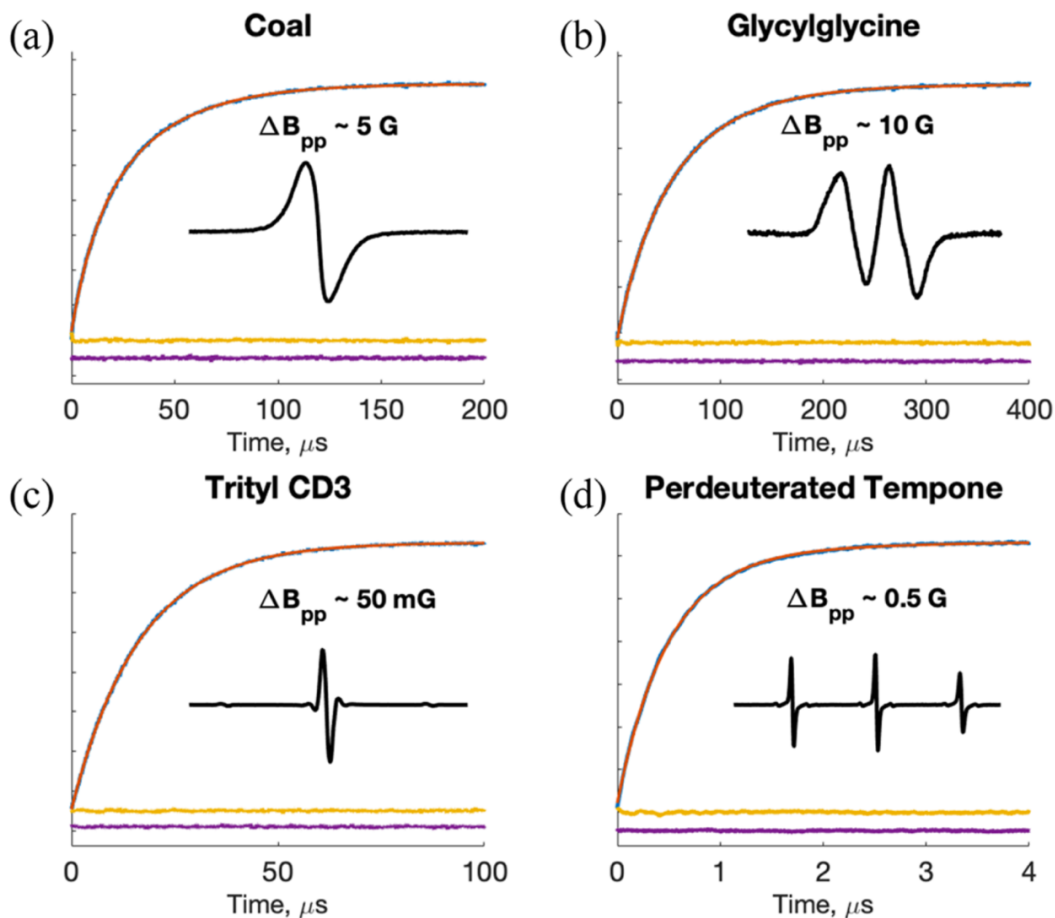


Fig 3.11: SR data collected with the digital SR instrument for coal (a), irradiated glycylglycine (b), trityl- CD_3 (c), and PDT (d), where saturation recovery data are shown in blue, an exponential fit is overlaid in red, a residual analysis is shown in yellow after subtracting the fit from the data, and an off resonance collected SR curve is shown in purple. The CW spectrum is shown as an inset and an approximate linewidth for each spectrum is given. Reproduced with permission from McPeak et al.²⁹

In addition to the standard samples shown above, irradiated fused quartz was measured using the digital SR system as a challenge to record long relaxation times. It is known that the relaxation time for the EPR signal produced by γ -irradiation varies with position in the line.¹⁴⁵ The resulting T_1 measurements with respect to field position of the

irradiated fused-quartz sample are shown in Fig 3.13. Each T_1 value reported is the average of 5 replicates collected without replacing the sample or altering sample position. The data acquisition time for each replicate measurement was approximately 90 seconds. The associated error is reported for T_1 at the given field positions. The error increases with decreasing S/N in the integrated CW signal (Fig 3.12). Low microwave B_1 was required to prevent saturation effects which may lead to the observation of an erroneously fast T_1 relaxation rate.

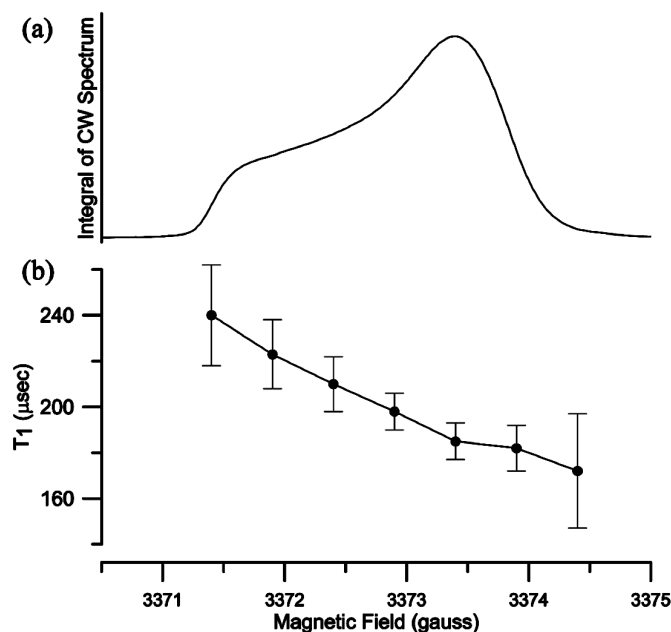


Fig 3.12: Relaxation data collected with the digital SR instrument for irradiated fused-quartz. The integrated CW spectrum (a) and the average T_1 recorded at each field position (b) are shown with the same field axis. Reproduced with permission from McPeak et al.²⁹

As mentioned previously, the digital SR instrument does not utilize automatic frequency control (AFC), and could be susceptible to instrument instabilities due to fluctuations in the source output or the resonator frequency. The most common reason to utilize an AFC is to provide a feedback loop to adjust the operating frequency of the instrument when the frequency of the resonator changes. This occurs in small EPR

resonators due to heating of the resonator by the incident power and therefore a change in the frequency. The large incident power required for the saturating portion of the SR experiment combined with the switching to very low incident power creates a large differential in heat generation with respect to time. To account for this, the instrument must reach a steady state before performing measurements on any specific sample of interest. Two examples are shown in Fig 3.13 of the stability of the instrument when performing measurements on the coal and trityl-CD₃ samples. After a steady state has been achieved, replicate measurements of the recovery curve for the coal sample were recorded over a period of 16 hours. The observed deviation in T₁ and S/N were 1% and 8% over the full 16-hour period, demonstrating considerable instrument stability achieved without an AFC circuit. Greater variance was observed in the relaxation measurements of trityl-CD₃, primarily due to the much smaller linewidth. The observed CW linewidth of coal is approximately 5 Gauss, which yields a tolerance in frequency drift of approximately 7 MHz from the center of the spectrum. However, the observed CW linewidth of trityl-CD₃ is much smaller, only 50 mG, and may only tolerate a frequency drift of 70 kHz before departing from resonance. The increased error reported when measuring relaxation times in the lower S/N regions of the irradiated fused-quartz sample suggests that the large decrease in S/N with respect to time in the stability measurements using trityl-CD₃ is due to measurements on the wings of the signal (Fig 3.13). An extended instrument stability measurement was performed with the coal sample and it was found that, once steady state has been achieved, the instrument demonstrated only small deviations when measuring T₁ continuously for 60 hours, or close to three days.

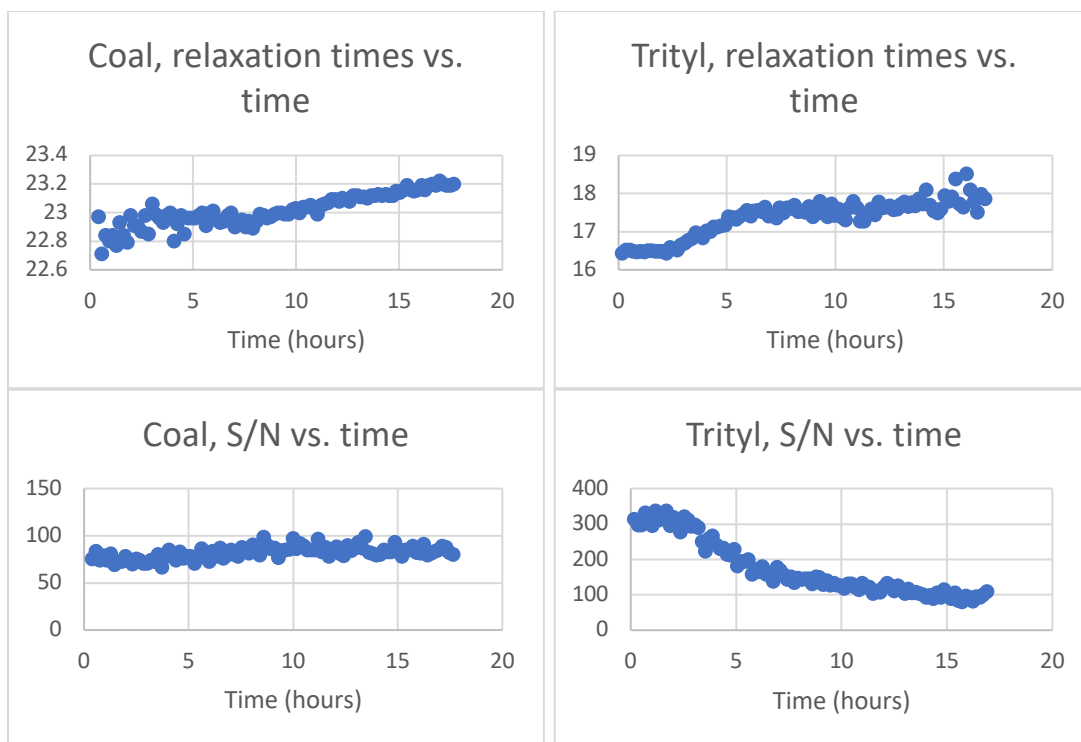


Fig 3.13: Time dependence of T_1 of coal (*left*) and trityl- CD_3 (*right*) reflecting the stability of the instrument. The top panel shows the variability when measuring T_1 and the bottom panel shows the variability of the S/N of each measurement. Each was recorded continuously for 16 hours.

3.2 Comparisons with a conventional SR spectrometer

The S/N and reproducibility of T_1 were compared for the digital SR spectrometer and a conventional SR spectrometer previously designed by Richard Quine.⁷ The conventional system has been upgraded by replacing the Varian E3 microwave bridge and digitizer in use at the time of the original paper with a more modern Bruker ER048 microwave bridge and SpecJet fast digitizer. End-to-end gain and noise figure for the overall detection system were investigated using the y-factor method and calibrated noise source described above. The calibrated noise source was placed before the coaxial signal input to the homebuilt bridge and after the circulator mimicking placement of the

calibrated noise source when characterizing the new spectrometer. The gain and noise figures for the detection systems of both the conventional SR and digital SR spectrometers are listed in Table 3.3. Both the gain and noise figure are higher in the digital system; however, the detection amplifier in the digital system is slightly improved relative to the conventional system. A video gain of 54 dB was used in both measurements. The video amplifier in the conventional system has a significantly lower noise figure (~15 dB less) while maintaining equivalent values of gain (34-54 dB) when compared to the newer video amplifier present in the digital SR instrument.

Table 3.3: Comparison of the detection systems in the digital SR and conventional SR systems. Reproduced with permission from McPeak et al.²⁹

	Conventional SR system		Digital SR system*	
	Detection amplifier (dB)	End-to-end gain/NF (dB)	Detection amplifier (dB)	End-to-end gain/NF (dB)
Gain	32	78	34	84
Noise figure	1.4	5	1.3	7

*The gain and noise figure were measured with the DBM path and the CLR2 input path, which is the path with lowest microwave loss.

The S/N of three standard samples, coal, irradiated glycylglycine, and the amino acid nitroxide DICPO, were compared for the conventional SR and digital SR systems. Because the Bruker SpecJet fast digitizer that is used in the conventional system is an earlier generation than the Bruker SpecJet II fast digitizer used in the digital SR spectrometer, the settings of the newer digitizer were selected to be within the bounds of the older generation of hardware. Data were acquired at the same position in the spectrum of each standard sample. A Bruker ER4102 ST TE₁₀₂ cavity resonator was used on both systems for all comparisons. It is a reflection resonator so the digital SR instrument was operated in reflection mode (CLR/LGR1). In the digital system the two selectable mixers were compared. As expected, the S/N of the recovery curves was decreased by a factor of

1.2-1.5 when using the quadrature mixer due to increased microwave loss associated with division of the signal between two outputs when compared to the lower loss double balanced mixer. When measuring coal and irradiated glycylglycine, both the S/N and the reproducibility were improved in the digital system relative to the conventional system when using the double balanced mixer rather than the quad mixer. When measuring the amino acid DICPO, the S/N was greater using the conventional system. However, the error associated with replicate measurements of S/N was decreased substantially when using the new system. In all cases, when using the new system, the variance associated with replicate measurements was decreased regardless of the mixer selected relative to the error observed when using the conventional system. A summary of results is provided in Table 3.4, where the microwave excitation was 5 mG in all measurements. The detection bandwidth of the conventional system was approximately 1.3 MHz, which is slightly lower than the bandwidth of the new system, approximately 2.1 MHz, which increases the amount of high frequency noise recorded in the new system and decreases the overall S/N by about 27%.

Table 3.4: S/N of standard samples measured with the conventional SR spectrometer, the digital SR spectrometer and double balanced mixer, and the digital SR spectrometer and quadrature (I/Q) mixer. Reproduced with permission from McPeak et al.²⁹

Instrument	Coal	Glycylglycine	DICPO
Conventional SR	890 ± 270	380 ± 110	350 ± 110
AWG-SR, DBM	1100 ± 90	430 ± 40	240 ± 30
AWG-SR, I/Q	730 ± 110	280 ± 60	200 ± 30

3.3 Resonators

The SR experiment is greatly affected by the properties of the resonator. The SR experiment requires that the resonator be critically coupled because the microwave power is applied during signal detection.³⁰ The reflected power from an overcoupled resonator could overwhelm the detector and the signal.¹²⁷ Employing resonators with higher Q could increase signal intensity.¹³ However, a resonator with higher Q has a longer ring-down time, which increases the deadtime and makes it more difficult to measure samples with shorter T_1 .¹²⁷ Dead time in the SR experiment is defined as the time between the conclusion of the saturating waveform and the beginning of data collection and is typically the result of instrumental artifacts and switching transients masking the signal of interest. Specifically related to the resonator, ring-down is the time required to dissipate excess energy.¹³ If these large voltages persist for a time that is too long relative to the relaxation time, they can mask the very low voltage EPR signal.³⁰ When using a double balanced mixer as the detector, the ring-down decay time constant, τ , can be calculated from resonator Q as follows,

$$Q = \pi \nu \tau \quad \text{Eq. 3.6}$$

where ν is the resonator frequency.¹¹ To take account of resonator ring-down and switching transients, a background spectrum collected off-resonance and assumed to be free of EPR signal is subtracted from the spectrum collected on-resonance. Ring-down is approximately an exponential decay function and immediately after the saturating pulse the resonator ring-down voltage is far too large to be appropriately recorded by the digitizer. To permit accurate subtraction the ring-down and switching transients must be on-scale to the digitizer. Resonator characteristics and the observed dead time when using

the digital SR spectrometer are listed in Table 3.5, including a newly designed crossed-loop resonator designed and built by Dr. George Rinard.

Table 3.5: Efficiency, loaded Q, and dead time of several resonators employed during the development of the digital saturation recovery spectrometer. Reproduced with permission from McPeak et al.²⁹

Resonator	$\Lambda = G/\sqrt{W}$	Loaded Q	Dead time (μs)
ER-4118X-MD-5	3.8	9000	2-3
ER-4118X-MS-5	2	3000	1-1.5
ER4102 ST	1	3000	1-1.5
5-loop-4-gap ¹²⁷	3.2	1300	0.6-0.8
CLR ¹³⁵	1	300	0.6-0.8

When the resonator ring-down has been taken into account or minimized with low Q, the next most important contributor to instrumental dead time is the video amplifier. This contribution becomes the limiting factor when Q is very low, as seen in Table 3.5. The spectrometer has three mechanisms for limiting detection system saturation, a detector blanking switch following the 2-watt power amplifier, a limiter placed on the input to the 34 dB LNA, and an adjustable LO delay for the mixer. Together, these greatly decrease problems with saturation in the detection system. However, the use of both high gain and low bandwidth increase the time required for the video amplifier to recover from saturation. High gain increases the duration of saturation while low bandwidth (ca. 100 kHz or less) increases the time constant of the filter. Therefore, when dead time is a concern it is better to use low gain and high bandwidth even though this is typically detrimental to S/N. The shortest instrumental deadtime observed was between 0.6 to 0.8 μs , limiting measurements to relaxation times to samples with T_1 longer than about 0.5 μs or samples with shorter T_1 and very large signal intensity such that a relaxation signal is detectable after multiple decay time constants.

3.3.1 An X-band crossed-loop resonator

Significant engineering effort was allocated to accommodate a newly developed crossed-loop resonator for use at X-band with the digital SR spectrometer. It was anticipated that source noise from the AWG would be a barrier to using the digital SR spectrometer, and for this reason, the proper circuitry was incorporated to tune and operate a crossed-loop resonator. Crossed-loop resonators have previously been employed at 250 MHz, 700 MHz, 1 GHz, and 2.5 GHz in the Eaton lab.^{28,146–150} Based on these designs, an X-band crossed-loop resonator was developed and built by Dr. George Rinard consisting of two orthogonal loop-gap resonators. When properly isolated, the source noise in the detection resonator is reduced proportional to the isolation between the orthogonal resonators.¹⁵¹

To implement the crossed-loop resonator in the digital SR system, additional tuning circuitry was required, described above (Fig 3.4). The crossed-loop resonator has tuning adjustment on both the excitation and detection resonators as well as the isolation between resonators. The excitation resonator, or driven resonator, has adjustment for both frequency and coupling. Two adjustment screws vary the capacitance within the gaps of the sample loop, one varies capacitance at the inner conductor of the coaxial cable (coupling) and one varies capacitance at the opposite end of the loop (frequency) shown in Fig 3.14. The detection resonator only has coupling adjustment via variable capacitance at the SMA connector. An additional rotational adjustment allows the excitation and detection resonators to pivot relative to one another, thereby varying the isolation between the two loop-gap resonators (Fig 3.15). Each resonator may be used

independently as a reflection resonator or both may be used as intended in the crossed-loop configuration when performing experiments with the digital SR instrument.

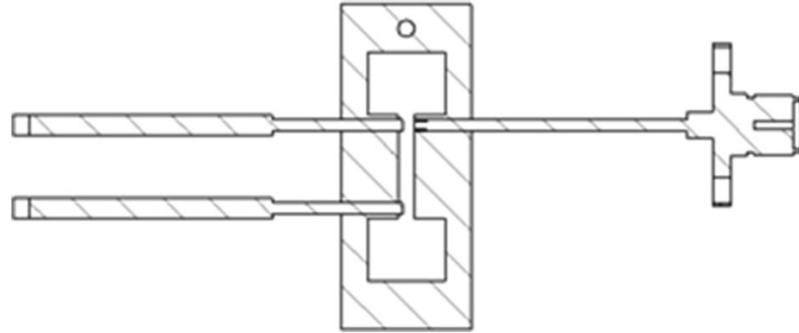


Fig 3.14: Tuning adjustment in the excitation resonator of the crossed-loop resonator. The coupling adjustment is performed by rotating an adjustment screw adjacent to the inner conductor of the coaxial cable (*top*) to vary capacitance. The frequency is varied by rotating a similar adjustment screw (*bottom*) at the opposite end of the resonant loop. Reproduced with permission from Rinard et al.¹³⁵

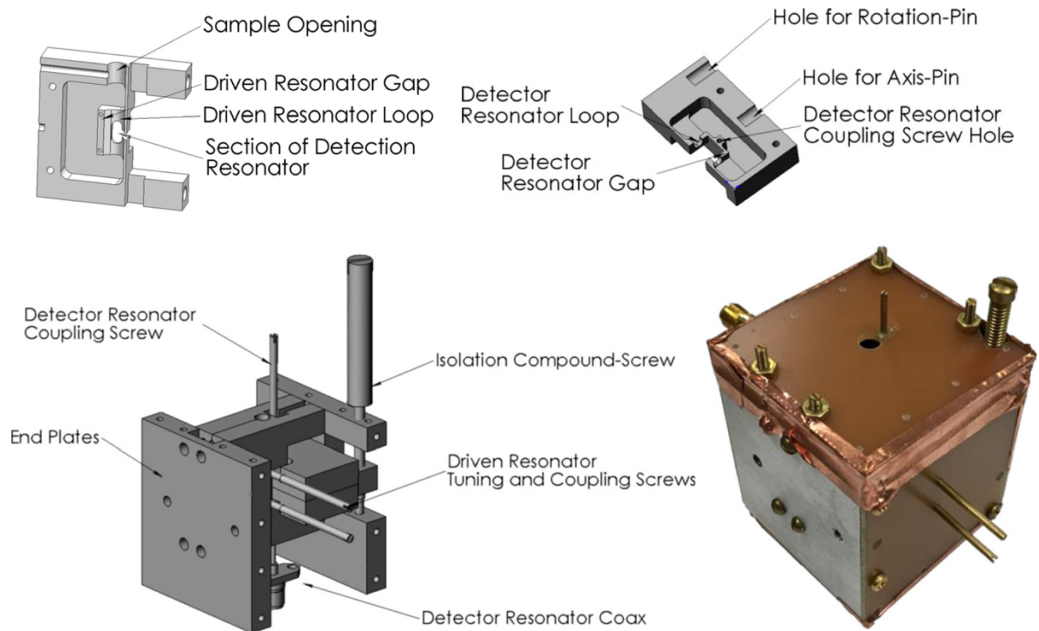


Fig 3.15: The X-band crossed-loop resonator. A graphical depiction of the internal resonators of the crossed-loop resonator, shown with coupling, frequency, and isolation adjustment screws for the driven resonator (*top, left*), the detection resonator (*top, right*) and the two assembled orthogonally (*bottom, left*). A photograph of the resonator, with microwave shielding in place is also shown (*bottom, right*). Each resonator has a separate coaxial connector. Reproduced with permission from Rinard et al.¹³⁵

The effective tunable microwave frequencies, critically coupled Q values, and resonator efficiency were measured using the crossed-loop resonator and an Anritsu network analyzer. The observed mechanical and transmission properties are listed in Table 3.6. The resonator efficiency is approximately $1.0 \text{ G}/\sqrt{\text{W}}$ and was determined by varying microwave B_1 and the length of pulse required for a 90° turning angle based on the following relationship,

$$\theta = \gamma B_1 t_P \quad \text{Eq. 3.7}$$

where θ is the pulse turning angle, γ is the gyromagnetic ratio of the electron, B_1 is the microwave excitation field strength, and t_P is the length of the microwave pulse.¹⁵²

Experiments were performed using the digital SR instrument and a sample of trityl- CD_3 .

Table 3.6: Properties of orthogonal resonators within the crossed-loop resonator. Reproduced with permission from Rinard et al.¹³⁵

Driven (sample) resonator	
Loop size	4.06 mm diameter
Gap dimensions	10 x 1.35 x 1.5 (gap) mm
Frequency	9.855 GHz
Critically coupled Q	380
Detector (cross) resonator	
Loop size	2.55 x 5.41 (rounded ends) mm
Gap dimensions	7.6 x 1.9 x 1.8 (gap) mm
Frequency	8.2 to 10.2 GHz
Critically coupled Q	350
Isolation	-33 dB

The largest barrier to using the CLR with the digital SR instrument is the physical placement of the resonator in the magnet of the Bruker E500T. At the time of reporting (Ref. ¹³⁵), the CLR was placed in the magnet and the connections between the bridge and the resonator were comprised of 4 ft. coaxial cables creating very large microwave losses in both the excitation and detection systems. The digital SR system was used to demonstrate the capabilities of the resonator and SR measurements were performed using

coal and the amino acid nitroxide DICPO investigated above. The results of these experiments are shown in Fig 3.16. While recovery times are comparable to prior measurements, the resultant S/N reflects the additional loss introduced in the system by the long coaxial cables required for resonator placement.

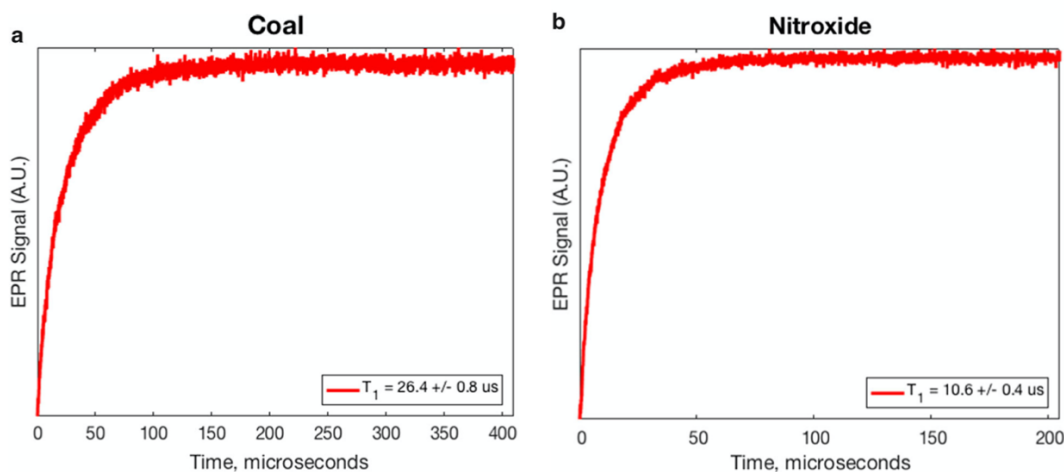


Fig 3.16: SR measurements of coal (*left*) and the amino acid DICPO (*right*) using the digital SR spectrometer and the X-band CLR. Reproduced with permission from Rinard et al.¹³⁵

The problems associated with microwave loss when using the CLR were subsequently reduced greatly by the use of waveguide, replacing the coaxial cabling connecting the detection resonator to the digital SR bridge. This effectively eliminates the microwave loss between the resonator and detection system in the bridge, restoring the noise figure measured above and greatly reducing the noise during SR measurements. A comparison between the S/N observed when measuring the relaxation of coal when using the coaxial cabling in the detection system and when using waveguide connections in the detection system is presented in Fig 3.17. The S/N is much better with the use of waveguide, greatly increasing the utility of the resonator for samples with low spin concentrations. Because the SR experiment does not require high power, microwave loss

is much more tolerable during excitation; however, the SMA connection between the bridge and the excitation resonator could be replaced with waveguide, increasing available power for samples with fast relaxation and therefore less saturation at higher powers.

Coal using CLR on Digital SR with waveguide

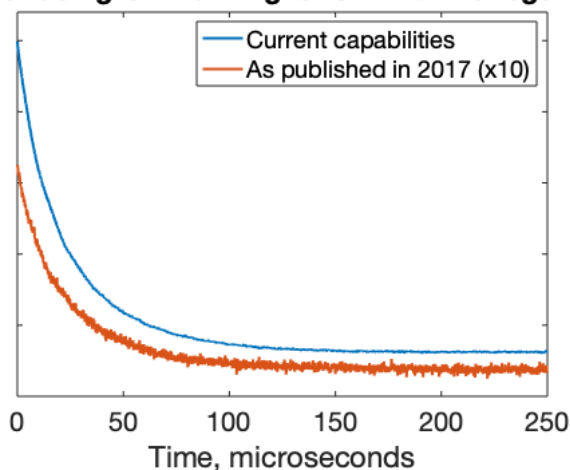


Fig 3.17: Comparison of S/N observed when measuring coal relaxation using the CLR with coaxial cabling (*orange*) and waveguide (*blue*) connections in the detection system under similar spectrometer operating conditions.

The use of waveguide increases S/N such that it is now relevant to compare the digital SR instrument operation with the CLR to operation with prior results for reflection resonators. SR measurements were performed using coal, irradiated glycyglycine, and the amino acid DICPO to compare performance with the CLR to the performance observed and reported in Table 3.4. The results of which are reported in Table 3.7 with prior experimental data repeated for convenience. When using the CLR, the double balanced mixer was selected in the microwave bridge because it has lower microwave loss, maximizing the signal from the resonator. S/N was expected to be lower when compared to the TE₁₀₂ cavity (Q ~3000) because the Q of 350 for the CLR is significantly lower.

Table 3.7: The S/N and T_1 observed when measuring coal, glycylglycine, and DICPO using the CLR and the digital SR spectrometer compared to the experiments reported in Table 3.4 of the conventional and digital SR spectrometers when using the TE_{102} cavity resonator.

Instrument	Resonator	Coal	Glycylglycine	DICPO
S/N				
Conventional SR	TE_{102}	890 +/- 270	380 +/- 30	350 +/- 110
Digital SR, DBM	TE_{102}	1100 +/- 90	430 +/- 40	240 +/- 30
Digital SR, I/Q	TE_{102}	730 +/- 110	280 +/- 60	200 +/- 30
Digital SR, DBM	CLR	350 +/- 40	170 +/- 20	80 +/- 10
T_1 (μ s)				
Conventional SR	TE_{102}	26.5 +/- 1.5	60.6 +/- 3.8	10.9 +/- 0.9
Digital SR, DBM	TE_{102}	26.2 +/- 0.2	58.1 +/- 0.5	11.0 +/- 0.2
Digital SR, I/Q	TE_{102}	28.1 +/- 0.4	58.5 +/- 0.7	11.3 +/- 0.4
Digital SR, DBM	CLR	24.3 +/- 0.2	56.5 +/- 0.5	10.3 +/- 0.2

The data in Table 3.7 show that the CLR has lower S/N; however, the reproducibility in both the S/N and T_1 measurements is improved when using the CLR. This is due to the rejection of source noise when using a CLR and is improved with increasing isolation.¹⁵¹ In addition to the decrease in source noise, the transmission of reflected power is also reduced when using a CLR, decreasing baseline drifts.¹⁵¹ This is especially important, as the noise is calculated from the standard deviation observed at the baseline of a SR experiment, where drifting would increase deviation. A low Q resonator inherently decreases the susceptibility of the signal to changes in reflected power due to frequency drift; and, the isolation of the resonator further reduces this.

3.4 Nitroxides relevant to dynamic nuclear polarization

The spin-lattice relaxation time is defined as the time required for the spin system to return to thermal equilibrium after perturbation.¹⁵³ The time dependence of Zeeman energy level populations, n and n_0 , following microwave excitation satisfying the resonance condition is described by,

$$\frac{dn}{dt} = -\frac{(n - n_0)}{T_1} \quad \text{Eq. 3.8}$$

where the spin-lattice relaxation time, T_1 , is the time constant for return to the electronic ground state.¹⁵³ Formal definitions of T_1 have been derived from the Bloch equations for magnetization as the time required for complete return to equilibrium of net magnetization along the z-axis following excitation.¹⁵³ In the absence of competing relaxation mechanisms, the return to thermal equilibrium may be modeled by a single exponential process; however, practically speaking this is often not the case.¹⁵³ A variety of relaxation processes may be present in the observed recovery curve depending on the specifics of the sample and the experimental parameters employed.^{153–155} It has been observed in early SR experiments by Fajer that biexponential modeling was necessary when using short pulses.¹⁵⁶ The time constants observed were attributed to a spectral diffusion process and the true electron spin-lattice relaxation.¹⁵⁶ Longer pump times were shown to permit the spin system to achieve thermal equilibrium before measurement, resulting in an exponential decay that is free of spectral diffusion.¹⁵⁶ Modern interpretations include many more relaxation processes such as electron-nuclear dipolar coupling, g and hyperfine anisotropy, Heisenberg exchange, and many others depending on the nature of the lattice.^{47,153–155,157,158} Depending on the experimental conditions, certain contributions to spin-lattice relaxation may be isolated to better define each contribution to the relaxation as a whole.^{45,47,153,157,158} To accurately define multiple time constants in a single experiment, significant resolution is required to prevent aliasing of very fast components due to inadequate digitizer sampling rates.¹⁵⁹ Additionally, the S/N required to accurately define multiple time constants in a single experiment increases

with both the number of time constants present and the closeness in magnitude of the anticipated time constants, making the digital SR spectrometer advantageous in measurements of multiple contributions to spin-lattice relaxation.^{160,161}

In the early literature, SR experiments were performed to relate the observed relaxation rate to the molecular tumbling rate of isotropically tumbling small organic radicals.^{156,162–164} These experiments, along with many others, have paved the way for extensive theoretical analysis of the relaxation mechanisms of rapidly tumbling radical species, some of which form the basis for investigation in the following section. Significant work has also been done to elucidate the effects of varying microwave frequency and temperature on the resulting relaxation phenomena.^{158,165–169} All work described in this chapter was performed at X-band using the digital SR spectrometer at room temperature.

The relaxation mechanisms for two nitroxide radicals commonly employed for dynamic nuclear polarization (DNP) experiments were investigated with a specific focus on higher concentrations than those frequently used for routine EPR experiments. Concentration dependence was investigated via electron spin echo and SR methods to enable accurate calculation of both the saturation factor and the anticipated signal enhancement of the NMR signal in DNP experiments. This was performed through careful modeling of both the spin-spin relaxation (T_2) and the spin-lattice relaxation (T_1) mechanisms. Similar experiments were performed with Whylder Moore to investigate the relaxation mechanisms present in an isotopically labeled triarylmethyl radical.¹⁷⁰ Prior investigations of the natural abundance triarylmethyl radicals, as well as investigations in

relaxation mechanisms present in other rapidly tumbling organic radicals, served as a comparison to investigate the impact of isotopic labeling on relaxation.^{47,157,171}

The most widely used paramagnetic agents for DNP experiments are the nitroxides and triarylmethyl radicals.^{44,172–175} In the DNP experiment, saturating power is applied at the Zeeman frequency of the paramagnetic species.⁴⁴ The resultant spin polarization is coupled to nearby nuclei, enhancing the NMR signal relative to the NMR signal under thermal conditions.⁴⁴ The DNP experiment has been given significant consideration in the literature within the last 20-30 years due to advances in technologies and components available for spectrometer construction.⁴⁴ DNP experiments when applied to three-dimensional spatially resolved imaging experiments greatly increase signal intensity and will pave the way for metabolic imaging when properly interfaced with isotopic labelling studies.^{175,176}

The primary motivation for creating a model of the DNP experiment is to guide experiments toward the maximum signal enhancement possible for a given target molecule. The signal enhancement for each DNP experiment depends greatly on the paramagnetic species and the target nuclei and each new species requires evaluation of several experimental parameters. It has been demonstrated previously that the expected signal enhancement, ε , may be calculated in the following manner,

$$\varepsilon = 1 - \rho s f \frac{|\gamma_s|}{\gamma_I} \quad \text{Eq. 3.9}$$

where s is the saturation factor, ρ is the coupling factor, f is the leakage factor, and $\gamma_{s,I}$ are the gyromagnetic ratios of the electron and nucleus, respectively.^{43,44} The leakage factor describes the change in spin-lattice relaxation time of the nucleus when interacting with a

polarized electron.⁴³ The coupling factor describes both the electron spin and nuclear spin contributions to the relaxation rate.⁴³ The saturation factor, s , is described previously (Eq 1.7). In other sections these time constants are designated as T_1 and T_2 but in this section ‘e’ is added to the labels to distinguish from the corresponding nuclear processes. To accurately estimate the saturation factor, and thereby the signal enhancement expected from the DNP experiment, it is necessary to know the values of T_{1e} and T_{2e} .

Dr. Joshua Biller (TDA Research, Inc.) sought to investigate the relationship between relaxation and concentration in two small, rapidly tumbling nitroxides carboxyproxyl and tempol (Fig 3.18) to estimate the enhancement factor. Dr. Biller designed this project, performed spin echo and inversion recovery experiments, and analyzed those data. I performed the saturation recovery experiments, analyzed that data, and contributed to the modeling. This work was published in Ref.⁴⁵ The reader is referred to the published manuscript for a thorough analysis of the spin-spin relaxation parameters and experiments. Since my participation was only in the spin-lattice relaxation measurements with the digital SR spectrometer, only T_{1e} contributions will be discussed here.⁴⁵

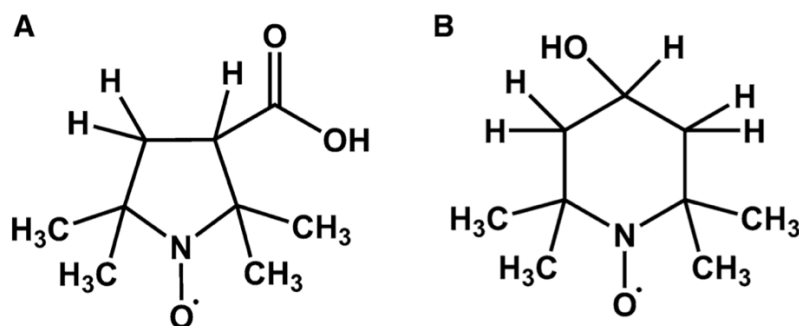


Fig 3.18: Chemical structures of carboxyproxyl (3-carboxy-2,2,5,5-tetramethyl-1-pyrrolidinyloxy, *left*) and tempol (4-hydroxy-2,2,6,6-tetramethylpiperidin-1-oxyl, *right*) employed for the investigation of relaxation mechanisms and their impact on the DNP experiment.

There have been extensive reports in the literature of models for spin-spin and spin-lattice relaxation.¹⁵³ The contribution to T_2 for small, rapidly tumbling nitroxides have been extensively investigated by Freed.¹⁵⁵ Contributions to T_1 for nitroxides have been discussed by Robinson in terms of four processes: spin-rotation, electron-nuclear dipolar interactions, spin diffusion, and Heisenberg exchange with paramagnetic oxygen.⁴⁶ Relative to most CW-EPR experiments, high concentrations of nitroxide radicals are used when performing DNP experiments such that relaxation contributions from Heisenberg exchange between nitroxides in solution becomes relevant.¹⁷² In molecules that demonstrate large g anisotropy, modulation of g anisotropy by molecular tumbling also contributes to relaxation.⁴⁷ For the rapidly tumbling nitroxides at X-band, g anisotropy contributions are small and may be ignored.¹⁵⁷ Relaxation contributions from Heisenberg exchange with oxygen may also be ignored if oxygen is significantly removed from all samples before making SR measurements, as was the case in the experiments described.

3.4.1 Carboxylproxyl and tempol measurements

Carboxylproxyl (Fig 3.18, *left*) was studied in aqueous solution from which O_2 was removed by purging with N_2 for a period of at least 60 minutes prior to performing measurements. Purging with N_2 continued for the duration of all measurements described. Measurements were performed in Denver, Colorado where the approximate atmospheric pressure is 630 mTorr. Tempol (Fig 3.18, *right*) was studied in toluene from which O_2 was removed by seven consecutive freeze-pump-thaw cycles in which frozen

solutions were evacuated to 5 mTorr, after which the tube was flame sealed. Measurements were performed over a concentration range of 0.5-20.8 mM. SR experiments were performed using the digital SR spectrometer and the 5-loop-4-gap resonator with $Q = 2600$ and a microwave efficiency of $3.2 \text{ G}/\sqrt{\text{W}}$.¹²⁷ A saturating pulse of $\sim 800 \text{ mW}$ with a duration of $60 \mu\text{s}$ was applied followed by a low power continuous observation of $\sim 25 \mu\text{W}$. The saturating pulse was repeated every $200 \mu\text{s}$. The reference waveform and digitizer trigger were placed in time after a slight delay to avoid saturation of the video amplifier. Several thousand averages were accumulated and an off-resonance subtraction was performed to minimize instrumental artifacts. The reported time constants (Fig 3.19) resulted from ten replicate measurements each, recorded sequentially, without disruption of the spectrometer tuning or sample placement.

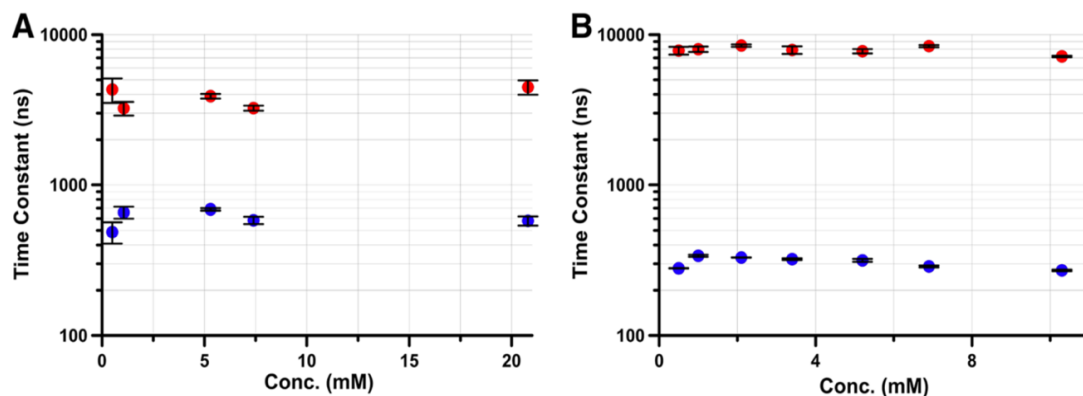


Fig 3.19: Relaxation times obtained using the digital SR spectrometer for carboxyproxyl (*left, A*) and tempol (*right, B*). Data were fit with biexponential models with a fast component (*blue*) and a slow component (*red*). Reproduced with permission from Biller et al.⁴⁵

Three exponentially decaying processes were observed when performing a global analysis of both three pulse inversion recovery experiments and SR experiments. The SR experiments were performed to characterize the processes that contribute to the time constants that were observed in the inversion recovery data. The SR curves were modeled

with a biexponential fit, which demonstrated significantly smaller standard deviation in a residual analysis than a single exponential (Fig 3.20). Exponential fits were performed in Bruker Xepir software. Residual curves were produced by subtraction of the fit from the recovery data. Standard deviations were calculated in Matlab (Mathworks). Fits of the experimental data for carboxyproxyl, averaged over all concentrations, were $(3.8 \pm 0.8) \times 10^3$ and $(0.60 \pm 0.08) \times 10^3$ ns. Fits of the experimental data for tempol, averaged over all concentrations, were $(7.9 \pm 0.5) \times 10^3$ and $(0.31 \pm 0.03) \times 10^3$ ns. In prior studies of spin-lattice relaxation, the time constants obtained by inversion recovery and by SR agreed within 10%.⁴⁷

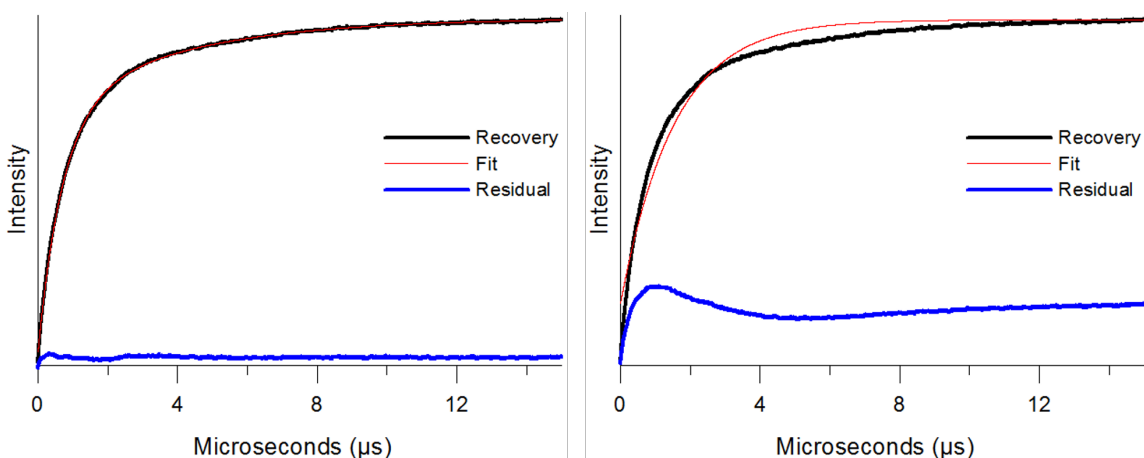


Fig 3.20: Residual analysis of a biexponential (*left*) and single exponential (*right*) fit of the SR data obtained from 5.3 mM carboxyproxyl in the absence of oxygen. The standard deviation of the single exponential residual curve is much larger than that of the biexponential fit. Reproduced with permission from Biller et al., *Supplementary information*.⁴⁵

In the DNP experiment, saturating power is distributed to all m_I components of the nitroxide signal either by Heisenberg exchange or nuclear relaxation, depending on the tumbling correlation time.¹⁷² Contributions from Heisenberg exchange may be observed in spin-lattice relaxation experiments; however, the time constant of Heisenberg exchange (T_{IHE}) decreases with increasing concentration and is quickly lost in the dead

time of the SR instrument.^{45,47,157,177,178} Therefore the shortest time constant, present only in inversion recovery data recorded by Dr. Biller, was attributed to Heisenberg exchange. Estimates of the tumbling correlation time may be calculated using the Debye-Stokes-Einstein relationship or by spectral simulation using EasySpin.^{99,162} At long tumbling correlation times, the nitrogen nuclear relaxation time constant (T_{1N}) is much longer than either T_{1HE} or T_{1e} and the dominant contribution to saturation transfer between hyperfine lines is Heisenberg exchange, the fastest process present.^{46,47,157,172,177,178} The short components in the observed SR measurements match well with the low-concentration measurements via inversion recovery of T_{1e}^* and with other literature values of T_{1e} .⁴⁵ Values of T_{1N} were calculated as a function of tumbling correlation times. For carboxyproxyl in aqueous solution, the tumbling correlation time is in the range of 18-20 ps and yields a calculated T_{1N} of approximately 2.7×10^3 ns. The measured value of T_{1N} of $(3.8 \pm 0.8) \times 10^3$ ns for carboxyproxyl is within a factor of two of this calculation and is considered to be in good agreement. Similarly, the tumbling correlation time for tempol in toluene is much faster, in the range of 4-6 ps, resulting in a calculated T_{1N} of approximately 6×10^3 to 8×10^3 ns and is in good agreement with the observed $(7.9 \pm 0.5) \times 10^3$ ns.

The digital SR spectrometer has allowed measurements of fast relaxing nitroxides with high enough S/N to permit separation of two components of the SR signal via biexponential fits. Direct comparison is then possible between T_{1e} and T_{1N} obtained by SR and by inversion recovery. From this comparison, it was established that values of T_{1e} , T_{1N} , and Heisenberg exchange rate may be obtained from inversion recovery and SR measurements. The digital SR spectrometer has aided in this analysis to separate

contributions to overall relaxation and has shown utility in the characterization of relaxation parameters relevant to estimation of the saturation factor in DNP experiments.

Chapter Four: Adapting rapid scan EPR to low temperatures

“Reasonable? There is no reasoning with helium.”

- Dr. Sandra Eaton

Performing CW experiments at cryogenic temperatures is a challenge due to long relaxation times and wide linewidths observed in some EPR active metal centers below 77 K, such as in spectra of vanadyl porphyrins.¹³ To properly record the lineshapes of slowly relaxing metal centers by CW, low microwave power and very slow field modulation are required.^{51,105,112,179} Because of this, the most frequently used EPR techniques when operating at cryogenic temperatures are pulse experiments that do not require magnetic field modulation. Pulse spectrometers require high-power (~1 kW) amplifiers at X-band (ca .9 GHz) and are not as commonplace as CW spectrometers. Attempts to record CW spectra of metal centers at low temperature (< 20 K) typically result in the recording of passage effects, a phenomenon that occurs when the rate of passage through resonance of an EPR active transition is fast relative to relaxation processes.¹⁷⁹ Currently, the only EPR technique that allows for true resolution of spectra exhibiting passage effects is RS.^{51,105,112} In a RS experiment, passage effects may be removed mathematically by deconvolving the spectrum from the transient passage effects due to scan rate.^{34,111} The resultant “slow-scan” spectrum is free of passage effects.^{51,105,112}

Single crystal samples with long relaxation times ($T_m \sim \mu\text{s}$, $T_1 \sim \text{ms}$) were chosen to explore the potential advantages of the RS method at low temperatures. For doped solids such as VO(Zn)tetraphenylporphyrin and Cu(Zn)(diethyldithiocarbamate)₂, it is extremely difficult to obtain CW spectra at low temperature with accurate lineshapes because the relaxation times are so long that the spectra are subject to passage effects.¹³ For these samples the CW spectrum of a down-field scan may appear to be the mirror image relative to the spectrum recorded in an upfield scan when using typical CW parameters.¹³ By using RS and deconvolution of the passage effects, undistorted lineshapes and well resolved hyperfine can be obtained if the microwave B_1 is in the linear response region.^{34,37} Deconvolution only alleviates passage effects related to the magnetic field scan rate and not those related to high microwave B_1 beyond the linear response region. The dispersion signal saturates less readily than the absorption signal so it is possible that only deconvolved dispersion spectra are free of passage effects at very low temperatures in samples with extremely long relaxation.^{34,36,37} Because some of the samples chosen to explore the technique have very large linewidths, the previously reported field-stepped direct-detection (FSDD) algorithms were improved to include samples with linewidths much larger than the effective field sweep width of each individual segment.⁴⁰ Expanding on the work of Dr. Zhelin Yu, signals extending over several segments may now be collected, combined and deconvolved. Early versions of Matlab programs used in the deconvolution and reconstruction of FSDD spectra were published by Dr. Zhelin Yu.⁴⁰ Updated versions were compiled and a universal field-stepped direct-detection program was written by Lukas Woodcock and will be documented in his dissertation.

Beyond the exploration of samples with very long relaxation times, a separate investigation was undertaken to study the spectral characteristics of the lanthanide ions in frozen solutions. Some work has been done previously concerning lanthanides in single crystals and doped solids but few EPR studies have measured lanthanide ions in frozen solutions. Using FSDD, CW, and pulse methods for measuring relaxation, the lanthanide ions were investigated in water:ethanol frozen solutions.

4.1 Temperature dependence of relaxation

The intensity of an EPR signal is proportional to the difference in populations between the upper and lower energy states for the electron spin (*Eq 1.3*).¹³ The relative populations at X-band are quite small, with the difference in relative populations often less than one percent at room temperature.¹³ This population difference becomes much larger at lower temperatures, resulting in significant increases in signal amplitude.¹³ As temperature decreases, T_m increases from a few hundred nanoseconds to a few microseconds and T_1 increases from a few microseconds to milliseconds at 4.2 K for many organic radicals, greatly increasing the saturation factor (*Eq 1.7*) for relative microwave excitation, B_1 .⁴⁵ Longer relaxation times greatly limit the microwave power that can be used for CW experiments. RS has been found to be less susceptible to saturation effects as scan rates can be much faster, limiting the time spent on resonance.^{34,36,37}

4.1.1 Passage effects

Passage effects were reported in the lineshapes of NMR signals by Bloembergen et al. and Jacobsohn and Wangness in 1948.^{180,181} Subsequent observations in EPR experiments were first presented by Portis and were further explored by Hyde, Weger, and others.^{182–186} The most well-known example of passage effects is demonstrated in the CW spectra shown in Fig 4.1.¹⁷⁹ When performing CW experiments, the derivative lineshape is expected due to the field modulation employed with lock-in detection to increase S/N relative to direct detection. The observed CW signal in Fig 4.1 deviates greatly from the expected derivative lineshape and instead resembles an absorption lineshape when sweeping the main field from low field to high field and resembles the mirror image when sweeping the main field in the opposite direction.

Power saturation is dictated by the relaxation rate of the excited species and is often used as an indication as to whether passage effects are expected. Mathematically, passage effects may be observed at any point when the change in scanning field, $\frac{dB}{dt}$, is faster than the observed relaxation product, T_1T_2 , originally described by Portis in 1955 and confirmed by Weger in 1960,

$$\frac{B_1}{\left[\left(\frac{dB}{dt}\right)(T_1T_2)^{\frac{1}{2}}\right]} < 1 \quad \text{Eq. 4.1}$$

where B_1 is the microwave excitation.^{17,182,185} In a typical CW experiment, there are two processes contributing to the change in scanning field. The main magnetic field is slowly ramped to create the magnetic field axis in the resultant EPR spectrum and is generally assumed to be too slow to contribute to passage effects. However, the field modulation typically employed is a sinusoidal modulation oscillating at 10-100 kHz with an

amplitude of up to about 4 G resulting in scan rates on the order of kG/s. In a RS experiment, field scans with up to 60 kHz frequency and up to 155 G amplitude result in much faster scan rates. However, the deconvolution process can remove effects due to rapidly passing through resonance.¹⁷ The observation of accurate lineshapes is important for all EPR spectra. For many metals, relaxation is too fast at room temperature to detect the signal so experiments are limited to low temperature. At low temperatures, T_1 can have a very strong dependence on temperature ($\sim T^9$ in some cases) which can result in a very small temperature range in which T_1 is both long enough to observe an EPR signal and yet still short enough to not observe passage effects.¹⁸⁷ Performing RS at cryogenic temperatures is most advantageous when accurate spectra are not obtained by CW methods.^{51,105,188}

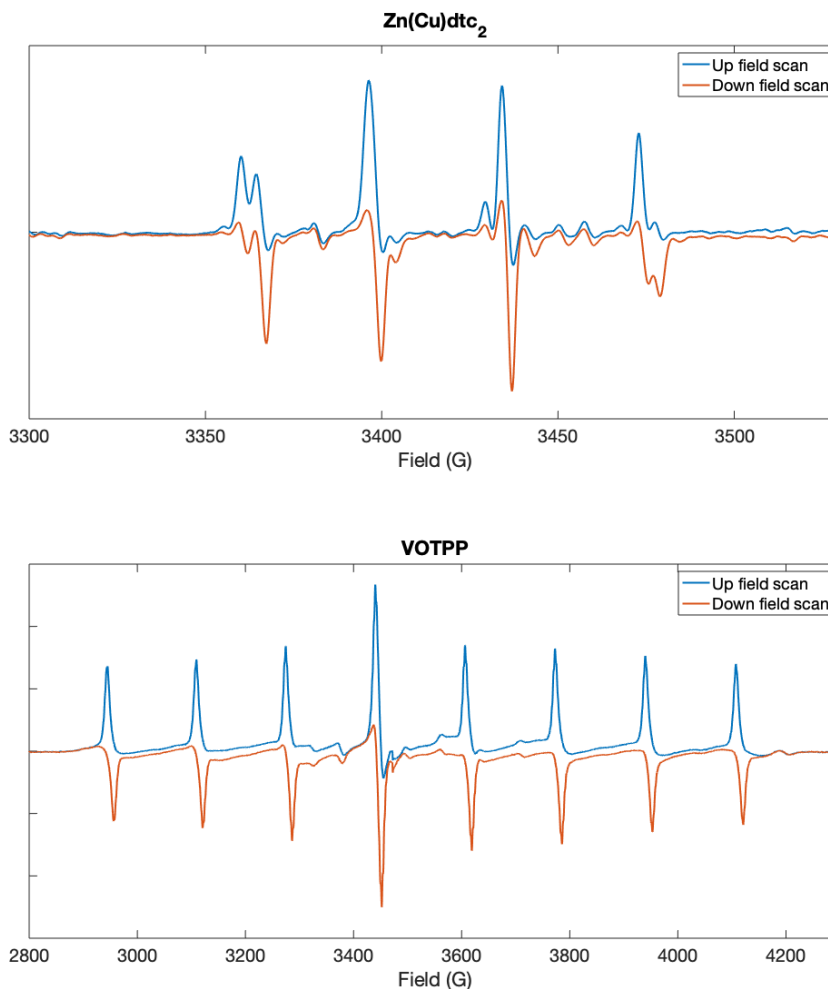


Fig 4.1: CW spectra of 0.5% VO(Zn)TPP (*top*) and 0.67% Cu(Zn)dtc₂ (*bottom*) recorded at 4 K exhibiting extreme passage effects where the mirror image of the observed signal amplitude relative to the baseline is dependent on the direction of the field sweep. Spectra were recorded using 89 mG B₁, 6 kHz modulation frequency and either 0.05 G (Cu) or 0.1 G (VO) modulation amplitude.

4.2 Instrument considerations

When envisioning the replacement of the CW spectrometer with a modern RS spectrometer, it became necessary to consider the adaptation of RS to low temperature measurements. Many samples exhibit slow relaxation at low temperatures, which is a regime in which RS techniques have shown significant improvements.^{37,51,189} To collect RS data, a homogeneous RS field must be created over the sample. This usually involves

a larger volume than is possible with scan coils placed inside a cryostat. It is possible to perform RS using the small modulation coils embedded in Bruker Flexline resonators; however, this is not advantageous over large sample volumes given the small diameter of the coils.³⁸ New, larger coils than previously used in RS experiments were designed and built by Dr. George Rinard. These larger coils can be mounted on the exterior of a cryostat that is similar in dimensions to the Oxford cryostats typically used in EPR instruments. The scanning field must be able to penetrate the walls of the cryostat, which is not feasible with the usual metal cryostats and necessitated a new, primarily plastic design from ColdEdge Industries and Bruker Biospin. This design allows magnetic field scan coils to be mounted external to the cryostat to obtain a larger homogenous field region than could be obtained with coils inside the cryostat. Samples are cooled by flowing He gas, using a “Stinger” closed-loop helium recirculation system also developed by ColdEdge and Bruker Biospin. The system operates stably for periods of several days to a few weeks while maintaining temperatures near 5-10 K. Additional modifications to the detection system, such as the incorporation of high-pass filters to remove low-frequency oscillations from the helium recirculation system, were incorporated when dictated by artifacts in data collection.

Until recently, RS experiments were hardware-limited to ~155 G sweep widths. However, FSDD was developed to apply the principles of RS to very wide spectra (~6000 G).^{40,42} FSDD was investigated by Dr. Zhelin Yu in the Eaton lab and also by Hyde and coworkers and has been previously described and evaluated at room temperature.^{40,42} In an FSDD experiment, triangular waveforms are synthesized and applied to scan the magnetic field at a constant scan rate as the main field is increased in

discrete steps. The resultant field sweeps ($\Delta B_{RS-sweep}$), performed over a range of linearly increased steps of the main magnetic field, are aligned and combined into one wide spectrum. In the report by Yu et al., the reconstructed wide spectrum was then subjected to the mathematical deconvolutions normally applied to RS spectra collected at a single main field position.⁴⁰

In prior FSDD experiments, it was demonstrated that passage effects were effectively resolved when the entire transient effects was recorded in a single RS spectrum of the larger FSDD array ($\Delta B_{spectral\ width} < \Delta B_{RS-sweep}$) before deconvolution and spectral reconstruction.^{40,134} It is the goal of this research to adapt the FSDD technique to samples that exhibit passage effects spanning a greater width than any single RS segment collected during the experiment ($\Delta B_{spectral\ width} \gg \Delta B_{RS-sweep}$). Data collected in this manner is of particular interest in scenarios where the lowest available microwave B_1 and modulation rates used in typical CW spectrometers produce spectra containing passage effects.

4.2.1 A metal-free, closed-loop cryogen EPR system

The “Stinger” system consists of two closed-loop pumping systems. The primary cooling system consists of a recirculating helium compression system, designed to flow across a large radiator that then removes heat from a continuously recirculating gas stream of ultra-pure helium gas. The cryocooled helium gas enters the cryostat and cools the resonator, a Bruker ER-4118X-MD-5, to approximately 5 K when evacuated and free of interfering contaminants. A picture of the “Stinger” system is shown in Fig. 4.2 (*left*).

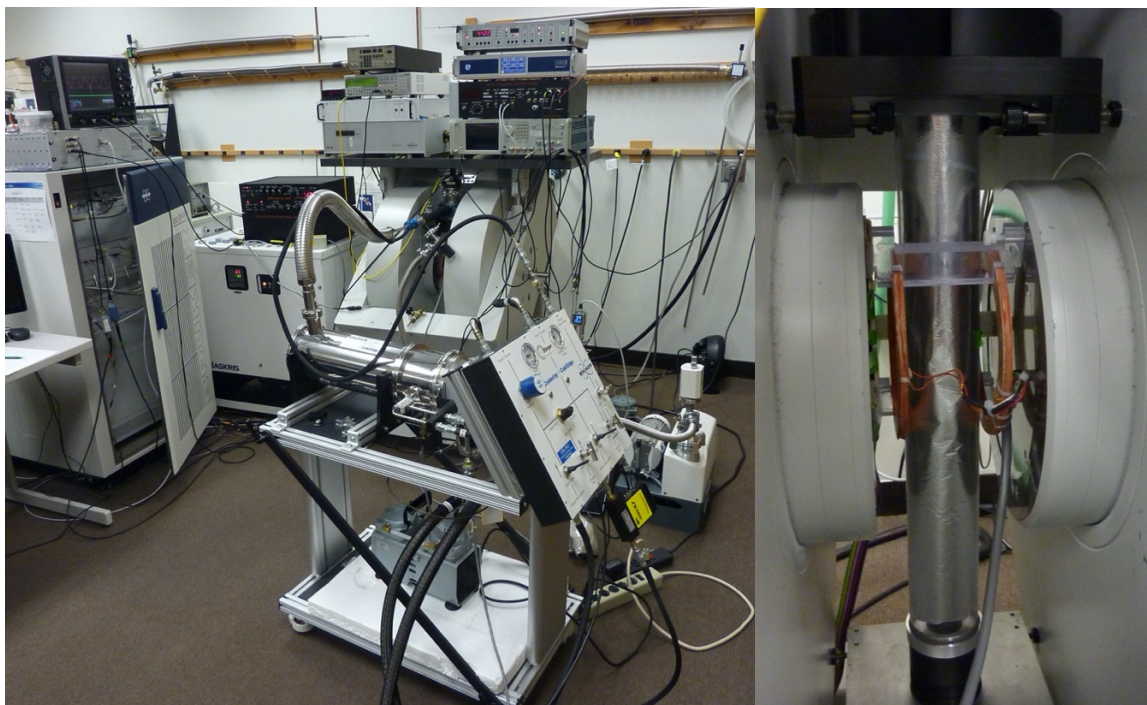


Fig 4.2: Left, the Stinger helium recirculation system in use on a Bruker E500T X-band spectrometer. Right, the RS cryostat containing a “metal-free” region of low conductivity and RS coils mounted inside a Bruker E500T X-band spectrometer magnet. The magnet has larger spacing than is in the usual EPR magnet to accommodate RS coils external to a Bruker Flexline resonator.

The cryostat, specifically designed for the RS experiment, maintains similar shape and adaptability for use with Bruker FlexLine resonators and is similar in construction to prior Oxford designs that interface well with these resonators. A “metal-free” region of low conductivity was incorporated such that the scan coils may be mounted external to the cryostat, creating a large homogeneous scanning region. This region is made up of a plastic shell wrapped in thin, aluminized mylar sheets followed by a second plastic shell completing the typical vacuum chamber comprising the cryostat walls. Vertical copper strips were used to help create a uniform temperature throughout the entire length of the cryostat. These copper runners have been implemented in a way that avoids completed loops, decreasing eddy currents that may oppose or distort the rapidly alternating

magnetic field and is an enabling technology for low temperature RS.³³ A picture demonstrating the RS coils mounted on the cryostat is in Fig 4.2 (*right*).

Once properly purged with ultra-pure helium and evacuated sufficiently, the system cools to 5 K over the course of a few hours and maintains temperature indefinitely if not disturbed. In routine operation, changing the sample may introduce air into the system, eventually leading to a clogged capillary flow system and necessitating a return to higher temperatures for purging before resuming operation. The system as used in our lab is stable for several weeks of operation, rising only 0.3 K/day on average (Fig 4.3). This is mostly due to gases introduced during sample changes and can be controlled somewhat with the addition of helium gas to the system both during and after changing samples followed by vacuum evacuation of the sample space. Continuous operation requires the addition of helium at a very slow rate, using approximately one full tank (~7000 L) every 3-6 months, depending on frequency of sample changes and required temperatures. Temperature is adjusted using a dedicated controller interfaced to two thermocouples and a resistance heater within the cryostat. A flow controller is also utilized to vary temperature, as the heater alone may be insufficient to reach higher temperatures (~50-70 K) when helium flow is at full velocity.

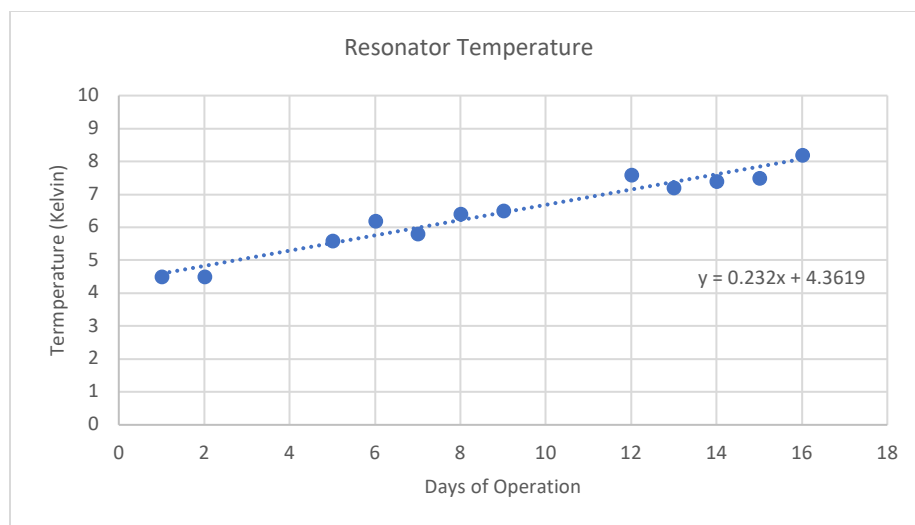


Fig 4.3: Operating temperature vs. days of operation when using the “Stinger” system and metal-free cryostat for RS experiments. The helium consumption is fairly low when operating for periods of weeks, changing samples approximately once every two days.

4.2.2 The RS scanning and detection systems

Experiments were performed on a modified Bruker E500T X-Band spectrometer equipped with a Bruker SpecJet II transient data collection digitizer. A previously developed RS coil driver supplied the necessary oscillating current to a set of homebuilt RS coils composed of 90 turns of 220/46 Litz wire.¹⁰ The coils are approximately 5” in diameter with Helmholtz spacing designed to fit on the outside of the ColdEdge cryostat. The coils created a scanning field of approximately 13 G for every ampere of current supplied by the coil driver. Experiments were performed using approximately 3-5 kHz triangular scanning waveforms and 20-30 G RS sweep widths. The triangular waveforms were selected, instead of sinusoidal waveforms, to have a constant scan rate throughout the scan. The Hall probe that is part of the feedback circuit that controls the main magnetic field was moved from its standard location on the pole faces of the Bruker magnet to a position further from the center to minimize interference from the large RS

coils. Placement of the Hall probe was performed empirically by monitoring the stability of the main magnetic field while oscillating the RS field. Optimum placement was found just outside the scan field (~1-2 in. outside the RS coils) at the center of the main magnet pole spacings. This relocation resulted in decreased time required for field stabilization when incrementing the main magnetic field in discrete steps. The spacing between the pole faces of the main magnet was approximately 4 inches and is larger than is usually delivered with the Bruker E500T spectrometer. The wide gap magnet was purchased to accommodate the cryostat, RS coils, and Hall probe in an orientation that provides stable field scans.

Two investigations of standard samples at room temperature, a sample of trityl- CD_3 in water (0.41 mM) and a solution of $\text{Cu}(\text{diethyldithiocarbamate})_2$ in toluene (1.14 mM) were used to confirm that RS spectra were not distorted by the metal-free cryostat (Fig 4.4). Trityl- CD_3 measurements were performed using triangular scanning waves without any stepping of the main field; however, copper measurements required FSDD methods. In both cases, measurements were in good agreement with analogous CW measurements of the same sample, that were recorded without disturbing the tuning or sample placement within the spectrometer. CW measurements were performed with modulation coils present within the Bruker ER 4118X-MD-5 resonator and FSDD measurements were performed with the large scanning coils external to the cryostat.

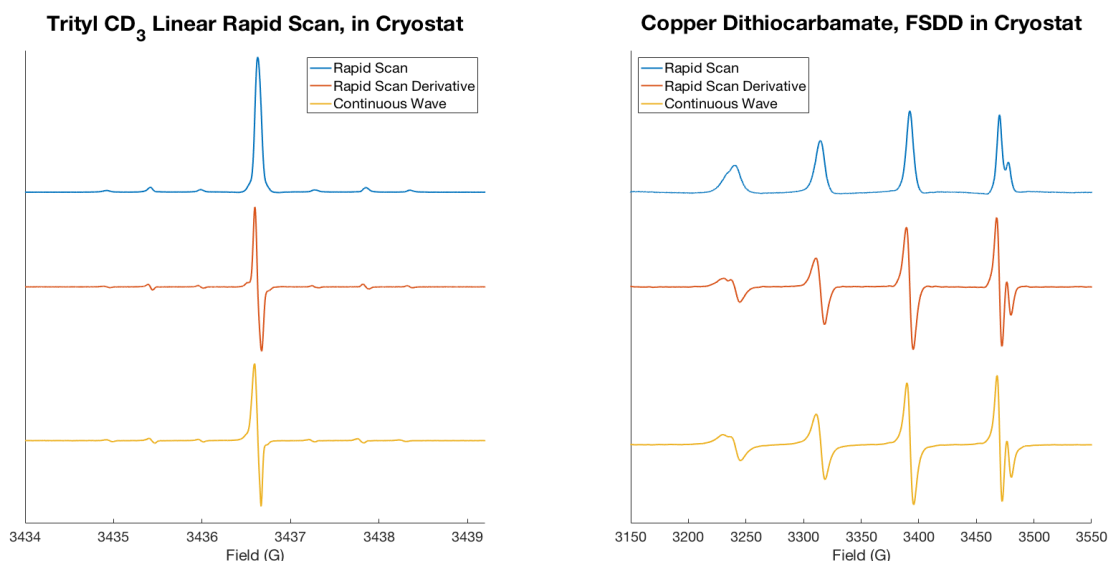


Fig 4.4: Left, use of the cryostat does not affect the lineshape of trityl-CD₃ when performing single-spectrum RS using triangular scans. Right, use of the cryostat does not affect the lineshape of Cu(dtc)₂ in toluene when using field-stepped direct-detection RS methods at room temperature. The ⁶³Cu, ⁶⁵Cu isotope splittings are well resolved in spectra of Cu(dtc)₂.

The recirculation systems required for closed-loop cryogenic systems create considerable low frequency interference when performing EPR experiments. Most of the observed interfering frequencies were within the low audible range, typically below 600 Hz. Because the RS frequency is much higher than this, high pass filters were designed with the assistance of Richard Quine, with a cutoff frequency of 2 kHz to effectively filter the observed low-frequency vibrations generated from the cryogen pumping system while preserving the RS signal. A 4-pole Butterworth filter was chosen to give sharp cutoff without filtering the RS frequency (3-10 kHz). A schematic diagram of the filter, as used, is given in Fig 4.5. The filters were placed on the input to the SpecJet II digitizer. To confirm filter operation, signal attenuation was measured over several octaves by using a signal generator to supply waveforms of known peak-to-peak intensities. The observed attenuations are plotted against the signal frequencies supplied by the generator

(Fig 4.5). Little to no attenuation was found above 3 kHz. Two identical filters were constructed, one for each digitizer input channel, and were used to filter RS data recorded in quadrature.

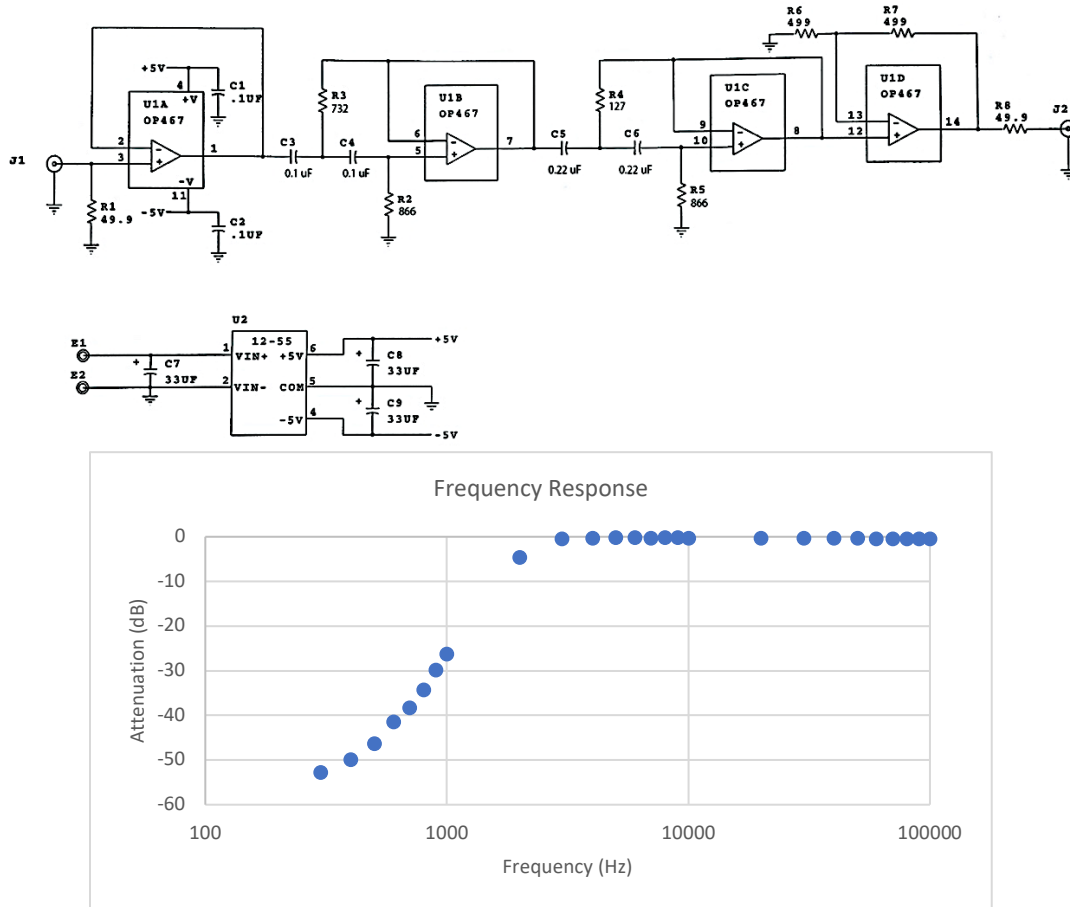


Fig 4.5: Diagram (*top*) of the high pass filters employed in low temperature RS data collection and the measured attenuation at several octaves (*bottom*). Two identical channels were constructed to filter both digitizer inputs when collecting data in quadrature.

4.2.3 Resonator background at low temperatures

Two dielectric resonators were used, a Bruker ER4118X-MD-5-W1 when performing experiments with a Bruker E580 spectrometer (CW, pulse) and a Bruker ER4118X-MD-5 when performing experiments with a modified Bruker E500T

spectrometer. Both resonators consist of a single crystal of sapphire. The resonator has little to no background signal detectable when operating near room temperature. However, at 4-10 K several EPR active regions may be seen in CW and RS experiments and a single EPR active region is visible in field-swept echo-detected spectra.

Under conservative operating conditions, signals present near $g = 4$ and $g = 2$ are reproducible and are attributed to impurities in sapphire. RS and CW spectra of the resonator background signals are shown in Fig 4.6. Power saturation was different for signals at the different g -values and are shown in the inset of Fig 4.6. No echoes were observed in two pulse echo decay experiments of the resonator background, with the exception of a very low intensity signal near $g = 2$ (data not shown). Saturation recovery measurements were performed near these positions and values of $T_1 = 11 \mu\text{s}$ and $26 - 40 \mu\text{s}$ were observed near $g = 4$ and $g = 2$, respectively.

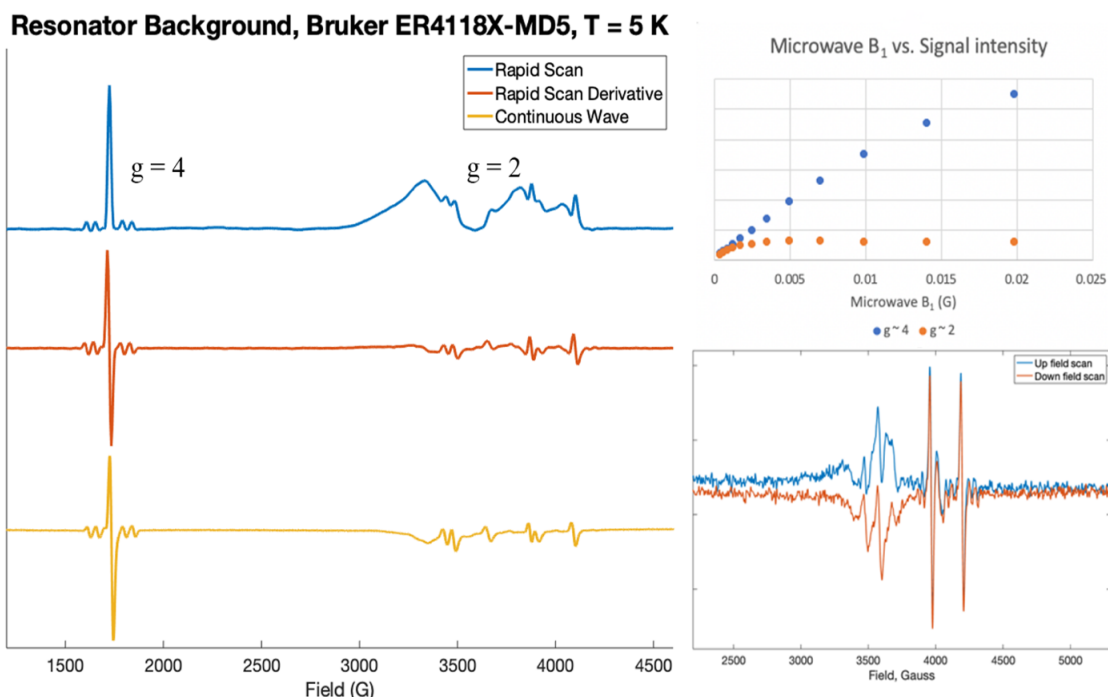


Fig 4.6: Left, the RS absorption spectrum (*blue*), calculated derivative of the RS absorption spectrum (*orange*), and CW spectrum (*yellow*) of the ER-4118X-MD-5 resonator at 5 K. Power saturation curves, recorded via CW, are shown (*right, above*) for both $g = 4$ (*blue*) and $g = 2$ (*orange*). Right, below, CW spectrum of the ER4118X-MD-5-W1 collected while sweeping the main field from low field to high field (*blue*) and in the opposite direction (*orange*). The background signals from the two similar sapphire resonators were very similar.

Concerning the impurities seen in the sapphire resonator background, similar spectra have been reported in the literature for each region of interest allowing speculation concerning the impurity signals present. During the forging process of the sapphire, several impurities may be introduced such as Cr, Ti, Mo, and many other metals.¹⁹⁰ The dominant impurity signal near $g = 4$ (low field) in Fig 4.6 may be attributed to molybdenum and is consistent with prior reported g -values and spin-lattice relaxation times and may be simulated in EasySpin using an ^{95,97}Mo ($I = 5/2$) nucleus.^{99,191,192} The EPR active region near $g = 2$ and below (high field) is speculated to be the contribution of a rapidly relaxing titanium center and a slowly relaxing copper center.¹⁹³ It has also been reported that molybdenum may also give a signal near $g = 2$,

further complicating characterization.^{191,192} CW spectra collected while varying the scan direction of the main field showed an inversion of some, but not all, of the signals present near $g = 2$ (Fig 4.6), implying two independent species with differing relaxation times and a slight presence of passage effects in some but not all of the species present. The more slowly relaxing signal is attributed to copper. It is likely that the copper is not present in the sapphire, but instead the B_1 field of the resonator extends out far enough to include the coupling antenna that delivers power to the resonator.

4.3 Low temperature spectroscopy

Several 3d transition metals and an organic radical with slow relaxation rates were investigated at 4-10 K. These included single crystals of the following; 0.2% tempol (4-hydroxy-2,2,6,6-tetramethylpiperidin-1-oxyl) doped in a diamagnetic amine analog, 0.67% copper doped in zinc diethyldithiocarbamate, manganese doped in magnesium acetylacetonate, and vanadium (0.5%) in zinc triphenylporphyrin. A powder sample 0.01% Cu^{2+} and 0.01% Ni^{3+} in Ni(II) maleonitriledithiolate (KB-79), provided by Dr. Petr Neugebauer, was investigated and has been previously described.^{194,195} Cobalt trispyrazolylborate (CoTp_2), provided by Dr. Surendra Mahapuro, dissolved in 9:1 toluene:dichloromethane (12 mM) was also investigated due to large g anisotropy that would challenge the stability of the FSDD technique. Pulse, CW, and FSDD methods were performed on all samples.

In addition to slowly relaxing metal centers listed above, rapidly relaxing lanthanide ions in frozen solution were investigated via low temperature FSDD spectroscopy. Frozen solutions of 1:1 water/ethanol were prepared with approximately 10

mM of each of the following: $\text{Ce}(\text{NO}_3)_3$, $\text{Pr}(\text{NO}_3)_3$, NdCl_3 , $\text{Sm}(\text{NO}_3)_3$, GdCl_3 , TbCl_3 , DyCl_3 , $\text{Ho}(\text{NO}_3)_3$, $\text{Er}(\text{NO}_3)_3$, TmCl_3 , and $\text{Yb}(\text{acac})$. Each solution was controlled to pH = 2.5 or below by the addition of concentrated HCl, added dropwise while measuring pH using a standard probe. $\text{Ce}(\text{NO}_3)_3$ and GdCl_3 solutions were diluted to 1 mM for relaxation measurements. $\text{Yb}(\text{OOCCH}_3)_3$ was used in pulse experiments and will be investigated by CW and FSDD in the future. Field-swept spectra are shown for all techniques and relaxation times are reported at several temperatures. Some field dependence of relaxation (T_1) was observed; however, the reported relaxation times are an average of all field positions recorded. The field-dependence of relaxation will be investigated further and reported elsewhere.

4.3.1 Slowly relaxing metal centers

CW measurements were performed on either a Bruker E500T X-band spectrometer and an ER4118X-MD-5 dielectric resonator or a Bruker E580 X-band spectrometer and an ER4118X-MD-5-W1 dielectric resonator. Modulation frequency was varied between 10 and 100 kHz and modulation amplitude was varied between 0.5 and 4 G. Passage effects were most visible at the highest scan rates and high microwave B_1 . In cases where microwave attenuation was insufficient to avoid saturation when using the Bruker E500T microwave bridge, a previously described digital saturation recovery microwave bridge and Tektronix arbitrary waveform generator (AWG) were used in place of the Bruker bridge while continuing to use the Bruker E500T magnet and power supply, digitizer, and console.²⁹ The digital saturation recovery bridge was not optimized for FSDD experiments.

FSDD experiments (Fig 4.7) were performed on a modified Bruker E500T X-Band spectrometer with a dielectric resonator ER4118X-MD-5 and a SpecJet II fast digitizer. Triangular scanning waveforms were employed at a rate of 1.7×10^5 G/s.¹⁰ As was the case in CW experiments, a previously described digital saturation recovery microwave bridge and Tektronix arbitrary waveform generator (AWG) were used in place of the Bruker bridge while continuing to use the Bruker E500T magnet and power supply, digitizer, and console.²⁹ The low temperature system was used as described above. FSDD spectra were collected using Bruker Xepr software. Locally written software was used to perform deconvolution and spectral reconstruction based on prior efforts.^{34,40}

Pulse experiments (Fig 4.7, Table 4.1) were performed on a Bruker E580 X-band spectrometer and an ER4118X-MD-5-W1 dielectric resonator. Phase memory time (T_m) was measured via two-pulse echo decay. Pulse lengths and tau values were on the order of hundreds of nanoseconds to microseconds in two pulse echo experiments to suppress the effects of nuclear modulation. Spin-lattice relaxation time, T_1 , was measured via three-pulse inversion recovery using pulse lengths of 40 and 80 ns. T_1 values recorded via three-pulse inversion recovery were on the order of hundreds of microseconds to hundreds of milliseconds.

Relaxation times, both spin-lattice relaxation times (T_1) and phase memory time (T_m) were calculated from 3-pulse inversion recovery or 2-pulse spin echo measurements, respectively (Table 4.1). Data were fit with a single exponential for T_m measurements and with a stretched exponential for T_1 measurements. Power saturation behavior was recorded for slowly relaxing organic radicals and 3d transition metals, both via CW and

FSDD. Saturation was defined as more than a 5% deviation from linearity of increasing signal amplitude. FSDD absorption spectra and the mathematically computed FSDD derivative spectra are shown for all samples in Fig 4.8. Phase was adjusted during post-processing in Matlab.³⁶ Deconvolved FSDD spectra were compared to the reconstructed spectra in the absence of deconvolution for evaluating the benefits of using the deconvolution on spectra of these samples.

Table 4.1: Relaxation times at temperatures between 4-10 K recorded by two-pulse spin echo and three-pulse inversion recovery for T_m and T_1 , respectively.

Sample	Observation temperature (K)	T_m (μ s) Echo Decay*	T_1 (ms) Inversion Recovery*
Tempol	4	0.7	7.1
	10	0.7	3.1
	20	0.7	2.6
Cu(dtc) ₂	4	2.0	78
	10	0.8	3.7
Mn(acac) ₂	4	4.3	210
	10	4.4	49
VOTPP	4	2.8	2.0
	10	2.4	0.9
KB-79	5	7.4	6.2
	10	7.6	0.5
CoTp ₂	6	0.6	0.017

*Reported values are an average of multiple measurements taken at several field positions fit with a single exponential (T_m) or a stretched exponential (T_1).

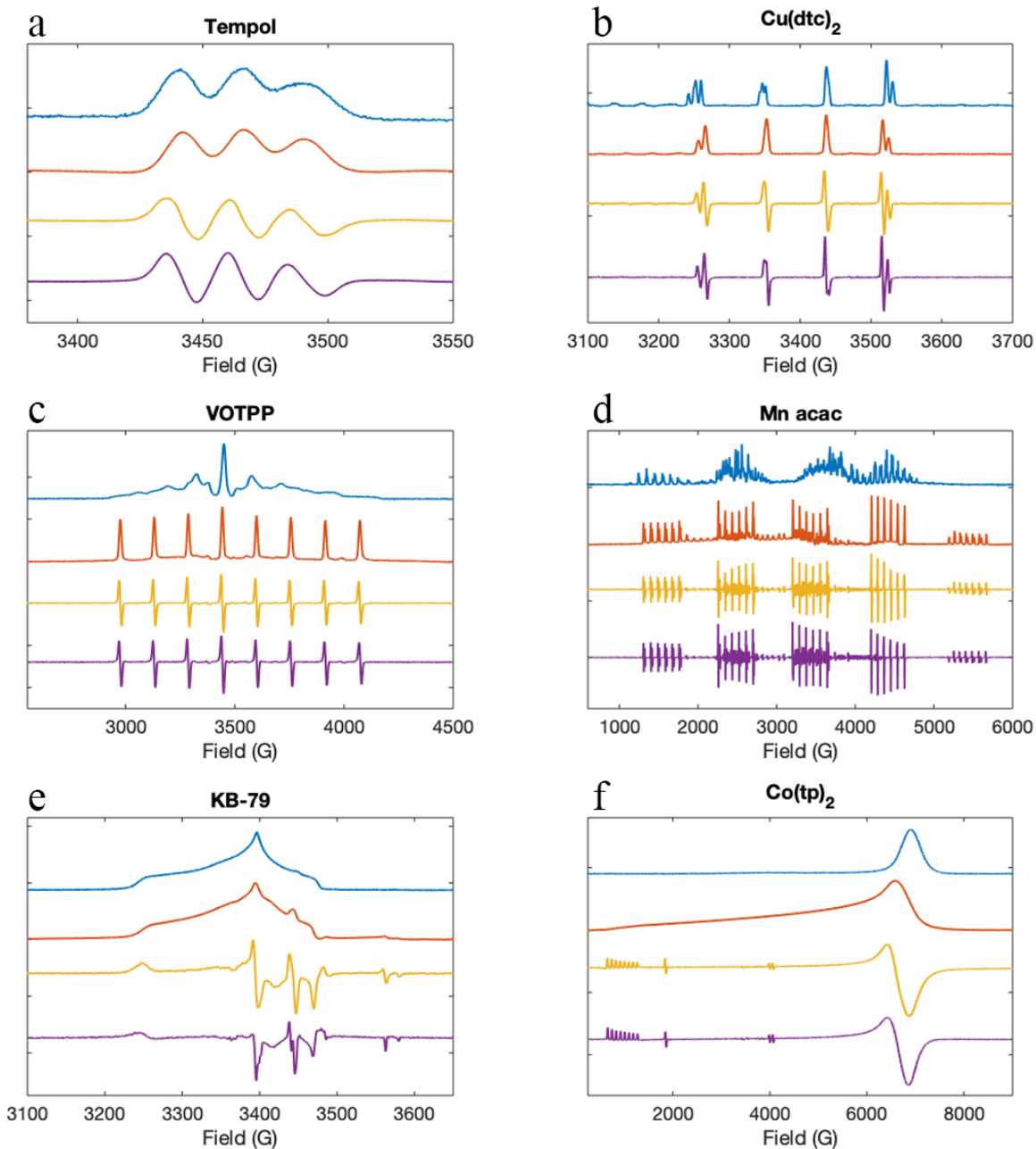


Figure 4.7: Field-swept echo-detected spectra (*blue*), FSDD absorption spectra (*red*), calculated derivatives of the FSDD absorption spectra (*yellow*), and CW spectra (*purple*) for the following samples recorded between 4-10 K, (a) Tempol, (b) Cu(Zn)(dte)₂, (c) VO(Zn)TPP, (d) Mn(Mg)(acac)₂, (e) 0.01% Cu²⁺ and 0.01% Ni³⁺ maleonitriledithioilate (KB-79) powder, (f) CoTp₂, 12 mM in 9:1 toluene:dichloromethane. Orientations of the single crystal samples were slightly different in the field-swept echo-detected spectra and FSDD spectra in parts a, b, and d. The field-swept echo-detected spectrum for VOTPP is for a power sample although the FSDD and CW spectra are for a single crystal. CoTp₂ nuclear modulation reduces echo intensity at low field, preventing the observation of the hyperfine splitting seen in FSDD and CW spectra.

The most frequently observed passage effects are a distortion of lineshape in the CW spectrum. Less frequently observed, spectra resembling a mirror image of the lineshape with respect to field direction (Fig 4.1) are indicative of passage effects. Power saturation is dictated by the relaxation rate of the excited species which can be used to predict passage effects. In the relaxation times reported, cross-relaxation is suspected to dominate the observed T_m in the tempol crystal studied, giving a T_m of ~ 0.7 microseconds between 4-10 K when longer relaxation would be expected for magnetically dilute organic radicals.¹⁹⁶⁻¹⁹⁸

By using RS and deconvolution, undistorted lineshape and well resolved hyperfine can be obtained if the B_1 is in the region of linear response with respect to microwave power and the entire spectrum is excited in a single sweep.^{34,37} Because deconvolution only alleviates passage effects related to the magnetic field scan rate and not those related to high microwave B_1 beyond the linear response region, it was found that deconvolution had little effect on the spectra of the slowly relaxing metal centers. Efforts to reduce microwave B_1 below the limit of the Bruker E500T microwave bridge were undertaken; however, microwave leakage prevented decreasing power by more than 60 dB which is approximately equal to 2 mG B_1 . The digital saturation recovery bridge was used to achieve microwave B_1 values between 2 mG and 0.2 μ G. Microwave leakage was also observed in the digital saturation recovery bridge; however, the power levels achievable allowed the recording of undistorted CW and FSDD spectra in these samples as shown in Fig 4.7. These spectra do not exhibit rapid-scan oscillations. For these samples the FSDD technique did not achieve the rapid passage regime (scan rate $\gg T_2^*$ or T_2^{eff}), using the currently achievable scan rates, and gives some idea of the

homogeneity of spin packet distribution in the observed lineshapes.^{14,199} Expansion of FSDD methods to include a larger scan width while preserving the fast scan rates employed will be necessary to reach the RS regime for samples exhibiting wide spectra.

4.3.2 Lanthanide aquo-ions

The rare earth elements are of considerable interest for a variety of applications including magnetic resonance imaging and quantum computing.²⁰⁰ The lanthanides, or rare earth elements, make up the f-block of the periodic table and remain a challenge for EPR. Free ions of the lanthanides in solution are very fast relaxing, requiring operating temperatures below 60 K and often below 10 K.^{201–205} Most prior studies of these elements are in the form of crushed powders or single crystals, often introduced into other diamagnetic materials and host lattices.^{14,201} Many of the lanthanides are widely used as catalysts for synthesis reactions with their mechanisms of action often under studied.²⁰⁰ Little is known about the electronic structures of these ions in frozen solution due to their extremely wide spectra, greatly varying g-factors, and fast relaxation.^{201,202,205–207} One of the primary goals of adapting FSDD methods to low temperature is to investigate the EPR active lanthanide ions in frozen solution.

Electrons in the f-shell do not typically exhibit ligand hyperfine interactions due to the shielding effect of the electron clouds with larger radii, such as the s and p shells, leading to primarily ionic bonding character and minimal delocalization.¹⁴ This effect is compounded when considering the large orbital angular momentum observed, preventing coupling to nearby ligand nuclei; though, some calculations of the hyperfine present within the paramagnetic lanthanide nucleus have been performed.¹⁴ Fast relaxation is

often observed even at very low temperatures, preventing EPR observation at room temperature because relaxation rates are faster than the EPR timescale. Spin-orbit coupling leads to large zero-field splitting, creating a challenge specifically in RS.^{14,65} Because the spectrum does not always begin at baseline in the low-field region or go to zero at the highest fields accessible with typical X-band magnets and power supplies, background removal procedures typically employed are no longer useful.^{65,66,208} Instrument stability is critical in these measurements due to the wide spectral features present.

Of the trivalent lanthanide ions, all but lanthanum, lutetium, and europium which have $J = 0$ ground states, are expected to be EPR active. Of these, promethium was not undertaken because it is radioactive. Praseodymium and holmium gave low-intensity CW spectra that were very similar and have been omitted from FSDD investigations at the current stage; however further investigation of this discrepancy will be performed in the future. Due to limitations of the X-band magnet power supply used in low temperature FSDD experiments, the resonance of samarium is beyond the upper limit and was not investigated by FSDD methods.²⁰⁹ The remaining lanthanides were all measured by pulse, CW, and FSDD experiments. Comparisons are drawn to prior examples in the literature though there are few investigations of the lanthanides in fluid solution. All samples were prepared in 1:1 water:ethanol, approximately 10 mM, and pH controlled to less than 2.5 with HCl to prevent precipitation during storage. An overview of the electronic configurations of the trivalent lanthanides is given in Table 4.2.²⁰⁰

Table 4.2: The electronic configurations of the trivalent lanthanide ions. La, Pm, Eu, and Lu were not studied in the present work. Adapted from Huang et al.²⁰⁰

Ion	Number of 4f electrons	L	S	J	Ground state
La ³⁺	0	0	0	0*	¹ S ₀
Ce ³⁺	1	3	1/2	5/2	² F _{5/2}
Pr ³⁺	2	5	1	4	³ H ₄
Nd ³⁺	3	6	3/2	9/2	⁴ I _{9/2}
Pm ³⁺	4	6	2	4	⁵ I ₄
Sm ³⁺	5	5	5/2	5/2	⁴ H _{5/2}
Eu ³⁺	6	3	3	0*	⁷ F ₀
Gd ³⁺	7	0	7/2	7/2	⁸ S _{7/2}
Tb ³⁺	8	3	3	6	⁷ F ₆
Dy ³⁺	9	5	5/2	15/2	⁶ H _{15/2}
Ho ³⁺	10	6	2	8	⁵ I ₈
Er ³⁺	11	6	3/2	15/2	⁴ I _{15/2}
Tm ³⁺	12	5	1	6	³ H ₆
Yb ³⁺	13	3	1/2	7/2	² F _{7/2}
Lu ³⁺	14	0	0	0*	¹ S ₀

*No EPR spectrum is expected for ions with J = 0.

A summary of the relaxation times observed in the samples presented is in Table 4.3. Samples were prepared with O₂ removed in He backfilled, flame sealed 4 mm EPR tubes as in the slowly relaxing metal centers. Relaxation measurements were performed with a Bruker ER4118X-MD-5-W1 dielectric resonator using 40 ns $\pi/2$ and 80 ns π pulses. No echo was observed for Pr³⁺, Dy³⁺, or Ho³⁺. FSDD and CW measurements were performed analogous to those for the slowly relaxing metal centers (Fig 4.8). The power saturation behavior allowed use of the Bruker E500T bridge for all FSDD and CW measurements. Absorption and dispersion data did not show saturation and were combined in the final reconstructed spectrum. CW measurements were performed on Sm³⁺ on the Bruker E580 system (data not shown) which also permits operation at Q band (ca. 34 GHz) and is equipped with a magnet capable of accessing higher fields. Sm³⁺ transitions are observed at low g-values (0.6) and high magnetic field (13,000 G at

X-band). RS spectra were limited by the maximum field strength allowed by the Bruker E500T magnet power supply (~9000 G max).

Table 4.3: Relaxation times of lanthanide ions in frozen solutions recorded by two-pulse spin echo and three-pulse inversion recovery for T_m and T_1 , respectively.

Lanthanide*	Temperature (K)	T_m (ns)	T_1 (μ s)
Ce^{3+}	4.3	500	97
	5	464	28
	6.5	377	5.3
	8	301	2.1
Nd^{3+}	4.2	612	372
	5	563	124
	6	484	36
	7.9	310	5.2
	9.8	180	1.4
Sm^{3+}	4.9	599	17
	5.9	434	4.9
	6.9	363	3.2
	8.9	207	3.7
Gd^{3+}	4.3	810	229
	6.9	573	43
	11.8	497	11
	19.8	314	3.2
Tb^{3+}	4.2	227	31
	5	202	17
	5.9	189	7.7
	6.9	135	3.8
	8.4	120	1.5
Er^{3+}	5	127	2.5
Tm^{3+}	4.2	334	72
	5	288	42
	5.9	250	21
	6.9	215	12
	8.4	176	9.9
Yb^{3+}	9.9	153	2.9
	5	276	36
	5.9	237	13
	6.9	206	5.5
	7.9	225	2.5
	9.8	150	1

* Ce^{3+} and Gd^{3+} were measured using 1 mM concentrations.

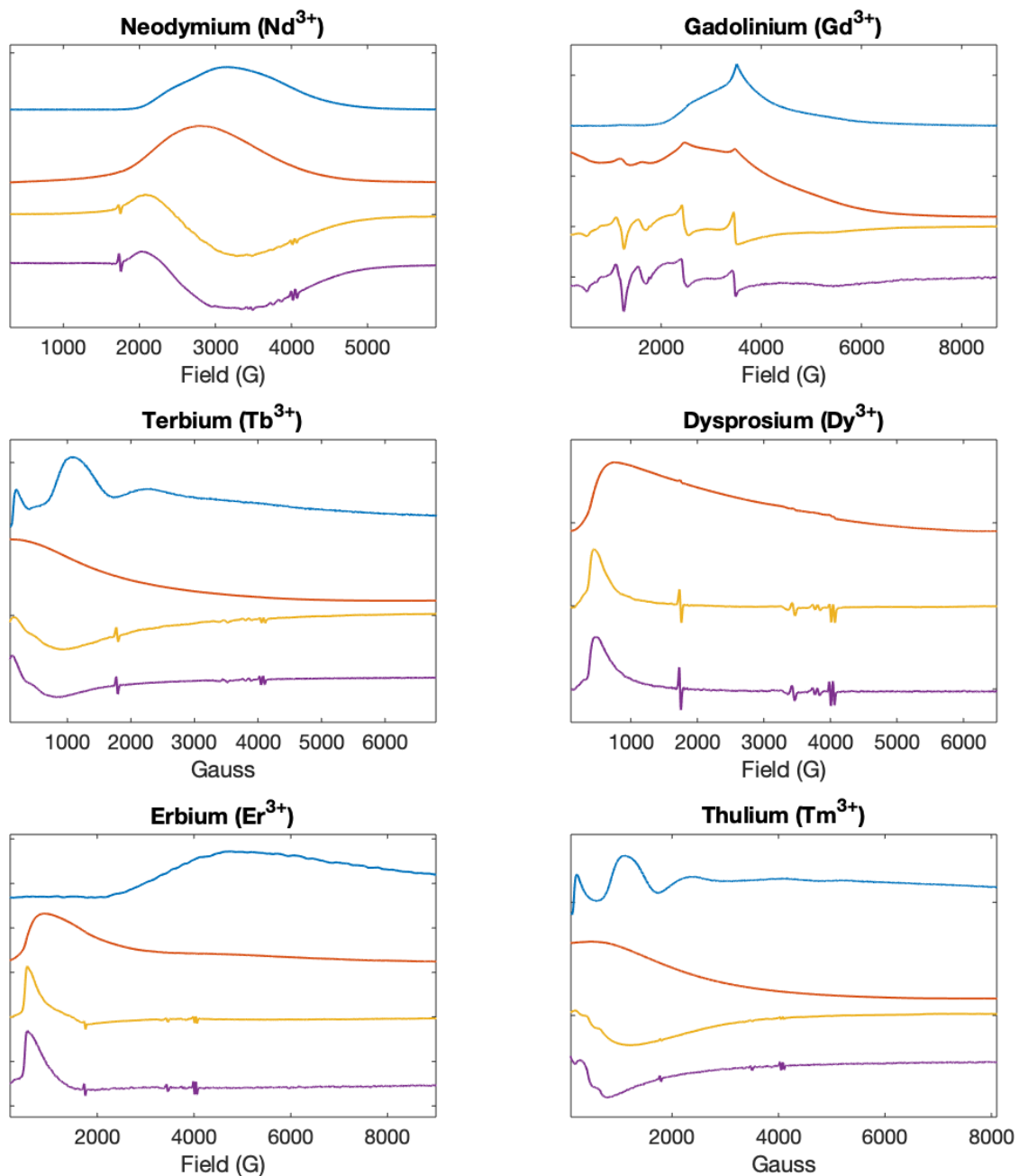


Fig 4.8: Field-swept echo-detected spectra (*blue*), RS absorption spectra (*red*), calculated derivatives of the RS absorption spectra (*yellow*), and CW spectra (*purple*) for the lanthanide ions in frozen solution recorded between 4-10 K. Spectra have been scaled to have comparable signal amplitude. Methods are being developed to remove the acquired cumulative error that is present in FSDD spectra, see text. The field-swept echo detected spectrum of Gd was recorded using a 1 mM sample. The field-swept echo detected spectra of Tb^{3+} and Tm^{3+} were recorded by Dr. Gareth Eaton. No echo was observed for Dy^{3+} .

Because the intensity of the lanthanide spectra extend across the entire accessible magnetic field, background removal methods require special attention relative to narrower FSDD spectra where baseline is present.⁴⁰ It is not possible to obtain the linear cumulative correction that is typically required in FSDD experiments directly from the acquired spectrum. Alternative methods are being developed to carefully characterize the linear correction required for quantitative measurements. Nevertheless, the FSDD spectral acquisition methods developed for low temperatures work equally well for samples where passage conditions are not expected. The combined results for slowly and rapidly relaxing species gave reliable spectra for a wide range of relaxation rates at low temperatures when operating in the linear regime with respect to microwave B_1 .

Chapter Five: Conclusions and comments on future work

“Write the grant you want, then worry about the guidelines”

- Dr. Joshua Biller

The following sections serve as an outline for future experiments related to the projects described as well as provide brief summaries of some developments enabling the future experiments to be performed. This dissertation work was described in three sections. The first, detailed in chapter 2, described the development of applications possible with the current generation of RS hardware in use at the University of Denver and under development at Bruker Biospin. The second, detailed in chapter 3, described the design and construction of a saturation recovery spectrometer using an AWG as the microwave source as well as an application of the spectrometer to investigate rapidly relaxing nitroxides commonly used in DNP experiments. Additionally, and to be described in the thesis of Whylder Moore, the saturation recovery instrument has been employed to investigate the effects of isotopic labeling (^{13}C) on the relaxation of trityl- CD_3 , a radical investigated during the testing and development of the instrument.¹⁷⁰ The third section, detailed in chapter 4, described the adaptation of RS to low temperatures and demonstrated the technique when investigating slowly relaxing metal centers and rapidly relaxing lanthanide ions in frozen solution.

The general themes and motivations surrounding the developments in EPR spectroscopy detailed here are to improve the amount of information gained, in a shorter time than prior measurements, for the application of EPR to new investigations. The exploratory examples of new applications of the RS technique (Ch. 2) were described first and these likely are the examples the reader will seek first. It is the work described in chapters 3 and 4 that expands the uses of EPR, first through the improvement of the electronics employed in making measurements and second through the development of new operating regimes for existing techniques. Conclusions and suggestions for future work related to selected sections are described below.

5.1 Proposed improvements to the saturation recovery spectrometer

While the original digital EPR spectrometer design included specifications only for the performance of the saturation recovery experiment, during its development it evolved into a versatile spectrometer capable of single-channel or quadrature detection with the ability to perform CW, RS, saturation recovery, and pulse measurements of species with long relaxation times such as trityl-CD₃. The AWG enables many experiments beyond that of traditional saturation recovery and standard CW measurements, such as the ability to shape pulses for increased excitation bandwidth.¹²⁴ With a relatively simple modification, a pulse amplifier could be added to the saturation recovery spectrometer using the diagnostic path in the excitation switching array (Fig 5.1).²⁹ Though careful attention and potentially additional protection circuitry may be necessary, the addition of pulse capabilities would not only allow the relaxation experiments performed in chapter 3 to be performed in tandem with saturation recovery

experiments but would also take advantage of the pulse-shaping capabilities of the AWG to access experiments not currently available in many commercial pulse spectrometers, such as long pulse saturation recovery with spin-echo detection.^{124,125,210}

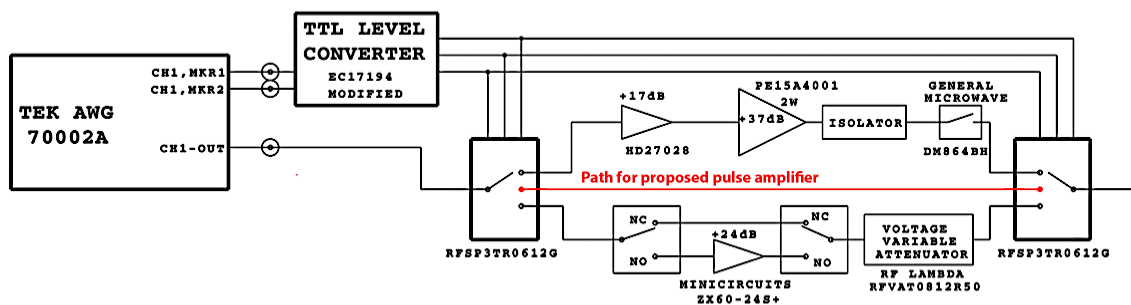


Fig 5.1: Diagram of the digital saturation recovery spectrometer, with the diagnostic microwave excitation path highlighted (red) for the possible implementation of a pulse amplifier. Adapted from McPeak et al.²⁹

In addition to expanding pulse capabilities, further expansion of the saturation recovery spectrometer may be possible with the inclusion of the low temperature systems described in chapter 4. Because the digital saturation recovery system can be operated using Bruker Flexline resonators, the low temperature closed-cycle helium system is compatible with the digital saturation recovery system and will enable more low temperature saturation recovery measurements in the future. Currently, only a few measurements have been made using the saturation recovery spectrometer at low temperatures, including the background signals present in the MD-5 sapphire resonator and a few of the other samples investigated in chapter 4. The vibrations of the closed-cycle system do not permit measurements with long acquisition times in its current state; though, implementations similar to the high-pass filters employed for low temperature RS may also be possible for saturation recovery measurements. Adaptation of the mixing frequency to above DC such that either an analog notch filter may be added or post-acquisition digital filtering may be implemented in the future.²¹¹ In the pursuit of low

temperature saturation recovery measurements, it may also be of interest to explore alternative approaches to the saturation recovery measurement such as those described in the dissertation of Dr. Laura Buchanan.²¹²

Further developing the instrument to perform RS measurements is also of great interest. The saturation recovery spectrometer was employed during low temperature measurements detailed in chapter 4, specifically in measurements of the slowly relaxing metal centers due to the requirement of non-saturating microwave B_1 in the deconvolution.^{34,36,37} The saturation recovery spectrometer may be attenuated to far lower power levels than most commercially available spectrometers, which is advantageous when performing low temperature measurements. Additional characterization of the quadrature detection system is necessary for proper RS measurements, because the orthogonality of the absorption and dispersion signals is a crucial parameter in RS data reconstruction.³⁶ Incorporating microwave switches with greater isolation may be required when attempting to accurately define the microwave power incident on the resonator at high attenuation values, specifically when operating with the microwave amplifiers bypassed *and* attenuation via the voltage-gated attenuator (Fig 5.1).²⁹ In addition to the pulse capabilities outlined above, the improvement of RS capabilities would solidify the AWG-based spectrometer as a very versatile EPR spectrometer with few experiments absent from its repertoire.

5.2 Expanded use of the X-band crossed-loop resonator

In the absence of the fast switching in the digital saturation recovery spectrometer, the AWG may be used to change the excitation frequency very quickly.

Much like the switching of power levels, if the change in excitation frequency is fast relative to the spin-lattice relaxation time of the sample of interest, measurements of spin-lattice relaxation time are made possible by this method.²¹² Because the crossed-loop resonator contains two orthogonal resonators, the changing of frequencies may be implemented such that the excitation frequency is matched to the excitation resonator while the orthogonal, detection resonator may be matched to an additional frequency offset from the excitation frequency and within the bandwidth of the overall resonator assembly and instrument as is performed in other double resonance techniques.^{16,135} When implemented correctly, the change in frequency allows for a constant microwave B_1 incident on the resonator while preserving the ability to observe recovery from saturation.²¹² Because there is no change in microwave power to the resonator, this method has the potential to greatly decrease instrument dead time that arises from amplifier saturation while expanding experimental possibilities to include the probing of spectral diffusion, molecular motion, and cross relaxation processes.^{156,166,213} Briefly, instrument deadtime in frequency-stepped experiments at X-band were as short as 200 ns; though, this was not thoroughly investigated. An in-depth explanation of frequency-stepped saturation recovery methods are given in the dissertation of Dr. Laura Buchanan.²¹²

In conjunction with the work of Dr. Buchanan at L-band frequencies, similar experiments were performed at X-band using the newly developed crossed-loop resonator described in chapter 3. Standard samples were used to probe the efficacy of frequency-stepped saturation recovery at X-band; coal, irradiated glycylglycine, and the amino acid DICPO in PVA/borate glass, crushed. The effects of the difference in frequencies of the

two resonators was examined for the three samples; and, it was found that an optimum difference in frequencies correlated well with the intensity width of the absorption peak of the EPR signal. Data from coal are shown in Fig 5.2 where a difference in resonator frequencies was approximately 62 MHz, corresponding to approximately 22 G in magnetic field. Using this frequency difference and the saturating power path in the digital saturation recovery spectrometer, the field position of observation was varied over 100 G in 1 G steps, starting from the position of maximum absorption in the integrated CW spectrum, resulting in 100 recovery curves collected. As shown in Fig 5.2, the time constant of the recovery curve is relatively constant over the intensity of the CW linewidth. Outside of this linewidth, the recovery time constant deviates from the time constant observed at the center of the line; and, is distorted by an oscillatory pattern. The oscillatory pattern occurs at field positions far from the center of the line; and, an explanation was not investigated in the current work. Additionally, results obtained with irradiated glycylglycine suggested some spectral diffusion, which was also observed by Harbridge et al. in inversion recovery measurements, when using the frequency-stepped saturation recovery methods (not shown) and merits further investigation.¹⁴⁴ As described by Dr. Laura Buchanan, frequency-stepped methods present a hybrid between traditional saturation recovery and this new saturation recovery where B_1 is *somewhat* constant.²¹² The variations in microwave B_1 relative to the experiment are further detailed in the dissertation of Dr. Laura Buchanan and merit further investigation in the future.²¹²

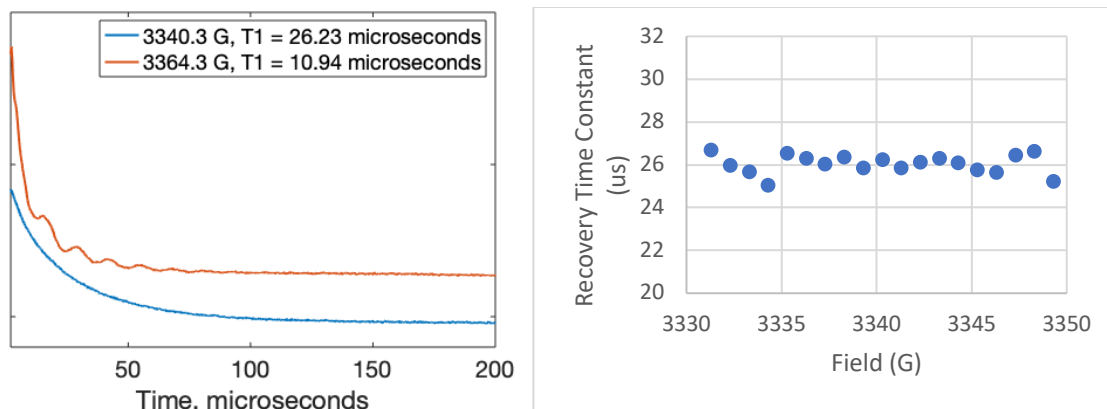


Fig 5.2: Frequency-stepped saturation recovery experiment of coal using a frequency difference of approximately 62 MHz. Saturation recovery spectra shown for two field positions (*left*). The time constant is not dependent on field position over the total linewidth (*right*).

5.3 The next challenge in low temperature rapid scan

The implementation of FSDD at low temperatures of very wide spectra described in chapter 4 is not without limitations. This work was performed using triangular waveforms operated at a continuous scan rate while incrementing the magnetic field in discrete steps.^{40,42} Functionally, when performing this experiment in the Bruker Xepr software, an array of many sequentially recorded discrete spectra is collected. The file size of the data array is very large; and, is very slow to collect and record. A spectrum collected over the full range of the magnet power supply (~9000 G) requires data acquisition times on the order of hours, which is much longer than CW data collection times of similar sweep width. Additionally, the reconstruction and deconvolution takes a very long time to compute when using consumer-grade computers or a student laptop. The time required to completely record and reconstruct a complete spectrum currently creates a challenge in the stability of the cryogen system and will need considerable automation if it is to be incorporated into a commercial spectrometer.

In the future, one could envision the development of FSDD incorporated into a commercial spectrometer similar to the current instrumental data acquisition methods of traditional CW. The main field ramping and field modulation must be synchronized in time to decrease the instrument overhead associated with discretization of the FSDD experiment. Additionally, minimizing the errors between scans would decrease the amount of spectral overlap required in the field domain, decreasing the number of spectra that need to be recorded. Less total spectral pieces would then decrease the computational time required for reconstruction because of the reduction in array size. A successful implementation in a commercial spectrometer may eliminate entirely the need for the end-user to reconstruct data and is likely deployable in current commercial spectrometers equipped with Python environments, such as the Bruker spectrometers described in this dissertation and specifically Bruker Xepr software.

The hardware requirements for triangular scan waveform synthesis are much greater than those required for sinusoidal scan waveform synthesis making variable rate FSDD the next target in development efforts. Currently, the individual spectra are aligned in the field domain and combined before performing deconvolution, requiring a constant scan rate throughout for the proper alignment of passage effects and significant spectral overlap.⁴⁰ A variable rate, or sinusoidally scanned FSDD spectrum, requires that the entirety of passage effects be recorded in a single spectrum because there are no current methods that resolve the differences in scan rate between adjacent field-stepped sinusoidally scanned spectra. Any attempts at FSDD with sinusoidal scanning in the current generation of software would require deconvolution of each spectral piece; which, has not only proven to be problematic in terms of the required baseline corrections but

also demonstrates additional spectral artifacts in the final reconstructed spectrum. Further details on the overall spectral reconstruction process and potential improvements will be published at a later date in the dissertation of Lukas Woodcock.

In addition to the work focused on improving the stepping abilities of the FSDD technique, there is additional motivation to sweep the entire 9000 G field range using a single RS field sweep. The FSDD technique is currently very limited in its ability to achieve the rapid passage regime. Current hardware capabilities do not allow larger than ~155 G sweeps; however, better current control and improved heat removal in future generations of RS spectrometers will increase the capabilities of the single-sweep RS techniques, negating the need for FSDD methods. Complimentary to the approach of widening the field sweep capabilities in the RS experiment is the application of frequency-swept RS experiments. Very wide frequency sweeps at high magnetic fields have been achieved through the use of a resonator-free EPR approach, which does not carry the same hardware requirements of the field-swept RS and FSDD experiments reported here.²¹⁴ Both of these approaches to the same problem will provide increased capabilities and access to new RS experiments in the future.

5.4 The greatest barriers to rapid scan kinetics experiments

In the reported kinetics experiments shown in chapter 2, the RS system at the University of Denver was adapted to perform kinetics experiments using the RS system described above. The basis of the spectrometer is a Bruker E500T X-band system with a SpecJet II fast digitizer and Xepr software. Locally written Python programs were implemented in the Bruker Xepr software to perform kinetics experiments, recorded as

full field-swept RS spectra with respect to reaction time. The limiting factors in terms of data collection include the onboard memory of the SpecJet II and the data transfer interface as well as the ability of the host computer to write to the internal memory. High latencies and instrumental dead times were observed in the reactions reported. To reduce the latency observed, further development of both the instrumentation and experimental design are necessary as outlined in the following two scenarios.

It is possible to envision the kinetics experiment in two scenarios, each enabling a different approach to the kinetics experiment in the context of RS. The first is an improvement to the methods utilized in chapter 2 and necessitates improvements in speed of both the writing of data in the host computer and the transfer of data between the digitizer and the host computer. The SpecJet II acts as a standalone unit, interfacing via ethernet with the host computer which is currently an older personal computer. It stores data via SATA on a hard disk drive. A much faster interface, such as an internal digitizer PCI Express card that can continuously record data to an adjacent PCI Express solid state drive in the host computer may drastically reduce the latency of data transfer such that many more complete RS spectra may be recorded with respect to reaction time. RS spectra often require significant signal averaging; and, may be limited in time by the number of averages required for adequate S/N rather than the latency of data transfer.

The second possible scenario instead requires the expansion of digitizer onboard memory; which, may also benefit from continuously recorded data across a PCI Express interface but is not immediately required. The SpecJet II has a finite memory of 65,536 spectral data points in the time axis. Therefore, all periodic cycles recorded in the RS experiment must be contained within the limit of this axis and can yield only 64 full field-

swept RS spectra (32 RS cycles) when using 1024 points per spectrum. Expansion of the digitizer memory will allow many more cycles to be recorded in the digitizer in sequence without the added latency required to transfer data to the host computer. This method achieves true RS frequency-limited latency and is the fastest possible data collection method in RS experiments and allows kinetic resolution between each individual RS spectrum recorded. However, the ability to perform spectral averaging is lost when using this approach. It is possible to perform some spectral averaging by summing subsequent spectra in blocks, sometimes called binning, but this does not utilize the speed and memory of the digitizer.

Bibliography

- (1) Hyde, J. S.; Eaton, S. S.; Eaton, G. R. EPR at work: Part 1. *Concepts Magn. Reson. Part A* 2006, *28A* (1), 1–25. <https://doi.org/10.1002/cmr.a.20047>.
- (2) Hyde, J. S.; Eaton, S. S.; Eaton, G. R. EPR at work: Part 2. *Concepts Magn. Reson. Part A* 2006, *28A* (1), 26–50. <https://doi.org/10.1002/cmr.a.20054>.
- (3) Hyde, J. S.; Eaton, S. S.; Eaton, G. R. EPR at work: Part 3. *Concepts Magn. Reson. Part A* 2006, *28A* (1), 51–75. <https://doi.org/10.1002/cmr.a.20059>.
- (4) Hyde, J. S.; Eaton, S. S.; Eaton, G. R. EPR at work: Part 4. *Concepts Magn. Reson. Part A* 2006, *28A* (1), 76–100. <https://doi.org/10.1002/cmr.a.20060>.
- (5) Poole Jr., C. P. *Electron Spin Resonance*, Second.; John Wiley & Sons, Ltd, 1983.
- (6) Quine, R. W.; Eaton, G. R.; Eaton, S. S. Pulsed EPR spectrometer. *Rev. Sci. Instrum.* 1987, *58* (9), 1709–1723. <https://doi.org/10.1063/1.1139373>.
- (7) Quine, R. W.; Eaton, S. S.; Eaton, G. R. Saturation recovery electron paramagnetic resonance spectrometer. *Rev. Sci. Instrum.* 1992, *63* (10), 4251–4262. <https://doi.org/10.1063/1.1143722>.
- (8) Quine, R. W.; Rinard, G. A.; Ghim, B. T.; Eaton, S. S.; Eaton, G. R. A 1–2 GHz pulsed and continuous wave electron paramagnetic resonance spectrometer. *Rev. Sci. Instrum.* 1996, *67* (7), 2514–2527. <https://doi.org/10.1063/1.1147206>.
- (9) Quine, R. W.; Harbridge, J. R.; Eaton, S. S.; Eaton, G. R. Design of a programmable timing unit. *Rev. Sci. Instrum.* 1999, *70* (11), 4422–4432. <https://doi.org/10.1063/1.1150088>.
- (10) Quine, R. W.; Czechowski, T.; Eaton, G. R. A linear magnetic field scan driver. *Concepts Magn. Reson. Part B Magn. Reson. Eng.* 2009, *35B* (1), 44–58. <https://doi.org/10.1002/cmr.b.20128>.
- (11) Quine, R. W.; Mitchell, D. G.; Eaton, G. R. A general purpose Q-measuring circuit using pulse ring-down. *Concepts Magn. Reson. Part B Magn. Reson. Eng.* 2011, *39B* (1), 43–46. <https://doi.org/10.1002/cmr.b.20188>.
- (12) Quine, R. W.; Mitchell, D. G.; Tseitlin, M.; Eaton, S. S.; Eaton, G. R. A resonated coil driver for rapid scan EPR. *Concepts Magn. Reson. Part B Magn. Reson. Eng.* 2012, *41B* (4), 95–110. <https://doi.org/10.1002/cmr.b.21222>.
- (13) Eaton, G. R.; Eaton, S. S.; Barr, D. P.; Weber, R. T. *Quantitative EPR*; Springer Vienna: Vienna, 2010. <https://doi.org/10.1007/978-3-211-92948-3>.
- (14) Abragam, A.; Bleaney, B. *Electron Paramagnetic Resonance of Transition Ions*; Clarendon Press: Oxford, 1970.
- (15) Weil, J. A.; Bolton, J. R. *Electron Paramagnetic Resonance*, Second.; John Wiley & Sons, Inc.: Hoboken, NJ, USA, 2007.
- (16) Schweiger, A.; Jeschke, G. *Principles of Pulse Electron Paramagnetic Resonance*; Oxford University Press: New York, 2001.
- (17) Misra, S. K. *Multifrequency Electron Paramagnetic Resonance*; Misra, S. K., Ed.; Wiley-VCH Verlag GmbH & Co. KGaA: Weinheim, Germany, 2014. <https://doi.org/10.1002/9783527672431>.
- (18) Salikhov, K. M.; Zavoiskaya, N. E. Zavoisky and the discovery of EPR. *Resonance* 2015, *20* (11), 963–968. <https://doi.org/10.1007/s12045-015-0264-6>.
- (19) Rana, S.; Chawla, R.; Kumar, R.; Singh, S.; Zheleva, A.; Dimitrova, Y.; Gadjeva,

- V.; Arora, R.; Sultana, S.; Sharma, R. K. Electron paramagnetic resonance spectroscopy in radiation research: Current status and perspectives. *J. Pharm. Bioallied Sci.* 2010, 2 (2), 80. <https://doi.org/10.4103/0975-7406.67006>.
- (20) Eaton, G. R.; Eaton, S. S.; Salikhov, K. M. *Foundations of Modern EPR*; World Scientific: River Edge, NJ, 1998.
- (21) Brustolon, M.; Giamello, E. *Electron Paramagnetic Resonance*; John Wiley & Sons, Inc.: Hoboken, NJ, USA, 2009.
- (22) Eaton, S. S.; Woodcock, L. B.; Eaton, G. R. Continuous wave electron paramagnetic resonance of nitroxide biradicals in fluid solution. *Concepts Magn. Reson. Part A Bridg. Educ. Res.* 2018, 47A (2), 1–16. <https://doi.org/10.1002/cmr.a.21426>.
- (23) Eaton, S. S.; More, K. M.; Sawant, B. M.; Boymel, P. M.; Eaton, G. R. Metal-nitroxyl interactions. 29. EPR studies of spin-labeled copper complexes in frozen solution. *J. Magn. Reson.* 1983, 52 (3), 435–449. [https://doi.org/10.1016/0022-2364\(83\)90169-5](https://doi.org/10.1016/0022-2364(83)90169-5).
- (24) Tseitlin, M.; Quine, R. W.; Rinard, G. A.; Eaton, S. S.; Eaton, G. R. Digital EPR with an arbitrary waveform generator and direct detection at the carrier frequency. *J. Magn. Reson.* 2011, 213 (1), 119–125. <https://doi.org/10.1016/j.jmr.2011.09.024>.
- (25) Yang, X.; Babakhani, A. A Single-Chip Electron Paramagnetic Resonance Transceiver in 0.13- μm SiGe BiCMOS. *IEEE Trans. Microw. Theory Tech.* 2015, 63 (11), 3727–3735. <https://doi.org/10.1109/TMTT.2015.2481895>.
- (26) Band, A.; Donohue, M. P.; Epel, B.; Madhu, S.; Szalai, V. A. Integration of a versatile bridge concept in a 34 GHz pulsed/CW EPR spectrometer. *J. Magn. Reson.* 2018, 288, 28–36. <https://doi.org/10.1016/j.jmr.2018.01.010>.
- (27) EPR Resonators. In *User Service Training Course*; Bruker Biospin; p 26.
- (28) Buchanan, L. A.; Rinard, G. A.; Quine, R. W.; Eaton, S. S.; Eaton, G. R. Tabletop 700 MHz electron paramagnetic resonance imaging spectrometer. *Concepts Magn. Reson. Part B Magn. Reson. Eng.* 2018, 48B (2). <https://doi.org/10.1002/cmr.b.21384>.
- (29) McPeak, J. E.; Quine, R. W.; Eaton, S. S.; Eaton, G. R. An x-band continuous wave saturation recovery electron paramagnetic resonance spectrometer based on an arbitrary waveform generator. *Rev. Sci. Instrum.* 2019, 90 (2). <https://doi.org/10.1063/1.5043316>.
- (30) Eaton, S. S.; Eaton, G. R. Saturation Recovery EPR. *Biomed. EPR, Part B Methodol. Instrumentation, Dyn.* 2005, 3–18. https://doi.org/10.1007/0-306-48533-8_1.
- (31) Rinard, G. A.; Quine, R. W.; Song, R.; Eaton, G. R.; Eaton, S. S. Absolute EPR Spin Echo and Noise Intensities. *J. Magn. Reson.* 1999, 140 (1), 69–83. <https://doi.org/10.1006/jmre.1999.1823>.
- (32) Eaton, G. R.; Eaton, S. S. Rapid-Scan Electron Paramagnetic Resonance. *eMagRes* 2016, 5 (4), 1529–1542. <https://doi.org/10.1002/9780470034590.emrstm1522>.
- (33) Joshi, J. P.; Eaton, G. R.; Eaton, S. S. Impact of resonator on direct-detected rapid-scan EPR at 9.8 GHz. *Appl. Magn. Reson.* 2005, 28 (3–4), 239–249. <https://doi.org/10.1007/BF03166759>.

- (34) Joshi, J. P.; Ballard, J. R.; Rinard, G. A.; Quine, R. W.; Eaton, S. S.; Eaton, G. R. Rapid-scan EPR with triangular scans and fourier deconvolution to recover the slow-scan spectrum. *J. Magn. Reson.* 2005, *175* (1), 44–51. <https://doi.org/10.1016/j.jmr.2005.03.013>.
- (35) Eaton, S. S.; Shi, Y.; Woodcock, L.; Buchanan, L. A.; McPeak, J.; Quine, R. W.; Rinard, G. A.; Epel, B.; Halpern, H. J.; Eaton, G. R. Rapid-scan EPR imaging. *J. Magn. Reson.* 2017, *280*. <https://doi.org/10.1016/j.jmr.2017.02.013>.
- (36) Tseitlin, M.; Quine, R. W.; Rinard, G. A.; Eaton, S. S.; Eaton, G. R. Combining absorption and dispersion signals to improve signal-to-noise for rapid-scan EPR imaging. *J. Magn. Reson.* 2010, *203* (2), 305–310. <https://doi.org/10.1016/j.jmr.2010.01.013>.
- (37) Harbridge, J. R.; Rinard, G. A.; Quine, R. W.; Eaton, S. S.; Eaton, G. R. Enhanced signal intensities obtained by out-of-phase rapid-passage EPR for samples with long electron spin relaxation times. *J. Magn. Reson.* 2002, *156* (1), 41–51. <https://doi.org/10.1006/jmre.2002.2526>.
- (38) Mitchell, D. G.; Quine, R. W.; Tseitlin, M.; Weber, R. T.; Meyer, V.; Avery, A.; Eaton, S. S.; Eaton, G. R. Electron spin relaxation and heterogeneity of the 1:1 α,γ -Bisdiphenylene- β -phenylallyl (BDPA)/benzene complex. *J. Phys. Chem. B* 2011, *115* (24), 7986–7990. <https://doi.org/10.1021/jp201978w>.
- (39) Quine, R. W. Scan Coil Drivers. In *Rapid Scan Workshop*; University of Denver: Denver, Colorado, 2013.
- (40) Yu, Z.; Liu, T.; Elajaili, H.; Rinard, G. A.; Eaton, S. S.; Eaton, G. R. Field-stepped direct detection electron paramagnetic resonance. *J. Magn. Reson.* 2015, *258*, 58–64. <https://doi.org/10.1016/j.jmr.2015.06.011>.
- (41) Yu, Z.; Quine, R. W.; Rinard, G. A.; Tseitlin, M.; Elajaili, H.; Kathirvelu, V.; Clouston, L. J.; Boratyński, P. J.; Rajca, A.; Stein, R.; McHaourab, H.; Eaton, S. S.; Eaton, G. R. Rapid-scan EPR of immobilized nitroxides. *J. Magn. Reson.* 2014, *247*, 67–71. <https://doi.org/10.1016/j.jmr.2014.08.008>.
- (42) Hyde, J. S.; Bennett, B.; Kittell, A. W.; Kowalski, J. M.; Sidabras, J. W. Moving difference (MDIFF) non-adiabatic rapid sweep (NARS) EPR of copper(II). *J. Magn. Reson.* 2013, *236*, 15–25. <https://doi.org/10.1016/j.jmr.2013.08.004>.
- (43) Ravera, E.; Luchinat, C.; Parigi, G. Basic facts and perspectives of Overhauser DNP NMR. *J. Magn. Reson.* 2016, *264*, 78–87. <https://doi.org/10.1016/j.jmr.2015.12.013>.
- (44) Lilly Thankamony, A. S.; Wittmann, J. J.; Kaushik, M.; Corzilius, B. Dynamic nuclear polarization for sensitivity enhancement in modern solid-state NMR. *Prog. Nucl. Magn. Reson. Spectrosc.* 2017, *102–103*, 120–195. <https://doi.org/10.1016/j.pnmrs.2017.06.002>.
- (45) Biller, J. R.; McPeak, J. E.; Eaton, S. S.; Eaton, G. R. Measurement of T_{1e} , T_{1N} , T_{1HE} , T_{2e} , and T_{2HE} by Pulse EPR at X-Band for Nitroxides at Concentrations Relevant to Solution DNP. *Appl. Magn. Reson.* 2018, *49* (11). <https://doi.org/10.1007/s00723-018-1049-3>.
- (46) Robinson, B. H.; Haas, D. A.; Mailer, C. Molecular dynamics in liquids: Spin-lattice relaxation of nitroxide spin labels. *Science* (80-). 1994, *263* (5146), 490–493. <https://doi.org/10.1126/science.8290958>.

- (47) Biller, J. R.; Elajaili, H.; Meyer, V.; Rosen, G. M.; Eaton, S. S.; Eaton, G. R. Electron spin-lattice relaxation mechanisms of rapidly-tumbling nitroxide radicals. *J. Magn. Reson.* 2013, *236*, 47–56. <https://doi.org/10.1016/j.jmr.2013.08.006>.
- (48) Yang, Z.; Bridges, M.; Lerch, M. T.; Altenbach, C.; Hubbell, W. L. *Saturation Recovery EPR and Nitroxide Spin Labeling for Exploring Structure and Dynamics in Proteins*, 1st ed.; Elsevier Inc., 2015; Vol. 564. <https://doi.org/10.1016/bs.mie.2015.07.016>.
- (49) Eaton, S. S.; Quine, R. W.; Tseitlin, M.; Mitchell, D. G.; Rinard, G. A.; Eaton, G. R. Rapid-Scan Electron Paramagnetic Resonance. In *Multifrequency Electron Paramagnetic Resonance*; Wiley-VCH Verlag GmbH & Co. KGaA: Weinheim, Germany, 2014; pp 3–67. <https://doi.org/10.1002/9783527672431.ch2>.
- (50) Eaton, S. S.; Eaton, G. R. Rapid-Scan EPR of Nitroxide Spin Labels and Semiquinones. In *Methods in Enzymology*; Elsevier Inc., 2015; Vol. 563, pp 3–21. <https://doi.org/10.1016/bs.mie.2015.06.027>.
- (51) Mitchell, D. G.; Tseitlin, M.; Quine, R. W.; Meyer, V.; Newton, M. E.; Schnegg, A.; George, B.; Eaton, S. S.; Eaton, G. R. X-band rapid-scan EPR of samples with long electron spin relaxation times: A comparison of continuous wave, pulse and rapid-scan EPR. *Mol. Phys.* 2013, *111* (18–19), 2664–2673. <https://doi.org/10.1080/00268976.2013.792959>.
- (52) Elajaili, H.; Rinard, G. A.; Yu, Z.; Mitchell, D. G.; Quine, R. W.; Eaton, S. S.; Eaton, G. R. Rapid-scan coherence signals in X-band EPR spectra of semiquinones with small hyperfine splittings. *J. Magn. Reson.* 2015, *259* (10), 20–23. <https://doi.org/10.1016/j.jmr.2015.07.010>.
- (53) Mitchell, D. G.; Rosen, G. M.; Tseitlin, M.; Symmes, B.; Eaton, S. S.; Eaton, G. R. Use of rapid-scan EPR to improve detection sensitivity for spin-trapped radicals. *Biophys. J.* 2013, *105* (2), 338–342. <https://doi.org/10.1016/j.bpj.2013.06.005>.
- (54) Mitchell, D. G.; Quine, R. W.; Tseitlin, M.; Eaton, S. S.; Eaton, G. R. X-band rapid-scan EPR of nitroxyl radicals. *J. Magn. Reson.* 2012, *214*, 221–226. <https://doi.org/10.1016/j.jmr.2011.11.007>.
- (55) Reyes, R. A.; Romanyukha, A.; Olsen, C.; Trompier, F.; Benevides, L. A. Electron paramagnetic resonance in irradiated fingernails: Variability of dose dependence and possibilities of initial dose assessment. *Radiat. Environ. Biophys.* 2009, *48* (3), 295–310. <https://doi.org/10.1007/s00411-009-0232-1>.
- (56) Romanyukha, A.; Trompier, F.; Reyes, R. A.; Christensen, D. M.; Iddins, C. J.; Sugarman, S. L. Electron paramagnetic resonance radiation dose assessment in fingernails of the victim exposed to high dose as result of an accident. *Radiat. Environ. Biophys.* 2014, *53* (4), 755–762. <https://doi.org/10.1007/s00411-014-0553-6>.
- (57) Trompier, F.; Romanyukha, A.; Reyes, R.; Vezin, H.; Queindec, F.; Gourrier, D. State of the art in nail dosimetry: Free radicals identification and reaction mechanisms. *Radiat. Environ. Biophys.* 2014, *53* (2), 291–303. <https://doi.org/10.1007/s00411-014-0512-2>.
- (58) Aretz, C. D.; McPeak, J. E.; Eaton, G. R.; Eaton, S. S.; Cowen, B. J. Mechanism of SmI₂ Reduction of 5-Bromo-6-oxo-6-phenylhexyl Methanesulfonate Studied by Spin Trapping with 2-Methyl-2-nitrosopropane. *J. Org. Chem.* 2018, *83* (17),

- 10688–10692. <https://doi.org/10.1021/acs.joc.8b01517>.
- (59) Yu, Z.; Romanyukha, A.; Eaton, S. S.; Eaton, G. R. X-Band Rapid-Scan Electron Paramagnetic Resonance of Radiation-Induced Defects in Tooth Enamel. *Radiat. Res.* 2015, *184* (2), 175. <https://doi.org/10.1667/RR14032.1.1>.
- (60) Reyes, R. A.; Trompier, F.; Romanyukha, A. Study of the stability of signals after irradiation of fingernail samples. *Health Phys.* 2012, *103* (2), 175–180. <https://doi.org/10.1097/HP.0b013e31824ac338>.
- (61) Swartz, H. M.; Burke, G.; Coey, M.; Demidenko, E.; Dong, R.; Grinberg, O.; Hilton, J.; Iwasaki, A.; Lesniewski, P.; Kmiec, M.; Lo, K. M.; Javier Nicolalde, R.; Ruuge, A.; Sakata, Y.; Sucheta, A.; Walczak, T.; Williams, B. B.; Mitchell, C. A.; Romanyukha, A.; Schauer, D. A. In vivo EPR for dosimetry. *Radiat. Meas.* 2007, *42* (6–7), 1075–1084. <https://doi.org/10.1016/j.radmeas.2007.05.023>.
- (62) Elajaili, H.; McPeak, J.; Romanyukha, A.; Aggarwal, P.; Eaton, S. S.; Eaton, G. R. Comparison of Continuous Wave and Rapid Scan X-band Electron Paramagnetic Resonance of Irradiated Clipped Fingernails. *Radiat. Prot. Dosimetry* 2016, *172* (1–3), 133–138. <https://doi.org/10.1093/rpd/new162>.
- (63) Yaemsiri, S.; Hou, N.; Slining, M. M.; He, K. Growth rate of human fingernails and toenails in healthy American young adults. *J. Eur. Acad. Dermatology Venereol.* 2010, *24* (4), 420–423. <https://doi.org/10.1111/j.1468-3083.2009.03426.x>.
- (64) Nuclear Science Abstracts. *US At. Energy Adm. United States Energy Res. Dev.* 1965, *19* (7), 2966.
- (65) Tseitlin, M.; Czechowski, T.; Quine, R. W.; Eaton, S. S.; Eaton, G. R. Background removal procedure for rapid scan EPR. *J. Magn. Reson.* 2009, *196* (1), 48–53. <https://doi.org/10.1016/j.jmr.2008.10.012>.
- (66) Buchanan, L. A.; Woodcock, L. B.; Quine, R. W.; Rinard, G. A.; Eaton, S. S.; Eaton, G. R. Background correction in rapid scan EPR spectroscopy. *J. Magn. Reson.* 2018, *293*, 1–8. <https://doi.org/10.1016/j.jmr.2018.05.010>.
- (67) Juniewicz, M.; Ciesielski, B.; Marciniak, A.; Prawdzik-Dampc, A. Time evolution of radiation-induced EPR signals in different types of mobile phone screen glasses. *Radiat. Environ. Biophys.* 2019, *58* (4), 493–500. <https://doi.org/10.1007/s00411-019-00805-1>.
- (68) Sono, M.; Hanamura, S. I.; Furumaki, M.; Murai, H.; Tori, M. First direct evidence of radical intermediates in samarium diiodide induced cyclization by ESR spectra. *Org. Lett.* 2011, *13* (21), 5720–5723. <https://doi.org/10.1021/ol202403q>.
- (69) Perkins, M. J. Spin Trapping. In *Advances in Physical Organic Chemistry*; Research Triangle Park, NC, 1980; pp 1–64. [https://doi.org/10.1016/S0065-3160\(08\)60127-6](https://doi.org/10.1016/S0065-3160(08)60127-6).
- (70) Alberti, A.; Benaglia, M.; Macciantelli, D. Mechanistic Studies of Radical-Based Processes. Use and Misuse of EPR Spectroscopy. *Org. Lett.* 2000, *2* (11), 1553–1555. <https://doi.org/10.1021/ol005741j>.
- (71) Triquigneaux, M.; Charles, L.; André-Barrès, C.; Tuccio, B. A combined spin trapping/EPR/mass spectrometry approach to study the formation of a cyclic peroxide by dienolic precursor autoxidation. *Org. Biomol. Chem.* 2010, *8* (6), 1361–1367. <https://doi.org/10.1039/b921694d>.

- (72) Reis, A.; Domingues, P.; Ferrer-Correia, A. J. V.; Domingues, M. R. M. Identification by electrospray tandem mass spectrometry of spin-trapped free radicals from oxidized 2-oleoyl-1-palmitoyl-sn-glycero-3-phosphocholine. *Rapid Commun. Mass Spectrom.* 2004, *18* (10), 1047–1058. <https://doi.org/10.1002/rcm.1444>.
- (73) Iwahashi, H.; Parker, C. E.; Mason, R. P.; Tomer, K. B. Combined Liquid Chromatography/Electron Paramagnetic Resonance Spectrometry/Electrospray Ionization Mass Spectrometry for Radical Identification. *Anal. Chem.* 1992, *64* (19), 2244–2252. <https://doi.org/10.1021/ac00043a011>.
- (74) Janzen, E. G.; Haire, D. L.; Coulter, G. A.; Stronks, H. J.; Krygsman, P. H.; Towner, R. A.; Hilborn, J. W. Locating Spin Traps in Heterogeneous Media by ¹³C NMR Spectroscopy. Investigations in SDS Micelles, DMPC Vesicles, and Rat Liver Microsomes. *J. Org. Chem.* 1989, *54* (12), 2915–2920. <https://doi.org/10.1021/jo00273a027>.
- (75) Okazaki, M.; Kuwata, K. A stopped-flow ESR study on the reactivity of some nitroxide radicals with ascorbic acid in the presence of β -cyclodextrin. *J. Phys. Chem.* 1985, *89* (21), 4437–4440. <https://doi.org/10.1021/j100267a008>.
- (76) Bobko, A. A.; Kirilyuk, I. A.; Grigor'ev, I. A.; Zweier, J. L.; Khramtsov, V. V. Reversible reduction of nitroxides to hydroxylamines: Roles for ascorbate and glutathione. *Free Radic. Biol. Med.* 2007, *42* (3), 404–412. <https://doi.org/10.1016/j.freeradbiomed.2006.11.007>.
- (77) Buettner, G. R. Spin Trapping - Electron-Spin-Resonance Parameters of Spin Adducts. *Free Radic. Bio. Med.* 1987, *3* (4), 259–303. [https://doi.org/10.1016/s0891-5849\(87\)80033-3](https://doi.org/10.1016/s0891-5849(87)80033-3).
- (78) Davies, M. J.; Gilbert, B. C.; Stell, J. K.; Whitwood, A. C. Nucleophilic substitution reactions of spin adducts. Implications for the correct identification of reaction intermediates by EPR/spin trapping. *J. Chem. Soc. Perkin Trans. 2* 1992, No. 3, 333–335. <https://doi.org/10.1039/p29920000333>.
- (79) Ghassemzadeh, L.; Peckham, T. J.; Weissbach, T.; Luo, X.; Holdcroft, S. Selective formation of hydrogen and hydroxyl radicals by electron beam irradiation and their reactivity with perfluorosulfonated acid ionomer. *J. Am. Chem. Soc.* 2013, *135* (42), 15923–15932. <https://doi.org/10.1021/ja408032p>.
- (80) Gadelha, F. R.; Hanna, P. M.; Mason, R. P.; Docampo, R. Evidence for free radical formation during horseradish peroxidase-catalyzed N-demethylation of crystal violet. *Chem. Biol. Interact.* 1992, *85* (1), 35–48. [https://doi.org/10.1016/0009-2797\(92\)90051-L](https://doi.org/10.1016/0009-2797(92)90051-L).
- (81) Stamenković, S.; Pavićević, A.; Mojović, M.; Popović-Bijelić, A.; Selaković, V.; Andjus, P.; Bačić, G. In vivo EPR pharmacokinetic evaluation of the redox status and the blood brain barrier permeability in the SOD1G93A ALS rat model. *Free Radic. Biol. Med.* 2017, *108* (March), 258–269. <https://doi.org/10.1016/j.freeradbiomed.2017.03.034>.
- (82) Yamada, K. ichi; Yamamiya, I.; Utsumi, H. In vivo detection of free radicals induced by diethylnitrosamine in rat liver tissue. *Free Radic. Biol. Med.* 2006, *40* (11), 2040–2046. <https://doi.org/10.1016/j.freeradbiomed.2006.01.031>.
- (83) Tada, M.; Ono, Y.; Nakai, M.; Harada, M.; Shibata, H.; Kiso, Y.; Ogata, T.

- Evaluation of antioxidative effects of sesamin on the in vivo hepatic reducing abilities by a radiofrequency ESR method. *Anal. Sci.* 2013, 29 (1), 89–94. <https://doi.org/10.2116/analsci.29.89>.
- (84) Marchand, V.; Charlier, N.; Verrax, J.; Buc-Calderon, P.; Levêque, P.; Gallez, B. Use of a cocktail of spin traps for fingerprinting large range of free radicals in biological systems. *PLoS One* 2017, 12 (3), 1–15. <https://doi.org/10.1371/journal.pone.0172998>.
- (85) Madden, K. P.; Taniguchi, H. An in Situ Radiolysis Time-Resolved Electron Spin Resonance Study of 2-Methyl-2-nitrosopropane Spin Trapping Kinetics. *J. Am. Chem. Soc.* 1991, 113 (15), 5541–5547. <https://doi.org/10.1021/ja00015a004>.
- (86) Kagan, H. B. Twenty-five years of organic chemistry with diiodosamarium: An overview. *Tetrahedron* 2003, 59 (52), 10351–10372. <https://doi.org/10.1016/j.tet.2003.09.101>.
- (87) Molander, G. A.; Hahn, G. Lanthanides in Organic Synthesis. 2. Reduction of α -Heterosubstituted Ketones. *J. Org. Chem.* 1986, 51 (7), 1135–1138. <https://doi.org/10.1021/jo00357a040>.
- (88) Aretz, C. D.; Escobedo, H.; Cowen, B. J. Cyclopentane Formation from Flexible Precursors Using Samarium(II) Reagents. *European J. Org. Chem.* 2018, 2018 (16), 1880–1884. <https://doi.org/10.1002/ejoc.201800102>.
- (89) Rudkin, I. M.; Miller, L. C.; Procter, D. J. Samarium enolates and their application in organic synthesis. *Organomet. Chem.* 2008, 34, 19–45. <https://doi.org/10.1039/b606111g>.
- (90) Prasad, E.; Flowers, R. A. Mechanistic study of β -substituent effects on the mechanism of ketone reduction by SmI₂. *J. Am. Chem. Soc.* 2002, 124 (22), 6357–6361. <https://doi.org/10.1021/ja020051r>.
- (91) Merino, G.; Vela, A.; Heine, T. Description of electron delocalization via the analysis of molecular fields. *Chem. Rev.* 2005, 105 (10), 3812–3841. <https://doi.org/10.1021/cr030086p>.
- (92) Nilsen, A.; Braslau, R. Nitroxide decomposition: Implications toward nitroxide design for applications in living free-radical polymerization. *J. Polym. Sci. Part A Polym. Chem.* 2006, 44 (2), 697–717. <https://doi.org/10.1002/pola.21207>.
- (93) Symons, M. C. R. Dibromonitroso benzene sulphonate spin-adducts - Why no hyperfine coupling to bromine? *Free Radic. Res.* 2000, 32 (1), 25–29. <https://doi.org/10.1080/10715760000300031>.
- (94) Picone, R. F.; Rogers, M. T. ESR study of a bromine-containing radical in γ -irradiated bromomalonamide. *J. Chem. Phys.* 1974, 61 (11), 4814–4819. <https://doi.org/10.1063/1.1681807>.
- (95) Balasivasubramanian, E.; Manoharan, P. T. Ligand hyperfine and exchange interactions in a low-spin d⁷ system. *Proc. Indian Acad. Sci. - Chem. Sci.* 1985, 95 (1–2), 141–157. <https://doi.org/10.1007/BF02839724>.
- (96) Pou, S.; Rosen, G. M.; Wu, Y.; Keana, J. F. W. Synthesis of Deuterium- and ¹⁵N-Containing Pyrroline 1-Oxides: A Spin Trapping Study. *J. Org. Chem.* 1990, 55 (14), 4438–4443. <https://doi.org/10.1021/jo00301a042>.
- (97) Spulber, M.; Schlick, S. Fragmentation of perfluorinated membranes used in fuel cells: Detecting very early events by selective encapsulation of short-lived

- fragments in β -cyclodextrin. *J. Phys. Chem. B* 2011, *115* (43), 12415–12421. <https://doi.org/10.1021/jp208177s>.
- (98) Singh, R. J.; Hogg, N.; Joseph, J.; Kalyanaraman, B. Photosensitized decomposition of S-nitrosothiols and 2-methyl-2-nitrosopropane Possible use for site-directed nitric oxide production. *FEBS Lett.* 1995, *360* (1), 47–51. [https://doi.org/10.1016/0014-5793\(95\)00065-H](https://doi.org/10.1016/0014-5793(95)00065-H).
- (99) Stoll, S.; Schweiger, A. EasySpin, a comprehensive software package for spectral simulation and analysis in EPR. *J. Magn. Reson.* 2006, *178* (1), 42–55. <https://doi.org/10.1016/j.jmr.2005.08.013>.
- (100) Venkataraman, B.; Fraenkel, G. K. Proton-deuteron hyperfine structure in paramagnetic resonance: a π - σ interaction. *J. Chem. Phys.* 1956, *24* (4), 737–740. <https://doi.org/10.1063/1.1742600>.
- (101) Chen, K.; Swartz, H. M. Oxidation of hydroxylamines to nitroxide spin labels in living cells. *Biochim. Biophys. Acta - Mol. Cell Res.* 1988, *970* (3), 270–277. [https://doi.org/10.1016/0167-4889\(88\)90126-7](https://doi.org/10.1016/0167-4889(88)90126-7).
- (102) Morin, M.; Bador, R.; Dechaud, H. Detection of europium(III) and samarium(III) by chelation and laser-excited time-resolved fluorimetry. *Anal. Chim. Acta* 1989, *219*, 67–77. [https://doi.org/10.1016/S0003-2670\(00\)80334-7](https://doi.org/10.1016/S0003-2670(00)80334-7).
- (103) Chiu, T. M.; Siemiarczuk, A.; Wong, S. K.; Bolton, J. R. Time resolution enhancement technique applied to a study of the absolute rate of reaction of ketyl radicals with a spin trap using flash photolysis electron paramagnetic resonance. *J. Phys. Chem.* 1985, *89* (15), 3343–3347. <https://doi.org/10.1021/j100261a037>.
- (104) Connelly, N. G.; Geiger, W. E. Chemical redox agents for organometallic chemistry. *Chem. Rev.* 1996, *96* (2), 877–910. <https://doi.org/10.1021/cr940053x>.
- (105) Mitchell, D. G.; Quine, R. W.; Tseitlin, M.; Meyer, V.; Eaton, S. S.; Eaton, G. R. Comparison of continuous wave, spin echo, and rapid scan EPR of irradiated fused quartz. *Radiat. Meas.* 2011, *46* (9), 993–996. <https://doi.org/10.1016/j.radmeas.2011.03.035>.
- (106) Rinard, G. A.; Quine, R. W.; Harbridge, J. R.; Song, R.; Eaton, G. R.; Eaton, S. S. Frequency Dependence of EPR Signal-to-Noise. *J. Magn. Reson.* 1999, *140* (1), 218–227. <https://doi.org/10.1006/jmre.1999.1798>.
- (107) Brik, M. E. Oxidation of secondary amines to nitroxides with oxone in aqueous buffered solution. *Tetrahedron Lett.* 1995, *36* (31), 5519–5522. [https://doi.org/10.1016/0040-4039\(95\)01053-K](https://doi.org/10.1016/0040-4039(95)01053-K).
- (108) Darabad, R. R. Exploiting Quantum Effects in Electron-Nuclear Coupled Molecular Spin Systems. In *Electron Spin Resonance (ESR) Based Quantum Computing*; Takui, T., Berliner, L., Hanson, G., Eds.; Springer US, 2016; pp 25–50.
- (109) Lin, T. S. EPR study of diphenylnitroxide in benzophenone. *J. Chem. Phys.* 1972, *57* (6), 2260–2264. <https://doi.org/10.1063/1.1678578>.
- (110) Tseitlin, M.; Eaton, S. S.; Eaton, G. R. Uncertainty analysis for absorption and first-derivative electron paramagnetic resonance spectra. *Concepts Magn. Reson. Part A* 2012, *40A* (6), 295–305. <https://doi.org/10.1002/cmr.a.21248>.
- (111) Tseitlin, M.; Rinard, G. A.; Quine, R. W.; Eaton, S. S.; Eaton, G. R. Deconvolution of sinusoidal rapid EPR scans. *J. Magn. Reson.* 2011, *208* (2), 279–

283. <https://doi.org/10.1016/j.jmr.2010.11.015>.
- (112) Stoner, J. W.; Szymanski, D.; Eaton, S. S.; Quine, R. W.; Rinard, G. A.; Eaton, G. R. Direct-detected rapid-scan EPR at 250 MHz. *J. Magn. Reson.* 2004, *170* (1), 127–135. <https://doi.org/10.1016/j.jmr.2004.06.008>.
- (113) Eaton, S. S.; Ngendahimana, T.; Eaton, G. R.; Jupp, A. R.; Stephan, D. W. Electron paramagnetic resonance of a ^{10}B -containing heterocyclic radical. *J. Magn. Reson.* 2018, *290*, 76–84. <https://doi.org/10.1016/j.jmr.2018.03.007>.
- (114) Ozawa, T.; Miura, Y.; Ueda, J. I. Oxidation of spin-traps by chlorine dioxide (ClO_2) radical in aqueous solutions: First ESR evidence of formation of new nitroxide radicals. *Free Radic. Biol. Med.* 1996, *20* (6), 837–841. [https://doi.org/10.1016/0891-5849\(95\)02092-6](https://doi.org/10.1016/0891-5849(95)02092-6).
- (115) Sang, H.; Janzen, E. G.; DuBose, C. M.; Geelsb, E. J.; Lee Poyer, J. EPR and mass spectroscopic identification of radical adducts produced spontaneously from reactions of phosgene, chlorine gas and bromine with C-phenyl N-tert-butyl nitron (PBN). *J. Chem. Soc. Perkin Trans. 2* 1996, *53* (9), 1985. <https://doi.org/10.1039/p29960001985>.
- (116) Grinbaum, B.; Freiberg, M. Bromine. In *Kirk-Othmer Encyclopedia of Chemical Technology*; John Wiley & Sons, Inc.: Hoboken, NJ, USA, 2011; Vol. 17. <https://doi.org/10.1002/0471238961.0218151310010311.a01.pub3>.
- (117) Bernofsky, C.; Bandara, B. M. R.; Hinojosa, O. Electron spin resonance studies of the reaction of hypochlorite with 5,5-dimethyl-1-pyrroline-N-oxide. *Free Radic. Biol. Med.* 1990, *8* (3), 231–239. [https://doi.org/10.1016/0891-5849\(90\)90068-T](https://doi.org/10.1016/0891-5849(90)90068-T).
- (118) McCall, A. S.; Cummings, C. F.; Bhave, G.; Vanacore, R.; Page-Mccaw, A.; Hudson, B. G. Bromine is an essential trace element for assembly of collagen IV scaffolds in tissue development and architecture. *Cell* 2014, *157* (6), 1380–1392. <https://doi.org/10.1016/j.cell.2014.05.009>.
- (119) Huisjen, M.; Hyde, J. S. A pulsed EPR spectrometer. *Rev. Sci. Instrum.* 1974, *45* (5), 669–675. <https://doi.org/10.1063/1.1686710>.
- (120) Percival, P. W.; Hyde, J. S. Pulsed EPR spectrometer, II. *Rev. Sci. Instrum.* 1975, *46* (11), 1522–1529. <https://doi.org/10.1063/1.1134096>.
- (121) Mailer, C.; Danielson, J. D. S.; Robinson, B. H. Computer-controlled pulsed electron-paramagnetic-resonance spectrometer. *Rev. Sci. Instrum.* 1985, *56* (10), 1917–1925. <https://doi.org/10.1063/1.1138445>.
- (122) Quine, R. W.; Eaton, S. S.; Eaton, G. R. Pulsed saturation recovery 250 MHz electron paramagnetic resonance spectrometer. *Concepts Magn. Reson. Part B Magn. Reson. Eng.* 2005, *26* (1), 23–27. <https://doi.org/10.1002/cmr.b.20043>.
- (123) Doll, A.; Pribitzer, S.; Tschaggelar, R.; Jeschke, G. Adiabatic and fast passage ultra-wideband inversion in pulsed EPR. *J. Magn. Reson.* 2013, *230*, 27–39. <https://doi.org/10.1016/j.jmr.2013.01.002>.
- (124) Spindler, P. E.; Zhang, Y.; Endeward, B.; Gershernzon, N.; Skinner, T. E.; Glaser, S. J.; Prisner, T. F. Shaped optimal control pulses for increased excitation bandwidth in EPR. *J. Magn. Reson.* 2012, *218*, 49–58. <https://doi.org/10.1016/j.jmr.2012.02.013>.
- (125) Kaufmann, T.; Keller, T. J.; Franck, J. M.; Barnes, R. P.; Glaser, S. J.; Martinis, J. M.; Han, S. DAC-board based X-band EPR spectrometer with arbitrary waveform

- control. *J. Magn. Reson.* 2013, 235, 95–108.
<https://doi.org/10.1016/j.jmr.2013.07.015>.
- (126) Rinard, G. A.; Quine, R. W.; Eaton, S. S.; Eaton, G. R. Frequency dependence of EPR signal intensity, 250 MHz to 9.1 GHz. *J. Magn. Reson.* 2002, 156 (1), 113–121. <https://doi.org/10.1006/jmre.2002.2530>.
- (127) Rinard, G. A.; Quine, R. W.; Eaton, S. S.; Eaton, G. R.; Froncisz, W. Relative Benefits of Overcoupled Resonators vs Inherently Low-Q Resonators for Pulsed Magnetic Resonance. *Journal of Magnetic Resonance, Series A.* 1994, pp 71–81. <https://doi.org/10.1006/jmra.1994.1090>.
- (128) Bhagyaveni, M. A.; Kalidoss, R.; Vishvaksean, K. S. *Introduction to Analog and Digital Communication*; 2016.
- (129) *IEEE Standard Definitions of Physical Quantities for Fundamental Frequency and Time Metrology--Random Instabilities*; IEEE Std, 2009; Vol. 1139–2008. <https://doi.org/10.1109/IEEESTD.2008.4797525>.
- (130) Hajimiri, A.; Limotyakis, S.; Lee, T. H. Jitter and Phase Noise in Ring Oscillators. *IEEE J. Solid-State Circuits* 1999, 34 (6), 790–804. <https://doi.org/10.1109/4.7668135>.
- (131) Herzel, F.; Razavi, B. A study of oscillator jitter due to supply and substrate noise. *IEEE Trans. Circuits Syst. II Analog Digit. Signal Process.* 1999, 46 (1), 56–62. <https://doi.org/10.1109/82.749085>.
- (132) Zanchi, A.; Bonfanti, A.; Levantino, S.; Samori, C. General SSCR vs. cycle-to-cycle jitter relationship with application to the phase noise in PLL. In *2001 Southwest Symposium on Mixed-Signal Design (Cat. No.01EX475)*; IEEE, 2001; pp 32–37. <https://doi.org/10.1109/SSMSD.2001.914933>.
- (133) Shannon, C. E. Communication in the Presence of Noise. *Proc. IRE* 1949, 37 (1), 10–21. <https://doi.org/10.1109/JRPROC.1949.232969>.
- (134) Yu, Z. Rapid Scan Electron Paramagnetic Resonance (EPR) and Digital EPR Development, Dissertation, University of Denver, 2015.
- (135) Rinard, G. A.; Quine, R. W.; McPeak, J.; Buchanan, L.; Eaton, S. S.; Eaton, G. R. An X-Band Crossed-Loop EPR Resonator. *Appl. Magn. Reson.* 2017, 48 (11–12). <https://doi.org/10.1007/s00723-017-0945-2>.
- (136) Demir, A.; Mehrotra, A.; Roychowdhury, J. Phase noise in oscillators: a unifying theory and numerical methods for characterization. *IEEE Trans. Circuits Syst. I Fundam. Theory Appl.* 2000, 47 (5), 655–674. <https://doi.org/10.1109/81.847872>.
- (137) Electronics Notes. Phase Noise Specifications https://www.electronics-notes.com/articles/basic_concepts/electronic-rf-noise/phase-noise-jitter-specifications.php (accessed Dec 19, 2019).
- (138) Göğüş, F. Z.; Karlık, B.; Harman, G. Identification of Pulmonary Disorders by Using Different Spectral Analysis Methods. *Int. J. Comput. Intell. Syst.* 2016, 9 (4), 595–611. <https://doi.org/10.1080/18756891.2016.1204110>.
- (139) Byrom, B. Personal Communication. Tektronix 2017.
- (140) High Accuracy Noise Figure Measurements Using the PNA-X Series Network Analyzer. Keysight 2014.
- (141) Phase Noise Basics https://www.ieee.li/pdf/essay/phase_noise_basics.pdf (accessed Aug 5, 2020).

- (142) Owenius, R.; Eaton, G. R.; Eaton, S. S. Frequency (250 MHz to 9.2 GHz) and viscosity dependence of electron spin relaxation of triarylmethyl radicals at room temperature. *J. Magn. Reson.* 2005, *172* (1), 168–175. <https://doi.org/10.1016/j.jmr.2004.10.007>.
- (143) Harbridge, J. R.; Eaton, G. R.; Eaton, S. S. Impact of spectral diffusion on apparent relaxation times for the stable radical in irradiated glycyl-glycine. In *Biophysics to Materials Science, Proceedings of the 1st Asia-Pacific EPR/ESR Symposium*; Kowloon, Hong Kong, 1997; pp 220–225.
- (144) Harbridge, J. R.; Eaton, S. S.; Eaton, G. R. Electron Spin-Lattice Relaxation Processes of Radicals in Irradiated Crystalline Organic Compounds. *J. Phys. Chem. A* 2003, *107* (5), 598–610. <https://doi.org/10.1021/jp021504h>.
- (145) Eaton, S. S.; Eaton, G. R. Irradiated fused-quartz standard sample for time-domain EPR. *Journal of Magnetic Resonance - Series A.* 1993, pp 354–356. <https://doi.org/10.1006/jmra.1993.1116>.
- (146) Rinard, G. A.; Quine, R. W.; Eaton, G. R. An L-Band Crossed-Loop (Bimodal) EPR Resonator. *J. Magn. Reson.* 2000, *144* (1), 85–88. <https://doi.org/10.1006/jmre.2000.2014>.
- (147) Rinard, G. A.; Quine, R. W.; Ghim, B. T.; Eaton, S. S.; Eaton, G. R. Easily tunable crossed-loop (bimodal) EPR resonator. *J. Magn. Reson. - Ser. A* 1996, *122* (1), 50–57. <https://doi.org/10.1006/jmra.1996.0173>.
- (148) Rinard, G. A.; Quine, R. W.; Biller, J. R.; Eaton, G. R. A wire-crossed-loop resonator for rapid scan EPR. *Concepts Magn. Reson. Part B Magn. Reson. Eng.* 2010, *37B* (2), 86–91. <https://doi.org/10.1002/cmr.b.20161>.
- (149) Rinard, G. A.; Quine, R. W.; Eaton, G. R.; Eaton, S. S. 250 MHz crossed-loop resonator for pulsed electron paramagnetic resonance. *Concepts Magn. Reson. Part B Magn. Reson. Eng.* 2002, *15* (1), 37–46. <https://doi.org/10.1002/cmr.10016>.
- (150) Buchanan, L. A.; Woodcock, L. B.; Rinard, G. A.; Quine, R. W.; Shi, Y.; Eaton, S. S.; Eaton, G. R. 250 MHz Rapid Scan Cross Loop Resonator. *Appl. Magn. Reson.* 2019, *50* (1–3), 333–345. <https://doi.org/10.1007/s00723-018-1078-y>.
- (151) Rinard, G. A.; Quine, R. W.; Ghim, B. T.; Eaton, S. S.; Eaton, G. R. Dispersion and superheterodyne EPR using a bimodal resonator. *J. Magn. Reson. - Ser. A* 1996, *122* (1), 58–63. <https://doi.org/10.1006/jmra.1996.0174>.
- (152) Rinard, G. A.; Eaton, G. R. Loop-Gap Resonators. In *Biomedical EPR, Part B: Methodology, Instrumentation, and Dynamics*; Eaton, S. S., Eaton, G. R., Berliner, L. J., Eds.; Springer Science, 2005; pp 19–52.
- (153) Eaton, G. R.; Eaton, S. S. Relaxation Times of Organic Radicals and Transition Metal Ions. In *Distance Measurements in Biological Systems by EPR*; Berliner, L. J., Eaton, G. R., Eaton, S. S., Eds.; Kluwer Academic Publishers: New York, 2002; pp 29–155.
- (154) Hyde, J. S.; Subczynski, W. K. Spin-Label Oximetry. In *Spin Labeling Theory and Applications*; Berliner, L. J., Reuben, J., Eds.; Plenum Press: New York, 1989; pp 399–427. <https://doi.org/10.1007/978-1-4613-0743-3>.
- (155) Freed, J. H. Theory of Multiple Resonance and ESR Saturation in Liquids and Related Media. In *Multiple Electron Resonance Spectroscopy*; Dorio, M. M., Freed, J. H., Eds.; Plenum Press: New York, 1979; pp 73–143.

- <https://doi.org/10.1007/978-1-4684-3441-5>.
- (156) Fajer, P.; Thomas, D. D.; Feix, J. B.; Hyde, J. S. Measurement of rotational molecular motion by time-resolved saturation transfer electron paramagnetic resonance. *Biophys. J.* 1986, *50* (6), 1195–1202. [https://doi.org/10.1016/S0006-3495\(86\)83562-7](https://doi.org/10.1016/S0006-3495(86)83562-7).
- (157) Biller, J. R.; Meyer, V.; Elajaili, H.; Rosen, G. M.; Kao, J. P. Y.; Eaton, S. S.; Eaton, G. R. Relaxation times and line widths of isotopically-substituted nitroxides in aqueous solution at X-band. *J. Magn. Reson.* 2011, *212* (2), 370–377. <https://doi.org/10.1016/j.jmr.2011.07.018>.
- (158) Biller, J. R.; Meyer, V. M.; Elajaili, H.; Rosen, G. M.; Eaton, S. S.; Eaton, G. R. Frequency dependence of electron spin relaxation times in aqueous solution for a nitronyl nitroxide radical and perdeuterated-tempone between 250 MHz and 34 GHz. *J. Magn. Reson.* 2012, *225*, 52–57. <https://doi.org/10.1016/j.jmr.2012.10.002>.
- (159) Moore, W. S.; Yalcin, T. The experimental measurement of exponential time constants in the presence of noise. *J. Magn. Reson.* 1973, *11* (1), 50–57. [https://doi.org/10.1016/0022-2364\(73\)90080-2](https://doi.org/10.1016/0022-2364(73)90080-2).
- (160) Clayden, N. J.; Hesler, B. D. Multiexponential analysis of relaxation decays. *J. Magn. Reson.* 1992, *98* (2), 271–282. [https://doi.org/10.1016/0022-2364\(92\)90132-Q](https://doi.org/10.1016/0022-2364(92)90132-Q).
- (161) Koenig, S. H.; Brown, R. D. Determinants of Proton Relaxation Rates in Tissue. *Magn. Reson. Med.* 1984, *1* (4), 437–449. <https://doi.org/10.1002/mrm.1910010404>.
- (162) Rengen, S. K.; Khakhar, M. P.; Prabhananda, B. S.; Venkataraman, B. Electron spin-lattice relaxation in organic free radicals in solutions. *Pure Appl. Chem.* 1972, *32* (1–4), 287–306. <https://doi.org/10.1351/pac197232010287>.
- (163) Atkins, P. W.; Kivelson, D. ESR linewidths in solution. II. Analysis of spin-rotational relaxation data. *J. Chem. Phys.* 1966, *44* (1), 169–174. <https://doi.org/10.1063/1.1726440>.
- (164) Hornak, J. P.; Freed, J. H. ELDOR Spin Echoes and Slow Motions. *Chem. Phys. Lett.* 1983, *101* (2), 115–119.
- (165) Froncisz, W.; Camenisch, T. G.; Ratke, J. J.; Anderson, J. R.; Subczynski, W. K.; Strangeway, R. A.; Sidabras, J. W.; Hyde, J. S. Saturation recovery EPR and ELDOR at W-band for spin labels. *J. Magn. Reson.* 2008, *193* (2), 297–304. <https://doi.org/10.1016/j.jmr.2008.05.008>.
- (166) Mailer, C.; Nielsen, R. D.; Robinson, B. H. Explanation of spin-lattice relaxation rates of spin labels obtained with multifrequency saturation recovery EPR. *J. Phys. Chem. A* 2005, *109* (18), 4049–4061. <https://doi.org/10.1021/jp0446711>.
- (167) Owenius, R.; Terry, G. E.; Williams, M. J.; Eaton, S. S.; Eaton, G. R. Frequency dependence of electron spin relaxation of nitroxyl radicals in fluid solution. *J. Phys. Chem. B* 2004, *108* (27), 9475–9481. <https://doi.org/10.1021/jp036020f>.
- (168) Sato, H.; Kathirvelu, V.; Fielding, A.; Blinco, J. P.; Micallef, A. S.; Bottle, S. E.; Eaton, S. S.; Eaton, G. R. Impact of molecular size on electron spin relaxation rates of nitroxyl radicals in glassy solvents between 100 and 300 K. *Mol. Phys.* 2007, *105* (15–16), 2137–2151. <https://doi.org/10.1080/00268970701724966>.

- (169) Sato, H.; Bottle, S. E.; Blinco, J. P.; Micallef, A. S.; Eaton, G. R.; Eaton, S. S. Electron spin-lattice relaxation of nitroxyl radicals in temperature ranges that span glassy solutions to low-viscosity liquids. *J. Magn. Reson.* 2008, *191* (1), 66–77. <https://doi.org/10.1016/j.jmr.2007.12.003>.
- (170) Moore, W.; McPeak, J. E.; Poncelet, M.; Driesschaert, B.; Eaton, S. S.; Eaton, G. R. ¹³C isotope enrichment of the central trityl carbon decreases fluid solution electron spin relaxation times. *J. Magn. Reson.* 2020, *318*, 106797. <https://doi.org/10.1016/j.jmr.2020.106797>.
- (171) Fielding, A. J.; Carl, P. J.; Eaton, G. R.; Eaton, S. S. Multifrequency EPR of four triarylmethyl radicals. *Appl. Magn. Reson.* 2005, *28* (3–4), 231–238. <https://doi.org/10.1007/BF03166758>.
- (172) Armstrong, B. D.; Han, S. A new model for Overhauser enhanced nuclear magnetic resonance using nitroxide radicals. *J. Chem. Phys.* 2007, *127* (10). <https://doi.org/10.1063/1.2770465>.
- (173) Enkin, N.; Liu, G.; Gimenez-Lopez, M. D. C.; Porfyrakis, K.; Tkach, I.; Bennati, M. A high saturation factor in Overhauser DNP with nitroxide derivatives: The role of ¹⁴N nuclear spin relaxation. *Phys. Chem. Chem. Phys.* 2015, *17* (17), 11144–11149. <https://doi.org/10.1039/c5cp00935a>.
- (174) Keshari, K. R.; Wilson, D. M. *Chemistry and biochemistry of ¹³C hyperpolarized magnetic resonance using dynamic nuclear polarization*; 2014; Vol. 43. <https://doi.org/10.1039/C3CS60124B>.
- (175) Kurhanewicz, J.; Vigneron, D. B.; Ardenkjaer-Larsen, J. H.; Bankson, J. A.; Brindle, K.; Cunningham, C. H.; Gallagher, F. A.; Keshari, K. R.; Kjaer, A.; Laustsen, C.; Mankoff, D. A.; Merritt, M. E.; Nelson, S. J.; Pauly, J. M.; Lee, P.; Ronen, S.; Tyler, D. J.; Rajan, S. S.; Spielman, D. M.; Wald, L.; Zhang, X.; Malloy, C. R.; Rizi, R. Hyperpolarized ¹³C MRI: Path to Clinical Translation in Oncology. *Neoplasia (United States)* 2019, *21* (1), 1–16. <https://doi.org/10.1016/j.neo.2018.09.006>.
- (176) Ardenkjær-Larsen, J. H.; Fridlund, B.; Gram, A.; Hansson, G.; Hansson, L.; Lerche, M. H.; Servin, R.; Thaning, M.; Golman, K. Increase in signal-to-noise ratio of >10,000 times in liquid-state NMR. *Proc. Natl. Acad. Sci. U. S. A.* 2003, *100* (18), 10158–10163. <https://doi.org/10.1073/pnas.1733835100>.
- (177) Popp, C. A.; Hyde, J. S. Electron-electron double resonance and saturation-recovery studies of nitroxide electron and nuclear spin-lattice relaxation times and Heisenberg exchange rates: Lateral diffusion in dimyristoyl phosphatidylcholine. *Biophysics (Oxf)*. 1982, *79* (April), 2559–2563.
- (178) Robinson, B. H.; Reese, A. W.; Gibbons, E.; Mailer, C. A unified description of the spin-spin and spin-lattice relaxation rates applied to nitroxide spin labels in viscous liquids. *J. Phys. Chem. B* 1999, *103* (28), 5881–5894. <https://doi.org/10.1021/jp990011i>.
- (179) Grinberg, N.; Rodriguez, S. *Ewing's Analytical Instrumentation Handbook, Fourth Edition*; Grinberg, N., Rodriguez, S., Eds.; CRC Press: Fourth edition / [edited by] Nelu Grinberg, Sonia Rodriguez. | Boca Raton : CRC Press, Taylor & Francis Group, 2019., 2019. <https://doi.org/10.1201/9781315118024>.
- (180) Jacobsohn, B. A.; Wangsness, R. K. Shapes of nuclear induction signals. *Phys.*

- Rev.* 1948, 73 (9), 942–946. <https://doi.org/10.1103/PhysRev.73.942>.
- (181) Bloembergen, N.; Purcell, E. M.; Pound, R. V. Relaxation effects in nuclear magnetic resonance absorption. *Phys. Rev.* 1948, 73 (7), 679–712. <https://doi.org/10.1103/PhysRev.73.679>.
- (182) Portis, A. M. Rapid passage effects in electron spin resonance. *Phys. Rev.* 1955, 100 (4), 1219–1221. <https://doi.org/10.1103/PhysRev.100.1219>.
- (183) Hyde, J. S. Magnetic resonance and rapid passage in irradiated LiF. *Phys. Rev.* 1960, 119 (5), 1483–1492. <https://doi.org/10.1103/PhysRev.119.1483>.
- (184) Hyde, J. S. Saturation of the magnetic resonance absorption in dilute inhomogeneously broadened systems. *Phys. Rev.* 1960, 119 (5), 1492–1495. <https://doi.org/10.1103/PhysRev.119.1492>.
- (185) Weger, M. Passage Effects in Paramagnetic Resonance Experiments. *Bell Syst. Tech. J.* 1960, 39 (4), 1013–1112. <https://doi.org/10.1002/j.1538-7305.1960.tb03951.x>.
- (186) Mailer, C.; Taylor, C. P. S. Rapid adiabatic passage EPR of ferricytochrome c: Signal enhancement and determination of the spin-lattice relaxation time. *BBA - Protein Struct.* 1973, 322 (2), 195–203. [https://doi.org/10.1016/0005-2795\(73\)90293-6](https://doi.org/10.1016/0005-2795(73)90293-6).
- (187) Eaton, S. S.; Eaton, G. R. Relaxation mechanisms. *eMagRes* 2016, 5 (4), 1543–1556. <https://doi.org/10.1002/9780470034590.emrstm1507>.
- (188) Kittell, A. W.; Camenisch, T. G.; Ratke, J. J.; Sidabras, J. W.; Hyde, J. S. Detection of undistorted continuous wave (CW) electron paramagnetic resonance (EPR) spectra with non-adiabatic rapid sweep (NARS) of the magnetic field. *J. Magn. Reson.* 2011, 211 (2), 228–233. <https://doi.org/10.1016/j.jmr.2011.06.004>.
- (189) Giordmaine, J. A.; Alsop, L. E.; Nash, F. R.; Townes, C. H. Paramagnetic relaxation at very low temperatures. *Phys. Rev.* 1958, 109 (2), 302–311. <https://doi.org/10.1103/PhysRev.109.302>.
- (190) Pishchik, V.; Lytvynov, L. A.; Dobrovinskaya, E. R. *Sapphire*; Springer US: Boston, MA, 2009. <https://doi.org/10.1007/978-0-387-85695-7>.
- (191) Bletskan, D. I.; Bratus', V. Y.; Luk'yanchuk, A. R.; Maslyuk, V. T.; Parlag, O. A. Determining residual impurities in sapphire by means of electron paramagnetic resonance and nuclear activation analysis. *Tech. Phys. Lett.* 2008, 34 (7), 612–614. <https://doi.org/10.1134/S1063785008070237>.
- (192) Sharoyan, E. G.; Torosyan, O. S.; Markosyan, E. A.; Gabrielyan, V. T. EPR and Spin–Lattice Relaxation of Mo³⁺ Ions in Corundum. *Phys. Status Solidi* 1974, 65 (2), 773–778. <https://doi.org/10.1002/pssb.2220650238>.
- (193) Halliburton, L. E.; Scripsick, M. P. An Investigation Of Epr Spectra In Ti-Doped Sapphire. *Laser Nonlinear Opt. Mater.* 1987, 0681 (March 1987), 109. <https://doi.org/10.1117/12.939625>.
- (194) Bader, K.; Dengler, D.; Lenz, S.; Endeward, B.; Jiang, S. Da; Neugebauer, P.; Van Slageren, J. Room temperature quantum coherence in a potential molecular qubit. *Nat. Commun.* 2014, 5 (May), 1–5. <https://doi.org/10.1038/ncomms6304>.
- (195) Lewis, G. R.; Dance, I. Crystal supramolecular motifs for [Ph₄P]⁺ salts of [M(mnt)₂]²⁻, [M(mnt)₂]⁻, [M(mnt)₂]₂²⁻, [M(mnt)₃]³⁻ and [M(mnt)₃]²⁻. *J. Chem. Soc. Dalton Trans.* 2000, No. 18, 3176–3185. <https://doi.org/10.1039/b000093k>.

- (196) Poot, J.; Wenckebach, W. T.; Poulis, N. J. A study of cross-relaxation by pulsed ENDOR. *Phys. B+C* 1980, *101* (3), 354–363. [https://doi.org/10.1016/0378-4363\(80\)90033-9](https://doi.org/10.1016/0378-4363(80)90033-9).
- (197) Bowman, M. K.; Norris, J. R. Cross relaxation of free radicals in partially ordered solids. *J. Phys. Chem.* 1982, *86* (17), 3385–3390. <https://doi.org/10.1021/j100214a024>.
- (198) Ichikawa, T.; Yoshida, H. Paramagnetic relaxation of radical species in γ -irradiated glassy ethanol solution of tetracyanoethylene anion radical. Role of spectral diffusion in cross relaxation. *J. Phys. Chem.* 1990, *94* (2), 949–953. <https://doi.org/10.1021/j100365a082>.
- (199) Livshits, V. A.; Páli, T.; Marsh, D. Relaxation Time Determinations by Progressive Saturation EPR: Effects of Molecular Motion and Zeeman Modulation for Spin Labels. *J. Magn. Reson.* 1998, *133* (1), 79–91. <https://doi.org/10.1006/jmre.1998.1434>.
- (200) Huang, C. *Rare Earth Coordination Chemistry*; Huang, C., Ed.; John Wiley & Sons, Ltd: Chichester, UK, 2010. <https://doi.org/10.1002/9780470824870>.
- (201) Standley, K. J.; Vaughan, R. A. *Electron Spin Relaxation Phenomena in Solids*; Plenum Press: New York, 1969. <https://doi.org/10.1007/978-1-4899-6539-4>.
- (202) Mangum, B. W.; Hudson, R. P. Spin-Lattice Relaxation in Some Rare-Earth Trichlorides. *J. Chem. Phys.* 1966, *44* (2), 704–713. <https://doi.org/10.1063/1.1726749>.
- (203) Brodbeck, C. M.; Iton, L. E. The EPR spectra of Gd^{3+} and Eu^{2+} in glassy systems. *J. Chem. Phys.* 1985, *83* (9), 4285–4299. <https://doi.org/10.1063/1.449041>.
- (204) Gordon, J. W.; Fain, S. B.; Rowland, I. J. Effect of lanthanide ions on dynamic nuclear polarization enhancement and liquid-state T_1 relaxation. *Magn. Reson. Med.* 2012, *68* (6), 1949–1954. <https://doi.org/10.1002/mrm.24207>.
- (205) Iton, L. E.; Turkevich, J. Electron paramagnetic resonance of rare earth ions in zeolites. *J. Phys. Chem.* 1977, *81* (5), 435–449. <https://doi.org/10.1021/j100520a015>.
- (206) Antipin, A. A.; Zapasskii, V. S.; Lunter, S. G. Laser-polarimetric studies of EPR and relaxation in glasses. *Fiz. Tverd. Tela* 1982, No. 24, 3248–3254.
- (207) Mims, W. B.; Davis, J. L. The local symmetry of Ce^{3+} , Nd^{3+} , Er^{3+} , and Yb^{3+} in frozen aqueous solutions as studied by EPR and the linear electric field effect. *J. Chem. Phys.* 1976, *65* (8), 3266–3274. <https://doi.org/10.1063/1.433500>.
- (208) Tseitlin, M.; Mitchell, D. G.; Eaton, S. S.; Eaton, G. R. Corrections for sinusoidal background and non-orthogonality of signal channels in sinusoidal rapid magnetic field scans. *J. Magn. Reson.* 2012, *223*, 80–84. <https://doi.org/10.1016/j.jmr.2012.07.023>.
- (209) Leniec, G.; Skibiński, T.; Kaczmarek, S. M.; Iwanowski, P.; Berkowski, M. Growth and EPR properties of $KSm(WO_4)_2$ and $KEr(WO_4)_2$ single crystals. *Cent. Eur. J. Phys.* 2012, *10* (2), 500–505. <https://doi.org/10.2478/s11534-011-0109-1>.
- (210) Motion, C. L.; Cassidy, S. L.; Cruickshank, P. A. S.; Hunter, R. I.; Bolton, D. R.; El Mkami, H.; Van Doorslaer, S.; Lovett, J. E.; Smith, G. M. The use of composite pulses for improving DEER signal at 94 GHz. *J. Magn. Reson.* 2017, *278*, 122–133. <https://doi.org/10.1016/j.jmr.2017.03.018>.

- (211) Tseitlin, M.; Yu, Z.; Quine, R. W.; Rinard, G. A.; Eaton, S. S.; Eaton, G. R. Digitally generated excitation and near-baseband quadrature detection of rapid scan EPR signals. *J. Magn. Reson.* 2014, *249*, 126–134.
<https://doi.org/10.1016/j.jmr.2014.10.011>.
- (212) Buchanan, L. A. Development of Low Frequency Electron Paramagnetic Resonance Methods and Instrumentation for Biological Applications, Dissertation, University of Denver, 2018.
- (213) Dalton, L. R.; Kwiram, A. L.; Cowen, J. A. Electron spin-lattice and cross relaxation in irradiated malonic acid. *Chem. Phys. Lett.* 1972, *14* (1), 77–81.
[https://doi.org/10.1016/0009-2614\(72\)87146-X](https://doi.org/10.1016/0009-2614(72)87146-X).
- (214) Laguta, O.; Tuček, M.; van Slageren, J.; Neugebauer, P. Multi-frequency rapid-scan HFEPR. *J. Magn. Reson.* 2018, *296*, 138–142.
<https://doi.org/10.1016/j.jmr.2018.09.005>.

Appendices

A.1 Matlab programs for generating waveforms for Digital SR

```
%% Chirp Pulse Synthesis Program for Resonator Tuning via FFT
```

Written by Joseph McPeak, Laura Buchanan, and Jason Yu

The purpose of this program is to synthesize a chirp waveform to observe the frequency absorption of an EPR resonator to accurately tune and perform measurements using the digital saturation recovery bridge. The function synthesizes a chirp waveform beginning at frequency `f_start` and ending at frequency `f_end` with a duration of `chirp_length`. A reference waveform will also be synthesized to be used as a local oscillator input such that the resultant FFT may be observed on any low sample rate oscilloscope after conversion to near DC levels. Both waveforms will be 100 us total length, unless modified, with 75 us of active chirping. The chirp waveform and reference waveform will be synthesized with names given by `waveform_name_1` and `waveform_name_2` respectively. These names will be visible after loading the generated files into the AWG. The filename is set by the text following "save" near the end and will be written to the folder from which this program is executed. Additional documentation on the syntax of the save function is provided by MathWorks.

```
%%
clc; clear all;

f_start = 9.3E9;           % starting frequency, in Hertz
f_end = 9.6E9;           % ending frequency, in Hertz
chirp_length = 75E-6;    % length of chirp, in seconds
fmax = 25E9;             % max sampling rate of AWG
tot_length = 100E-6;    % length of waveform, in seconds

k = (f_end-f_start)/chirp_length;
tb = 1/fmax;
x_points = tot_length/tb;
n = 0:x_points-1;
t = tb*n;
WF = zeros(size(t));
delay = 1E-6;
start_chirp = delay/tb;
np_chirp = chirp_length/tb;
end_chirp = start_chirp+np_chirp;

for kk=1:length(n);
    if n(kk)>=start_chirp && n(kk)<=end_chirp;
        WF(kk)=sin(2*pi*(f_start*t(kk)+(k.*t(kk).^2)/2));
    end
end

WF_ref = sin(2*pi*f_start*t);
marker1 = ones(size(t));
marker2 = ones(size(t));
marker3 = zeros(size(t));
```

```

enable = start_chirp;
blank = end_chirp;
marker1(enable:blank) = 1;
marker3(1:25000) = 1;

Waveform_Name_1 = 'Tune 9.3 to 9.6 MHz';
Waveform_Data_1 = WF;
Waveform_M1_1 = uint8(marker1);
Waveform_M2_1 = uint8(marker2);
Waveform_Name_2 = 'Tune 9.3 Reference';
Waveform_Data_2 = WF_ref;
Waveform_M1_2 = uint8(marker3);

save('Tune 9.3 to 9.6 GHz.mat', 'Wave*', '-v7.3');

```

```
return
```

```
%% Waveform Synthesis Program for Digital Saturation Recovery
```

Written by Joseph McPeak, Laura Buchanan, and Zhelin Yu with guidance from Bill Byrom of Tektronix

The purpose of this program is to synthesize waveforms at a fundamental frequency for operation of the digital saturation recovery bridge. The waveforms will be synthesized at an input carrier frequency and maximum sample rate of the AWG. The program will synthesize five waveforms, a pump waveform for saturation of the spin system, an observe waveform with both local oscillator and digitizer trigger delays, an observe waveform without a local oscillator delay or digitizer trigger, a reference waveform to accompany the pump waveform, and a single reference waveform for use with both observe waveforms. Reference waveforms are synthesized and employed as input to the local oscillator to record the signal using low sample rate digitizers after conversion to near DC levels. A reference waveform is synthesized to accompany the pump waveform; however, the reference waveform is set to zero output volts to protect the detection system during the pump waveform. The purpose of the local oscillator delay is to prevent saturation of the video amplifier by increasing the dead time of the detection system relative to the experiment and is useful when using resonators with very high Q values. A trigger delay is included to allow all instrumental artifacts to equilibrate before data is recorded in the digitizer. All timing settings and delays are specified in samples from the AWG. The effective length of the delay, in seconds, may be calculated by dividing the delay by the sampling rate. Waveform length is calculated based on a floating number of points per cycle such that the beginning and ending cycles of the waveform are congruent and do not contribute to the source noise. The current default naming scheme may be seen following the save command and may be adjusted. More information may be found in McPeak et al 2019.

```
%%
```

```
clc; clear all;
```

```
fs = 25E9; % Max Sampling rate of AWG
f1 = 9.41554E9; % Carrier frequency
```

```

trig_delay = 37500;           % Trigger delay, in samples
trig = 25000;                % Trigger length, in samples
LO_delay = 25000;           % LO delay, in samples
pump_length = 500000;       % Length of pump waveform, in samples

G = gcd(fs,f1);
N = fs/G;
i = 1:N;
dt = 1/fs;
t = i*dt;
WF1 = sin(2*pi*f1*t);

%% Markers
marker = WF1;
marker_low = marker*0;
marker(1:length(marker)) = 1;
marker_high = marker;
marker_trig = marker_low;
marker_trig(trig_delay:trig_delay+trig) = 1;

%% Create Waveform 1 (Double), pump

WFpump = WF1(1:pump_length);
marker_pump_high = marker_high(1:length(WFpump));
marker_pump_low = marker_low(1:length(WFpump));
Waveform_M1_1 = uint8(marker_pump_high);
Waveform_M2_1 = uint8(marker_pump_low);
Waveform_Name_1 = 'pump';
Waveform_Data_1 = WFpump;
save('pump', 'Wave*', '-v7.3');

%% Create Waveform 2 (Double), pump reference

Waveform_M1_1 = uint8(marker_pump_low);
Waveform_M2_1 = uint8(marker_pump_low);
Waveform_Name_1 = 'pumpref0v';
Waveform_Data_1 = WFpump*0;
save('pumpref0v', 'Wave*', '-v7.3');

%% Create Waveform 2 (Double), observe

Waveform_M1_1 = uint8(marker_high);
Waveform_M2_1 = uint8(marker_high);
Waveform_Name_1 = 'observe';
Waveform_Data_1 = WF1;
save('observe', 'Wave*', '-v7.3');

%% Create Waveform 2 (Double), observe reference

Waveform_M1_1 = uint8(marker_trig);
Waveform_M2_1 = uint8(marker_low);
Waveform_Name_1 = 'observeref_0v';
Waveform_Data_1 = WF1;
WF2 = WF1;
WF2(1:LO_delay) = 0;

```

```
Waveform_Data_1 = WF2;
save('observeref_0v', 'Wave*', '-v7.3');

%% Create Waveform 2 (Double), observe reference without trigger or
delays

Waveform_M1_1 = uint8(marker_low);
Waveform_M2_1 = uint8(marker_low);
Waveform_Name_1 = 'observeref_notrig';
Waveform_Data_1 = WF1;
save('observeref_notrig', 'Wave*', '-v7.3');

return
```

A.2 List of equations by section

Section	Equation	Equation number
1.1	$\Delta E = h\nu = g\mu_B B_0$	Eq. 1.1
1.1	$\mu_B = \frac{ e \hbar}{2m_e} = 9.27400949(80) \times 10^{-24} \text{ JT}^{-1}$	Eq. 1.2
1.1	$\frac{n_{\text{antiparallel}}}{n_{\text{parallel}}} = e^{-\frac{\Delta E}{kT}}$	Eq. 1.3
1.1	$N_{HFS} = \prod_i (2n_i l_i + 1)$	Eq. 1.4
1.2.1	$V_S = \chi'' \eta Q \sqrt{P_A Z_0}$	Eq. 1.5
1.2.1	$Q = \frac{v}{\Delta v}$	Eq. 1.6
1.2.3	$s = \frac{\gamma_e^2 B_1^2 T_{1e} T_{2e}}{1 + \gamma_e^2 B_1^2 T_{1e} T_{2e}}$	Eq. 1.7
2.3.1	$a_s = \pi f_s B_m \text{ G s}^{-1}$	Eq. 2.1
2.3.1	$a_t = 2 f_s B_m \text{ G s}^{-1}$	Eq. 2.2
2.3.1	$Q = \frac{v}{\Delta v} = \frac{v}{BW_{res}}$	Eq. 2.3
2.3.1	$BW_{RS} = \frac{v}{2Q}$	Eq. 2.4

2.3.1	$BW_{sig} = \frac{N\gamma}{2\pi} \alpha T_2^*$	Eq. 2.5
2.3.1	$T_2^* = T_2 = \frac{2}{\sqrt{3}\gamma\Delta B_{pp}}$	Eq. 2.6
2.3.1	$BW_{sig} = \frac{Na}{\sqrt{3}\pi\Delta B_{pp}}$	Eq. 2.7
3.1.5	$F_{1,2\dots n} = F_1 + \frac{(F_2 - 1)}{G_1} + \frac{(F_3 - 1)}{G_1 G_2} + \dots + \frac{(F_n - 1)}{G_1 G_2 \dots G_{n-1}}$	Eq. 3.1
3.1.5	$P_{in,cold} = -174 + (10 * \log(\text{Bandwidth}))$	Eq. 3.2
3.1.5	$\text{Gain} = \frac{\Delta P_{out}}{\Delta P_{in}}$	Eq. 3.3
3.1.5	$P_{in} + \text{Gain} = \text{Expected } P_{out}$	Eq. 3.4
3.1.5	$\text{Measured } P_{out} - \text{Expected } P_{out} = \text{Noise Figure (NF)}$	Eq. 3.5
3.3	$Q = \pi\nu\tau$	Eq. 3.6
3.3.1	$\theta = \gamma B_1 t_p$	Eq. 3.7
3.4	$\frac{dn}{dt} = -\frac{(n - n_0)}{T_1}$	Eq. 3.8
3.4	$\varepsilon = 1 - \rho s f \frac{ \gamma_s }{\gamma_l}$	Eq. 3.9

4.1.1	$\frac{B_1}{\left[\left(\frac{dB}{dt}\right) (T_1 T_2)^{\frac{1}{2}}\right]} < 1$	Eq. 4.1
-------	---	---------

A.3 List of abbreviations and common names

ACAC - acetylacetonate
A/D – analog to digital conversion
AFC – automated frequency control
API – application programming interface
AWG – arbitrary waveform generator
 B_0 – main magnetic field
 B_1 – microwave magnetic field or excitation field
BDPA – 1,3- bisdiphenylene-2-phenylallyl
BMPO - 5-tert-Butoxycarbonyl-5-methyl-1-pyrroline-N-oxide
 BW_{res} – resonator bandwidth
 BW_{RS} – resonator bandwidth available for rapid scan experiments
 BW_{sig} – signal bandwidth
Carboxyproxyl – 3-(carboxy)-2,2,5,5-tetramethyl-1-pyrrolidinyloxy
CLR – crossed-loop resonator
CTPO – 3-carbamoyl-2,2,5,5-tetramethyl-3-pyrroline-1-yloxy
CW – continuous wave
D/A – digital to analog conversion
dB – decibels, a measure of intensity with a logarithmic scale
DICPO - 7-aza-dispiro-hexadecane-7-oxyl-15-amino-15-carboxylic acid
DMPO – 5,5-dimethyl-1-pyrroline N-oxide
DNP – dynamic nuclear polarization
DPNO – diphenyl nitroxide
DPPH – 2,2-diphenyl-1-picrylhydrazyl
DU – University of Denver
DSR – Digital saturation recovery
DTBN – di-tert-butyl-nitroxide
DTC – diethyldithiocarbamate
ENDOR – electron nuclear double resonance
EPR – electron paramagnetic resonance
FID – free induction decay
FSDD – field-stepped direct-detection
G – gauss, a measure of magnetic field strength
Galvinoxyl - 2,6-di-tert-butyl- α -(3,5-di-tert-butyl-4-oxo-2,5-cyclohexadien-1-ylidene)-p-tolyloxy
G/s – gauss per second, a measure of magnetic field scan rate
Gy – grey, a measure of total accumulated radiation
HE – Heisenberg exchange
ID – inner diameter
LGR – loop gap resonator
LiPc – lithium phthalocyanine
Litz – wire constructed of many smaller wires for the conduction of AC current
LNA – low noise amplifier
MIS – mechanically induced signal

MNP – 2-methyl-2-nitrosopropane
Ms – mesylate
NMR – nuclear magnetic resonance
OD – outer diameter
PBN – N-tert-butyl- α -phenylnitrone
PCI – peripheral component interconnect, a data transfer interface
PDT – 4-oxo-2,2,6,6-tetramethyl piperidine-d₁₆-oxyl
POBN – α -(4-pyridyl-1-oxide)-N-tert-butyl nitrone
PVA – polyvinyl alcohol
RADAR – radio detection and ranging
RIS – radiation induced signal
RS – rapid scan
Sa/s – samples per second, a measure of digital sampling rate
SATA – serial advanced technology attachment, a data transfer interface
SMA – subminiature version A connector
S/N – signal to noise ratio
SPU – signal processing unit
SR – saturation recovery
T – tesla, a measure of magnetic field strength
T₁ – spin-lattice or longitudinal relaxation
T₂ – spin-spin or transverse relaxation
T_m – phase memory time
Tempol – 4-hydroxy-2,2,6,6-tetramethylpiperidine 1-oxyl
THF – tetrahydrofuran
TTL – transistor-transistor logic

A.4 List of publications and presentations

Publications

McPeak, J. E., Höfer, P., Kacprzak, S., Carl, P., Weber, R., Eaton, S. S., Eaton, G. R., Rapid scan electron paramagnetic resonance (EPR) of highly resolved hyperfine of organic radicals. (2020, in preparation).

McPeak, J. E., Woodcock, L. B., Quine, R. W., Rinard, G. A., Eaton, S. S., Eaton, G. R., Field-stepped direct-detection EPR of transition metal ions at temperatures between 4-10 K. (2020, in preparation).

McPeak, J. E., Alexander, D., Joseph, C., Eaton, S. S., Eaton, G. R., Electron spin relaxation of Tb^{3+} and Tm^{3+} ions. *Applied Magnetic Resonance*, (2020, in review).

Moore, W., McPeak, J. E., Poncelet, M., Driesschaert, B., Eaton, S. S., Eaton, G. R., ^{13}C isotope enrichment of the central trityl carbon decreases fluid solution electron spin relaxation times. *Journal of Magnetic Resonance*, 318, 106797 (2020).

McPeak, J. E., Quine, R. W., Eaton, S. S., Eaton, G. R., An X-band continuous wave saturation recovery electron paramagnetic resonance spectrometer based on an arbitrary waveform generator, *Review of Scientific Instruments*, 90, 024102, (2019).

Aretz, C. D.*, McPeak, J. E.*, Eaton, G. R., Eaton, S. S., Cowen B. J., Mechanism of Sml_2 reduction of 5-bromo-6-oxo-6-phenylhexyl methanesulfonate studied by spin trapping with 2-methyl-2-nitrosopropane, *Journal of Organic Chemistry*, 83(17), 10688-10692, (2018).

*C.D.A and J.E.M contributed equally.

Biller, J. R., McPeak, J. E., Eaton, S. S., Eaton, G. R., Measurement of T_{1e} , T_{1N} , T_{1HE} , T_{2e} , and T_{2HE} by Pulse EPR at X-band for nitroxides at concentrations relevant to solution DNP, *Applied Magnetic Resonance*, 49(11), 1235-1251, (2018).

Rinard, G. A., Quine, R. W., McPeak, J., Buchanan, L., Eaton, S. S., Eaton, G. R., An X-band crossed-loop EPR resonator, *Applied Magnetic Resonance*, 48(11-12), 1219-1226, (2017).

Eaton, S. S., Shi, Y., Woodcock, L., Buchanan, L. A., McPeak, J., Quine, R. W., Rinard, G. A., Epel, B., Halpern, H. J., Eaton, G. R., Rapid-Scan EPR Imaging, *Journal of Magnetic Resonance*, 280, 140-148, (2017).

Eaton, S. S., Huber, K., Elajaili, H., McPeak, J., Eaton, G. R., Longobardi, L. E., Stephan, D. W., Electron spin relaxation of a boron-containing heterocyclic radical, *Journal of Magnetic Resonance*, 276, 7-13, (2017).

Elajaili, H., McPeak, J., Romanyukha, A., Aggarwal, P., Eaton, S. S., Eaton, G. R., Comparison of Continuous Wave and Rapid Scan X-band Electron Paramagnetic Resonance of Irradiated Clipped Fingernails, *Radiation Protection Dosimetry*, 172(1-3), 133-138, (2016).

Elajaili, H., Biller, J. R., Rosen, G. M., Kao, J. P., Tseytlin, M., Buchanan, L. A., Rinard, G. A., Quine, R. W., McPeak, J., Shi, Y., Eaton, S. S., Eaton, G. R., Imaging Disulfide Dinitroxides at 250 MHz to Monitor Thiol Redox Status. *Journal of Magnetic Resonance*, 260, 77-82, (2015).

McPeak, J., Pohl, M. D., Von Nagy, C. L., Hurst, H., Rowe, M. W., Padilla Gutierrez, E. F., Russ, J., Physicochemical Study of Black Pigments in Prehistoric Paints from Oxtotitlán Cave, Guerrero, Mexico. *Archaeological Chemistry VIII, American Chemical Society*. 1147: 123-143, (2013).

Presentations

Workshop on Low Field Magnetic Resonance, NIST Boulder, August 12-13, 2019
Rapid scan EPR imaging experiments at 250 MHz, 700 MHz, and 1 GHz

60th Rocky Mountain Conference on Magnetic Resonance, July 21-25, 2019
Fast full-spectrum kinetics experiments by rapid scan EPR at X-band

International EPR Society/SharedEPR Summer School, July 17-21, 2019
Instructor, CW-EPR Basics, Rapid-Scan EPR

University of Denver Research and Scholarship Showcase, May 8, 2019
Field-stepped direct detection electron paramagnetic resonance of the rare earth ions

59th Rocky Mountain Conference on Magnetic Resonance, July 22-27, 2018
Field-stepped-direct-detection electron paramagnetic resonance (FSDD-EPR) at low temperatures using a metal free cryostat

University of Denver Research and Performance Summit, April 27, 2018
Probing the mechanism of Samarium mediated organic reductions by the trapping of transient reaction intermediates

20th Meeting of the International Society of Magnetic Resonance, July 23-28, 2017
Comparison of AWG-based saturation recovery with conventional saturation recovery and inversion recovery

EPR-2017, July 16-22, 2017
Investigating the mechanism of Samarium reduction via spin-trapping with PBN and MNP

58th Rocky Mountain Conference on Magnetic Resonance, July 17-21, 2016
An AWG-based digital X-band saturation recovery spectrometer for spin lattice relaxation measurements

University of Denver Research and Performance Summit, January 28, 2016
Improved detection of signals in fingernails that monitor potentially harmful radiation doses

245th Meeting of the American Chemical Society, April 7-11, 2013
Chemical analyses of black pigments from Olmec pictographs in southern Mexico